Diffusion-controlled electrolysis at a porous electrode, with gas injection

Peter Leonard Duffield

1966

Imperial College of Science and Technology

Preface

The work described here was one of a number of projects undertaken by research workers at Imperial College to investigate the use of barbotage* to simulate the hydrodynamics of boiling. The proposal to measure electrolytic mass transfer rates at a porous surface during barbotage was made by my Supervisor, Professor D.B. Spalding, to whom I owe sincere thanks for his guidance and advice throughout the project.

As far as I am aware, the work described here is original research and the application of the electrolytic technique to barbotage is, to the best of my knowledge, unique.

The major part of the first year was spent in gaining an understanding of the mass transfer technique and in developing it for the present application. In this connection I would like to thank Professor J.G.Hills, now in the Chemistry Department of the University of Southampton, who made many helpful suggestions which greatly assisted me in the early stages of the project. Special thanks are also due to Dr. A. Iribarne, at present at Imperial College, who gave much valuable advice and

---

* Barbotage is defined as the bubbling of a gas through a drilled or porous surface into a liquid.

assistance during the later stages of the experimental work.

I would like to record my gratitude to the Science Research Council (then the Department of Scientific and Industrial Research), whose financial support made it possible for me to pursue this course of study, and to the Ministry of Aviation, for the financial resources for equipment which were available.

Summary

The purpose of the work reported here is to investigate, experimentally, the effects of various parameters on the diffusion-controlled, electrolytic mass-transfer coefficient at a porous cathode, through which a gas is injected into a liquid. The electrolytic reaction employed was the cathodic reduction of ferricyanide to ferrocyanide.

It is found that the mass-transfer coefficient initially increases with the gas injection rate, because of the stirring action of the bubbles in the region of high concentration gradients near the mass-transfer surface. Above a certain critical gas injection rate, however, the mass transfer coefficient decreases; this decrease is similar to the fall in the heat-transfer coefficient which occurs in boiling as the burn-out condition is approached.

Dimensionless equations are derived from the results of the experimental work, relating the sub-critical conductance, the maximum conductance and the critical gas injection rate to independent variables. The independent variables in the investigation include gas, liquid and geometrical parameters.

From the analysis, it can be seen that the results fall into two distinct regions, one a 'pore-controlled'

region, in which the mass-transfer coefficient and the critical gas-injection rate are influenced by the gas viscosity and the dimensions of the pores in the cathode and the other, a region independent of the viscous forces in the pores.

The results obtained are compared with those of other investigations into simulated boiling-phenomena and with boiling heat transfer results. Good agreement from the critical gas flow rate comparisons lends support to the 'hydrodynamic crisis' theories for boiling burn-out. The results from the sub-critical region of this and other investigations compare favourably with the predictions of the turbulent kinetic energy model proposed in the theoretical section of this thesis, indicating that a similar approach in boiling could lead to a more general nucleate boiling correlation than exists at the present time.

Contents

		Page
Preface		1
Summary		3
Chapter 1	Introduction	6
Chapter 2	The electrolytic mass transfer technique	15
Chapter 3	Theoretical aspects of the investigation	28
Chapter 4	Description of apparatus	43
Chapter 5	Experimental procedure	52
Chapter 6	Reduction and presentation of data	70
Chapter 7	Analysis of results	99
Chapter 8	Discussion of results	153
Chapter 9	Conclusions	183
Notation		187
Literature cited		191
Appendix I	Calibration of instruments	204
Appendix II	Measurements of gas, liquid and geometrical properties	211
Appendix III	Table of experimental data	231

Chapter 1 Introduction

1.1 Background

Boiling is a complex process and, because of its importance as a means of transferring heat at high heat flux densities, has been the subject of numerous investigations. The simulation of the hydrodynamics of boiling by barbotage or by electrolytic gas evolution has provided useful information towards understanding the mechanisms involved in boiling.

Beginning with Yamagata in 1953 [77], several investigators have demonstrated that a considerable increase in the film heat transfer coefficient, can be achieved by generating gas bubbles on the heat transfer surface. These findings lend support to the theory that the stirring-action of the bubbles in the thermal boundary layer is at least partially responsible for the high heat transfer coefficients experienced in nucleate boiling.

A number of these investigations have also shown that above a certain critical value, a further increase in the rate of gas evolution from the heat transfer surface results in a decrease in the heat transfer coefficient. A similar decrease in the heat transfer coefficient occurs in boiling, as the burn-out heat flux is approached. It is postulated [41, 45, 37, 78] that both in boiling and in simulated boiling, the decrease in the heat transfer

coefficient is a result of a loss of stability of the liquid phase in the two-phase boundary layer, causing a continuous layer of gas or vapour to form over the heat-transfer surface.

Experiments have been carried out [41, 45, 37, 75] in both boiling and barbotage in which purely hydrodynamic measurements were made to detect the sudden change in the structure of the two-phase boundary layer. The results obtained show that a transition or crisis does in fact occur at a gas or vapour generation rate predicted by the burn-out correlations.

Apart from the hydrodynamic transition just described, very few comparisons of the hydrodynamics of boiling and of simulated boiling have appeared in the literature. It was, however, noted by Zuber [78] and by Wallis [74] that similar flow regimes are visible in both boiling and barbotage, as the vapour/gas generation rate is increased from zero to the critical point. These two authors also show that the same basic equation is used to describe the initiation of bubble growth in the two cases [78, 72]. Wallis further points out similarities in the bubble growth rates and in the growth times.

In the following section, a more detailed examination is made of previous investigations in which a boiling simulation was employed.

1.2 Previous investigations into the simulation of boiling, by barbotage and gas evolution.

In order to provide a framework for the presentation of the different types of simulated-boiling experiments, the following means of classifying them has been devised. Firstly a division is made according to the quantity measured and secondly according to the method of bubble generation, as set out below.

(i) Measurements of heat transfer coefficients. This can be further sub-divided into bubble generation by barbotage and bubble generation by electrolytic gas evolution.

(ii) Measurements relating to purely hydrodynamic quantities.

In class (i), the object of all the investigators was to relate the heat-transfer coefficient to other quantities, such as rate of bubble generation, and also, in most cases, to show the existence of a critical superficial velocity at which the heat-transfer coefficient was a maximum.

No sub-division is required of class (ii) since, in all cases, the bubbles were generated by barbotage and the sole object was to investigate the critical superficial velocity.

Table 1.1 presents investigations in which heat transfer measurements were made (class (i)) and Table 1.2 includes

the purely hydrodynamic investigations (class (ii)).

Investigations involving a net flow of liquid through the test section (simulated forced-convection boiling), are not included in this review. The work of Frea et al [24] is also excluded because their heat-transfer coefficient versus superficial velocity measurements were carried out at constant heat flux rather than at constant surface temperature. Insufficient data are presented for the necessary constant surface-temperature information to be extracted by cross-plotting.

1.3 Purpose of the present work.

The present investigation concerns the measurement of diffusion-controlled mass transfer coefficients at a porous electrode. The electrode takes the form of horizontal disc, through which a gas is injected at various rates into a pool of liquid. The objects of the investigation are:

1. To present dimensionless relations connecting (a) the mass transfer conductance in the sub-critical region, (b) the critical gas injection rate at which the maximum conductance occurs and (c) the maximum conductance, with relevant fluid and geometrical properties.

2. To compare these relations with those valid for other barbotage phenomena, and for boiling.

An electrolytic mass transfer technique is employed; this is fully described in the next chapter. One advantage of this technique is that results can be obtained more quickly than with similar heat transfer experiments. For this reason it has been possible to vary a large number of parameters in the investigation. The parameters varied include (i) the gas properties, by using different gases and by varying the system pressure (ii) the liquid properties, by varying the concentration of sodium hydroxide in the electrolyte solution and by varying the electrolyte temperature, (iii) various geometrical parameters, including porous electrode diameter, pool diameter, pool depth, and grade and thickness of the porous materials.

A major limitation of the electrolytic mass transfer technique is in the liquid property variation, which is restricted to solutions compatible with the electrolytic reaction. As a result, the lowest attainable Schmidt number

$$\left(\equiv \frac{\text{viscosity}}{\text{density} \times \text{diffusion coefficient}} \right)$$

is about 10^3.

1.4 Layout of the thesis.

A description of the electrolytic technique is provided in Chapter 2; the principles of the technique are fully explained and also how it can be advantageously

employed in the understanding of convective processes.

The remainder of the thesis may be divided into four parts, thus:

Theory

Experiment

Analysis

Comparisons.

In the theoretical chapter (Chapter 3), no attempt is made at a complete theoretical analysis of the problem; instead each of the three dependent variables of interest, namely the sub-critical conductance, the critical superficial velocity and the maximum conductance, are expressed non-dimensionally as unknown functions of independent dimensionless groups. These dimensionless relations, appearing as equations 3.9, 3.12 and 3.13, provide the basis for the experimentation.

The experimental work is dealt with fully in Chapters 4, 5 and 6, beginning with a description of the apparatus used. Chapter 5, Experimental Procedure, lists the independent variables of the investigation and links them with the dimensionless groups derived in Chapter 3. In Chapter 6, the experimental readings are processed and presented in Figures 6.2 to 6.18, as conductances versus superficial velocity.

The analysis of the data, in Chapter 7, provides the relationships between the proposed dependent and independent

dimensionless groups; the final results appear as equation 7.5 for the sub-critical conductance, as equation 7.13 for the critical superficial velocity and as equation 7.22 for the maximum conductance.

It was found convenient to provide some explanations and discussion of the results in the Analysis chapter.

In Chapter 8, the results obtained from this investigation are compared with those of other barbotage investigations and with boiling results.

The number of each equation, figure and table begins with the number of the chapter in which it appears. Figures are grouped at the end of each chapter. References and notation appear at the end of the thesis, before the appendices. Calibrations, measurements of liquid, gas and geometrical properties and tables of raw data are all included in appendices.

Authors	Details of bubble generation	Gases employed	Liquids employed	Other parameters varied	Range of N_{Pr} at surface conditions	Remarks concerning the maximum heat transfer coefficient
Gose, Acrivos & Petersen [28]	Barbotage with drilled and sintered plates	Air Helium	Water Ethylene Glycol Tellus Oil 15 Tellus Oil 69	Hole or pore diameter Porosity Plate orientation	3.4 to 574	Maximum heat transfer coefft. achieved with sintered plates but not with drilled plates
Akturk [2]	Barbotage with sintered plates	Air	Water	Surface temperature Plate diameter, Pool diameter	3.3 to 6.2	Maximum achieved in all cases
Mixon, Chon & Beatty [47]	Electrolytic gas evolution from a flat plate	Hydrogen	.05N sodium hydroxide solution	Surface temperature	2.5 to 8.1	Very low superficial velocities (max.1.7 x 10^{-4} ft/s). No maximum heat transfer coefficient.
Bhand, Patgaonkar & Gogate [8]	Electrolytic gas evolution from a fine wire	Oxygen	'Weak electrolyte'	Bulk temperature	Approx. 2 to 10	Low superficial velocities. One or two maxima achieved in heat transfer coefficient

Table 1.1 Summary of simulated boiling experiments by other workers in which heat transfer measurements were made.

Author	Details of gas injection	Injected fluids	Heavier phase fluids	Other parameters varied	Method of detecting hydrodynamic crisis
Kutateladze and Moskvicheva [41]	Perforated plates	Water	Mercury Carbon tetrachloride	Porosity Pool depth Hole diameter	Piezometers and Gammascope
Malenkov [45]	Sintered plates	Nitrogen	Water Ethyl alcohol Benzene	None	Measurements of: 1. electrical conductivity and 2. dialectric constant of the two-phase boundary layer.
Kutateladze [37]	Sintered plate	Air	Water Methyl alcohol Ethyl alcohol Acetone Benzene Carbon tetrachloride	None	Electrical conductivity measurements
Wallis [75]	Woven mesh plate	Air Freon-12	Water Carbon tetrachloride Methyl alcohol Iso-octane Benzene	System pressure	Counting the number of liquid droplets in the spray above the pool surface

Table 1.2 Summary of experiments by other workers in which the hydrodynamic crisis was investigated.

Chapter 2 The Electrolytic Mass Transfer Technique

The aims of this chapter are:

(i) To explain the principles of the electrolytic process and to examine the requirements necessary for the process to be diffusion-controlled.

(ii) To indicate the similarities between electrolytic mass transfer and convective heat transfer.

(iii) To enumerate the advantages of the electrolytic mass transfer method compared with methods in which heat transfer measurements are made.

2.1 The diffusion-controlled electrolytic reaction

2.1.1 Description of the electrolytic process

In order to understand the process of electrolysis it is necessary first to appreciate the concept of the ionic theory as applied to electrolytes. According to this theory, a proportion of the molecules of an electrolyte in solution dissociate into two or more separate particles, called ions. In the simple case of a binary electrolyte, one ion possesses a negative charge and the other a positive charge.

A reaction of ions at an electrode occurs when the applied potential difference across the electrode/electrolyte interface exceeds a certain value, known as the decomposition potential (a function of the reacting ion

species and the electrode material). At a cathode the reaction results in a transfer of electrons from the electrode to the reacting ions; at an anode, electrons are transferred from the reacting ions to the electrode. Thus, there is a net transfer of electrons from the cathode to the anode. This form of electron transport is referred to as an ionic current.

To sustain the electrode reaction, a constant supply of the reacting ions must be maintained to both anode and cathode. In certain cases, the electrode reactions may be so rapid that the rate of the process is controlled by the rate at which the reacting ions can be supplied to the electrodes. If, in addition, one electrode is larger than the other, the mass flux of ions to that electrode is greatly reduced and the rate of the process is limited by the higher mass flux to the smaller electrode. Limiting conditions at an electrode lead to a very low concentration of the reacting ion at the electrode surface.

The case of interest in the present investigation is one in which the rate of the process is controlled by the rate of supply of ions to a cathode by diffusion and convection only.

In general, ions are transported from the bulk solution to the electrode by three modes:

(a) Diffusion by reason of a concentration gradient.

(b) Electrical migration by reason of a potential gradient (recall that ions have an electric charge).

(c) Convection of the solution.

The second mode, electrical migration, is eliminated by reducing, almost to zero, the potential gradients in the electrolyte solution. This is achieved by introducing a high concentration of a non-reacting electrolyte (termed the supporting electrolyte) into the solution, thus increasing its electrical conductivity, [42] .

The removal of the products of the reaction, depends upon the particular reaction considered. Of interest in the present work is the case in which the products of the reaction are in the form of ions which are removed from the electrode surface by diffusion and convection. In this situation, there is no net mass transfer across the electrode/electrolyte interface.

2.1.2 Expression for the current density from convective mass transfer theory.

Using a theory of convective mass transfer [60] and applying it to the case of zero net transfer across the interface, the following expression is obtained for the mass flux of one ion species, i.

$$\dot{m}''_i = g_i \, (m_{i,G} - m_{i,s}) \qquad 2.1$$

where g_i is the conductance or mass transfer coefficient

m_i is the mass fraction of reacting ions, i

suffix G refers to the bulk state

suffix s refers to the liquid side of the surface.

The mass flux $\dot{m}''_i$ is related to the current density by Faraday's law of electrolysis which states that the net ionic current is equal to the product of the number of ions reacting at the electrode and the number of electrons, n exchanged per ion during the electrode reaction.

$$\text{i.e.} \quad I = \frac{nF}{M_i} \dot{m}''_i \qquad 2.2$$

where F is Faraday's constant

M_i is the molecular weight of the reacting ions.

Combining equations 2.1 and 2.2, the following expression for the current density is obtained:

$$I = \frac{nF}{M_i} g_i (m_{i,G} - m_{i,s}) \qquad 2.3$$

For the case in which the process is controlled by the diffusion of ions to the electrode, the concentration of the reacting ions at the electrode surface is small compared with the bulk concentration. Without this condition, it can be seen from equation 2.3 that it is necessary to know the value of $m_{i,s}$ in order to evaluate the conductance from the current density-measurements.

The following section examines the conditions under which the electrode reaction is sufficiently rapid to produce

a diffusion-controlled system.

2.1.3 Expression for current density from reaction rate theory.

An expression for the current density can be derived by assuming that the electrode reaction is a first order reaction and that the theory of absolute reaction rates is applicable [22, 23, 36]. With these assumptions, the expression for a cathodic reaction is:

$$I = An\,T\,m_{i,s} \exp\left[-\frac{1}{RT}\left(nF\Delta V_{CATH} + \Delta F_i\right)\right] \qquad 2.4$$

where A is a constant which is a combination of other known constants

T is the absolute temperature

ΔV_{CATH} is the potential drop at the cathode/electrolyte interface and has a negative value

ΔF_i is the standard free energy of activation.

The condition for a diffusion-controlled process is $m_{i,s} \ll m_{i,G}$. From equations 2.3 and 2.4 this condition becomes:

$$\frac{M_i AT}{Fg_i} \exp\left[-\frac{1}{RT}\left(nF\Delta V_{CATH} + \Delta F_i\right)\right] \gg 1 \qquad 2.5$$

Figure 2.1 represents the situation graphically, showing the current density I as a function of the surface concentration, $m_{i,s}$ for a fixed bulk concentration, $m_{i,G}$ of the reacting ions.

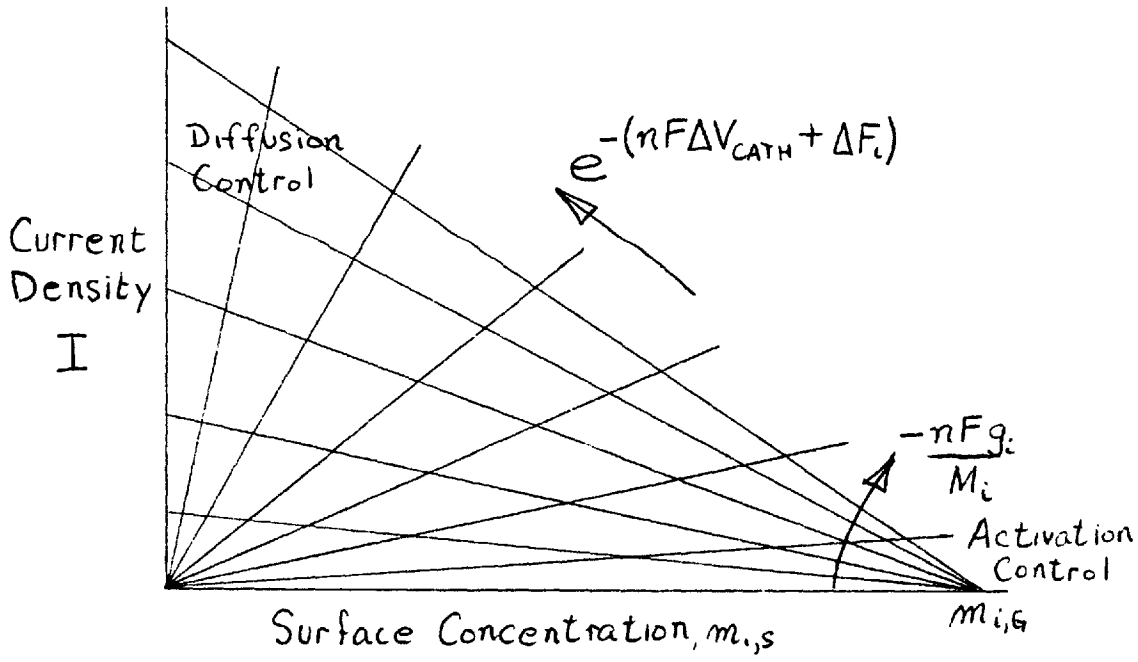

Fig.2.1

The requirements which favour a diffusion-controlled reaction are seen from condition 2.5 and figure 2.1 to be:

(i) Low activation energy, ΔF_i; this is dependent upon the electrochemical reaction and upon the electrode material, but it is also influenced by the presence of so-called electrode poisons. These poisons, which can take the form of either impurities in the solution or coatings on the electrode, increase the value of ΔF_i, in some cases

quite considerably [27].

(ii) High (negative) potential-drop between the cathode and bulk solution. The value of ΔV_{CATH}, however, should not be as high as the decomposition potential of other ion species in the solution.

(iii) High molecular weight, M_i of the reacting ions, dependent entirely upon the choice of electrode reaction.

(iv) Low mass transfer conductance. Conductance is a dependent variable and in the present investigation the values are, in general, high compared with values normally encountered in single phase flow.

(v) The effects of temperature are not obvious; however, in the present work the variation of the absolute temperature is extremely limited.

If values of the activation energy, ΔF_i and the decomposition potentials were known for a given reaction under various conditions of temperature, supporting electrolyte concentrations and electrode materials, it would be a simple matter to determine the range of values of conductance and potential difference for which the reaction was diffusion-controlled. However, such information is not available; it is therefore necessary to determine the ranges of diffusion-controlled conductance and potential difference by an experimental method. This method is described in the following section.

2.1.4. Test procedure for determining a diffusion-controlled reaction.

As indicated in Figure 2.1, the current is almost independent of the applied potential difference in the diffusion-controlled region. Indeed, by definition, the diffusion-controlled region is the region in which chemical kinetics, and hence ΔV, play no part in determining the rate of the process. The variation of current with voltage for a system which becomes diffusion-controlled is shown in Figure 2.2.

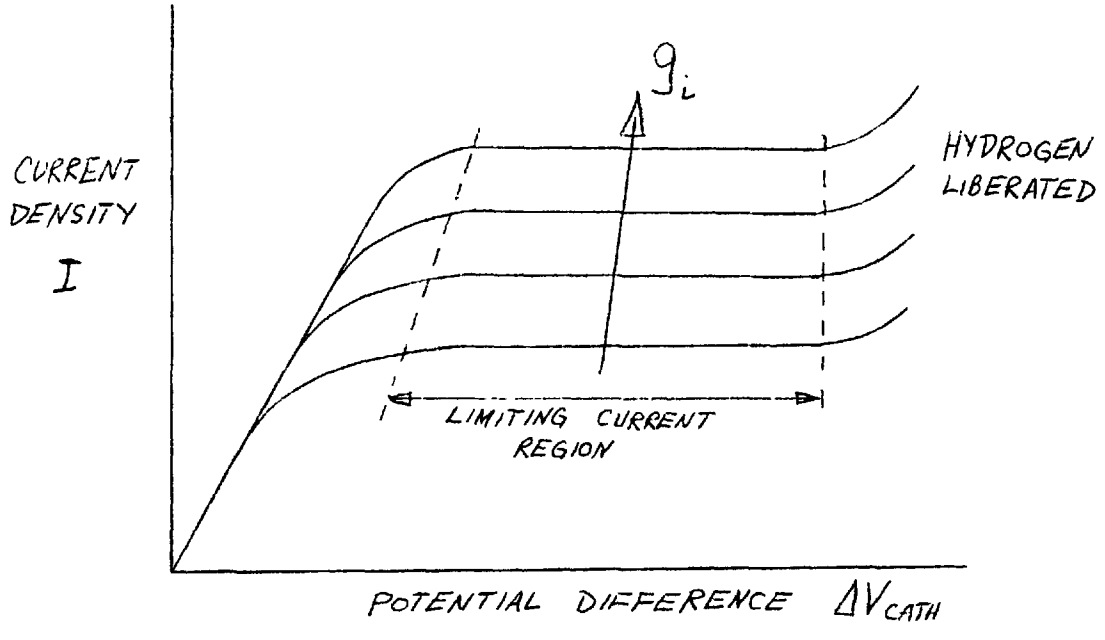

Fig.2.2.

For a system that does not become diffusion-controlled, the current/voltage curves do not exhibit the horizontal, 'limiting current' region; instead, the current always increases with voltage.

Here then, is a simple but effective means of testing an electrode/electrolyte combination in a given situation. It has already been shown that a high conductance is unfavourable to a diffusion-controlled reaction; it is essential, therefore, when carrying out the current/voltage measurements, to do so at the highest value of the conductance that is likely to be encountered.

2.1.5 The electrode reaction employed in the present investigation.

The reaction employed in this investigation is the reduction of ferricyanide ions to ferrocyanide ions at a nickel cathode,

$$\text{i.e.} \quad \left[Fe(CN)_6\right]^{3-} + e^- \rightleftharpoons \left[Fe(CN)_6\right]^{4-}$$

Thus one electron is exchanged at the cathode for each reacting ion, i.e. n=1. For this system, the anodic reaction is the reverse of the cathodic reaction, i.e. the oxidation of ferrocyanide ions to ferricyanide; this type of reaction is commonly termed a redox-reaction. An advantage of a redox-reaction is that the concentrations

of the reacting ions in the bulk solution remain constant. Deposition-type reactions are unsuitable for the present application because the rough nature of the metal deposited on the electrode surface [57] increases the effective transfer area of the electrode.

The reduction of ferricyanide was chosen because it was the only non-deposition reaction which gave a limiting current at the high conductances encountered in this work, (possibly because of the high molecular weight of the reacting ions (212) and of a low value of ΔF_i). Other advantages of the ferricyanide/ferrocyanide system are:

(i) The reactants, potassium ferricyanide and potassium ferrocyanide, are relatively inert and do not react (other than electrochemically) with the electrode material or the supporting electrolyte chosen.

(ii) The reactants are fairly stable i.e. do not decompose, except when subjected to strong light radiation [19]. It is the reaction most widely used by other investigators in the field of diffusion-controlled mass transfer [19, 32, 43, 51, 63, 67, 71].

Sodium Hydroxide was used for the supporting electrolyte; it was found to fulfil the following requirements:

(a) A high conductivity.

(b) A high decomposition potential compared with that of ferricyanide.

(c) It does not react with the reacting electrolyte,

the electrodes or the gases used in the investigation.

In order to select an electrode material, a series of tests was performed with several different materials. The tests consisted of measuring the variation of current with potential difference between two electrodes, one a large platinum anode and the other a small cathode made of the material under test. Vigorous stirring of the electrolyte close to the cathode was provided, to ensure a high conductance. The materials tested were platinum, nickel, copper, bronze, monel metal and stainless steel, of which only nickel and platinum produced a limiting current. As platinum is not readily available in a porous state, nickel has been used as the electrode material.

2.2 The 'analogy' between electrolytic mass transfer and heat transfer.

When the mass flux conservation equation for diffusion and convection in dilute electrolyte solutions is compared with the heat flux conservation equation for convective heat transfer, the two processes are seen to be similar

Mass transfer: $$\frac{\partial m_i}{\partial t} + V.\nabla m_i = D_i \nabla^2 m_i \qquad 2.6$$

Heat transfer: $$\frac{\partial T}{\partial t} + V.\nabla T = \left(\frac{k}{\rho C_p}\right)\nabla^2 T \qquad 2.7$$

(Both relations are written in a form which implies constant transport properties) where

V is the velocity vector at the point considered

m_i is the local concentration of the transferred substance

D_i is the diffusion coefficient of the transferred substance

T is the local temperature

$k/\rho C_p$ is the thermal diffusivity

$\frac{\partial}{\partial t}$ denotes partial derivative with respect to time.

The parallel between diffusion-controlled mass transfer to an electrode and convective heat-transfer to an isothermal wall is drwan in the following table:

Electrolytic mass transfer	Convective heat transfer
Mass flux of ions, $\dot{m}_i''$	Heat flux $\dot{q}''$
Concentration of reacting ions, m_i	Temperature, T
Conductance $\equiv \frac{\dot{m}_i''}{m_{i,G} - m_{i,s}}$	Heat transfer coefficient $\equiv \frac{\dot{q}''}{T_G - T_s}$
Diffusion coefficient of ion, D_i	Thermal diffusivity $\frac{k}{\rho C_p}$
Schmidt No., $N_{Sc} \equiv \frac{\mu}{D_i \rho}$	Prandtl No., $N_{Pr} \equiv \frac{\mu C_p}{k}$

2.3 Advantages of the electrolytic technique over heat transfer methods.

This technique has three main advantages over experimental methods involving heat transfer measurements. These are:

(i) The ionic current is a direct measure of the mass flux and can be recorded continuously with a high degree of accuracy. Complicated heat balances or heat loss estimations, which are necessary in heat transfer experiments, are avoided.

(ii) For a diffusion-controlled reaction, the surface concentration of the reacting ions is negligible compared with the bulk concentration; the concentration difference, or driving force, is therefore equal to the bulk concentration which can be measured with a 1% accuracy. In convective heat transfer, the measurement of surface temperature is a major problem.

(iii) Steady-state conditions are achieved almost instantaneously, permitting readings to be taken in rapid succession.

Chapter 3 Theoretical aspects of the investigation.

The purpose of this chapter is to derive dimensionless groups which provide a basis for the experimental part of the investigation. Three quantities are at the focus of the investigation, namely: (i) The sub-critical conductance, g_i, i.e. the conductance below the maximum, (ii) the critical superficial velocity, $\dot{V}^n_{CRIT}$ and (iii) the maximum conductance, $g_{i,MAX}$. In the following sections, each of these three quantities are treated in turn; use is made of models and dimensional analysis to achieve the desired results.

3.1 The sub-critical mass-transfer conductance.

A relation is derived between the mass transfer conductance at a porous surface with barbotage, and independent variables in the system. The derivation is based on a model originally proposed by Spalding for nucleate boiling [62] and later extended to barbotage [61]. The work done by the growing bubbles is equated to the dissipation of turbulent kinetic energy which is in turn related to the heat or mass transfer coefficient.

3.1.1 Description of the model.

The sketch below, Figure 3.1, shows the form of the distribution of turbulent kinetic energy, k along a normal to the porous surface.

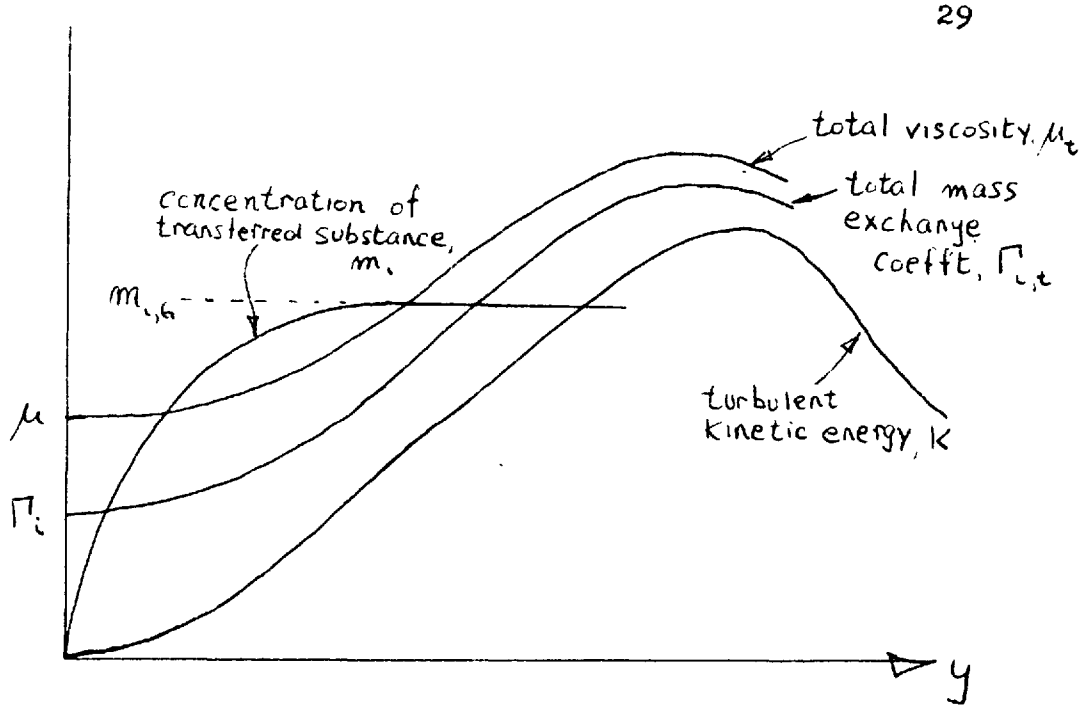

Fig. 3.1 A sketch of the distribution of properties along a normal to the porous surface.

Also shown in the sketch are the distributions of the total fluid viscosity, μ_t, the total exchange coefficient for mass, $\Gamma_t (= D_{i,t}\rho_f$ where $D_{i,t}$ is the total diffusion coefficient for the transferred substance), and the concentration of the transferred substance, m_i. In the ideal situation considered, the quantities shown in the sketch are assumed to be constant in directions parallel to the porous surface, and also to be time mean values. The analysis is restricted to a region of gas injection rates in which the bubble nucleation is profuse and the access of fresh liquid to the mass-transfer surface is unimpeded by the gas.

In barbotage, the transfer of heat or mass occurs through the liquid, between the porous wall and the bulk liquid. The role of the bubbles in the heat or mass transfer process is, therefore, solely to agitate the liquid.

3.1.2 Energy balance in the turbulent boundary layer.

The work done by the growing bubbles on the surrounding liquid is the only source of kinetic energy in the system. A bubble grows by reason of a pressure difference, $(P_b - P_f)$ between the inside of the bubble and the surrounding liquid. The rate of work done by a bubble is the product of this pressure difference $(P_b - P_f)$ and the volumetric bubble growth rate. For a porous surface having numerous bubble sites, the rate of work done by the bubbles, $\dot{W}$ per unit area is given by:

$$\dot{W} \text{ per unit area} = \dot{V}'' \, \overline{(P_b - P_f)} \qquad 3.1$$

where $\overline{(P_b - P_f)}$ is a time and area mean value of the excess pressure in the bubbles and $\dot{V}''$ is the total gas injection rate per unit area.

From the theory of isotropic turbulence, it is known that the rate of dissipation of turbulent kinetic energy into energy of molecular motion per unit volume is related to the kinetic energy level by the following proportionality:

$$\text{rate of dissipation of kinetic energy per unit volume} \quad \alpha \quad \frac{\rho_f k^{3/2} g_o^{\frac{1}{2}}}{l} \qquad 3.2$$

where ρ_f is the liquid density

g_o is the constant in Newton's Second Law of Motion

l is a length parameter characteristic of the turbulence.

The result is a consequence of dimensional analysis and has also been substantiated by experimental evidence [3, 21, 49] . It is supposed that departures from isotropicity result only in a change in the proportionality constant.

Applying this result to the case of barbotage, an appropriate characteristic length is the thickness of the turbulent boundary layer. If the kinetic energy dissipation rate per unit volume is multiplied by this turbulent boundary layer thickness, the dissipation rate per unit area is obtained. Relation 3.2 then becomes:

$$\text{rate of dissipation of kinetic energy per unit area} \quad \alpha \quad \rho_f k_e^{3/2} g_o^{\frac{1}{2}} \qquad 3.3$$

where k_e is an 'effective' value of the kinetic energy compatible with the definition of the turbulent boundary layer thickness used.

Equating the generation rate of kinetic energy from the bubble growth (3.1) to the kinetic energy dissipation

rate (3.3), the following relation is obtained:

$$\dot{V}'' \; (\overline{P_b - P_f})^{\alpha} \; \rho_f k_e^{3/2} \; g_o^{\frac{1}{2}} \qquad 3.4$$

3.1.3 The mass transfer coefficient.

It is postulated that the mass transfer conductance, g_i is a function of the properties of the turbulent boundary layer, i.e.

$$g_i = f_1 (k_e, \; \mu_f, \; D_i, \; \rho_f, \; g_o)$$

A Rayleigh-type dimensional analysis yields the result:

$$\frac{g_i}{\rho_f k_e^{\frac{1}{2}} g_o^{\frac{1}{2}}} = f_2 \left(\frac{\mu_f}{D_i \rho_f} \right) \qquad 3.5$$

$\frac{\mu_f}{D_i \rho_f}$ is the Schmidt Number of the liquid, and the group on the left-hand side has the form of a Stanton Number, since $(k_e g_o)^{\frac{1}{2}}$ has the dimensions of velocity.

Eliminating the kinetic energy from equation 3.5 by means of equation 3.4, the following expression is obtained:

$$\frac{g_i}{\left[\dot{V}'' \; (\overline{P_b - P_f}) g_o\right]^{\frac{1}{3}} \rho_f^{\frac{2}{3}}} = f_3(N_{Sc}) \qquad 3.6$$

3.1.4 The mean pressure difference $(\overline{P_b - P_f})$

In the above form, use cannot be made of equation 3.6 becauee the bubble mean pressure difference $(\overline{P_b - P_f})$

is unknown. For a system in which the gas is supplied at a constant pressure upstream of the porous plate, the mean bubble pressure difference is probably a function of the nucleation pressure difference and the viscous pressure drop through the porous plate. The nucleation pressure difference, $(P_b-P_f)_{NUCL.}$ is given by:

$$(P_b - P_f)_{NUCL} = \frac{4\sigma}{d_p} \sin\theta \qquad 3.7$$

where σ is the surface tension coefficient

θ is the bubble contact angle

d_p is an effective pore diameter,

and the viscous pressure drop is assumed to be a function of the gas properties ρ_g and μ_g and an effective pore diameter, d_p. The mean pressure difference $(\overline{P_b-P_f})$ is therefore assumed to be related to the following quantities:

$$\overline{P_b - P_f} = f_4(\sigma, g_o, \rho_g, \mu_g, d_p)$$

Dimensional analysis yields the following result:

$$\frac{\overline{P_b - P_f}}{\frac{\sigma g_o}{d_p}} = f_5\left[\frac{(\sigma g_o \rho_g d_p)^{\frac{1}{2}}}{\mu_g}\right] \qquad 3.8$$

For a contact angle of 90^o, equation 3.6 may be written as:

$$\frac{g_i}{\left(\frac{\dot{V}''\,\sigma g_o}{d_p}\right)^{\frac{1}{3}}\rho_f^{\frac{2}{3}}} = f\left[N_{Sc},\ \frac{(\sigma g_o \rho_g d_p)^{\frac{1}{2}}}{\mu_g}\right] \qquad 3.9$$

It now remains to determine the form of the function f by means of experiment.

For barbotage systems in which the viscous pressure drop through the pore is very small compared with the bubble pressure drop, the right-hand side of equation 3.9 becomes a function of the Schmidt Number only.

3.2 The critical superficial velocity.

No new model is presented for the critical superficial velocity in barbotage since a well established theory already exists. The theory referred to is the 'hydrodynamic crisis' theory for boiling burnout, proposed originally by Kutateladze [40] and afterwards by many other authors. Because the burnout phenomenon is postulated to be purely hydrodynamic, occurring at a particular vapour generation rate, it is reasonable to suppose that a similar crisis occurs in barbotage at a corresponding gas injection rate. Indeed several investigators including Kutateladze, have substantiated this supposition experimentally [37, 41, 45, 75] . The results of these investigators are discussed in Chapter 8.

3.2.1 The 'hydrodynamic crisis' theory.

The equation predicting the occurrence of the crisis is:

$$\frac{\dot{V}''_{CRIT}\,\rho_g^{\frac{1}{2}}}{\left[g_o g_{grav}\sigma(\rho_f-\rho_g)\right]^{\frac{1}{4}}} = \text{const} \qquad 3.10$$

where $\dot{V}''_{CRIT}$ = critical rate of gas or vapour generation per unit area

ρ_g = gas or vapour density

ρ_f = liquid density

σ = surface tension coefficient

g_{grav} = acceleration due to gravity

g_o = constant appearing in Newton's 2nd Law.

Basically this equation was derived by Kutateladze and later by other workers using dimensional analysis [40, 39, 9, 65, 34], the value of the constant was determined from experimental data. Analytical approaches to the critical rate of vapour formation [18, 12, 75, 34, 5, 6, 11, 78, 79, 82, 1] have also led to the above equation. These analyses are based on models describing the crisis, usually involving a condition for bubble coalescence or for instability of the liquid/vapour interface.

3.2.2 Application to the present investigation.

The postulate that the crisis is a purely hydrodynamic phenomenon is retained. The Kutateladze equation is used

to indicate which properties are likely to be important in the present work. In the case of barbotage, the additional process of viscous flow of the gas through the porous plate may influence the occurrence of the crisis. The following parameters are therefore included in the analysis to account for this additional process: gas viscosity, μ_g, a pore diameter, d_p, and the thickness of the porous plate, t.

The effects of liquid viscosity, and bubble site density, $\frac{n}{A}$ on the critical heat flux in boiling, are generally regarded as unimportant. However, in order to keep the present analysis as general as possible, these two properties are included. To summarise, the parameters which are assumed to influence the critical superficial velocity, $\dot{V}^n_{CRIT}$ are indicated in the following equation:

$$\dot{V}^n_{CRIT} = \varphi_1(\rho_g, \mu_g, \rho_f, \mu_f, \sigma, g_{grav}, g_o, d_p, {}^n/_A, t) \quad 3.11$$

where $\varphi_1(\quad)$ means some function of --

3.2.3 Formation of dimensionless groups.

A Rayleigh-type dimensional analysis was performed on equation 3.11. This method of dimensional analysis cannot discern between ρ_g and ρ_f, between μ_g and μ_f or between the three length parameters; these quantities were therefore replaced by unspecified ρ, μ and a length parameter, l.

The result obtained was:

$$\frac{\dot{V}''_{CRIT}\,\rho^{\frac{1}{4}}}{(\sigma g_o g_{grav})^{\frac{1}{4}}} = \varphi_2\left[\left(\frac{g_{grav}\rho}{\sigma g_o}\right)^{\frac{1}{2}}, \quad \frac{(\sigma g_o)^{\frac{3}{4}}\rho^{\frac{1}{4}}}{\mu g_{grav}^{1/4}}\right]$$

To complete the analysis, the above three groups were assigned the viscosity and the density of the liquid and the pore diameter, d_p was taken as the length parameter, . The gas properties and remaining length parameters were introduced as ratios of ρ_f, μ_f and d_p, resulting in the following relation:

$$\frac{\dot{V}''_{CRIT}\,\rho_f^{\frac{1}{4}}}{(\sigma g_o g_{grav})^{\frac{1}{4}}} = \varphi_3\left[\left(\frac{g_{grav}\rho_f}{\sigma g_o}\right)^{\frac{1}{2}} d_p, \frac{(\sigma g_o)^{\frac{3}{4}}\rho_f^{\frac{1}{4}}}{\mu_f g_{grav}^{\frac{1}{4}}}, \frac{t}{d_p}, \left(\frac{n}{A}\right)^{\frac{1}{2}} d_p, \frac{\rho_g}{\rho_f}, \frac{\mu_g}{\mu_f}\right]$$

By combining some of the above dimensionless groups, more meaningful groups were obtained; the physical significances of these groups are discussed in the next section. The new relation is:

$$\frac{\dot{V}''_{CRIT}\,\rho_g^{\frac{1}{2}}}{(\sigma g_o g_{grav}\rho_f)^{\frac{1}{4}}} = \varphi\left[\frac{\rho_g}{\rho_f}, \frac{(\sigma g_o \rho_g d_p)^{\frac{1}{2}}}{\mu_g}, \left(\frac{n}{A}\right)^{\frac{1}{2}}\left(\frac{\sigma g_o}{g_{grav}\rho_f}\right)^{\frac{1}{2}}, \left(\frac{n}{A}\right)^{\frac{1}{2}} d_p, \frac{(\sigma g_o)^{\frac{3}{4}}\rho_f^{\frac{1}{4}}}{\mu_f g_{grav}^{\frac{1}{4}}}, \frac{t}{d_p}\right] \qquad 3.12$$

This relation forms the basis for the experimental part

of the investigation, the object of which is to determine the function φ.

3.2.4 The significance of the dimensionless groups.

(i) Dimensionless critical superficial velocity.

This group has the same basic form as the dimensionless term appearing on the left hand side of the Kutateladze equation (3.10). In equation 3.10, the term $(\rho_f - \rho_g)$ appears in place of ρ_f in the above dimensionless $\dot{V}''_{CRIT}$. The omission of a term $(\rho_g - \rho_g)$ from the analysis is justified since its influence cannot be determined experimentally, as throughout the experimental part of the investigation ρ_g is always negligible compared with ρ_f.

(ii) The density ratio, ρ_g / ρ_f.

The inclusion of this group requires no justification; it is a group appearing in most two-phase flow analyses.

(iii) The 'pore' group, $\dfrac{(\sigma g_o \rho_g d_p)^{\frac{1}{2}}}{\mu_g}$.

This group was encountered in the last section (3.1); it is significant because it only contains terms associated with the flow of gas through the pores. It is a group characteristic of the barbotage process.

(iv) The liquid property group, $\dfrac{(\sigma g_o)^{\frac{3}{4}} \rho_f^{\frac{1}{4}}}{g_{grav}^{\frac{1}{4}} \mu_f}$.

This group contains only liquid properties which influence the hydrodynamics, and the gravitational accelera-

tion; it is therefore a constant for a given liquid at a given temperature under normal gravity conditions. If ρ_f is replaced by $(\rho_f - \rho_g)$ and the group is squared, it becomes what is known to Russian workers as the Archimedes Number. It results from a balance of viscous, surface tension and buoyancy forces on a bubble [73].

(v) The dimensionless group $(\frac{n}{A})^{\frac{1}{2}}\left(\frac{\sigma g_o}{g_{grav}\rho_f}\right)^{\frac{1}{2}}$

The quantity $\left(\frac{\sigma g_o}{g_{grav}\rho_f}\right)^{\frac{1}{2}}$ is proportional to the quasi-static bubble departure diameter for a fixed contact angle, predicted from the equation of Fritz [25] who equated the buoyancy force on a departing bubble to the surface tension force (again the ρ_f should, ideally, appear as $\rho_f - \rho_g$). In dynamic systems of boiling and barbotage, other forces, e.g. inertia, drag and pore resistance, are important and the Fritz equation becomes inaccurate. Nevertheless, a good estimate of bubble sizes in boiling is obtained from the Fritz equation, even at moderately high heat fluxes [26]. In the present investigation, the bubble departure diameters, measured photographically, were predicted to within 20% by the Fritz equation (a contact angle of 90^o was assumed).

Thus the quantity $\left(\frac{\sigma g_o}{g_{grav}\rho_f}\right)^{\frac{1}{2}}$ is a group of properties, having the dimension of length and a magnitude of the same order as a departing bubble.

The group $(\frac{n}{A})^{\frac{1}{2}}\left(\frac{\sigma g_o}{g_{grav}\rho_f}\right)^{\frac{1}{2}}$ can therefore be regarded as a measure of the ratio between the bubble departure diameter and the mean spacing between the bubble sites, i.e. a measure of the fraction of the surface occupied by gas.

(vi) The ratio $(\frac{n}{A})^{\frac{1}{2}} d_p$.

This is merely the ratio of the pore diameter to the pore spacing, i.e. a measure of the surface porosity of the porous material.

(vii) The ratio t/d_p .

This group is the most obvious form of the dimensionless porous plate thickness.

3.3 The maximum conductance.

The value of the maximum conductance depends upon the conductance-superficial velocity relation and the critical superficial velocity. It is reasonable to suppose then, that the dimensionless groups which are assumed important to the sub-critical conductance and to the critical velocity, are also the dimensionless groups which are important to the maximum conductance. This supposition leads to the following relation:

$$\frac{g_{MAX}}{\left(\frac{\dot{V}''_{CRIT}\,\sigma g_o}{d_p}\right)^{\frac{1}{3}}\rho_f^{\frac{2}{3}}} = F\left[\frac{\mu_f}{D_i\rho_f},\ \frac{\rho_g}{\rho_f},\ \frac{(\sigma g_o \rho_g d_p)^{\frac{1}{2}}}{\mu_g},\right.$$

$$\left.(\tfrac{n}{A})^{\frac{1}{2}}\left(\frac{\sigma g_o}{g_{grav}\rho_f}\right)^{\frac{1}{2}},\ (\tfrac{n}{A})^{\frac{1}{2}}d_p,\ \frac{(\sigma g_o)^{\frac{3}{4}}\rho_f^{\frac{1}{4}}}{\mu_f g_{grav}^{\frac{1}{4}}},\ \frac{t}{d_p}\right]$$

3.13

It remains to determine the form of the function F from the experimental information.

3.4 The gross geometry of the system.

The term 'gross geometry' refers to the extent of the liquid pool and the size of the porous plate. It was expected that, outside certain limits, the gross geometry would have no effect upon either the conductance or the critical superficial velocity. It was considered desirable to conduct the experimental investigation outside these limits. Consequently, preliminary tests were carried out to establish the limits.

Three length parameters were used to represent the gross geometry; these were the diameter of the circular electrode, d_{elec}, the diameter of the cylindrical pool, d_{pool}, and the depth of the pool, h. These quantities are more meaningful when expressed as dimensionless ratios thus:

$$d_{elec}\left(\frac{g_{grav}\rho_f}{\sigma g_o}\right)^{\frac{1}{2}},\quad d_{pool}/d_{elec},\ \text{and}\ h\left(\frac{g_{grav}\rho_f}{\sigma g_o}\right)^{\frac{1}{2}}.$$

The quantity $\left(\frac{\sigma g_o}{g_{grav} \rho_f}\right)^{\frac{1}{2}}$ has previously been discussed and is representative of the bubble departure diameter. All of the above dimensionless ratios have a lower limit of unity.

Chapter 4 Description of Apparatus

4.1 General description.

Basically, the apparatus consisted of a vessel containing the electrodes and electrolyte solution, hereafter termed the cell (figure 4.1). Through the porous cathode, located horizontally in the base of the cell, a metered supply of gas was injected into the electrolyte. A potential was applied between the electrodes, and the resulting ionic current was recorded.

4.2 The cell.

The cell, shown in figure 4.1, was constructed from a 4 inch diameter pyrex glass tube, 12 inches long, mounted in a vertical position. The nylon base of the cell, in which the porous cathode was located, was 'sandwiched' between the bottom of the cell tube and a second glass vessel which acted as a plenum chamber. A stainless steel cover (in earlier tests this was of polythene) sealed the top of the tube, enabling the cell to be operated at pressures above or below atmospheric pressure. The pressure in the cell was measured by a 30-inch mercury, U-tube manometer. A thermally insulating jacket, which also served the purpose of protecting the electrolyte from strong light radiation, was fitted round the outside of the cell.

4.2.1 The cathode.

For most of the tests in the investigation, the cathode was in the form of a 1-inch diameter 'porosint'* nickel disc, $\frac{1}{16}$ -inch thick. Changes in the diameter, thickness and material of the cathode were made for the tests in which geometry effects were investigated. These variations from the 'basic configuration' are discussed in section 5.1 of the next chapter.

The sealing of the cathode into the base of the cell presented some difficulties. Figure 4.2 shows how the disc was mounted. The lip or step shown in the diagram was unavoidable without resorting to cements, which were considered undesirable because of their tendencies to soak into the porous material. An effect of this lip is discussed in Chapter 6, 'Presentation of Results'.

4.2.2 The anode.

For the basic configuration, the anode consisted of a cylindrical nickel tube slightly smaller in diameter than the glass cell wall, and extending from the cell base to a height of 9 inches. The anode thus provided the circumferential boundary to the pool of electrolyte. It was found convenient for the series of tests in which

---

* 'porosint' is a trade name of Sintered Products Ltd. and refers to a sintered powder material.

the pool diameter was varied, to simply use anode tubes of different diameters.

A difficulty was encountered in the tests in which the electrolyte depth was varied. At the lower liquid depths it was found that the area of anode in contact with the electrolyte was no longer large compared with the cathode area. This was overcome by (i) using the smallest cathode diameter ($\frac{1}{4}$-inch) and (ii) constructing an anode to lie flat on the base of the cell, concentric with the cathode. This anode was used only for this one series of tests.

4.2.3 The electrolyte solution.

The concentrations of the electrolytes in the aqueous solution were:

0.001M* potassium ferricyanide

0.001M potassium ferrocyanide

2M sodium hydroxide.

'Analar' analytical grades of the chemicals were used to minimise the possibility of impurities in the solution; the water used was distilled. Measurements of the concentration of potassium ferricyanide in the solution were carried out using an absorptiometer, an instrument which utilizes the light absorbing properties of the solution.

---

* a 1M solution is a number of grams equal to the molecular weight of the substance in 1,000ccs of solution.

The calibration of this and all other instruments used in this investigation, are described in Appendix I.

The temperature of the electrolyte was maintained at 25°C ± 0.1 by a small electrical heater and a mercury-in-glass thermostat. Except in the tests when it was intentionally varied, a solution depth of 9-inches was maintained in the cell. Changes in the sodium hydroxide concentration and the solution temperatures were made in the tests in which the effects of liquid properties were investigated.

4.3 The gas flow system.

The gas injected through the porous cathode was supplied from a high pressure gas cylinder fitted with a diaphragm regulating valve; a fine control of the gas flow rate was provided by a needle valve. The gas flow rate was calculated from the pressure drop across a $\frac{1}{8}$-inch orifice, located downstream of the needle valve, as shown in figure 4.3. In earlier tests, the orifice pressure drop was measured by an inclined paraffin manometer, this was later replaced by a water-filled micro-manometer. The pressure immediately upstream of the orifice was measured by a 100-inch U-tube manometer containing a fluid of specific gravity 2.95.

An electric heater, located between the orifice and the plenum chamber, was used to heat the gas to a temperature equal to the electrolyte temperature. A copper-constantan thermocouple junction, positioned beneath the porous electrode in the plenum chamber, and another in a glass sheath in the electrolyte, were coupled to a 'Scalamp' centre-zero galvanometer. Any out-of-balance between the two temperatures at the thermocouple junctions was registered on the galvanometer and corrected manually by adjusting the 'Variac' transformer supplying the heater in the gas stream.

The purpose of the plenum chamber beneath the cell was to maintain a constant pressure behind the porous electrode at a given gas flow rate.

4.4 The electrical circuit.

Current was supplied to the cell from a motor-driven, variable potential divider, incorporating a 2-volt lead accumulator. The motorised facility was provided to enable continuous current voltage curves to be produced when required.

A schematic diagram of the electrical circuit is included in figure 4.3. The current was determined from the potential drop, measured by a 0-10 mV Honeywell pen recorder, across a calibrated resistance connected in series with the electrolytic cell. The potential difference

across the electrodes was measured by an 'Avometer'. It was found unnecessary to use a reference electrode in the cell, as the large anode provided a perfectly satisfactory reference point from which to measure the cathode potential.

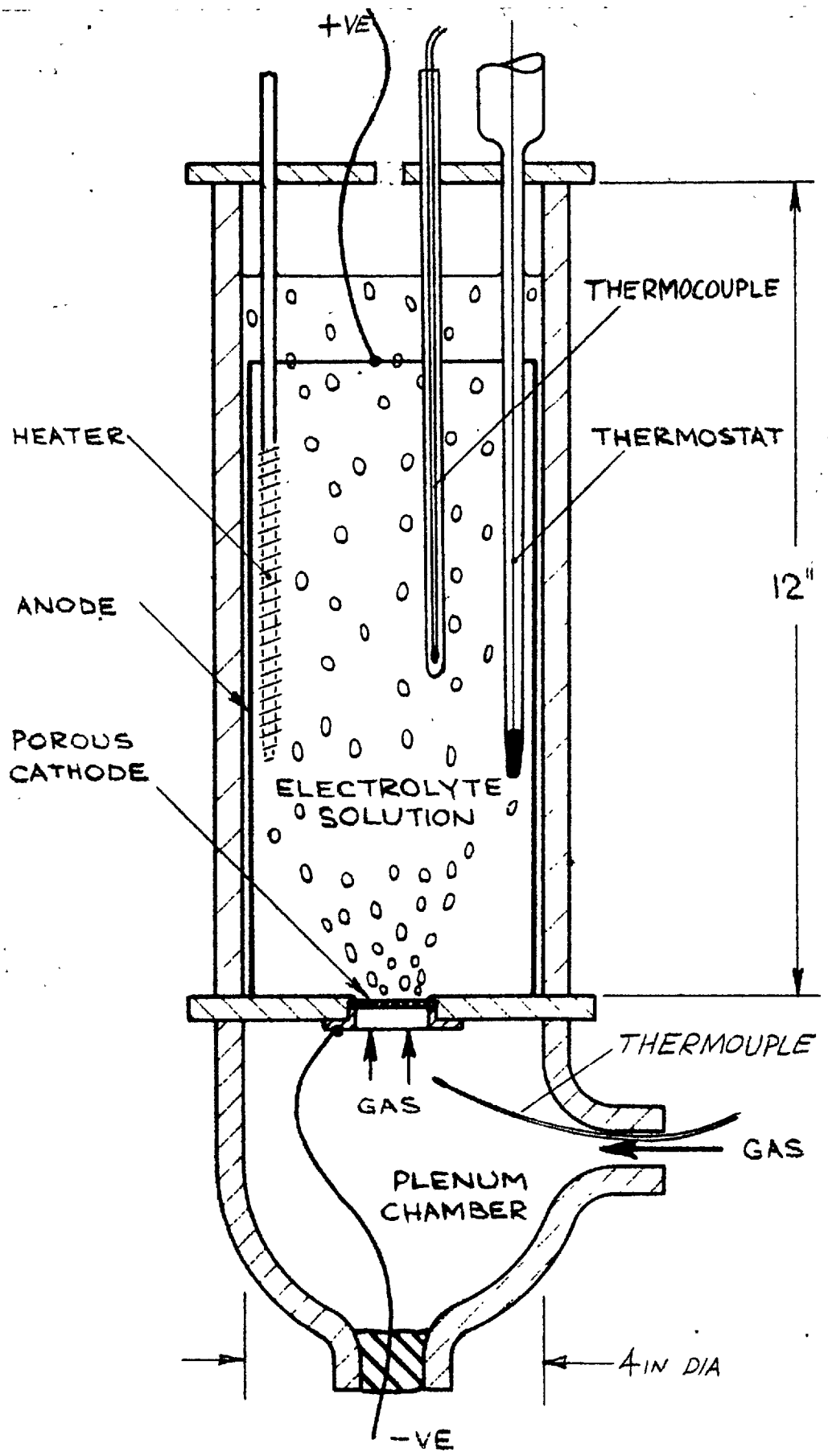

FIG 4.1 SECTIONAL VIEW OF CELL

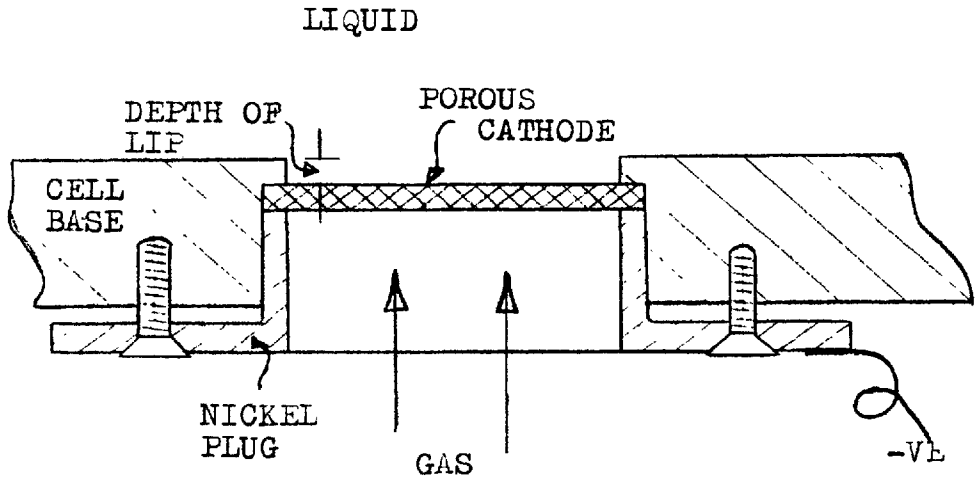

Fig. 4.2 METHOD OF CATHODE MOUNTING

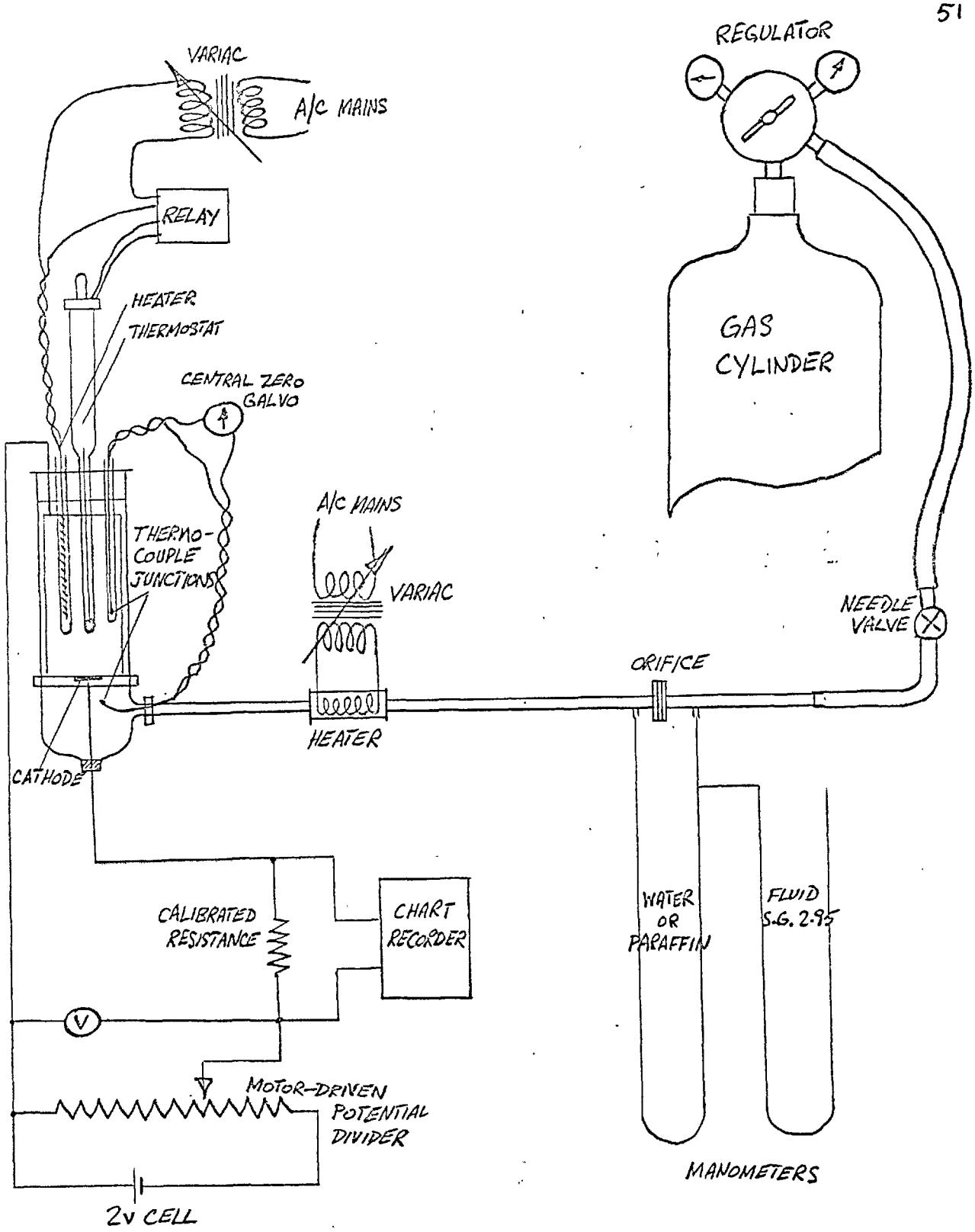

Fig.4.3 SCHEMATIC DIAGRAM OF THE APPARATUS

Chapter 5. Experimental Procedure

In the experimental part of the investigation tests were carried out to determine the variation of the ionic current (mass transfer rate) with gas injection rate. The tests were grouped into "test series"; in each series, the effects of varying a particular parameter were investigated. This chapter first describes the planning of the test series and gives details of the parameters varied. The preliminary work necessary before an actual test and the procedure during a test are then described.

5.1 Independent variables in the investigation

The object of the investigation was to relate a dimensionless conductance and a dimensionless critical superficial velocity to the independent dimensionless parameters proposed in Chapter 3. The experimental part of the project was planned to give the most useful information towards achieving this objective. Table 5.1 below, summarises the independent variables and dimensionless groups varied in each of the test series carried out.

In addition to the test series listed in Table 5.1, a test was performed in which a small quantity (0.15% by weight) of a surface active agent was added to the electrolyte solution. The results of this test were not used in the analysis or interpretation of the data, since the dynamic surface tension, liquid viscosity and diffusion

coefficient prevailing at the surface of the bubble are not known. However, the results are included in the chapter presenting the data.

Table 5.1 Summary of experimental work

Controlling parameters	Independent variables	Independent dimen'less groups
1. Pool depth	h	$h\left(\frac{g_{grav}\rho_f}{\sigma g_o}\right)^{\frac{1}{2}}$
2. Pool diameter	d_{pool}	d_{pool}/d_{elec}
3. Cathode diameter	d_{elec}	$d_{elec}\left(\frac{g_{grav}\rho_f}{\sigma g_o}\right)^{\frac{1}{2}}$
4. Pressure	ρ_g	ρ_g/ρ_f, $\frac{(\sigma g_o \rho_g d_p)^{\frac{1}{2}}}{\mu_g}$
5. Nature of gas	ρ_g, μ_g	ρ_g/ρ_f, $\frac{(\sigma g_o \rho_g d_p)^{\frac{1}{2}}}{\mu_g}$
6. NaOH concentration	$\rho_f, \mu_f, \sigma, D_i$	ρ_g/ρ_f, $\frac{(\sigma g_o \rho_g d_p)^{\frac{1}{2}}}{\mu_g}$, $\frac{\mu_f}{D_i \rho_f}$, $\frac{(\sigma g_o)^{\frac{3}{4}} \rho_f^{\frac{1}{4}}}{g_{grav}^{\frac{1}{4}} \mu_f}$
7. Temperature	$\rho_g, \mu_g, \rho_f, \mu_f, \sigma, D_i$	
8. Cathode thickness	t	t/d_p
9. Grade of porous material	d_p, n/A	t/d_p, $\frac{(\sigma g_o \rho_f d_p)^{\frac{1}{2}}}{\mu_g}$, $(\frac{n}{A})^{\frac{1}{2}}\left(\frac{\sigma g_o}{g_{gr}\rho_f}\right)^{\frac{1}{2}}$, $(\frac{n}{A})^{\frac{1}{2}} d_p$

Measurements of the gas, liquid and geometrical parameters are described in Appendix II. The following conditions and property values apply in all the tests except those where a parameter has been specifically varied:

Pressure within the cell	atmospheric
Temperature within the cell	25^{o}c
Concentration of NaOH	2M (7.5% w/w)
Schmidt Number	2,600
Injected gas	nitrogen
Material of cathode	Porosint
Thickness of material	$\frac{1}{16}$ - inch
Diameter of cathode	0.905-inch
Diameter of pool	3.44-inches
Depth of pool	9-inches.

In the following sections each of the test series listed in Table 5.1 is discussed in detail.

5.1.1 Varying the depth of the liquid pool

The special electrode arrangement for this series of tests has already been described in section 4.2.2. A further problem arose from the necessity of maintaining the solution at a constant temperature, since, at the lower values of liquid depth, the thermostat and heater were not fully submerged in the liquid. This problem was overcome by heating the full volume of electrolyte in the cell to slightly (0.5^{o}C) above the required temperature of 25^{o}C

and then, with the heating switched off, draining the cell to the required depth. By performing the tests quickly it was possible, because of the thermal insulation round the cell, to carry them out within the temperature range of 24.5°C to 25.5°C.

The range of the dimensionless group $h\left(\frac{g_{grav}\rho_f}{\sigma g_o}\right)^{\frac{1}{2}}$ covered in this series of tests was 2.36 to 75.5 corresponding to a range of liquid depth of $\frac{1}{4}$-inch to 8-inches.

5.1.2 Varying the diameter of the liquid pool

As described in section 4.2.2, the diameter of the pool was varied by using anode tubes of different diameters. A cathode of $\frac{1}{2}$-inch diameter was used giving values of the ratio pool diameter/cathode diameter within the range 1.38 to 6.88.

5.1.3 Varying the cathode diameter

Because of difficulties encountered in sealing the cathode, it was not possible to use a cathode diameter of less than $\frac{1}{4}$-inch. An upper limit of 1 inch diameter was imposed by the size of the cell and by the weakness of the porous material. The range of $d_{elec}\left(\frac{g_{grav}\rho_f}{\sigma g_o}\right)^{\frac{1}{2}}$ was, therefore, restricted to values between 2.36 and 9.5.

5.1.4 Varying the system pressure

In this series of tests, the density of the gas was varied by operating the cell at different pressures. No

other independent variable changed significantly, thus the independent dimensionless groups which varied were $\frac{\rho_g}{\rho_f}$ and $\frac{(\sigma g_o \rho_g d_p)^{\frac{1}{2}}}{\mu_g}$.

The pressure within the cell was increased by restricting the outflow of gas with a needle valve, and decreased by connecting the gas outlet to a vacuum pump. The highest pressure at which the cell was operated was 20-inches of mercury above atmospheric. This restriction was necessary to avoid exceeding the maximum safe working pressure of the plenum chamber and manometers. The lower limit of 20-inches of mercury below atmospheric was imposed by the vacuum pump.

Two gases, nitrogen and argon, were employed in these tests; the ranges of $\frac{\rho_g}{\rho_f}$ and $(\sigma g_o \rho_g d_p)^{\frac{1}{2}}/\mu_g$ covered in the tests are shown in Table 5.2 below.

Table 5.2 Ranges of the dimensionless groups

Gas	Range of $\frac{\rho_g}{\rho_f}$	$\frac{(\sigma g_o \rho_g d_p)^{\frac{1}{2}}}{\mu_g}$
Nitrogen	$.364 \times 10^{-3}$ to 1.79×10^{-3}	40.2 to 89.4
Argon	$.542 \times 10^{-3}$ to 2.58×10^{-3}	38.9 to 84.9

5.1.5 Varying the nature of the gas

Both the density and viscosity of the injected gas

were varied by using a number of different gases. In this series of tests, as in the previous series, two independent dimensionless groups, $\frac{\rho_g}{\rho_f}$ and $\frac{(\sigma g_o \rho_g d_p)^{\frac{1}{2}}}{\mu_g}$ were varied.

The range of gases was restricted to those which neither dissolved in the solution nor reacted with the electrolytes; all tests were performed at atmospheric pressure. Table 5.3 lists the gases used in the investigation, together with values of density, viscosity and the dimensionless groups $\frac{(\sigma g_o \rho_g d_p)^{\frac{1}{2}}}{\mu_g}$ and $\frac{\rho_g}{\rho_f}$.

Table 5.3 Gases employed in the investigation and their properties at 25°C and 14.7 p.s.i.

Gas	Density lb/ft^3	Viscosity lb/fth	ρ_g/ρ_f	$\frac{(\sigma g_o \rho_g d_p)^{\frac{1}{2}}}{\mu_g}$
Nitrogen	.0741	.0425	.001099	69
Argon	.1047	.0534	.00155	65.2
Hydrogen	.00570	.02195	.0000845	37
Helium	.01041	.0474	.0001542	26
Butane	.1328	.0221	.001965	188
Propane	.1097	.0227	.001623	158
Methane	.044	.0269	.000652	84
Nitrous Oxide	.1153	.0358	.00171	102
Freon 13	.276	.0354	.00409	159
Freon 22	.223	.0317	.0033	162
Freon 114	.441	.0283	.00654	180
70/30 N/H	.0523	.0412	.000775	59
50/50	.0386	.0394	.000572	54.3
30/70	.0253	.0368	.000373	47.1
20/80	.0186	.035	.000276	42.5
15/85	.0152	.0328	.000225	40.8
8/92	.0105	.0288	.000156	38.7
4.2/95.8	.0080	.0258	.000118	37.7

Note: (i) x/y signifies x% N_2, y% H_2 by volume.

(ii) the dimensionless groups are evaluated with the properties of a 2 N-NaOH solution and the 'Porosint' electrode material.

5.1.6 Varying the supporting electrolyte concentration

By varying the concentration of the supporting electrolyte (Sodium hydroxide), large changes were obtained in the liquid viscosity and in the diffusion coefficient of the ferricyanide ions as shown by fig.5.1. Small changes in the density and surface tension coefficient also occurred. Mass transfer tests were performed at different concentrations of the sodium hydroxide within the range 0.5M to 5.9M. Below 0.5M it was not possible to obtain a limiting current and above 5.9M the solution was unstable. The variations of the two dimensionless groups, $N_{Sc} \equiv \frac{\mu_f}{D_i \rho_f}$ and $\frac{(\sigma g_o)^{\frac{3}{4}} \rho_f^{\frac{1}{4}}}{g_{grav}^{\frac{1}{4}} \mu_f}$ with NaOH concentration, within the range of the investigation, are shown in fig.5.2. The quantity $\left(\frac{\sigma g_o}{\rho_f g_{grav}}\right)^{\frac{1}{2}}$ was found to be invariable with NaOH concentration.

5.1.7 Varying the temperature

A series of tests were carried out at various temperatures within the range 60°F to 105°F. As the cell was not equipped with a cooling device, it was not possible to operate the cell below the temperature of the laboratory. The upper limit of temperature (105°F) was set by the ferricyanide which decomposed above this temperature. The measured variations of liquid properties within this

temperature range are shown in fig.5.3.

For these tests, the variation of the dimensionless group $\frac{(\sigma g_o)^{\frac{3}{4}} \rho_f^{\frac{1}{4}}}{g_{grav}^{\frac{1}{4}} \mu_f}$ with N_{Sc} was almost the same as for the tests in which the NaOH concentration was varied. The quantity $\left(\frac{\sigma g_o}{\rho_f g_{grav}}\right)^{\frac{1}{2}}$ was again found to be constant. The results of these tests, therefore, did not provide any fresh evidence useful for determining the dependence of the dimensionless conductance and the critical superficial gas velocity on the liquid property groups. However, they were useful in providing additional experimental evidence to supplement the results of the tests described in the previous section.

The range of N_{Sc} and $\frac{(\sigma g_o)^{\frac{3}{4}} \rho_f^{\frac{1}{4}}}{g_{grav}^{\frac{1}{4}} \mu_f}$ corresponding to the temperature range of 60°F to 105°F, was considerably less than that corresponding to the range of NaOH concentrations of the previous section, as shown by figure 5.2.

5.1.8 Varying the cathode thickness

The 'Porosint' material used in these tests was available in one thickness only, namely $\frac{1}{16}$ -inch. The investigation of the effects of cathode thickness was made possible by constructing cathodes from several layers of material. Due to practical difficulties in accommodating the extra thick cathode in the cell base, the number of layers was limited to four.

Tests were performed at the following three values of t/d_p: 95, 190, and 380.

5.1.9 Varying the grade of porous material

Six different grades of porous nickel were used in this series of tests. These were: 'Porosint' nickel, used in most of the other tests in the investigation, four grades, C, D, E and F of a sintered nickel manufactured by Pall Corporation and a material specially produced for this work by the research laboratories of International Nickel. It is supposed that the grade of the porous cathode can be characterised by two properties of the material, namely pore size d_p and bubble site density n/A. These two quantities have been estimated for each of the six materials used, (see Appendix II). The values are listed in the table below.

Material	pore size, ft		Max. bubble site density, sites/ft^2
	Min	Max	
'Porosint'	$.501 \times 10^{-4}$	$.594 \times 10^{-4}$	27,000
Int. Nickel	$.715 \times 10^{-4}$	$.78 \times 10^{-4}$	11,500
Pall grade C	6.33×10^{-4}	7.25×10^{-4}	2,000
D	2.7×10^{-4}	3.48×10^{-4}	6,900
E	1.56×10^{-4}	1.92×10^{-4}	10,000
F	$.855 \times 10^{-4}$	$.957 \times 10^{-4}$	14,400

5.2 Electrode cleaning procedure

5.2.1 Electrode contamination

Early in the investigation, after a number of tests had been performed, a decrease in the conductance values was observed. This decrease was attributed to the formation of a coating on the cathode surface, commonly referred to as "electrode poison" [19]. Unsuccessful attempts were made to remove this coating and consequently it was necessary to renew the electrode at fairly frequent intervals. The criterion for renewing the electrode was a decrease of 10% in the maximum conductance of a reference test. It was found that the poisoning process was accelerated when certain gases, for example propane and butane, were employed as the injected gas. Renewing the electrode was unsatisfactory, since reproducibility between different electrodes was often no better than 20% for the conductance and 10% for the critical superficial velocity. For this reason the results of the early tests are grouped according to the electrode used; each electrode being designated a number.

5.2.2 The introduction of a method for cleaning the electrode

Eventually a chemical method of cleaning the cathode came to light [70]. The procedure was as follows:

(i) The cathode was thoroughly rinsed in distilled water to remove any electrolyte from the pores.

(ii) This was followed by a brief rinse in 50% hydrochloric acid and a further thorough rinse in distilled water.

(iii) The cathode was then activated by reducing it with hydrogen, cathodically, in a 5% sodium hydroxide solution for approximately one hour.

By carrying out this procedure before each test, reproducible results were obtained with the same cathode for a large number of tests. A similar cleaning procedure was used for the anode, but in this case it was carried out at less frequent intervals.

5.3 The determination of a working potential difference

It will be recalled from Chapter 2 that the mass transfer process is diffusion-controlled only within certain limits of the potential difference between the electrodes, and that within these limits the current is independent of the applied potential.

For the present investigation the range of diffusion-controlled potential difference was experimentally established by producing a continuous record of the ionic current as the potential difference was slowly increased by means of the motor-driven potential-divider. Figure

5.4 is an example of such traces, showing the horizontal limiting-current region.

The range of limiting-current potential difference is a function of the mass-transfer conductance and possibly of other variables in the investigation, such as solution temperature, supporting electrolyte concentration and electrode geometry. Thus, for each set of system parameters, it was necessary to produce two current-voltage traces, one at the highest conductance and the other at the lowest. From the two traces, a potential difference was selected which gave a limiting current in both cases. This value was employed, where appropriate, as the working potential-difference in subsequent tests.

5.4 Test procedure

This section describes the procedure for carrying out a single test to measure the ionic current at various rates of gas injection.

First the cathode was cleaned by the method described in section 5.2 and replaced in the cell. A slight pressure, (controlled by the needle valve) of one- or two-inches Hg was applied beneath the cathode to prevent seepage of the electrolyte solution, which was then poured into the cell. The pressure beneath the cathode was increased until the barbotage rate was sufficient to circulate the liquid in the cell whilst it was heated to the

required temperature. The potential difference between the electrodes was adjusted to the value predetermined by the method described in section 5.3.

Earlier experience had shown that the conductance was slightly dependent upon the previous history of the test and, in particular, upon the initial condition of the cathode. As an example, a comparison was made between a test in which the cathode was initially dry and a test in which the electrolyte was first allowed to seep into the pores of the cathode. In these extreme cases, the 'dry' electrode gave a 3% lower maximum conductance than the 'wet' electrode. The need for a 'standard procedure' was apparent and for subsequent tests the procedure was as follows:

(i) After the solution had reached the correct temperature, the pressure beneath the cathode was reduced to allow the solution to soak into the pores. This provided a simple means of obtaining a reproducible initial condition of the cathode.

(ii) The pressure in the plenum chamber was then slowly increased until the gas flow rate through the cathode reached a value of approximately 10% of the critical gas injection rate. (The critical value was roughly known in most cases, from experience of previous tests).

(iii) The temperature of the gas was made equal $\pm 1^{o}C$,

to that of the solution by manual adjustment of the current to the heater in the gas stream; any out-of-balance between the two temperatures being indicated on the central-zero galvanometer.

(iv) Readings were taken of the pressure drop across the orifice, and the pressure upstream of the orifice, during which time a trace of the ionic current was recorded on the pen recorder.

(v) Stages (ii), (iii) and (iv) were repeated at intervals of gas injection rate of approximately 10% of the critical value. The test was terminated after four or five sets of readings were taken beyond the critical gas injection rate. In general, readings were not taken in the direction of decreasing gas flow rates because of a slight hysteresis effect.

Samples of the electrolyte solution were taken before and after each test. The samples were analysed using the absorptiometer to determine the concentration of the ferricyanide. The pen recorder was calibrated for each test, as described in Appendix I. Readings were also taken of the laboratory pressure and temperature.

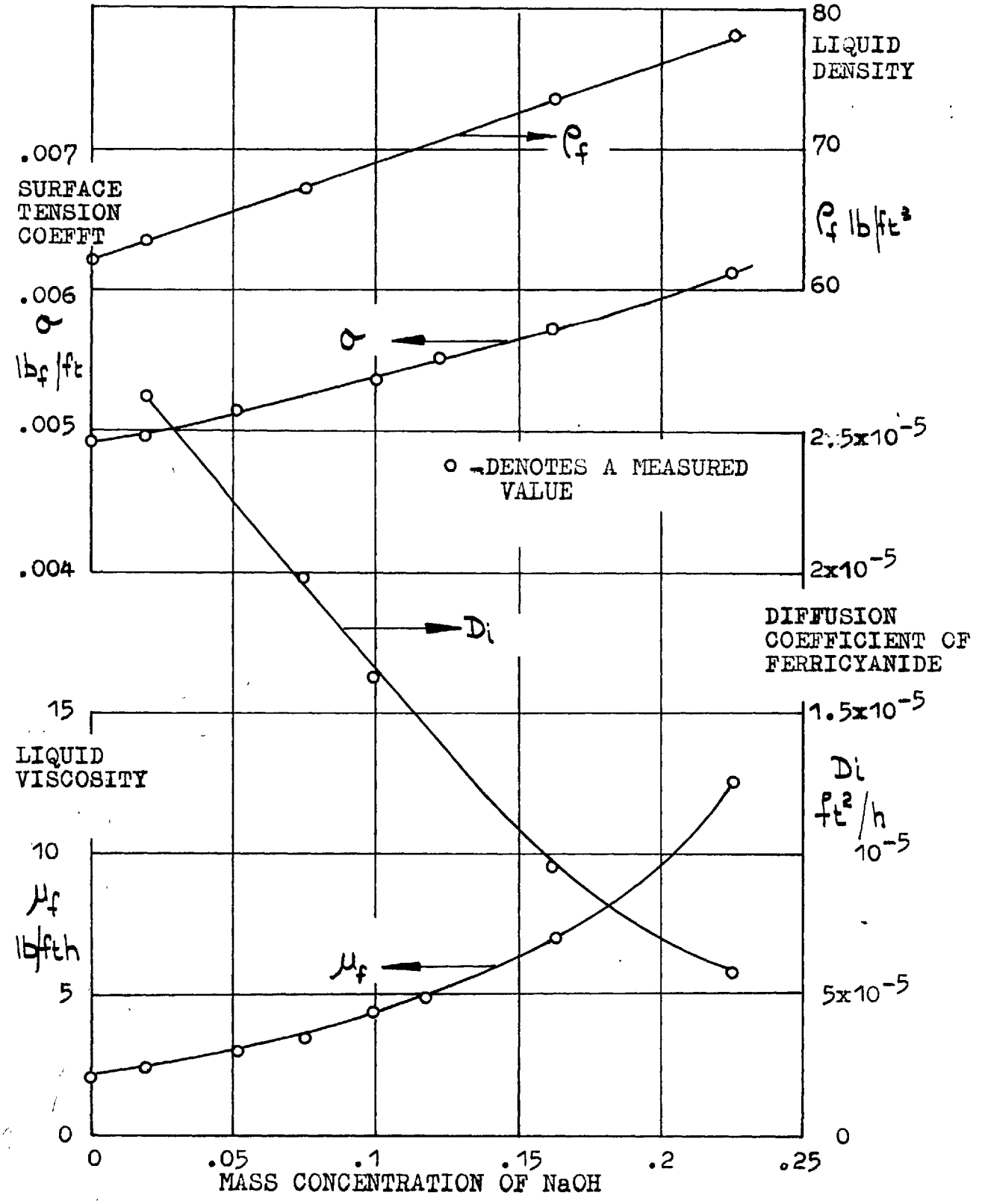

Fig.5.1 VARIATION OF LIQUID PROPERTIES WITH NaOH CONCENTRATION

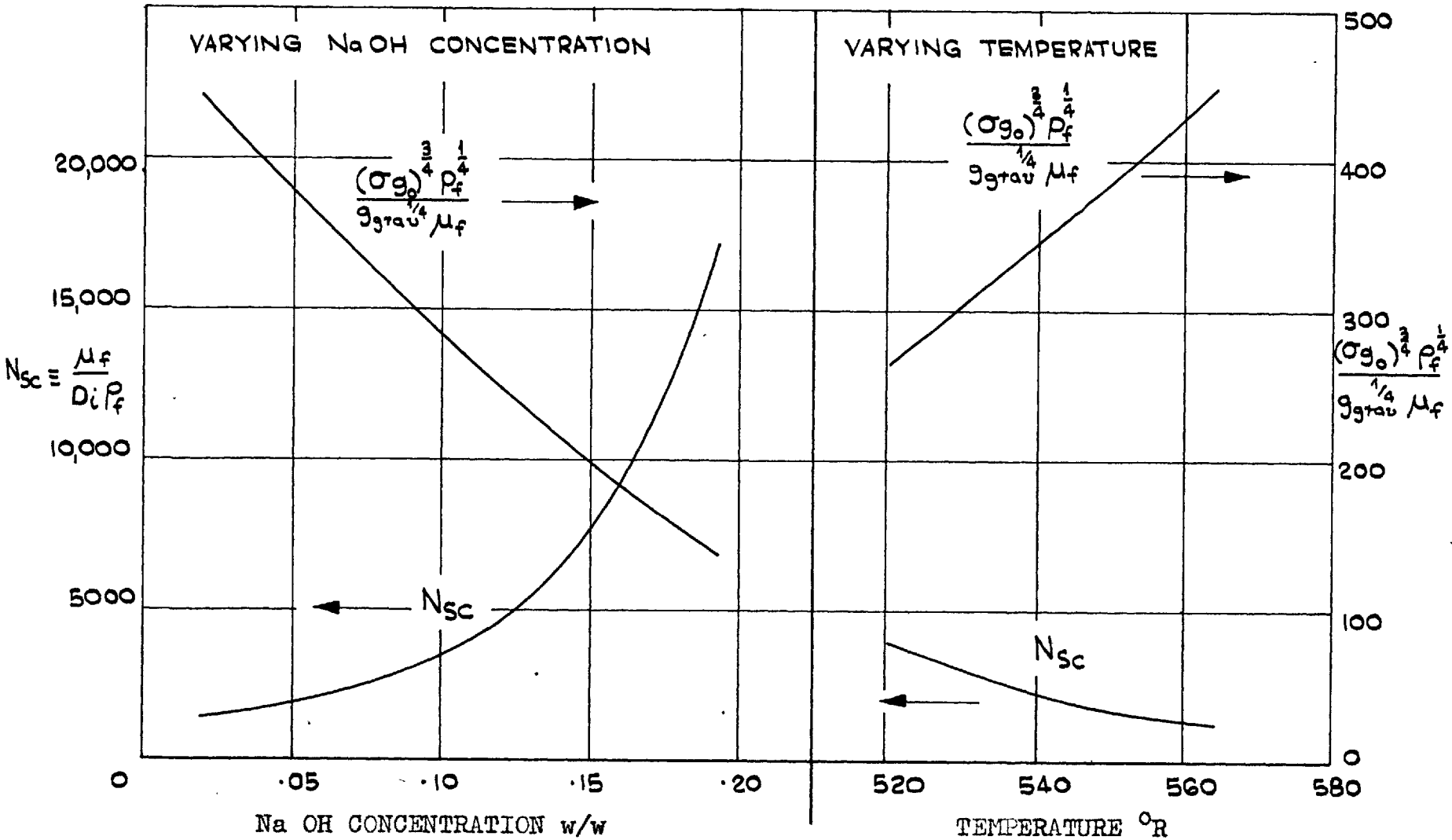

FIG. 5.2 RANGES OF DIMENSIONLESS GROUPS FOR THE TEST SERIES IN WHICH LIQUID PROPERTIES WERE VARIED

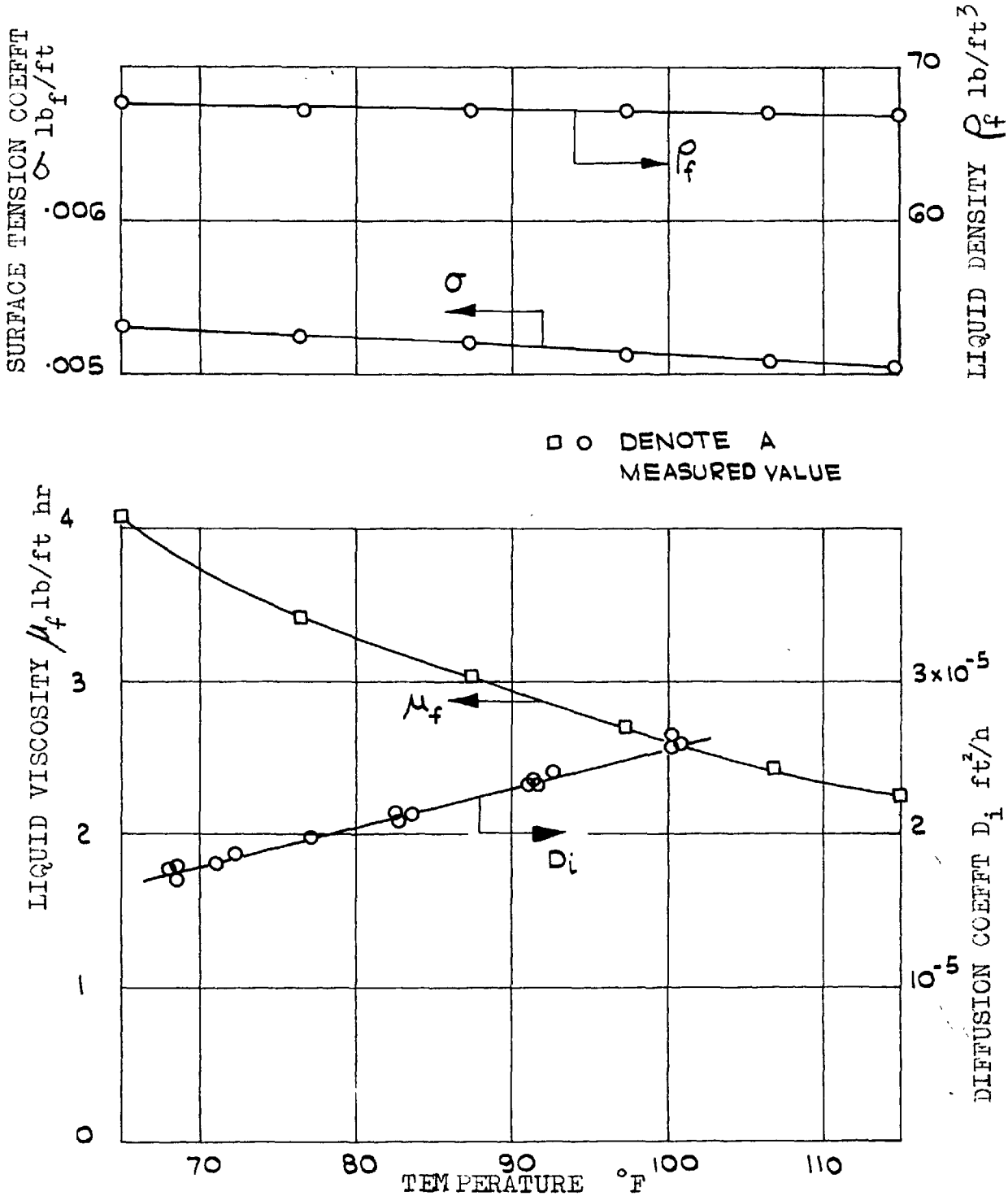

Fig. 5.3 VARIATION OF LIQUID PROPERTIES WITH TEMPERATURE

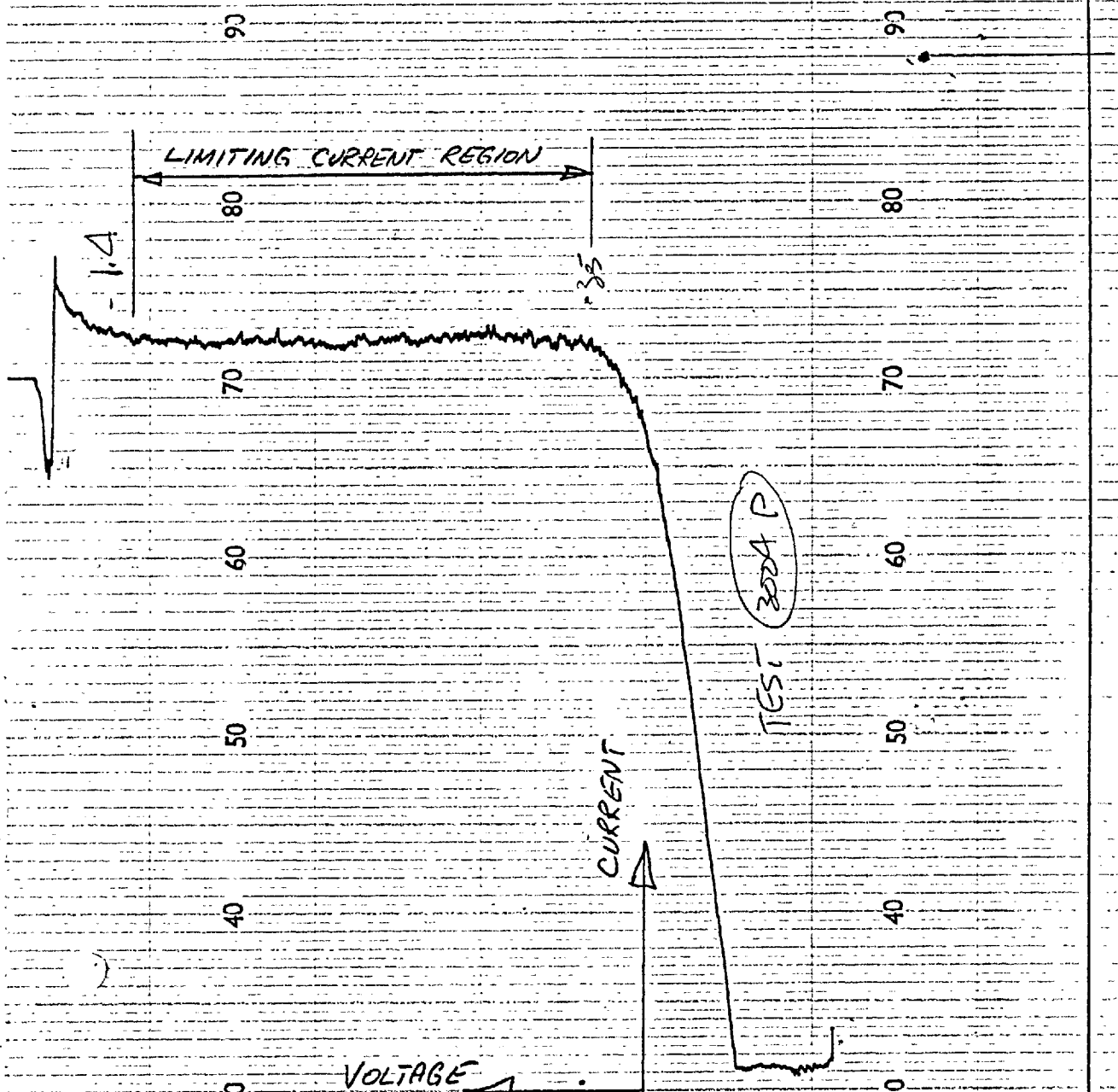

Fig. 5.4 TYPICAL TRACE OF CURRENT VERSUS VOLTAGE

Chapter 6 Reduction and presentation of data

6.1 Method of processing experimental readings.

The object of each test carried out was to determine the variation of the mass transfer conductance with the superficial velocity of the injected gas. This section describes how the experimental data were processed to give the conductances and superficial velocities.

6.1.1 The mass transfer conductance.

The conductance, g_i was evaluated from the current density, and the bulk concentration of the reacting ions, $m_{i,G}$. Equation 2.3 (page 18), relates the conductance to the current density, and for a diffusion controlled process ($m_{i,s} \ll m_{i,G}$) the equation, rearranged, is:

$$g_i = \frac{I.M_i}{m_{i,G} n F} \qquad 6.1$$

where M_i is the molecular weight of the reacting ions

n is the number of electrons exchanged per reacting ions

F is Faraday's constant = 96,500 coulombs/gm equiv.

Substituting the values of M_i and n for the reduction of ferricyanide i.e. n = 1 gm equiv/mole, M_i = 211.95, into equation 6.1, it becomes:

$$g_i = 0.0175 \frac{I}{m_{i,G}} \quad lb/ft^2h \qquad 6.2$$

where the units of I are amps/ft^2 and $m_{i,G}$ is a dimensionless mass ratio.

In the evaluation of the current density, the area used was the projected area of the electrode.

Figure 6.1 shows a recorder trace of the ionic current during a test. The trace shows an irregular oscillation of the current, at a frequency of around 20 cycles per second. The amplitude of the oscillations is seen to increase from almost zero at the lowest gas injection rate to about 2.5% of the mean value, at the highest gas injection rate. These oscillations are attributed to the formation of large bubbles of gas as a result of the coalescence of smaller bubbles leaving the porous surface.

A time-mean value of the current used in evaluating the conductance was estimated for each gas injection rate by drawing a line through the middle of the oscillations as shown in Figure 6.1. To test the accuracy of this method of determining the time-mean current, an oscilloscope, fitted with a cine-camera, was used to obtain an undamped recording of the current, on a time scale of 5 inches per second. Measurement of the area under the trace gave the time-mean value of the current, against which the estimated value was checked. In all cases, the difference between the values obtained by the two methods was less than 2%.

6.1.2 Superficial velocity of the gas.

The superficial velocity of the gas is defined as the volumetric gas injection rate per unit projected area of the porous electrode. It was evaluated at the temperature and pressure of the electrode surface.

Equation A.1.1 of Appendix I, relates the volumetric flow rate at standard conditions of 14.7 psi and 60°F to the measured quantities. This equation is:

$$\dot{V} = 90.5\ C_d \left(\frac{hP_o}{T_o \delta}\right)^{1/2} \qquad 6.3$$

where $\dot{V}$ is the volumetric flow rate of gas ft^3/h at 14.7 psi and 60°F.

h is the pressure differential across the orifice, in. H_2O

P_o is the pressure upstream of the orifice, in. Hg

T_o is the temperature upstream of the orifice °R

δ is the specific gravity of dry gas relative to dry air

C_d is the discharge coefficient of the orifice and is a function of the orifice Reynolds Number which is given by:

$$N_{Re,OR} = \frac{4\dot{V}\rho_g}{\pi d_{OR} \mu_g} \qquad 6.4$$

where ρ_g and μ_g are the gas density and viscosity at

the conditions upstream of the orifice and d_{OR} is the orifice diameter.

The calibration of the orifice is described in Appendix I, and the resulting calibration curve of C_d as a function of $N_{Re,OR}$ is shown as Figure A.1.1. To find the discharge coefficient for a particular flow condition, a value was initially guessed and by using an iterative procedure a more exact value was obtained from equations 6.3 and 6.4 and Figure A.1.1.

The superficial velocity was calculated from the following equation:

$$\dot{V}'' = \frac{2.56\ C_d}{A_p} \left(\frac{hP_o}{T_o \delta} \right)^{1/2} \frac{T_S}{P_S} \qquad 6.5$$

where A_p is the projected area of the cathode, ft^2 and suffix S refers to conditions at the surface of the electrode.

6.1.3 Method of computation.

The computations of the conductance and of the superficial velocity were carried out on the University of London Atlas computer. Although the operations involved were fairly simple, the use of a computer was justified by the large quantity of data.

6.1.4 A correction for electrode poisoning, applied in certain tests.

The test series investigating the effects of pool

diameter and of pool depth were performed prior to the introduction of the electrode cleaning procedure. Because of their relatively small influence on the conductance, the effects of these two parameters were partially masked by electrode contamination. It was possible to estimate the effects of the contamination in terms of a percentage reduction in the conductance compared with a fresh electrode, by repeating the first tests of each test series at the end of the series. A correction of approximately 2% was added to the conductances of each test to compensate for the poisoning effects. These corrections were only applied in the two test series mentioned above.

6.2 Presentation of the processed data.

The data are presented in graphical form as conductances versus superficial velocities and also in tabulated form in Appendix III. Each of the test series summarised in table 5.1 of the previous chapter, is represented by a separate figure. For the tests in which the effects of gas properties were investigated, a separate figure is included for each electrode used.

Table 6.1, below, summarises the data presented in the figures; the tabulated data presented in Appendix III are similarly sub-divided.

Table 6.1 Summary of data presented.

Description of tests			Figure number
1. Varying the pool depth			6.2
2. Varying the pool diameter			6.3
3.	Gas employed	Electrode No.	
	argon	7	6.4
Varying the	nitrogen	1	6.5
system pressure	nitrogen	4	6.6
	nitrogen	7	6.7
4.		Electrode No.	
		1	6.8
		3	6.9
Varying the nature of		8	6.10
the gas (constant pressure)		9	6.11
		10	6.12
		11	6.13
5. Tests with and without surfactant			6.14
6. Varying the sodium hydroxide concentration			6.15
7. Varying the temperature			6.16
8. Varying the cathode thickness			6.17
9. Varying the grade of the porous material			6.18

6.3 Description of data.

6.3.1 General relations between conductance and superficial velocity.

As the superficial velocity is increased, the variation of the conductance exhibits the same general trends for most of the tests carried out. These trends are shown as an initial increase in the conductance followed, above a critical superficial velocity, by a decrease in the conductance. The exceptions to these general trends occurred in the tests in which hydrogen and helium were used. In these tests, the conductance reached a maximum at two different values of the superficial velocity, one a low value (of the order of $\frac{1}{10}$ ths of ft/s), the other at a value an order of magnitude greater (see Figs. 6.13 and 6.8). An explanation of this untypical behaviour is suggested in the next chapter.

6.3.2 Effects of the parameters varied.

(i) Gross geometry.

The results of the tests to determine the limits of the pool geometry effects are shown in Figures 6.2 and 6.3. As expected, the only influence of the geometry ratios occurs for values approaching unity.

(ii) Gas properties.

The effect of increasing the density of the injected

gas by increasing the system pressure is seen from Figures 6.4 to 6.7 to be an increase in the conductance and a decrease in the critical superficial velocity. Changing the nature of the gas involves both the gas density and the viscosity. Thus it is not obvious, from Figures 6.8 to 6.13, what are the separate effects of these two variables. These effects are, however, revealed by the analysis of the data in the next chapter.

(iii) Liquid properties.

The addition of a surfactant to the electrolyte solution resulted in an increase in the conductance and a decrease in the critical superficial velocity, as shown by Figure 6.14. Decreasing the Schmidt Number, by means of the solution temperature and the NaOH concentration, (Figures 6.15 and 6.16) increased the conductance but had little effect on the critical superficial velocity.

(iv) Pore geometry.

The effect of the thickness of the porous cathode is shown in Figure 6.17. An increase in the thickness produced a decrease in the conductance but appeared to have no influence on the critical superficial velocity.

Figure 6.18 shows a very marked influence of the grade of the porous cathode material on both the conductance and on the critical superficial velocity. Since several inde-

pendent variables are needed to describe the grade of a porous material, it is not possible to interpret the effects shown in Figure 6.18 at this stage. The effects are, however, revealed by the analysis in the next chapter.

6.3.3 An effect of electrode mounting.

The method of mounting the porous cathode in the base of the cell was described in Chapter 4, Description of Apparatus, and is illustrated in Figure 4.2. In the early part of the experimental investigation, the material used for the construction of the cell base was polyethylene. With this material, the minimum permissible thickness of the lip against which the electrode was held, was found to be $\frac{1}{16}$ -inch; below this thickness the lip distorted under the pressure of the porous electrode resulting in leakage of gas round the edge of the electrode.

Subsequently, two improvements were made in the mounting of the electrode; firstly, the cell base was constructed from a harder, nylon material and secondly, a thin, soft teflon gasket was introduced between the lip and the porous cathode, thus reducing the pressure required to form a seal between them. These refinements enabled the thickness of the lip to be reduced to about 0.01 inches, resulting in an almost flush-mounted electrode.

This slight change in cathode mounting had a surprisingly marked effect on the results, as can be seen from a

comparison of Figures 6.11 and 6.13. The latter presents results obtained with the flush-mounted electrode and shows the conductances to be higher and the critical superficial velocities to be lower than those of Figure 6.11 which presents results obtained using the early method of electrode mounting.

In order to verify that the effect observed was a result of the electrode mounting, two tests were carried out in which only the method of mounting the electrode was different. The results of these tests, which provide the necessary verification, are shown in Figure 6.19.

This 'lip' effect is probably associated with the effect observed when the diameter of the pool is reduced to almost that of the porous plate. The surprisingly large effect of such a small lip is an indication that the mass-transfer process is controlled in a region very close to the electrode surface.

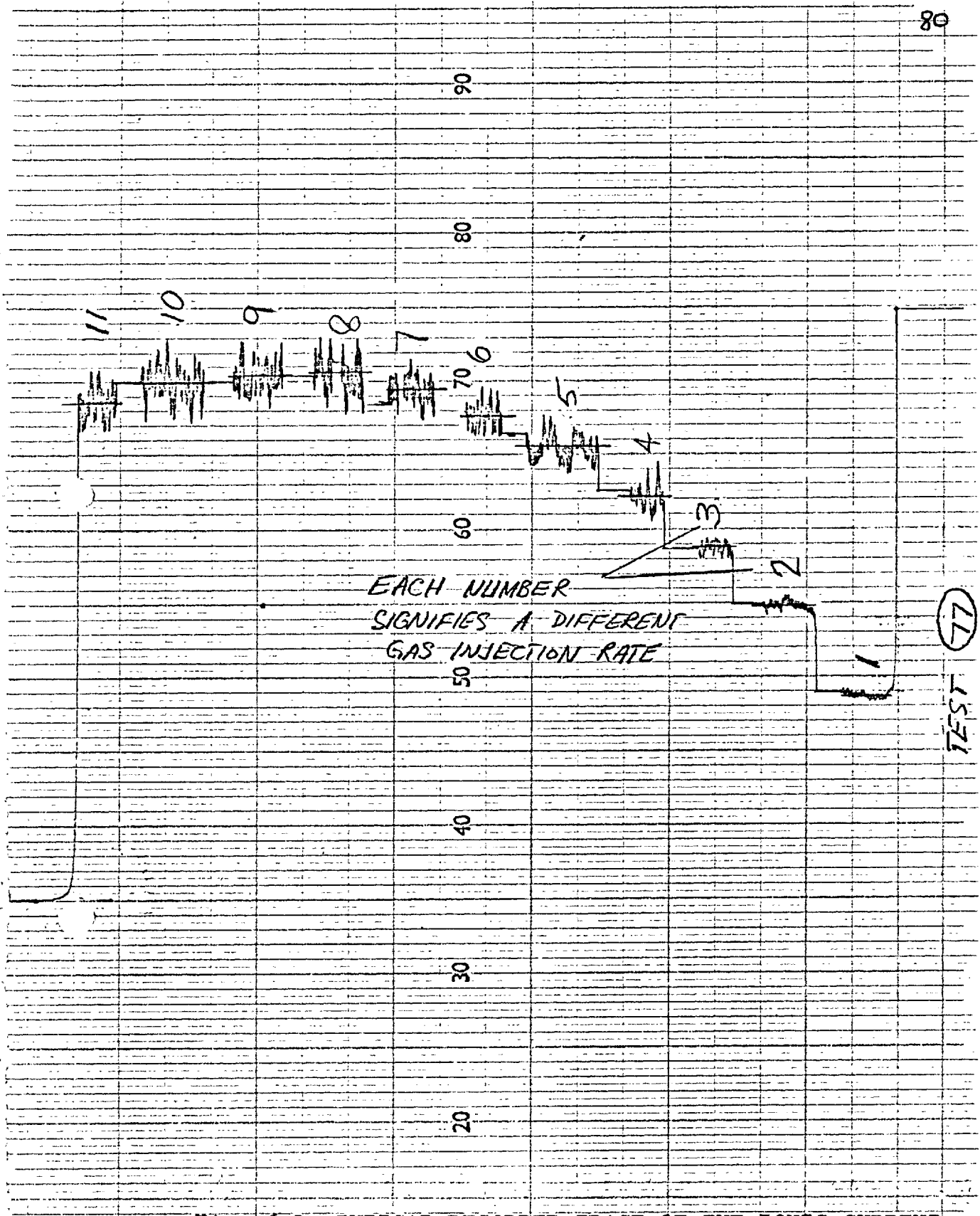

Fig. 6.1 TYPICAL RECORDER TRACE OF THE IONIC CURRENT DURING A TEST

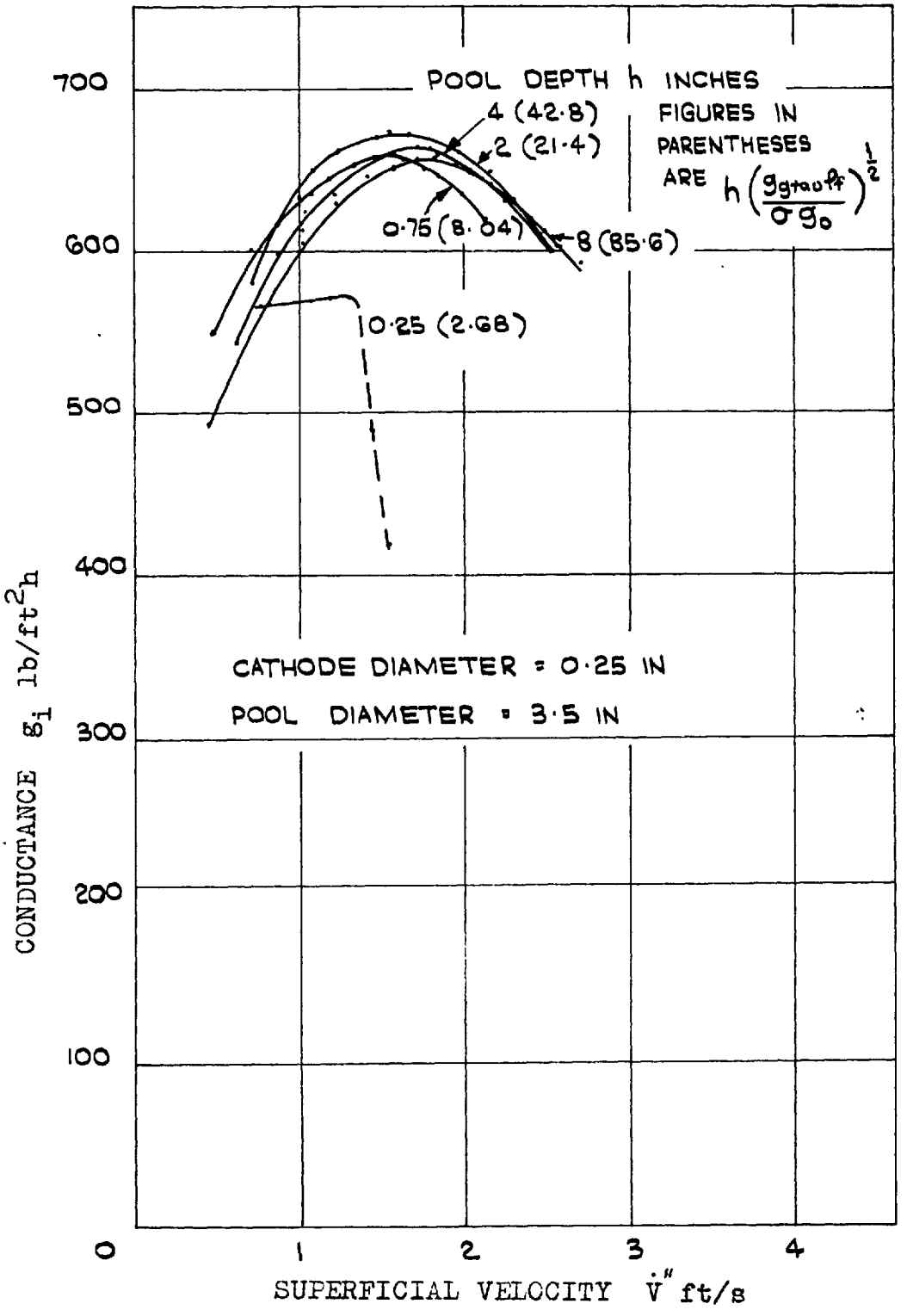

Fig. 6.2 EFFECT OF POOL DEPTH

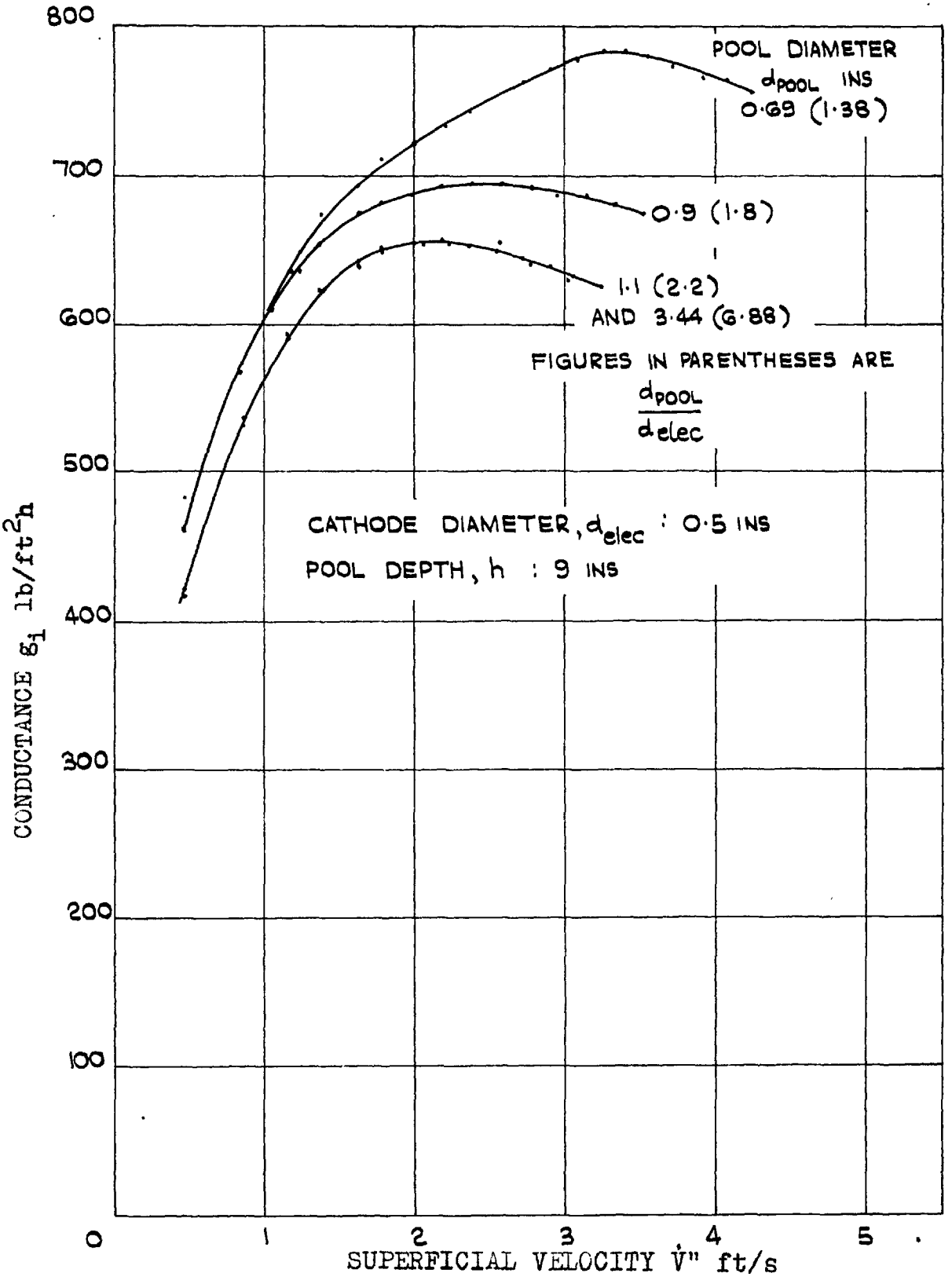

Fig. 6.3 CONDUCTANCE VERSUS SUPERFICIAL VELOCITY FOR VARIOUS POOL DIAMETERS

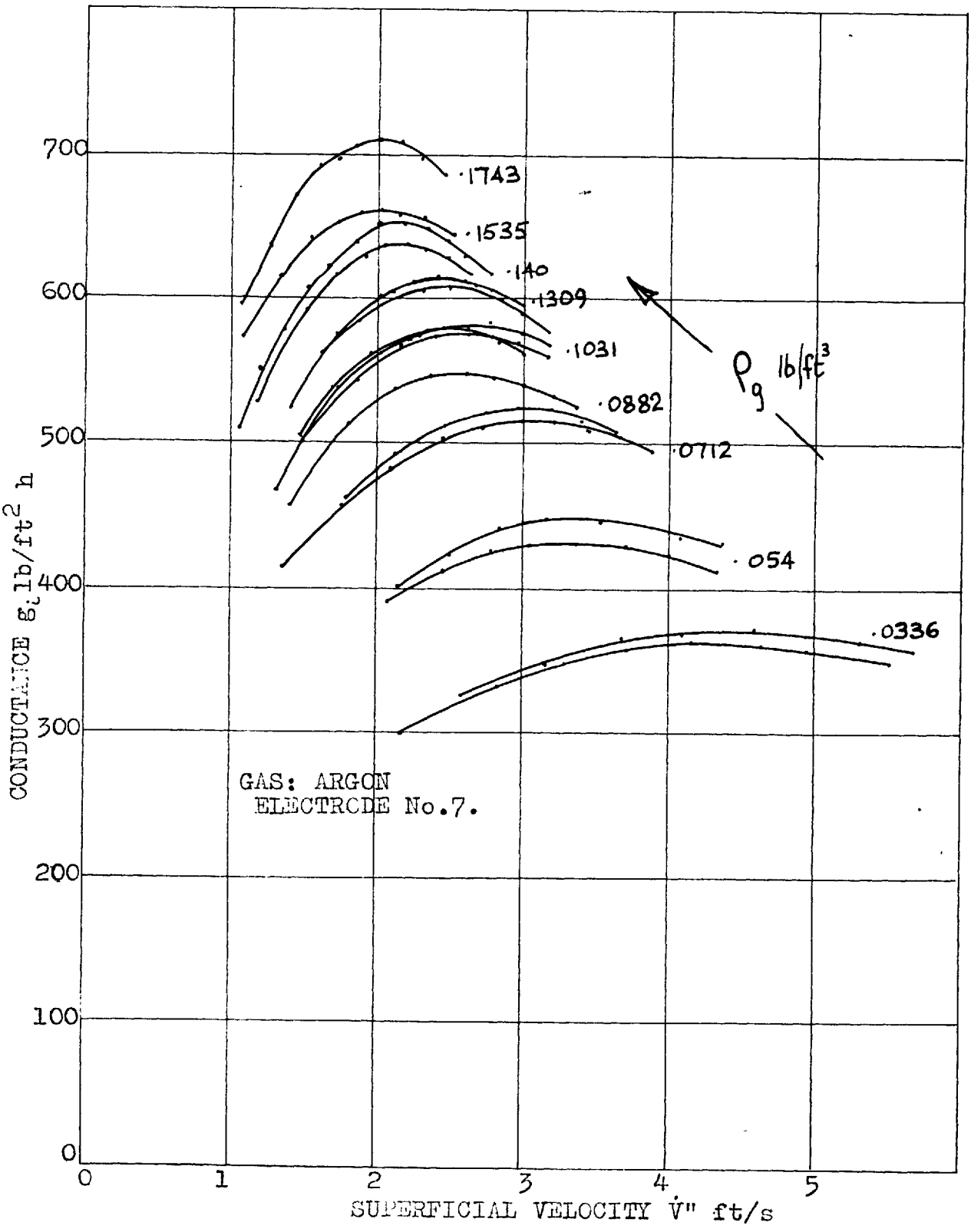

FIG. 6.4 CONDUCTANCE VERSUS SUPERFICIAL VELOCITY FOR ARGON AT VARIOUS PRESSURES.

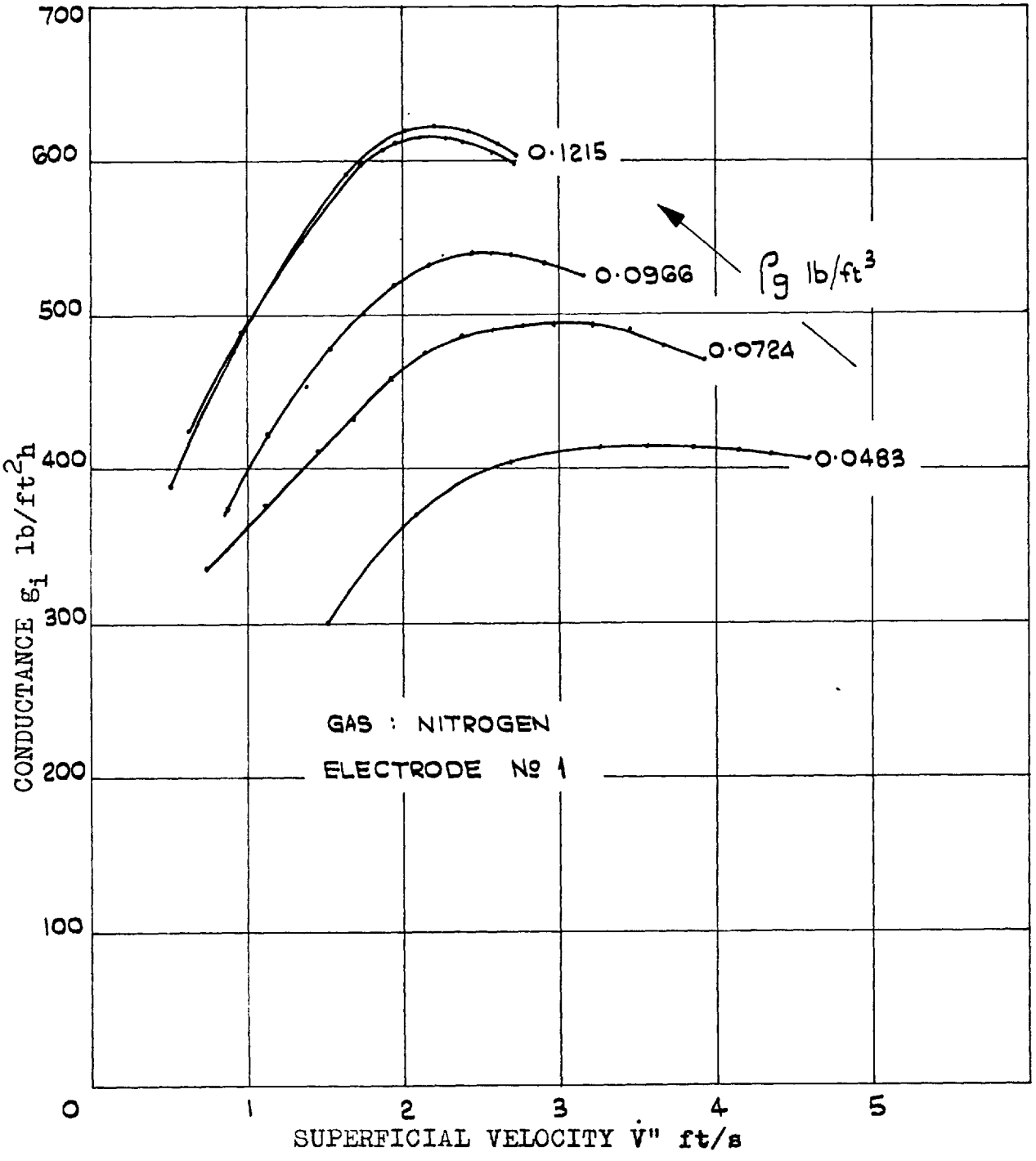

Fig. 6.5 CONDUCTANCE VERSUS SUPERFICIAL VELOCITY FOR NITROGEN AT VARIOUS PRESSURES

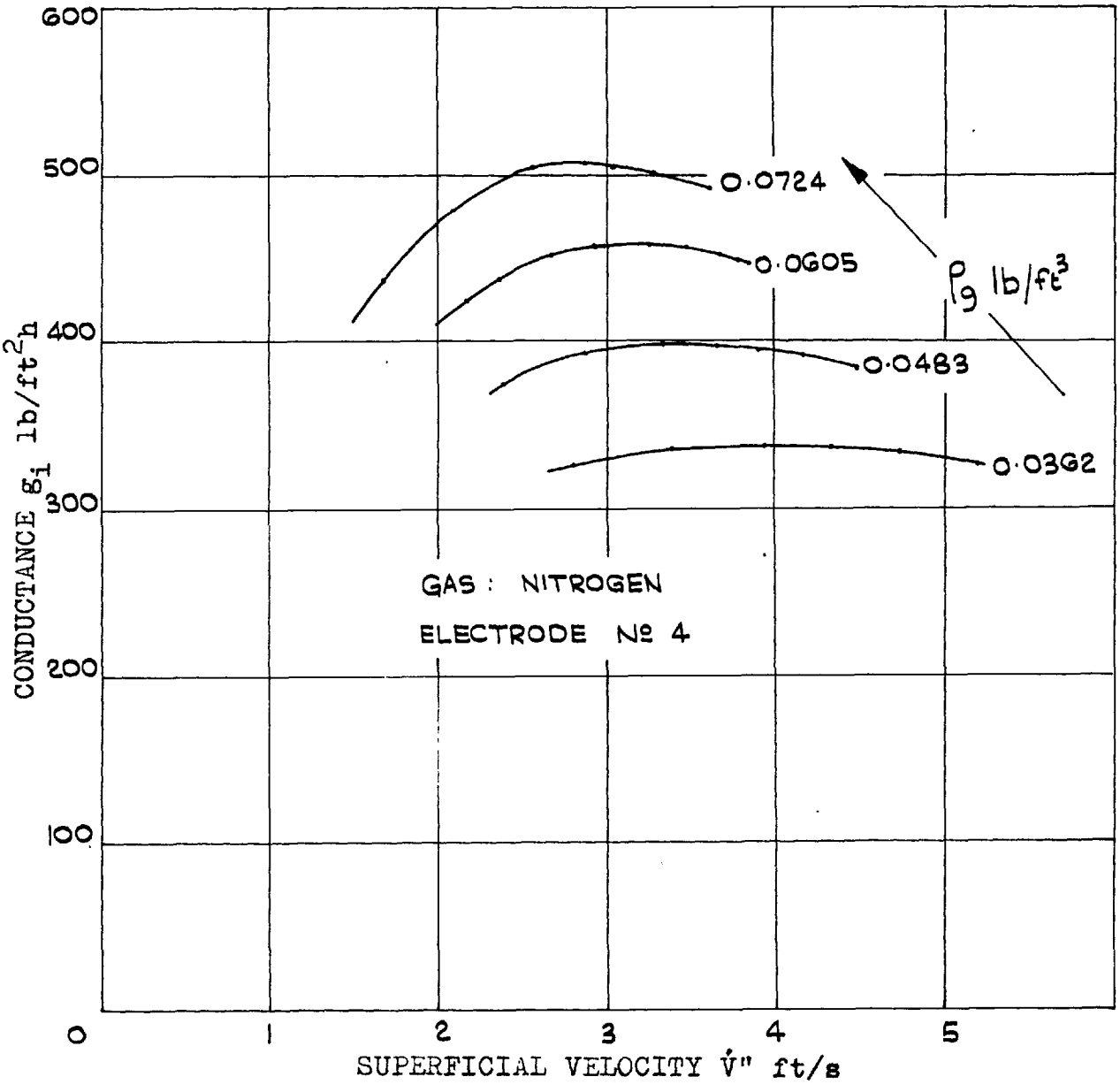

Fig. 6.6 CONDUCTANCE VERSUS SUPERFICIAL VELOCITY FOR NITROGEN AT VARIOUS PRESSURES

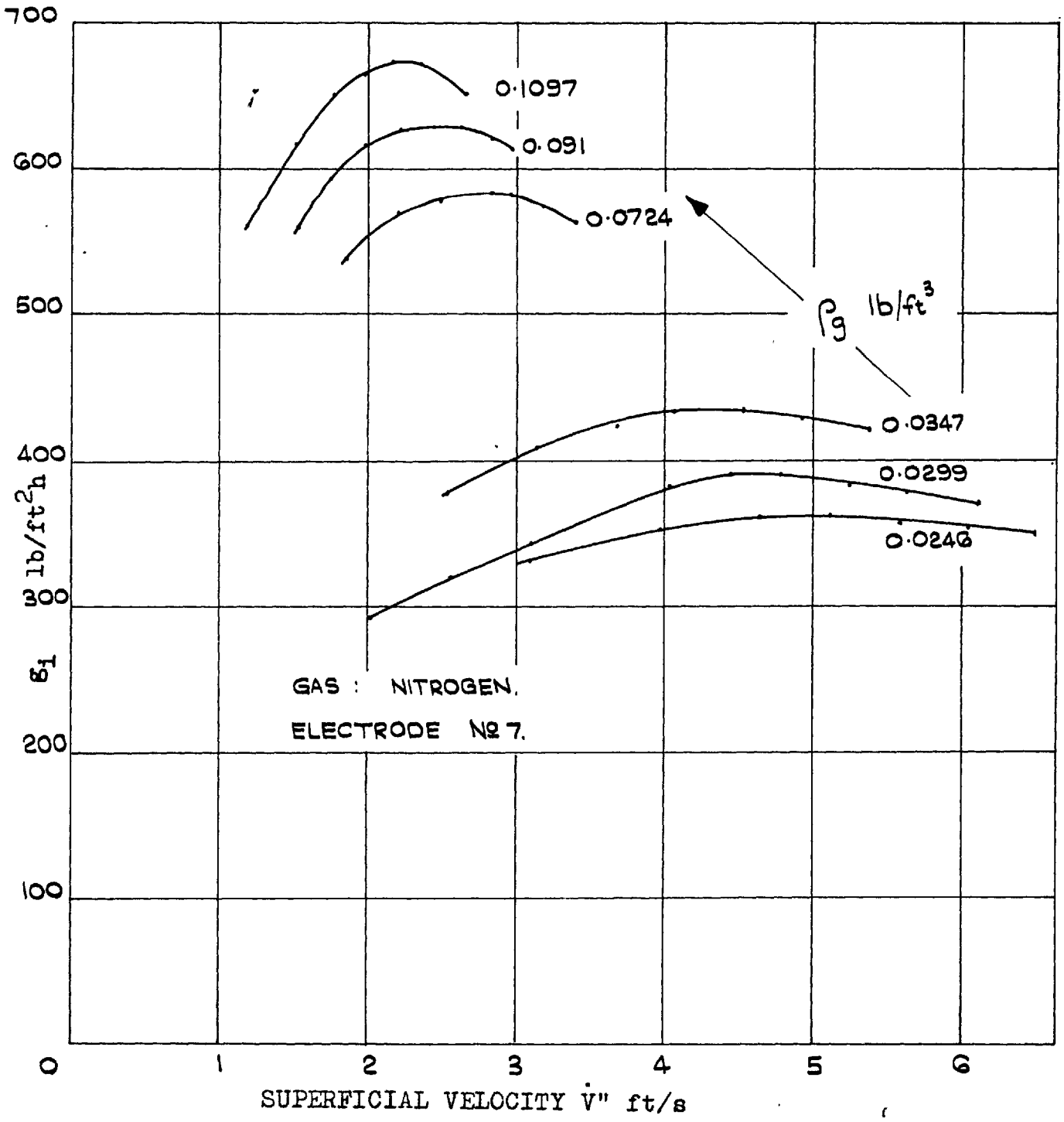

Fig. 6.7 CONDUCTANCE VERSUS SUPERFICIAL VELOCITY FOR NITROGEN AT VARIOUS PRESSURES

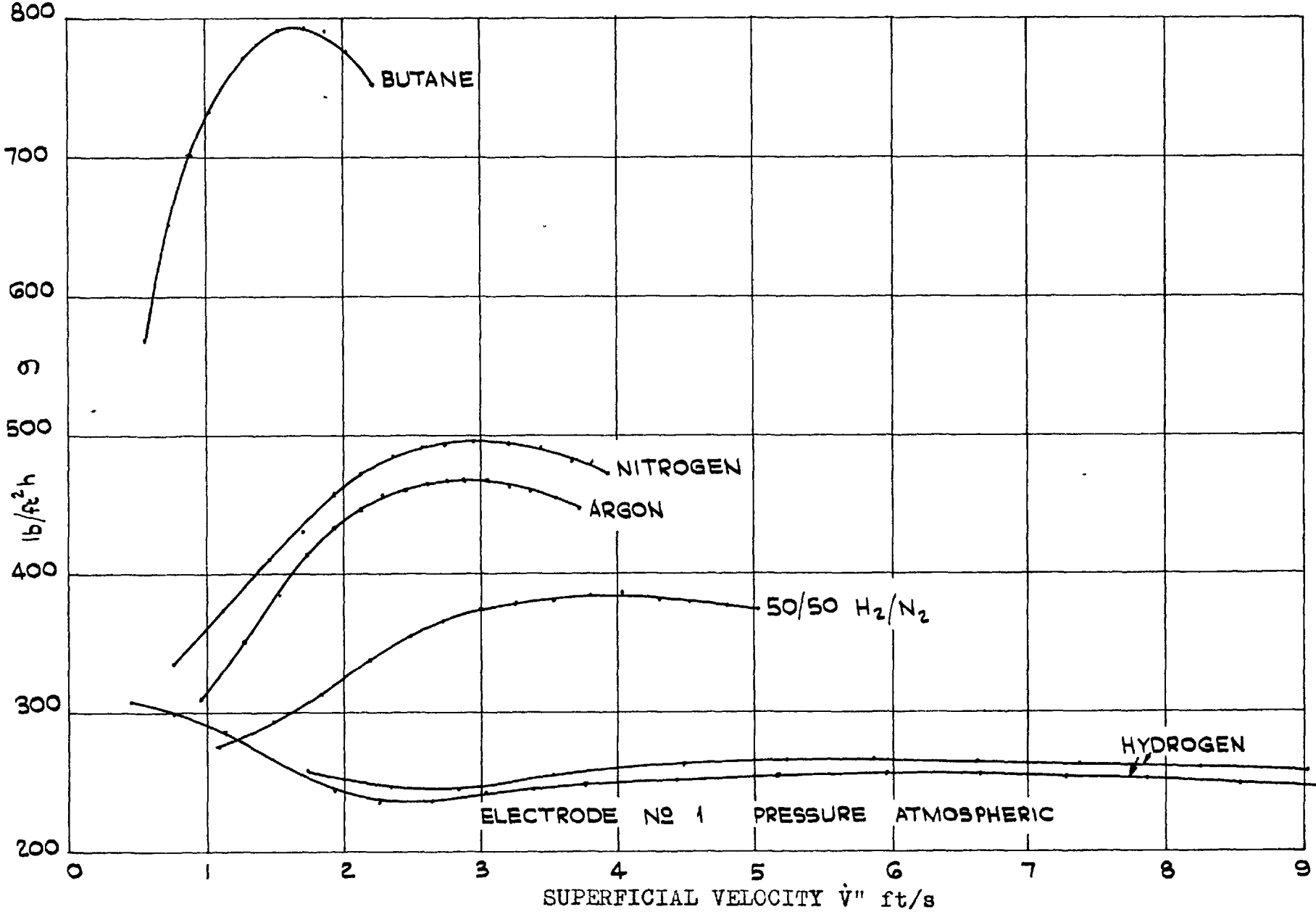

Fig. 6.8 CONDUCTANCE VERSUS SUPERFICIAL VELOCITY FOR VARIOUS GASES

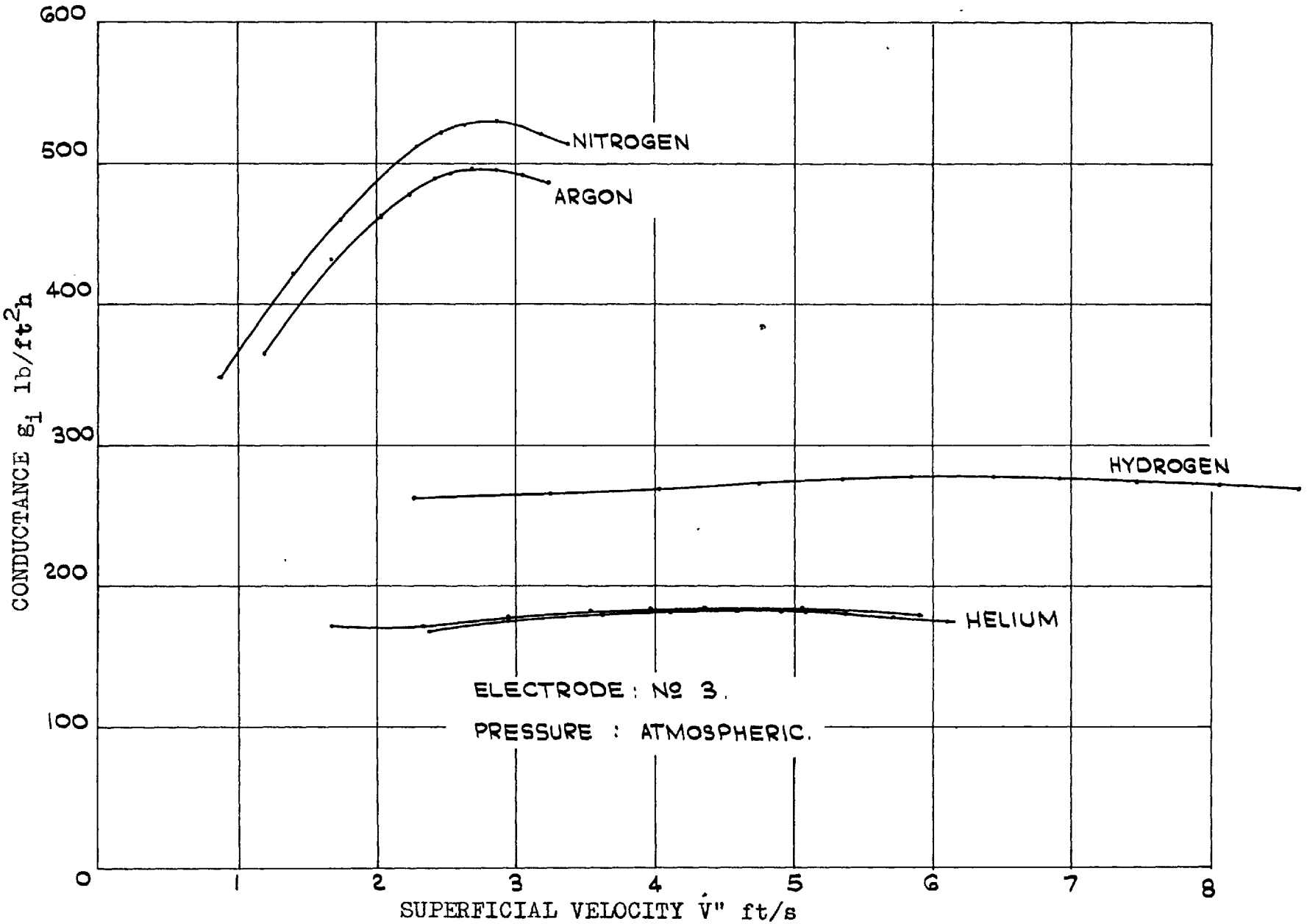

Fig. 6.9 CONDUCTANCE VERSUS SUPERFICIAL VELOCITY FOR VARIOUS GASES

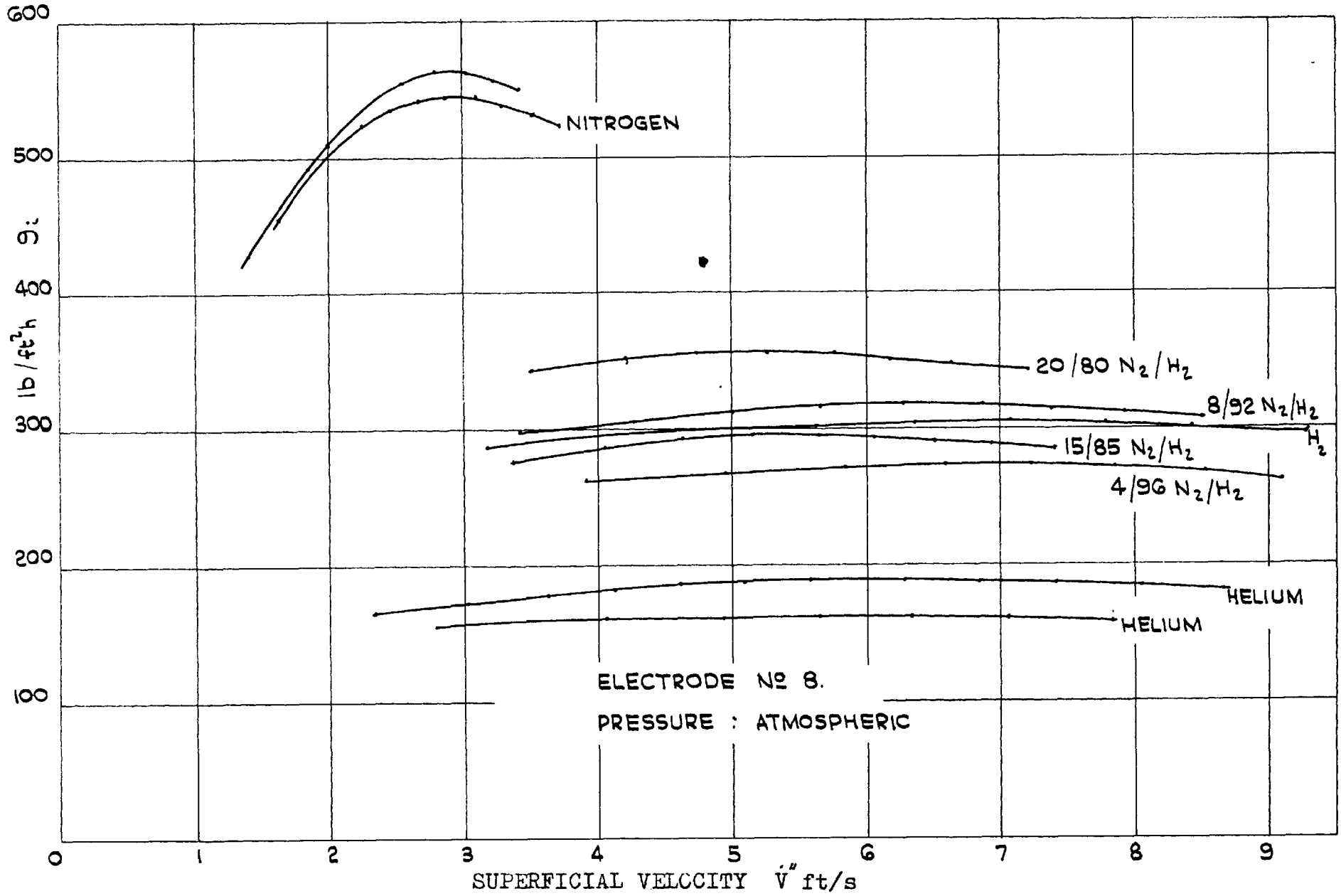

Fig. 6.10 CONDUCTANCE VERSUS SUPERFICIAL VELOCITY FOR VARIOUS GASES

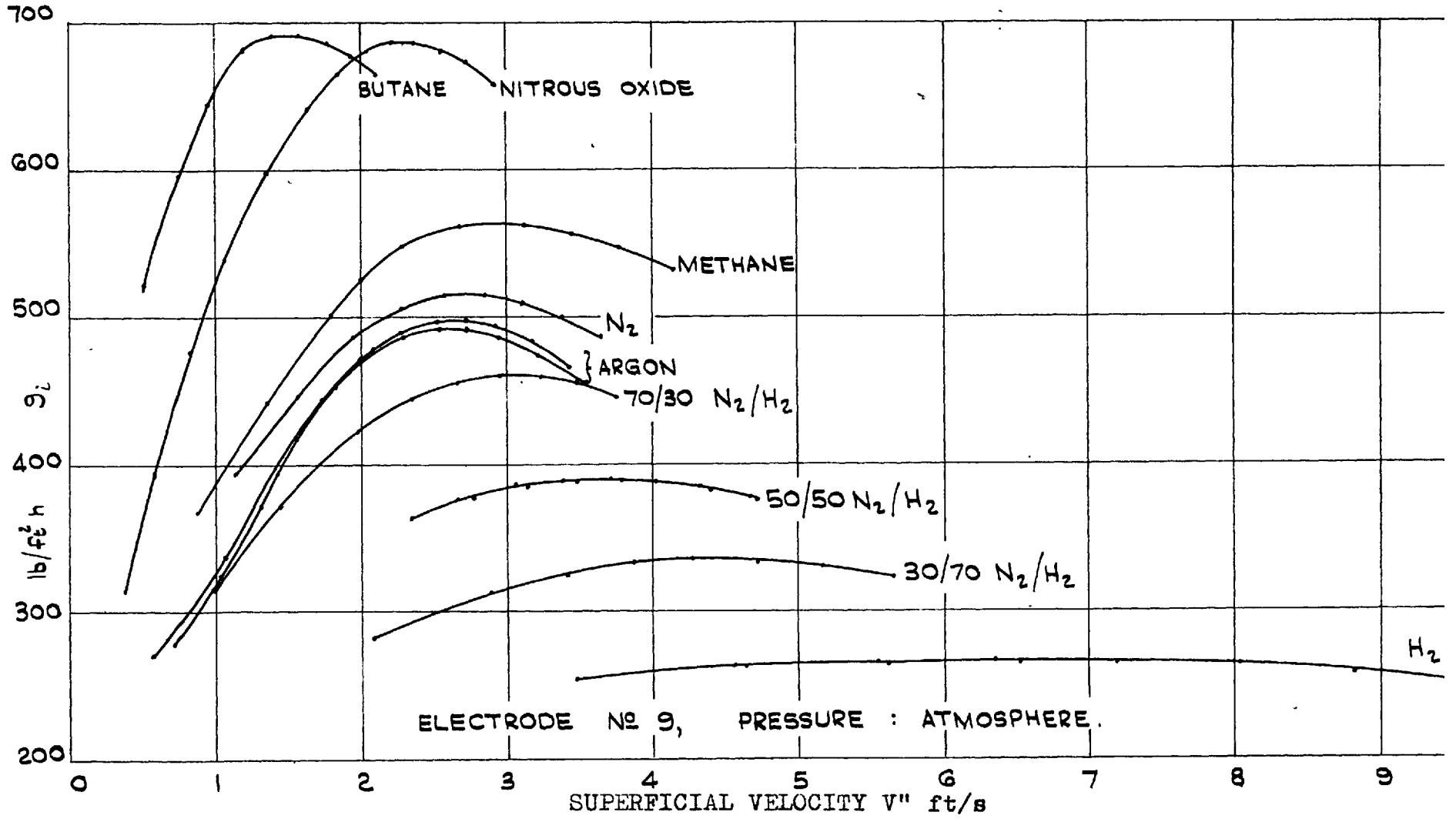

Fig. 6.11 CONDUCTANCE VERSUS SUPERFICIAL VELOCITY FOR VARIOUS GASES

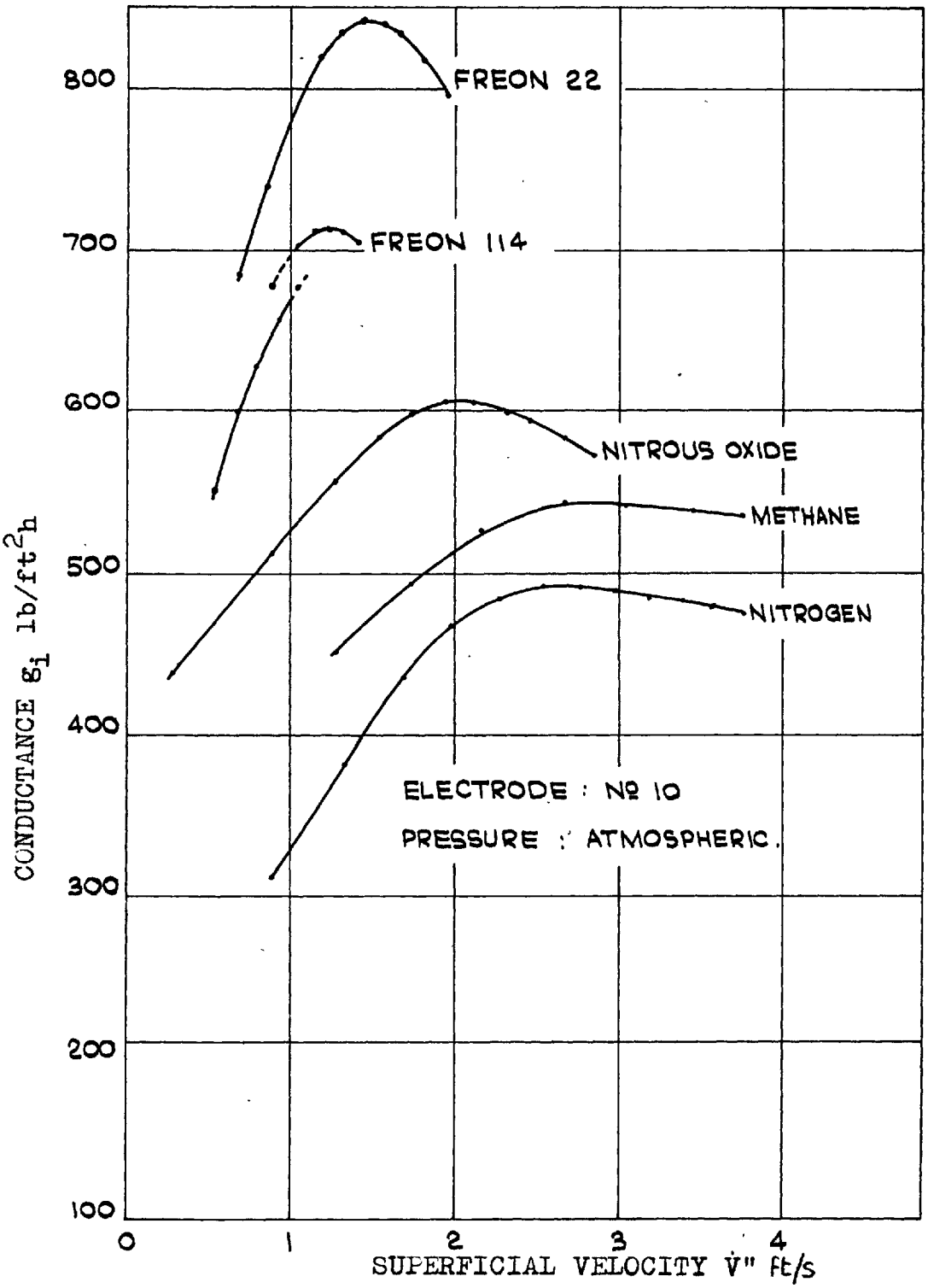

Fig. 6.12 CONDUCTANCE VERSUS SUPERFICIAL VELOCITY FOR VARIOUS GASES

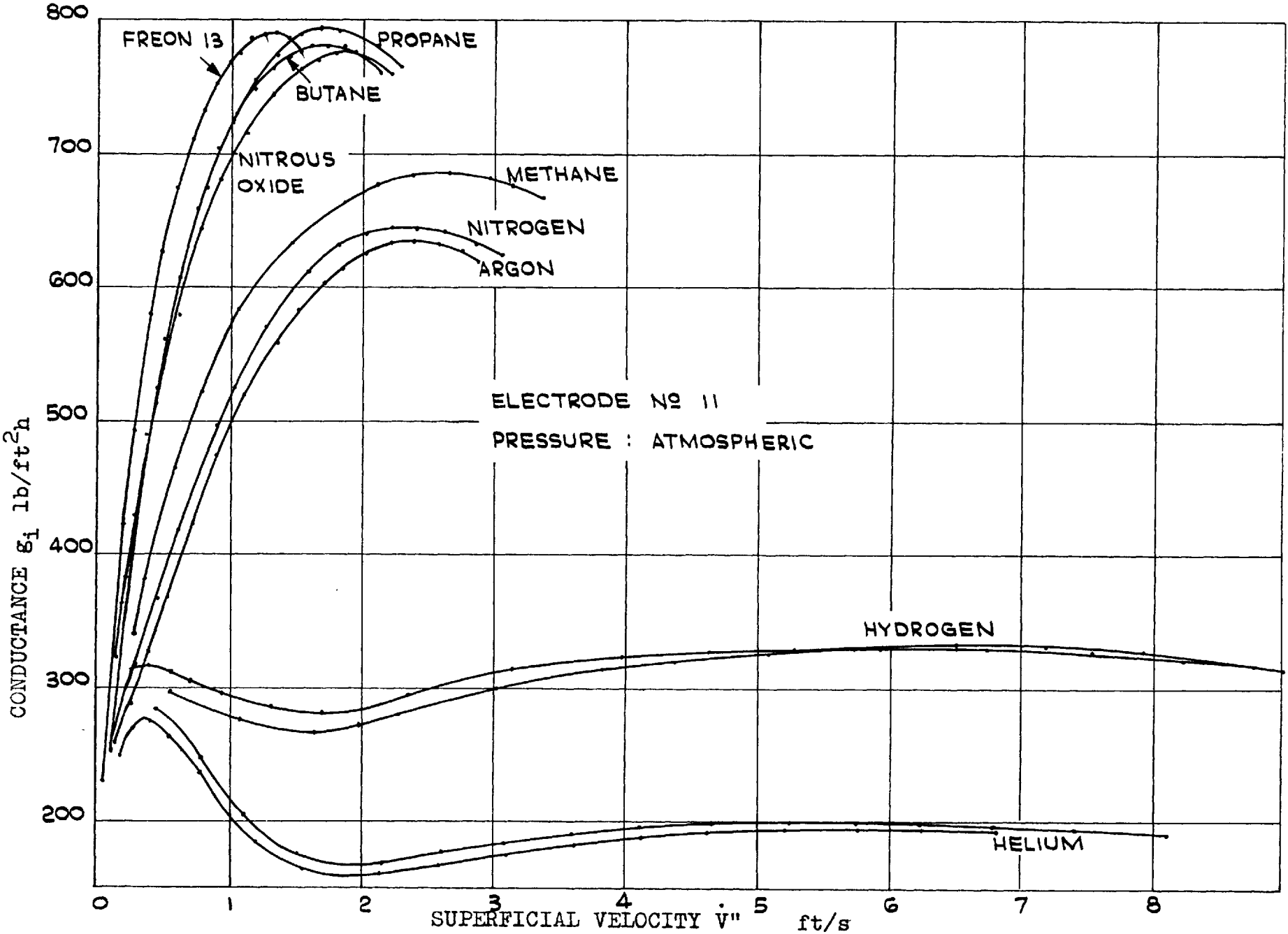

Fig. 6.13 CONDUCTANCE VERSUS SUPERFICIAL VELOCITY FOR VARIOUS GASES

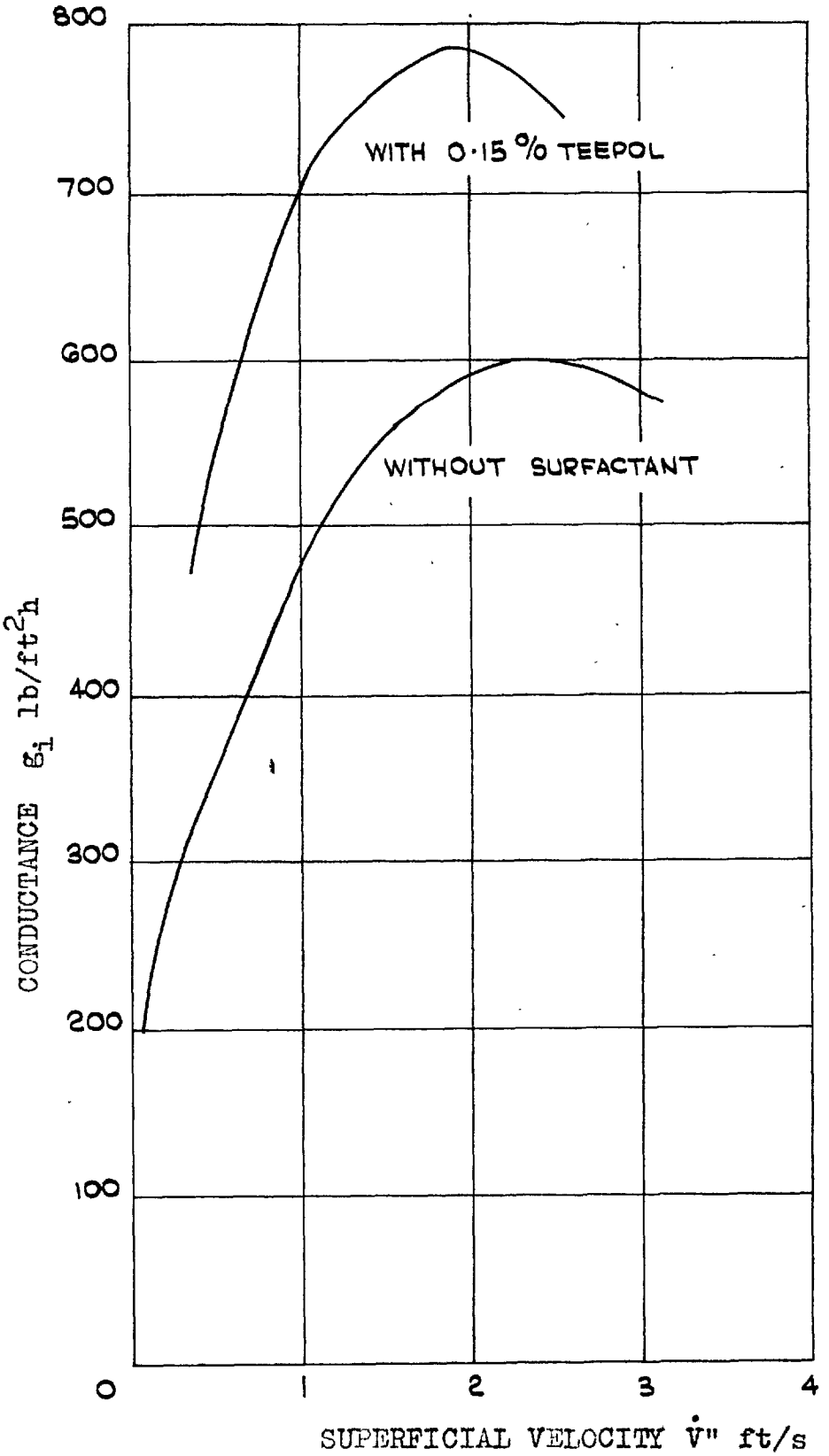

FIG. 6.14 CONDUCTANCE VERSUS SUPERFICIAL VELOCITY FOR TESTS WITH AND WITHOUT A SURFACTANT

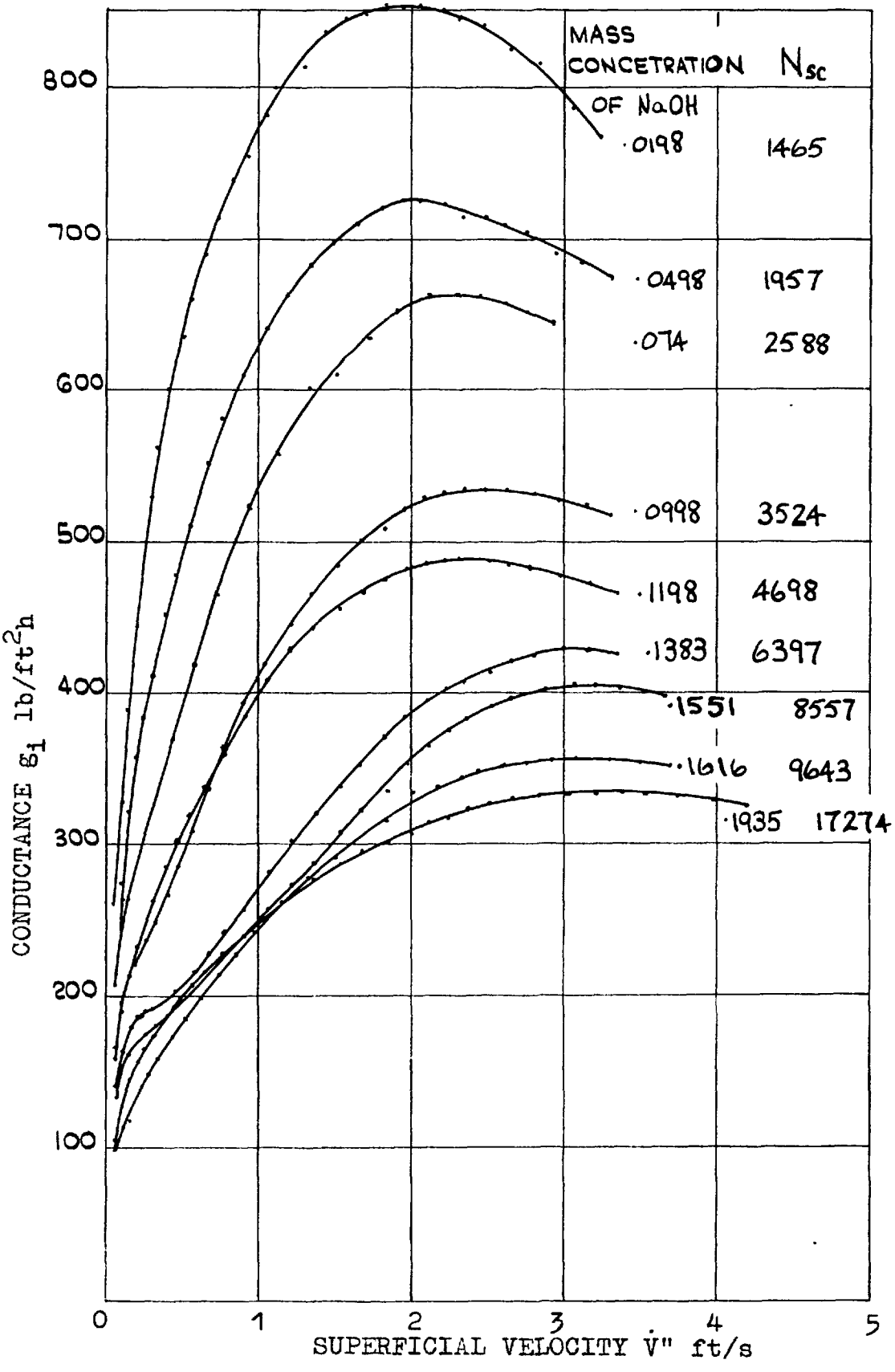

Fig. 6.15 CONDUCTANCE VERSUS SUPERFICIAL VELOCITY FOR VARIOUS NaOH CONCENTRATIONS

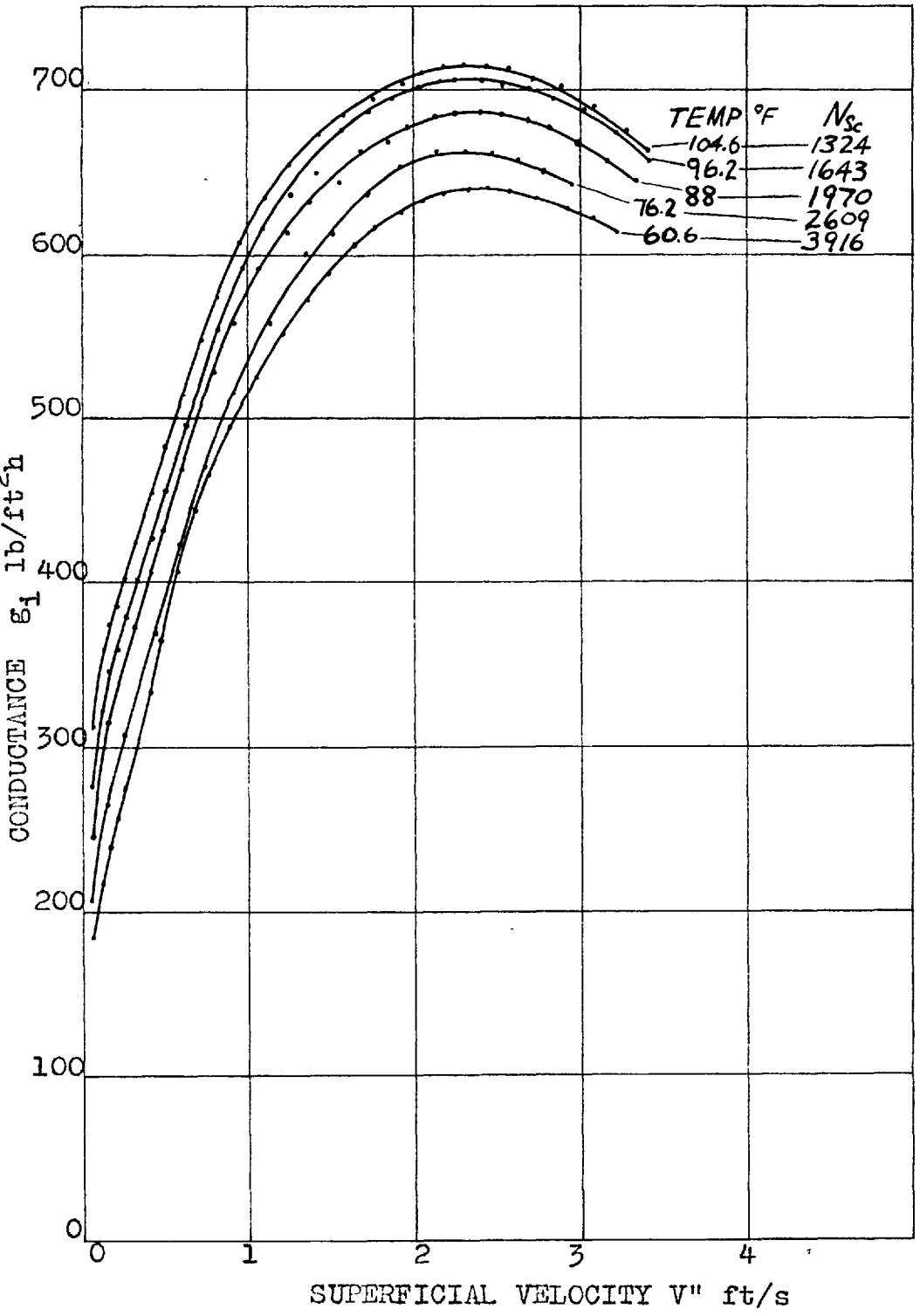

FIG. 6.16 CONDUCTANCE VERSUS SUPERFICIAL VELOCITY AT VARIOUS TEMPERATURES.

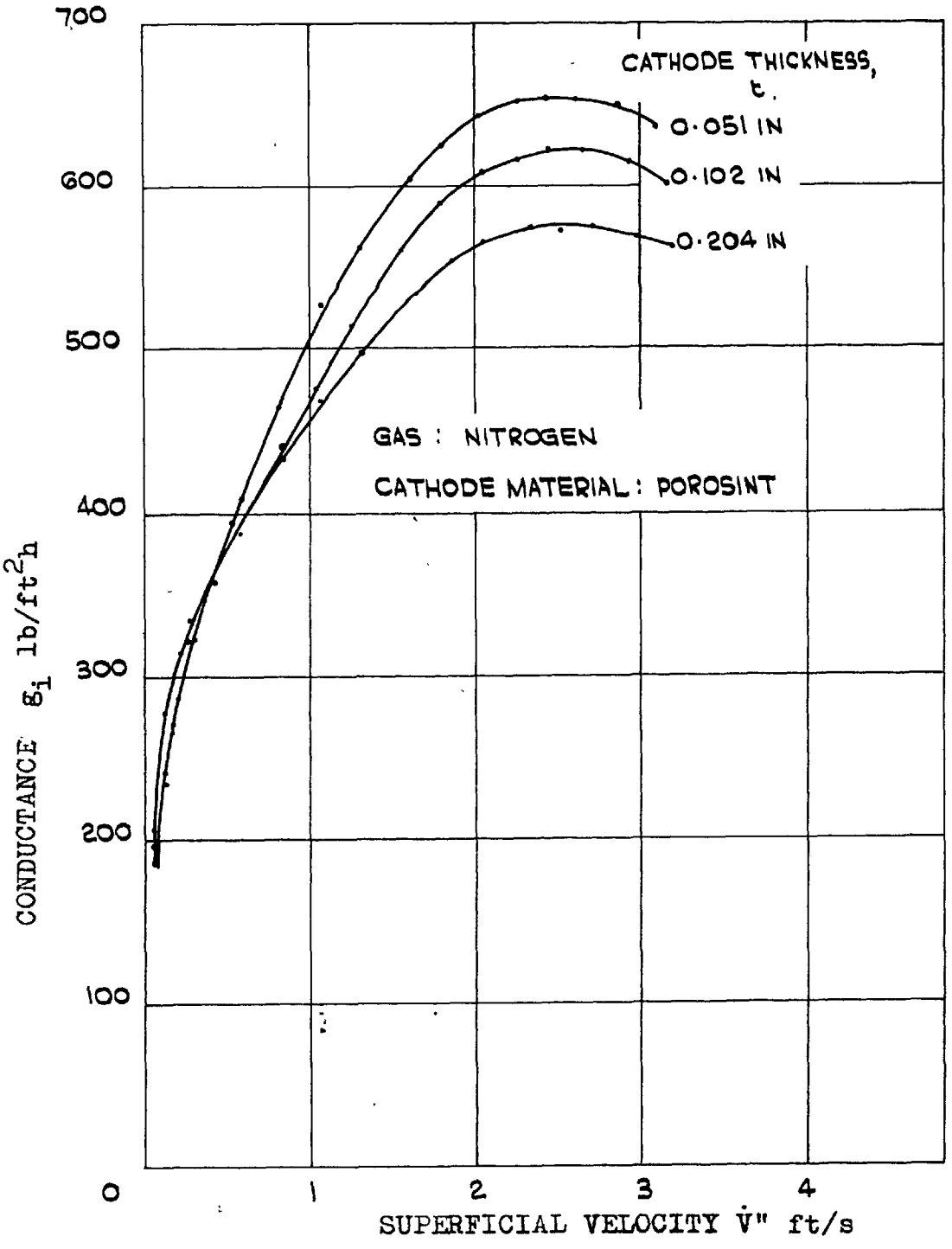

Fig. 6.17 CONDUCTANCE VERSUS SUPERFICIAL VELOCITY FOR VARIOUS CATHODE THICKNESSES

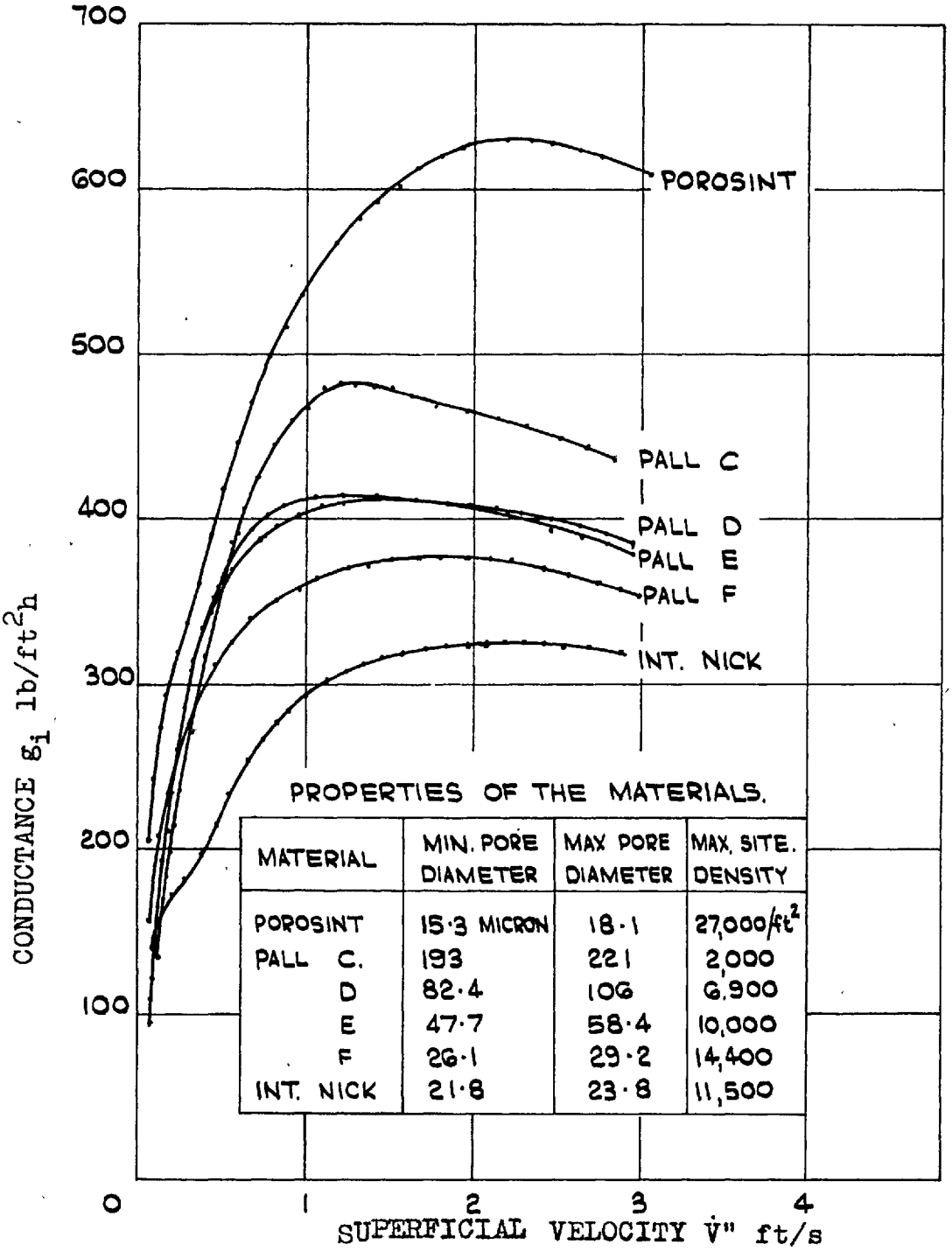

PROPERTIES OF THE MATERIALS.

MATERIAL	MIN. PORE DIAMETER	MAX PORE DIAMETER	MAX. SITE. DENSITY
POROSINT	15·3 MICRON	18·1	27,000/ft^2
PALL C.	193	221	2,000
D	82·4	106	6,900
E	47·7	58·4	10,000
F	26·1	29·2	14,400
INT. NICK	21·8	23·8	11,500

Fig. 6.18 CONDUCTANCE VERSUS SUPERFICIAL VELOCITY FOR VARIOUS POROUS MATERIALS

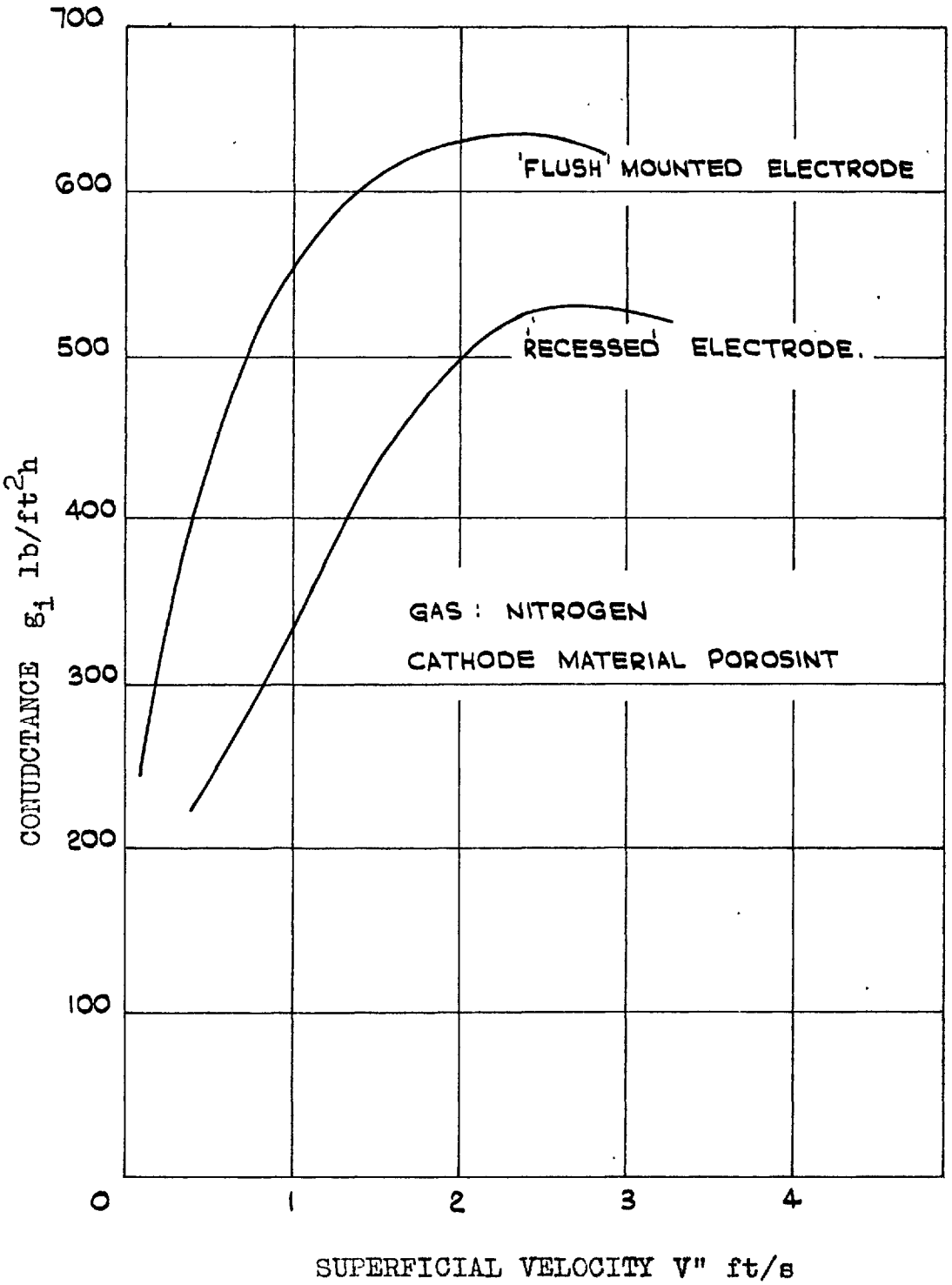

Fig. 6.19 AN EFFECT OF ELECTRODE MOUNTING

Chapter 7 Analysis of the results.

7.1 Objection of the analysis.

In chapter 3, dimensionless relations were derived to express the sub-critical conductance, the critical superficial velocity and the maximum conductance as functions of independent variables. These relations are:-

$$\frac{g_i}{\left(\frac{\dot{V}^n}{d_p}\right)^{\frac{1}{3}} g_o \rho_f^{\frac{2}{3}}} = f\left[N_{Sc}, \frac{(\sigma g_o \rho_g d_p)^{\frac{1}{2}}}{\mu_g}\right] \quad 7.1 \text{ (formerly 3.9)}$$

$$\frac{\dot{V}^n_{CRIT} \rho_g^{\frac{1}{2}}}{(\sigma g_o g_{grav} \rho_f)^{\frac{1}{4}}} = \phi\left[\frac{\rho_g}{\rho_f}, \frac{(\sigma g_o \rho_g d_p)^{\frac{1}{2}}}{\mu_g}, \left(\frac{n}{A}\right)^{\frac{1}{2}}\left(\frac{\sigma g_o}{g_{grav}\rho_f}\right)^{\frac{1}{2}}, \left(\frac{n}{A}\right)^{\frac{1}{2}} d_p, \frac{(\sigma g_o)^{\frac{3}{4}} \rho_f^{\frac{1}{4}}}{\mu_f g_{grav}^{\frac{1}{4}}}, \frac{t}{d_p}\right] \quad 7.2$$

(formerly 3.12)

$$\frac{g_{iMAX}}{\left(\frac{\dot{V}^n_{CRIT} \sigma g_o}{d_p}\right)^{\frac{1}{3}} \rho_f^{\frac{2}{3}}} = F\left[\frac{\mu_f}{D_i \rho_f}, \frac{\rho_g}{\rho_f}, \frac{(\sigma g_o \rho_g d_p)^{\frac{1}{2}}}{\mu_g}, \left(\frac{n}{A}\right)^{\frac{1}{2}}\left(\frac{\sigma g_o}{g_{grav}\rho_f}\right)^{\frac{1}{2}}, \left(\frac{n}{A}\right)^{\frac{1}{2}} d_p, \frac{(\sigma g_o)^{\frac{3}{4}} \rho_f^{\frac{1}{4}}}{\mu_f g_{grav}^{\frac{1}{4}}}, \frac{t}{d_p}\right] \quad 7.3$$

(formerly 3.13)

The object of the analysis is to determine the three functions f, ϕ and F from the experimentally determined evidence. During the course of the analysis, several

assumptions are made; these are necessary because the amount of experimental information obtained was not sufficient to permit a complete analysis of the variables in the system. The assumptions, which are suggested by results (theoretical and experimental) for boiling heat transfer, concern the influence of gravitational acceleration on the maximum conductance and the critical gas injection rate. An assumption is also made regarding the dependence of the maximum conductance on the Schmidt Number.

It has been found convenient in some instances, to include in this chapter explanations and discussions of some of the effects revealed by the analysis.

7.2 The effects of the gross geometry of the system.

Before proceeding with the main analysis, the preliminary tests investigating the effects of gross geometry are analysed. The purpose of these tests was to determine the limits of the dimensionless geometrical parameters, proposed in section 3.4, outside of which the effects of the gross geometry are negligible.

The three quantities investigated were the depth and diameter of the pool and the diameter of the porous plate.

7.2.1 Effect of pool depth.

Figure 7.1 shows the maximum conductance, g_{max} and the critical superficial velocity, $\dot{V}''_{CRIT}$ plotted against the dimensionless pool depth, $h\left(\frac{g_{grav}\rho_f}{\sigma g_o}\right)^{\frac{1}{2}}$. (The method of locating $\dot{V}''_{CRIT}$ is described later, in section 7.3.1). The limiting value of the dimensionless pool depth is seen to be approximately 10 for the maximum conductance and 15 for the critical superficial velocity.

7.2.2 Effects of pool diameter.

In Figure 7.2, the maximum conductance, and the critical superficial velocity, $\dot{V}''_{CRIT}$ are shown plotted against the dimensionless pool diameter $\frac{d_{pool}}{d_{elec}}$. For both g_{iMAX} and $\dot{V}''_{CRIT}$ the limiting value of the diameter ratio is approximately 2.5.

7.2.3 Effect of electrode diameter.

The maximum conductance and the critical superficial velocity are shown plotted against the dimensionless electrode diameter, $d_{elec}\left(\frac{g_{grav}\rho_f}{\sigma g_o}\right)^{\frac{1}{2}}$ in figure 7.3. For the limited range of electrode diameter tested, there appears to be no effect on either the maximum conductance or the critical superficial velocity. The fairly large amount of scatter in the latter case is understandable since it was necessary to construct and mount a fresh electrode

for each diameter tested; it has already been mentioned that the critical superficial velocity is often not reproducible to within 10% between different electrodes of the same material (section 5.2.1) and it is also affected by slight differences in the mounting geometry (section 6.3.3).

7.2.4 Application of the results.

The results of these preliminary tests provided evidence that the remainder of the experimental programme was uninfluenced by the gross geometry of the system. Table 7.1 summarises the limiting values of the dimensionless gross geometry groups and compares with them the values of the groups pertaining to the remaining tests.

Table 7.1 Limiting values of the gross geometry groups.

Dimensionless group	Limiting value for $g_{i,MAX}$	Limiting value for V_{CRIT}^{n}	Usual value employed
$h\left(\frac{g_{grav}\rho_f}{\sigma g_o}\right)^{\frac{1}{2}}$	10	15	100
$\frac{d_{pool}}{d_{elec}}$	2.3	2.5	4
$d_{elec}\left(\frac{g_{grav}\rho_f}{\sigma g_o}\right)^{\frac{1}{2}}$	< 2.3	< 2.3	8.5

7.3 Analysis for the sub-critical region.

7.3.1 The relation between conductance and superficial velocity.

A simple power law relation between the conductance, g_i and the superficial velocity, $\dot{V}''$ was predicted by the theoretical model in Chapter 3; this law is $g_i \propto \dot{V}''^{\frac{1}{3}}$. Figure 7.4 shows a plot on logarithmic co-ordinates of g_i versus $\dot{V}''$ for a test with 'Porosint' material and nitrogen gas. It is seen that up to approximately 75% of the critical superficial velocity, the experimental points lie on a straight line the slope of which is 0.38. This slope is typical of most of the tests carried out with the 'Porosint' material, the exceptions being tests using hydrogen and helium.

For tests carried out with materials other than 'Porosint', the region of constant $g_i/\dot{V}''^{\frac{1}{3}}$ was not apparent in every case, as shown in Figure 7.5. This was true of the coarser grades of porous material, namely 'Pall' grades C, D, and E i.e. the materials with fewer, larger pores. The remaining three materials, however, did exhibit the constant $g_i/\dot{V}''^{\frac{1}{3}}$ region; these were 'Pall grade F, 'International Nickel' and 'Porosint'.

A possible reason why the coarser materials produced results which did not agree with the theoretical predictions is that for the smaller number of larger bubbles produced

by these materials, the assumption of isotropic turbulence is not valid. It is reasonable to suppose that in such a case, the isotropocity would improve as the superficial velocity increases; this would explain why the slope of the conductance versus superficial velocity curve for the coarse materials is greater than one third for most of the sub-critical region, as shown in Figure 7.5.

In the following analysis of the experimental data, it is assumed, in accordance with the theoretical predictions of Chapter 3, that the dimensionless conductance,

$$\frac{g_i}{\left(\frac{\dot{V}''\sigma g_o}{d_p}\right)^{\frac{1}{3}} \rho_f^{\frac{2}{3}}}$$

is independent of the superficial velocity, $\dot{V}''$. Because of the slight variations of the conductance group experienced in practice with the 'Porosint' material, the group has been evaluated for each test at the lowest gas injection rate measured, and also at 75% of the critical superficial velocity, which was taken to be the upper limit of the subcritical region. In the graphical analysis of the data, both values of the group were plotted.

For the series of tests in which the effect of the grade of porous material was investigated, the dimensionless conductance was evaluated for each test at the point (or region) of maximum $g_i/\dot{V}''^{\frac{1}{3}}$.

7.3.2 The effect of varying gas properties.

(i) Varying the system pressure.

Figures 7.6 and 7.7 show the dimensionless conductance plotted, on logarithmic co-ordinates, against the 'pore' group $\frac{(\sigma g_o \rho_g d_p)^{\frac{1}{2}}}{\mu_g}$ for tests in which the pressure of the cell was varied. The results for both argon and nitrogen are seen to be almost straight lines with a slope of approximately unity, though the slope decreases slightly at high values of the pore group. Additional points to note are:

(a) The range of the dimensionless conductance caused by its slight variation with superficial velocity for each pressure, is small compared with the variation of dimensionless conductance with the 'pore' group.

(b) The conductances of the tests with electrode Number 7 are about 20% higher than those of tests with the other electrodes. It was noted in section 5.2 that replacing electrodes of the same material often produced differing results.

(ii) Varying the nature of the gas.

The tests in which different gases were employed show that above a value of the pore group, $\frac{(\sigma g_o \rho_g d_p)^{\frac{1}{2}}}{\mu_g}$ of 100, the dimensionless conductance, is independent of the

pore group (see Figures 7.8 and 7.9)*. Below this value, the two groups are approximately proportional, which is the result previously obtained by varying the pressure. It is surmised that for the region in which the value of the pore group, $\frac{(\sigma g_o \rho_g d_p)^{\frac{1}{2}}}{\mu_g}$ is less than 100, the bubble pressure is greatly influenced by the viscous forces in the porous material, resulting in the dependence of the conductance on the pore group; this region will be referred to as the pore-controlled region. For conditions in which the viscous forces in the pore are small i.e. large pore diameter or low gas viscosity and therefore large $\frac{(\sigma g_o \rho_g d_p)^{\frac{1}{2}}}{\mu_g}$, the bubble pressure is unaffected by the flow through the pores and is independent of the pore group.

To provide additional evidence of the existence of the latter region, a series of tests was performed, additional to those described in Chapter 5. The tests were carried out using the grade C porous material with four different gases, covering a range of the pore group of 230 to 560; the results are shown in Figure 7.10. The dimensionless conductance $\frac{g_i}{\left(\frac{V^n g_o}{d_p}\right)^{\frac{1}{3}} \rho_f^{\frac{2}{3}}}$ evaluated at the point of maximum $\frac{g_i}{V^{n\frac{1}{3}}}$, is seen in Figure 7.11 to be independent

---

* Note that the data for electrode Number 11 is plotted separate from the data of other electrodes to avoid confusion due to the effects of the different methods of electrode mounting employed (see section 6.3.3 of the previous chapter).

of the pore group, $\frac{(\sigma g_o \rho_g d_p)^{\frac{1}{2}}}{\mu_g}$. This result accords with the explanations given of the results of tests with the 'Porosint' material.

The concept of a pore-controlled and a pore-independent region can be used to explain the untypical behaviour of the conductance in tests carried out with hydrogen and with helium. Figure 6.3 shows a typical example of this behaviour; it is noted that two maxima occur with each of these two gases. At very low gas injection rates, the bubble pressure is uninfluenced by the behaviour of the gas flowing through the pores, and the conductance is independent of the gas properties. Thus, in this region, the curves for hydrogen and helium follow similar lines to those of other gases. At high gas injection rates, however, the conductances are pore-controlled and dependent upon the value of the pore group, $\frac{(\sigma g_o \rho_g d_p)^{\frac{1}{2}}}{\mu_g}$ in the manner indicated by Figure 7.8 or 7.9. Because of the low values of the pore group for hydrogen and helium, the transition from the pore-independent region at low gas injection rates to a pore-controlled region results in a decrease in the conductance (giving the 1st maximum). The occurrence of the first maximum is, therefore, in no way connected with the hydrodynamic crisis of the second maximum and the maxima obtained with other gases.

7.3.3 The effect of varying the liquid properties.

Figure 7.12 shows the dimensionless conductance corrected for changes in the pore group, $\frac{(\sigma g_o \rho_g d_p)^{\frac{1}{2}}}{\mu_g}$ plotted against the Schmidt Number for the two test series in which liquid properties were varied. The experimental points lie roughly on a straight line of slope -.67, though a large amount of scatter is apparent, particularly at the highest Schmidt Number (17,200). The correction applied for changes in the pore group is based on the result:

$$\frac{g_i}{\left(\frac{\dot{V}^n \sigma g_o}{d_p}\right)^{\frac{1}{3}} \rho_f^{\frac{2}{3}}} \propto \left[\frac{(\sigma g_o \rho_g d_p)^{\frac{1}{2}}}{\mu_g}\right]^{.9}$$

of the previous section, which appeared to be applicable to the range of values of the pore group for the tests of varying liquid properties, namely 67 to 74.

The dependence of the dimensionless conductance on the Schmidt Number from Figure 7.12 is given by

$$\frac{g_i}{\left(\frac{\dot{V}^n \sigma g_o}{d_p}\right)^{\frac{1}{3}} \rho_f^{\frac{2}{3}}} \propto N_{Sc}^{-.67} \qquad 7.4$$

7.3.4 The effect of the grade of porous material.

In Chapter 3, the dimensionless conductance was predicted to be a function of the Schmidt Number and the pore

group only. For the series of tests in which different grades of the porous material were employed, the pore group, $\frac{(\sigma g_o \rho_g d_p)^{\frac{1}{2}}}{\mu_g}$ varied through the pore diameter d_p. Figure 7.13 shows the dimensionless conductance plotted against the pore group. The result does not agree with the results of the tests in which gas properties were varied which indicated that the dimensionless conductance was independent of the pore group for values greater than 100. The reason for this disagreement between the results of the two methods of varying the pore group, is probably one of the following:

(i) Some quantity additional to the pore group, which is a function of the grade of the porous material, influences the dimensionless conductance. This other quantity might be the nucleation site density, a surface roughness affecting the 'effective' mass-transfer area or a pore roughness factor.

(ii) The length parameter, d_p estimated from pressure drop measurements (described in Appendix II) is not the relevant length parameter to include in the dimensionless conductance, $\frac{g_i}{\left(\frac{\dot{V}'' \sigma g_o}{d_p}\right)^{\frac{1}{3}} \rho_f^{\frac{2}{3}}}$.

(iii) The value of the pore group at which the transition from pore-dependent to pore-independent conductance occurs is not in fact 100 as predicted by the tests with

various gases, but some value greater. Alternatively, the transition value of the pore group is different for each material grade.

The plausibility of this explanation is illustrated by plotting on a single graph, all of the results obtained from tests in which the pore group was varied. Such a graph is shown as Figure 7.14, which includes the results from Figures 7.6 to 7.9, 7.11 and 7.13. Here a more appropriate transition value for the pore group is 200.

7.3.5 Final expression for the dimensionless conductance.

An empirical equation has been fitted to the collected results in Figure 7.14. The equation, shown by the broken line in Figure 7.14, is:

$$\frac{g_i}{\left(\frac{\dot{V}''\sigma g_o}{d_p}\right)^{\frac{1}{3}} \rho_f^{\frac{2}{3}}} = \frac{6.3 \times 10^{-4} N_{Sc}^{-.67}}{\left\{\left[\frac{(\sigma g_o \rho_g d_p)^{\frac{1}{2}}}{\mu_g}\right]^{-2.4} + .846 \times 10^{-5}\right\}^{\frac{1}{2}}} \qquad 7.5$$

For small values of the pore group, i.e. in the pore-controlled region, the equation becomes:

$$\frac{g_i}{\left(\frac{\dot{V}''\sigma g_o}{d_p}\right)^{\frac{1}{3}} \rho_f^{\frac{2}{3}}} = 6.3 \times 10^{-4} N_{Sc}^{-.67} \left[\frac{(\sigma g_o \rho_g d_p)^{\frac{1}{2}}}{\mu_g}\right] \qquad 7.6$$

and in the pore-independent region (large values of the pore group) it becomes:

$$\frac{g_i}{\left(\frac{\dot{V}''\sigma g_o}{d_p}\right)^{\frac{1}{3}} \rho_f^{\frac{2}{3}}} = 0.216\ N_{Sc}^{-.67} \qquad 7.7$$

7.4 Analysis for the critical superficial velocity.

7.4.1 Method of locating the critical superficial velocity.

No special mechanical operations were performed to locate the position of the maximum conductance for a given test. The data points were plotted on linear co-ordinates similar to the figures presented in the previous chapter, but to a larger scale. A smooth curve was then drawn through the points, ignoring any which did not follow the general trend, and the superficial velocity at which the maximum conductance occurred was judged by eye. Using this method, it is estimated that the critical superficial velocity could be located to within $\pm$ 2½% of the true value.

7.4.2 The effect of varying gas properties.

(i) Varying the system pressure.

Figures 7.15 and 7.16 show the critical superficial velocity, $\dot{V}''_{CRIT}$ plotted on logarithmic co-ordinates against the gas density, ρ_g for the series of tests in which the pressure of the system was varied. The experimental points lie very close to a straight line of slope -0.5,

suggesting the following result:

$$\dot{V}''_{CRIT} \propto \rho_g^{-.5} \qquad 7.8$$

This result cannot be expressed in terms of dimensionless groups at this stage, since two independent groups contain the gas density, namely $\frac{(\sigma g_o \rho_g d_p)^{\frac{1}{2}}}{\mu_g}$ and ρ_g/ρ_f.

(ii) Varying the nature of the gas.

The critical superficial velocity, $\dot{V}''_{CRIT}$, adjusted for changes in gas density by relation 7.8, was plotted against gas viscosity, μ_g for the tests carried out with different gases. Figure 7.17 shows the data plotted in this manner on logarithmic co-ordinates. A straight line of slope 0.5 fits the data reasonably well with the exceptions of the hydrogen and helium points which do not appear to fit in with the general trend. This result leads to the following relation:

$$\dot{V}''_{CRIT} \propto \left(\frac{\mu_g}{\rho_g}\right)^{.5}$$

In terms of the dimensionless groups proposed earlier, this result is:

$$\frac{\dot{V}''_{CRIT}\rho_g^{\frac{1}{2}}}{(\sigma g_o g_{grav} \rho_f)^{\frac{1}{4}}} \propto \left(\frac{\rho_g}{\rho_f}\right)^{\frac{1}{4}} \left[\frac{(\sigma g_o \rho_g d_p)^{\frac{1}{2}}}{\mu_g}\right]^{-\frac{1}{2}} \qquad 7.9$$

Figure 7.18 shows the data of Figure 7.17 replotted in

dimensionless co-ordinates. It is now seen that the hydrogen and helium data which in Figure 7.17 appeared to be inconsistent with the data of other gases, show a region in which this relation 7.9 does not apply. This region is approximately defined by:

$$\frac{(\sigma g_o \rho_g d_p)^{\frac{1}{2}}}{\mu_g} < 40$$

It is interesting to note that the critical superficial velocity does not become independent of the pore group above a value of 100, as might be expected from the results of the analysis for the conductance. However, the results of the additional test series, using various gases with grade C porous material (plotted in Figure 7.19) show the dimensionless critical superficial velocity to be independent of the pore group within the range 300 to 560. The slightly high methane point in Figure 7.19 suggests that the transition from pore-control to pore-independence occurs at a value of the pore group, $\frac{(\sigma g_o \rho_g d_p)^{\frac{1}{2}}}{\mu_g}$ of approximately 300.

7.4.3 The effect of varying the liquid properties.

In the two test series in which the liquid properties were varied, the independent dimensionless groups were:

$$\frac{\rho_g}{\rho_f}, \quad \frac{(\sigma g_o \rho_g d_p)^{\frac{1}{2}}}{\mu_g}, \quad \frac{(\sigma g_o)^{\frac{3}{4}} \rho_f^{\frac{1}{4}}}{g_{grav}^{\frac{1}{4}} \mu_f}$$

The dependence of the dimensionless critical superficial velocity on the density ratio and on the pore group, is given by the relation 7.9; thus, by plotting

$$\frac{\dot{V}''_{CRIT}\rho_g^{\frac{1}{2}}}{(\sigma g_o g_{grav}\rho_f)^{\frac{1}{4}}}\left(\frac{\rho_g}{\rho_f}\right)^{-\frac{1}{4}}\left[\frac{(\sigma g_o \rho_g d_p)^{\frac{1}{2}}}{\mu_g}\right]^{\frac{1}{2}} \text{ against } \frac{(\sigma g_o)^{\frac{3}{4}}\rho_f^{\frac{1}{4}}}{\rho_f g_{grav}^{\frac{1}{4}}},$$

the function of the third group is obtained. Figure 7.20 shows the data plotted in this manner on logarithmic coordinates; a considerable amount of scatter is evident. A straight line of slope -0.32 was drawn through the points, yielding the result:

$$\frac{\dot{V}''_{CRIT}\rho_g^{\frac{1}{2}}}{(\sigma g_o g_{grav}\rho_f)^{\frac{1}{4}}} \propto \left[\frac{(\sigma g_o)^{\frac{3}{4}}\rho_f^{\frac{1}{4}}}{\mu_f g_{grav}^{\frac{1}{4}}}\right]^{-.32} \qquad 7.10$$

7.4.4 The effect of electrode thickness.

From Figure 6.17, it is seen that the thickness of the porous electrode, t, has no effect on the critical superficial velocity. This result eliminates the dimensionless ratio t/d_p from the independent dimensionless groups of equation 7.2.

7.4.5 An assumption regarding the effect of g_{grav}.

Insertion of the results so far obtained into equation 7.2 reduces it to:

$$\frac{\dot{V}''_{CRIT}\rho_g^{\frac{1}{2}}}{(\sigma g_o g_{grav}\rho_f)^{\frac{1}{4}}} = \left(\frac{\rho_g}{\rho_f}\right)^{\frac{1}{4}} \left[\frac{(\sigma g_o \rho_g d_p)^{\frac{1}{2}}}{\mu_g}\right]^{-\frac{1}{2}} \left[\frac{(\sigma g_o)^{\frac{3}{4}}\rho_f^{\frac{1}{4}}}{\mu_f g_{grav}^{\frac{1}{4}}}\right]^{-.32}$$

$$f\left[(\frac{n}{A})^{\frac{1}{2}}\left(\frac{g_{grav}\rho_f}{\sigma g_o}\right)^{-\frac{1}{2}}, (\frac{n}{A})^{\frac{1}{2}} d_p\right] \qquad 7.11$$

where $f[\quad]$ means some function of - - -

The above equation contains an unknown function of two independent groups, $(\frac{n}{A})^{\frac{1}{2}}d_p$ and $(\frac{n}{A})^{\frac{1}{2}}\left(\frac{\sigma g_o}{g_{grav}\rho_f}\right)^{\frac{1}{2}}$. There is insufficient experimental evidence remaining to separate the effects of these two groups; additional information in the form of an assumption is therefore introduced. The assumption concerns the dependence of $\dot{V}''_{CRIT}$ on the gravitational acceleration, g_{grav}.

Both theory and experiment [58, 68, 16, 33] show that the critical heat flux, $\dot{q}''_{CRIT}$ in saturated pool boiling is related to the gravitational acceleration by the following relation:

$$\dot{q}''_{CRIT} \propto g_{grav}^{\frac{1}{4}}$$

It is assumed that the critical gas injection rate in the present investigation is similarly dependent upon g_{grav}, i.e. $\dot{V}''_{CRIT} \propto g_{grav}^{\frac{1}{4}}$. This assumption leads to the following dependence of the dimensionless critical superficial velocity on the group $(\frac{n}{A})^{\frac{1}{2}}\left(\frac{\sigma g_o}{g_{grav}\rho_f}\right)^{\frac{1}{2}}$:

$$\frac{\dot{V}''_{CRIT}\rho_g^{\frac{1}{2}}}{(\sigma g_o g_{grav}\rho_f)^{\frac{1}{4}}} \propto \left[(\frac{n}{A})^{\frac{1}{2}} \left(\frac{\sigma g_o}{g_{grav}\rho_f}\right)^{\frac{1}{2}}\right]^{.16} \qquad 7.12$$

7.4.5 The effect of the grade of the porous electrode.

For the tests in which different grades of porous material were used for the electrode, four independent dimensionless groups varied, these were:

$$(\frac{n}{A})^{\frac{1}{2}} \left(\frac{\sigma g_o}{g_{grav}\rho_f}\right)^{\frac{1}{2}}, \quad (\frac{n}{A})^{\frac{1}{2}} d_p, \quad \frac{t}{d_p} \quad \text{and} \quad \frac{(\sigma g_o \rho_g d_p)^{\frac{1}{2}}}{\mu_g} .$$

The analysis so far has shown the dimensionless $\dot{V}''_{CRIT}$ to be independent of $\frac{t}{d_p}$ and to be related to two of the remaining groups by equations 7.9 and 7.12. Thus, by plotting

$$\frac{\dot{V}''_{CRIT}\rho_g^{\frac{1}{2}}}{(\sigma g_o g_{grav}\rho_f)^{\frac{1}{4}}} \qquad \left[(\frac{n}{A})^{\frac{1}{2}}\left(\frac{\sigma g_o}{g_{grav}\rho_f}\right)^{\frac{1}{2}}\right]^{-.16} \left[\frac{(\sigma g_o \rho_g d_p)^{\frac{1}{2}}}{\mu_g}\right]^{\frac{1}{2}}$$

against $(\frac{n}{A})d_p$, the correlation of the effects of the grade of the electrode material is achieved. Figure 7.21 shows the experimental data plotted in this manner; the result indicates that the dimensionless $\dot{V}''_{CRIT}$ is independent of the group $(\frac{n}{A})^{\frac{1}{2}}d_p$.

7.4.6 Final expression for the critical superficial velocity.

The final expression for the dimensionless critical

superficial velocity for the pore-controlled region is:

$$\frac{\dot{V}''_{CRIT}\rho_g^{\frac{1}{2}}}{(\sigma g_o g_{grav}\rho_f)^{\frac{1}{4}}} = 38\left(\frac{\rho_g}{\rho_f}\right)^{\frac{1}{4}}\left[\frac{(\sigma g_o \rho_g d_p)^{\frac{1}{2}}}{\mu_g}\right]^{\frac{1}{2}}\left[\frac{(\sigma g_o)^{\frac{3}{4}}\rho_f^{\frac{1}{4}}}{g_{grav}^{\frac{1}{4}}\mu_f}\right]^{-.32}$$

$$\left[(\frac{n}{A})^{\frac{1}{2}}\left(\frac{\sigma g_o}{g_{grav}\rho_f}\right)^{\frac{1}{2}}\right]^{.16} \qquad 7.13$$

The corresponding expression for $\dot{V}''_{CRIT}$ in terms of the independent variables is:

$$\dot{V}''_{CRIT} = 38\ \rho_g^{-.5}\ \mu_g^{.5}\ g_{grav}^{.25}\ \sigma^{-.16}\ g_o^{-.16}\ \rho_f^{-.16}\ \mu_f^{.32}$$

$$d_p^{-.25}\ (\frac{n}{A})^{.08} \qquad 7.14$$

If it is assumed that for the pore-independent region, the only change required in equation 7.13 is the omission of the pore group $\frac{(\sigma g_o \rho_g d_p)^{\frac{1}{2}}}{\mu_g}$, then the expression for $\dot{V}''_{CRIT}$, for this region, becomes:

$$\dot{V}''_{CRIT} = 3\rho_g^{-.25}\ g_{grav}^{.25}(\sigma g_o)^{.08}\rho_f^{-.16}\ \mu_f^{.32}\ (\frac{n}{A})^{.08} \qquad 7.15$$

It should be noted that although the effects of gas properties were established experimentally in this region (from the additional tests with grade C material), there is not experimental evidence to support the assumption that the liquid property dependence is the same in both regions.

7.5 Analysis for the maximum conductance.

7.5.1 The effect of varying gas properties.

(i) Varying the system pressure.

The effect of the gas density, ρ_g on the maximum conductance is shown in Figure 7.22 which was plotted from the results of the tests in which the system pressure was varied. A line of slope 0.5 fits most of the experimental points except at the higher gas densities, where the points lie below the line. The dependence of $g_{i,MAX}$ on the gas density is then:

$$g_{i,MAX} \propto \rho_g^{.5}$$

The dimensionless maximum conductance contains the critical superficial velocity, $\dot{V}''_{CRIT}$ which is seen from equation 7.8 to depend upon the gas density thus:

$$\dot{V}''_{CRIT} \propto \rho_g^{-.5}$$

Combining these two results, the dependence of the dimensionless maximum conductance on the gas density is given by:

$$\frac{g_{i,MAX}}{\left(\frac{\dot{V}''_{CRIT}\sigma g_o}{d_p}\right)^{\frac{1}{3}} \rho_f^{\frac{2}{3}}} \propto \rho_g^{\frac{2}{3}} \qquad 7.16$$

(ii) Varying the nature of the gas.

The dimensionless pore group, $\frac{(\sigma g_o \rho_g d_p)^{\frac{1}{2}}}{\mu_g}$ was found

to correlate the maximum conductances of the tests using different gases, in which both the density and the viscosity of the gas varied. Figure 7.23 shows the dimensionless maximum conductance plotted on logarithmic coordinates against the pore group. The result is similar to that obtained for the sub-critical conductance; in the pore-controlled region i.e. $\frac{(\sigma g_o \rho_g d_p)^{\frac{1}{2}}}{\mu_g} < 100$ it is:

$$\frac{g_{i,MAX}}{\left(\frac{\dot{V}''_{CRIT}\ \sigma g_o}{d_p}\right)^{\frac{1}{3}} \rho_f^{\frac{2}{3}}} \propto \left[\frac{(\sigma g_o \rho_g d_p)^{\frac{1}{2}}}{\mu_g}\right]^{1.4} \qquad 7.17$$

From this, the density ratio, $\frac{\rho_g}{\rho_f}$ appears to be unimportant.

The results of the tests using grade C porous material are shown in Figure 7.24 as dimensionless maximum conductance versus the pore group. Apart from some experimental scatter, there is seen to be no variation in the maximum conductance in this region of high $\frac{(\sigma g_o \rho_g d_p)^{\frac{1}{2}}}{\mu_g}$: this was the expected result.

7.5.2 The effect of varying the liquid properties.

For the tests in which the effects of liquid properties were investigated, two independent dimensionless groups were involved; these were the Schmidt Number $\frac{\mu_f}{D_i \rho_f}$ and the group $\frac{(\sigma g_o)^{\frac{3}{4}} \rho_f^{\frac{1}{4}}}{g_{grav}^{\frac{1}{4}} \mu_f}$. Although two different methods of varying the liquid properties were employed,

i.e. by changing the system temperature and by changing the NaOH concentration, the relative variation between the two independent dimensionless groups was the same in both cases. It was therefore not possible to separate the effects of each of the two groups, from the experimental evidence.

So that the analysis could proceed, the dependence of the sub-critical conductance on the Schmidt Number was assumed to apply also to the maximum conductance i.e. $g_{i,MAX} \propto N_{Sc}^{-\frac{2}{3}}$. The effect of the remaining liquid property group was obtained by plotting

$$\frac{g_{i,MAX}}{\left(\frac{\dot{V}''_{CRIT}\sigma g_o}{d_p}\right)^{\frac{1}{3}} \rho_f^{\frac{2}{3}}} \left[\frac{(\sigma g_o \rho_g d_p)^{\frac{1}{2}}}{\mu_g}\right]^{-1.4} N_{Sc}^{\frac{2}{3}} \text{ against}$$

$$\frac{(\sigma g_o)^{\frac{3}{4}} \rho_f^{\frac{1}{4}}}{g_{grav}^{\frac{1}{4}} \mu_f}.$$ The result is shown in Figure 7.15 and is given by:

$$\frac{g_{i,MAX}}{\left(\frac{\dot{V}''_{CRIT}\sigma g_o}{d_p}\right)^{\frac{1}{3}} \rho_f^{\frac{2}{3}}} \propto \left[\frac{(\sigma g_o)^{\frac{3}{4}} \rho_f^{\frac{1}{4}}}{g_{grav}^{\frac{1}{4}} \mu_f}\right]^{-0.3} \qquad 7.18$$

A considerable amount of scatter of the experimental points is evident.

7.5.3 The effect of the electrode thickness.

Figure 7.26 shows the maximum conductance, $g_{i,MAX}$ plotted

against the thickness of the porous cathode material, t. The effect shown in Figure 7.26, which is expressed by the relation

$$g_{i,MAX} \propto t^{-0.08}$$

is very slight.

In dimensionless terms, this result is:

$$\frac{g_{i,MAX}}{\left(\frac{\dot{V}''_{CRIT}\sigma g_o}{d_p}\right)^{\frac{1}{3}} \rho_f^{\frac{2}{3}}} \propto \left(\frac{t}{d_p}\right)^{-.08} \qquad 7.19$$

7.5.4 An assumption regarding the effect of gravitational acceleration.

The analysis for $g_{i,MAX}$ is again inhibited because insufficient experimental information is available from the remaining test series for the effect of the remaining two dimensionless groups, $\left(\frac{n}{A}\right)^{\frac{1}{2}} \left(\frac{\sigma g_o}{g_{grav}\rho_f}\right)^{\frac{1}{2}}$ and $\left(\frac{n}{A}\right)^{\frac{1}{2}} d_p$ to be determined. An assumption is therefore made regarding the influence of g_{grav} on $g_{i,MAX}$, suggested by results for boiling heat transfer.

Several experimental investigations into the effect of g_{grav} on nucleate pool boiling [29, 14, 56, 17] show the heat transfer coefficient up to the maximum to be practically independent of g_{grav}. It is assumed that the maximum conductance in the present investigation is similarly

independent of g_{grav}. This assumption leads to the following dependence of $g_{i,MAX}$ on the dimensionless group $(\frac{n}{A})^{\frac{1}{2}} \left(\frac{\sigma g_o}{g_{grav}\rho_f}\right)^{\frac{1}{2}}$:

$$g_{i,MAX} \propto \left[(\frac{n}{A})^{\frac{1}{2}} \left(\frac{\sigma g_o}{g_{grav}\rho_g}\right)^{\frac{1}{2}}\right]^{.32} \qquad 7.20$$

7.5.5 The effect of the grade of the porous electrode.

Of the four independent dimensionless groups which varied in this series of tests, the effect of one group, $(\frac{n}{A})^{\frac{1}{2}} d_p$ remains unknown. In section 7.5.1, the pore group, $\frac{(\sigma g_o \rho_g d_p)^{\frac{1}{2}}}{\mu_g}$ was seen to be unimportant above the value of approximately 100. The range of values of the pore group for the various grades of porous material used was 70 to 240; it is assumed that the effect of the pore group was negligible for this range of values. It is further assumed that the electrode thickness effect is characteristic of the pore-controlled region and therefore unimportant in this series of tests.

Figure 7.27 shows the experimental data for the various grades of electrode material plotted on logarithmic coordinates as:

$$\frac{g_{i,MAX}}{\left(\frac{\dot{V}''_{CRIT}\,\sigma g_o}{d_p}\right)^{\frac{1}{3}}\rho_f^{\frac{2}{3}}}\left[\left(\frac{n}{A}\right)^{\frac{1}{2}}\left(\frac{\sigma g_o}{g_{grav}\rho_f}\right)^{\frac{1}{2}}\right]^{-.32} \quad \text{versus} \quad \left(\frac{n}{A}\right)^{\frac{1}{2}}d_p.$$

A straight line of slope 1.0 provides the best fit to the rather scattered points, leading to the result:

$$\frac{g_{i,MAX}}{\left(\frac{\dot{V}''_{CRIT}\,\sigma g_o}{d_p}\right)^{\frac{1}{3}}\rho_f^{\frac{2}{3}}} \propto \left(\frac{n}{A}\right)^{\frac{1}{2}} d_p \left[\left(\frac{n}{A}\right)^{\frac{1}{2}}\left(\frac{\sigma g_o}{g_{grav}\rho_f}\right)^{\frac{1}{2}}\right]^{.32} \qquad 7.21$$

7.5.6 Final expression for the maximum conductance.

The final equation expressing the dimensionless maximum conductance in terms of the independent dimensionless groups is:

$$\frac{g_{i,MAX}}{\left(\frac{\dot{V}''_{CRIT}\sigma g_o}{d_p}\right)^{\frac{1}{3}}\rho_f^{\frac{2}{3}}} = \left(\frac{\mu_f}{D_i\rho_f}\right)^{-.67}\left[\frac{(\sigma g_o)^{\frac{3}{4}}\rho_f^{\frac{1}{4}}}{g_{grav}^{\frac{1}{4}}\mu_f}\right]^{-.3}\left[\left(\frac{n}{A}\right)^{\frac{1}{2}}\left(\frac{\sigma g_o}{g_{grav}\rho_f}\right)^{\frac{1}{2}}\right]^{-.32}$$

$$\left[\left(\frac{n}{A}\right)^{\frac{1}{2}}d_p\right] \quad F\left[\frac{(\sigma g_o \rho_g d_p)^{\frac{1}{2}}}{\mu_g}, \frac{t}{d_p}\right] \qquad 7.22$$

In the pore-controlled region, i.e. $\frac{(\sigma g_o \rho_g d_p)^{\frac{1}{2}}}{\mu_g} < 100$, the function F has the form $\left[\frac{(\sigma g_o \rho_g d_p)^{\frac{1}{2}}}{\mu_g}\right]^{1.4}\left[\left(\frac{t}{d_p}\right)\right]^{-.08}$. For values of the pore group greater than 100, the function F is probably a constant equal to 0.46.

The corresponding expression for $g_{i,MAX}$ in terms of the independent variables for the 'Porosint' material in the pore-controlled region is:

$$g_{i,MAX} = 0.23\ \rho_g^{.7}\mu_g^{-1.4}D_i^{.67}(\sigma g_o)^{.97}\rho_f^{1.1}\mu_f^{-.37}d_p^{1.3}\left(\frac{n}{A}\right)^{.66}t^{-.08} \qquad 7.23$$

In the pore-independent region, the expression becomes:

$$g_{i,MAX} = 0.46\ D_i^{.67}(\sigma g_o)^{.27}\rho_f^{1.1}\mu_f^{-.37}d_p^{.68}\left(\frac{n}{A}\right)^{.66} \qquad 7.24$$

Due to the many assumptions made, these equations for the maximum conductance are probably the least reliable of the correlations presented in this Chapter. Nevertheless, the following features of the equations are worthy of note;

(i) In the pore-controlled region, the maximum conductance is strongly dependent upon the pore group.

(ii) The pore diameter and bubble site density appear as significant parameters. These may be important for the same reasons as surface fine-structure is important in boiling.

(iii) The surprisingly large dependence of $g_{i,MAX}$ on the liquid density results mainly from the importance of the liquid density in the dissipation of the kinetic energy of the bubbles, and from the assumed dependence of $g_{i,MAX}$ on the Schmidt Number.

Because of the uncertainties contained in the $g_{i,MAX}$

expression, and also because the maximum heat transfer coefficient in boiling and in other barbotage investigations is generally not correlated, no further discussions or comparisons of this relation are included in this thesis.

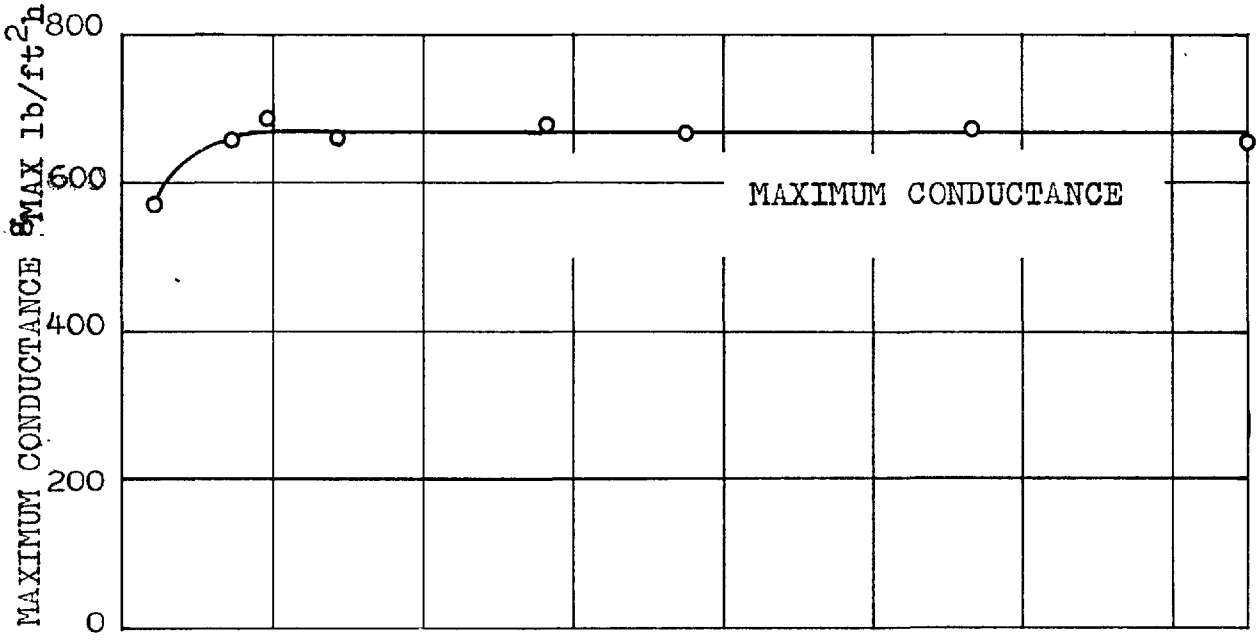

DIAMETER OF ELECTRODE, d_{ELEC}=0.25IN.
DIAMETER OF POOL, d_{POOL} = 3.4 IN.

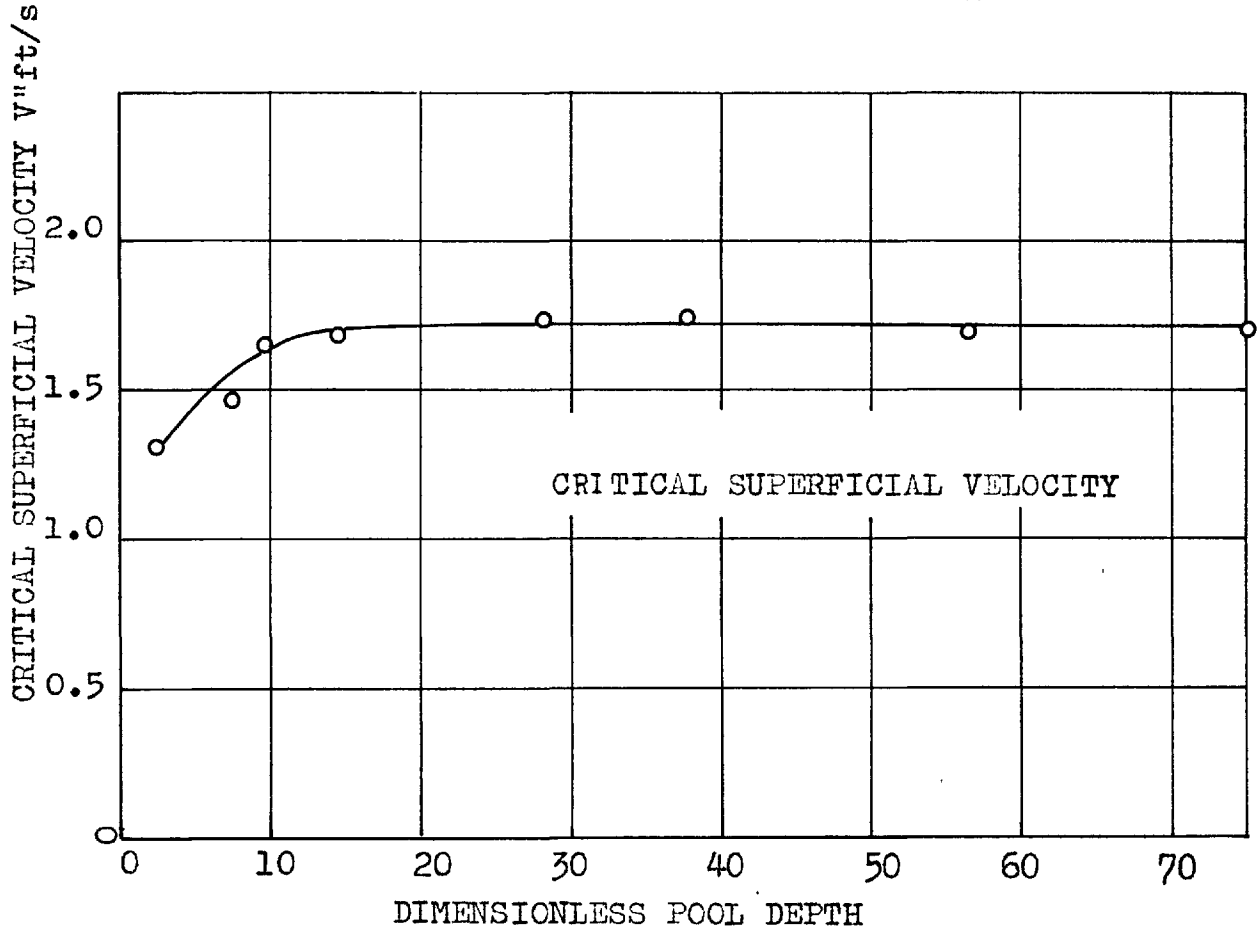

FIG.7.1 EFFECT OF POOL DEPTH ON $V"_{CRIT}$ AND g_{MAX}

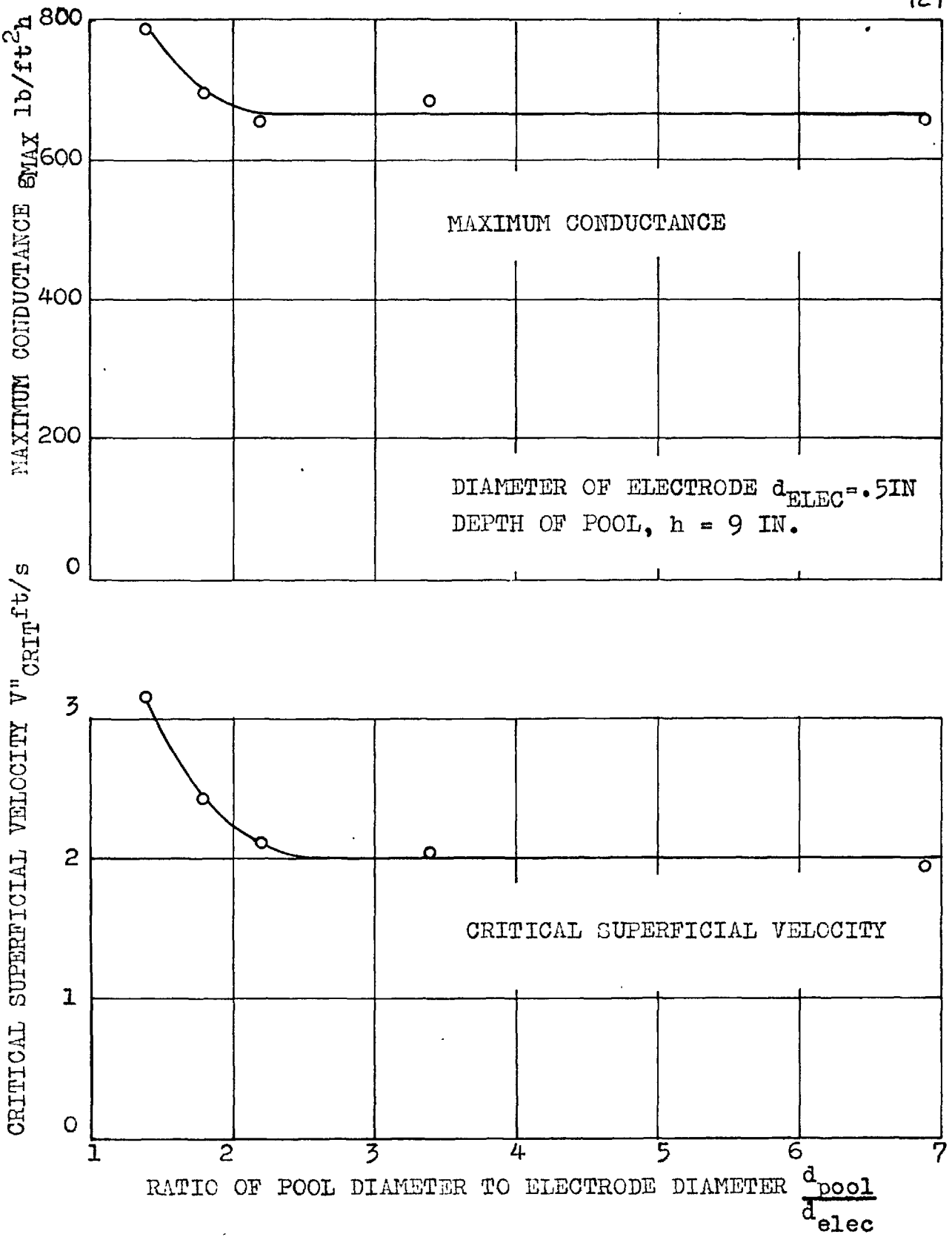

FIG. 7.2 EFFECT OF POOL DIAMETER ON V''_{CRIT} AND g_{MAX}

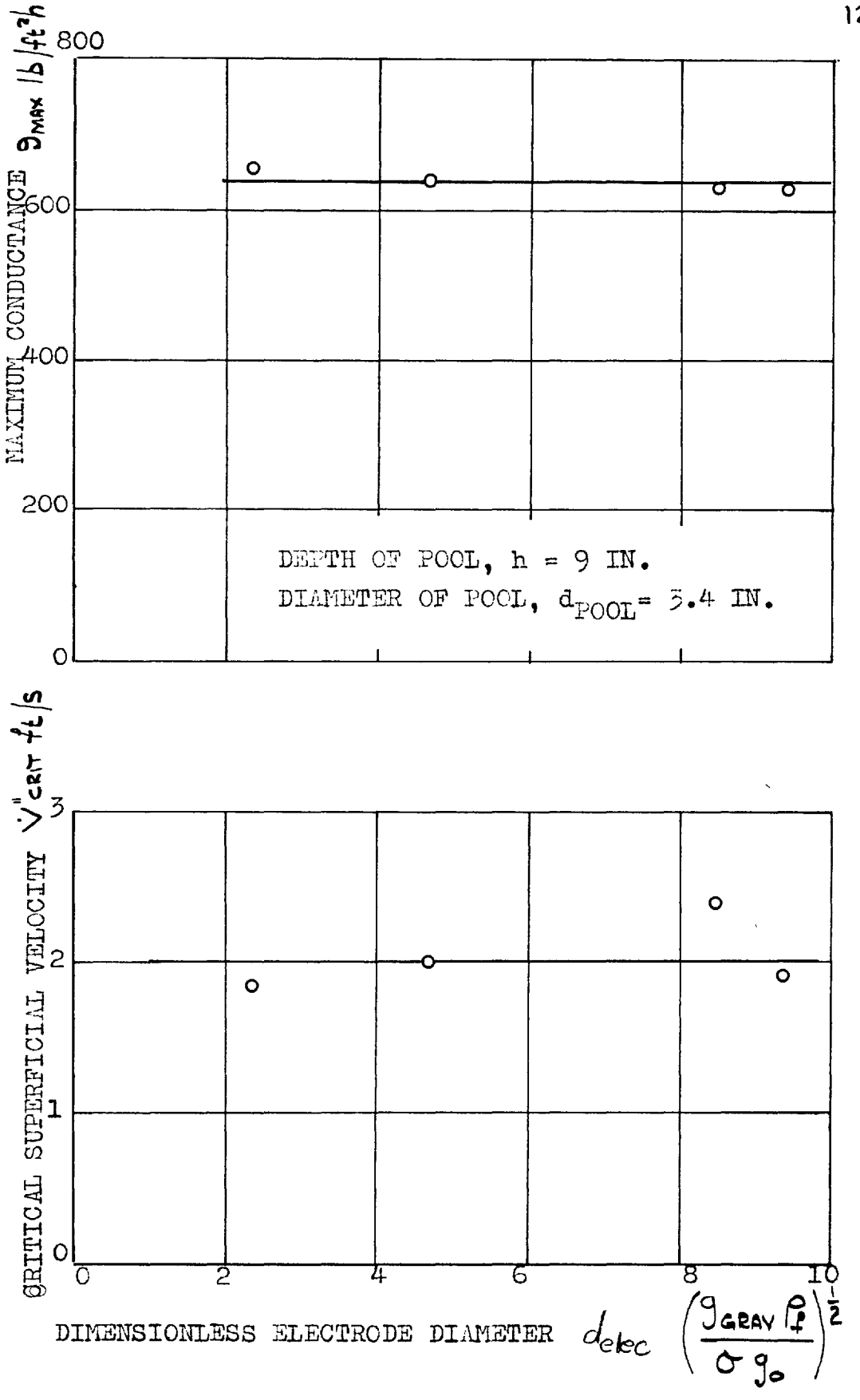

FIG. 7.3 EFFECT OF ELECTRODE DIAMETER ON V''_{CRIT} AND g_{MAX}.

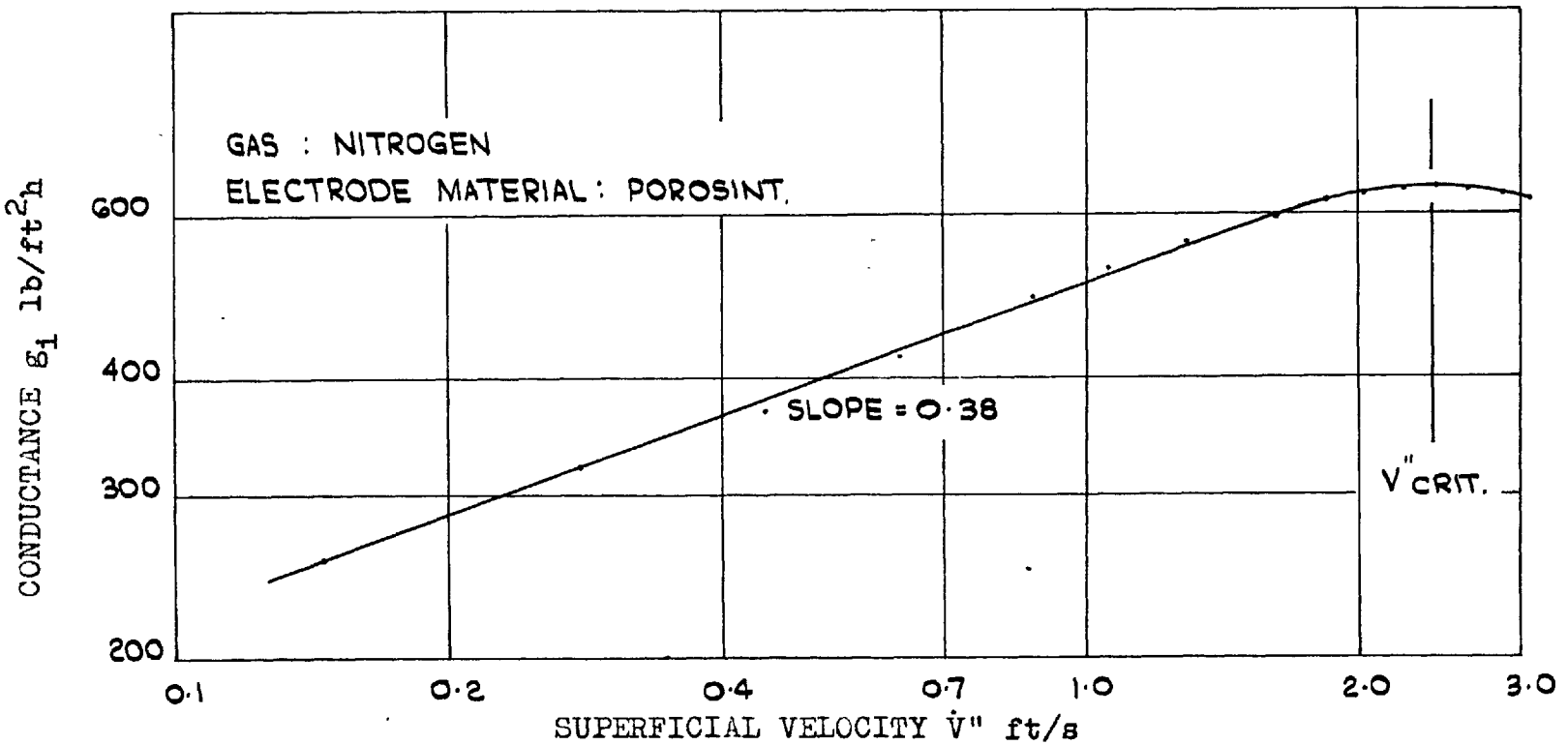

Fig.7.4 TYPICAL VARIATION OF CONDUCTANCE WITH SUPERFICIAL VELOCITY FOR THE POROSINT MATERIAL

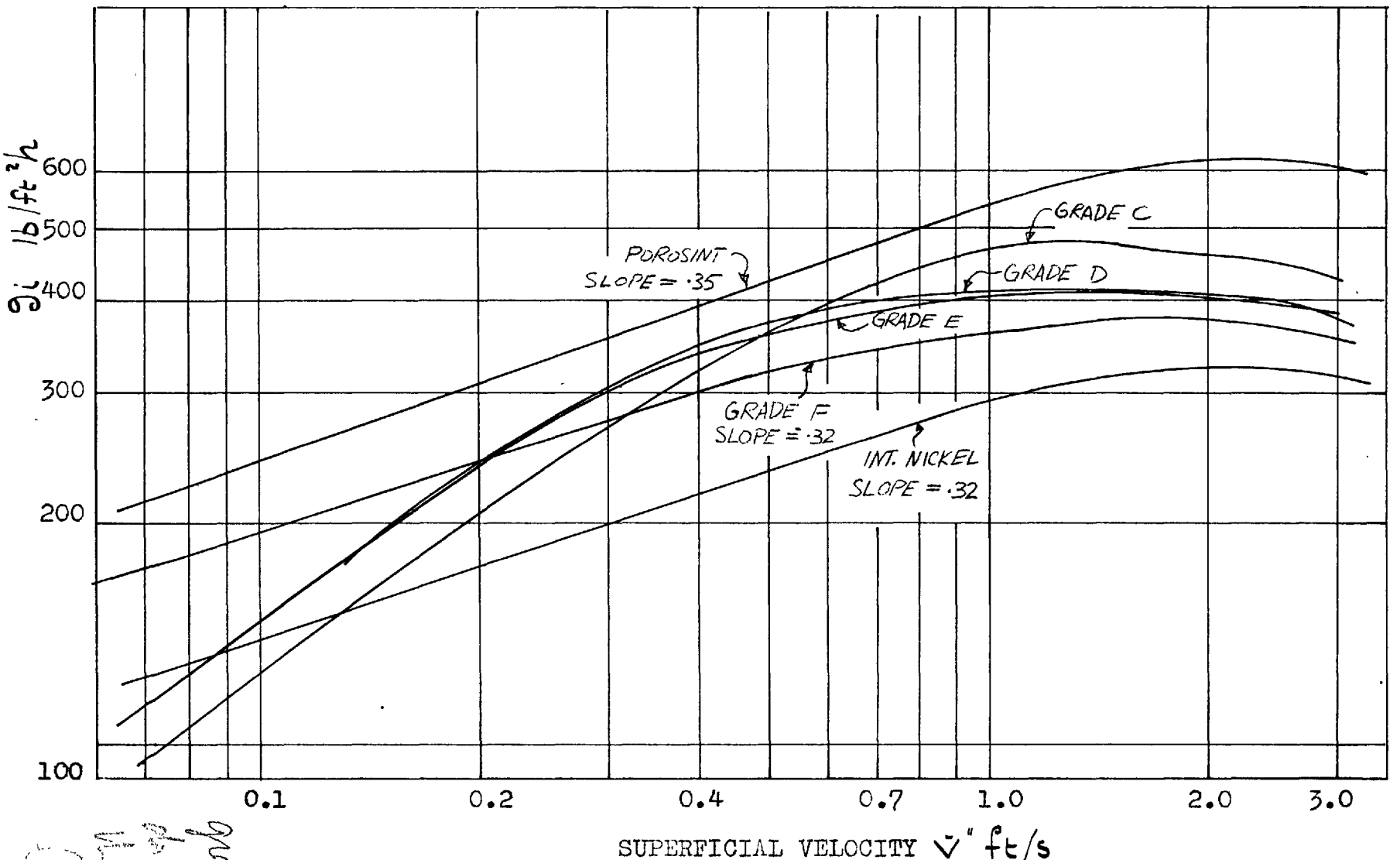

FIG. 7.5 CONDUCTANCE VERSUS SUPERFICIAL VELOCITY FOR DIFFERENT GRADES OF POROUS MATERIAL.

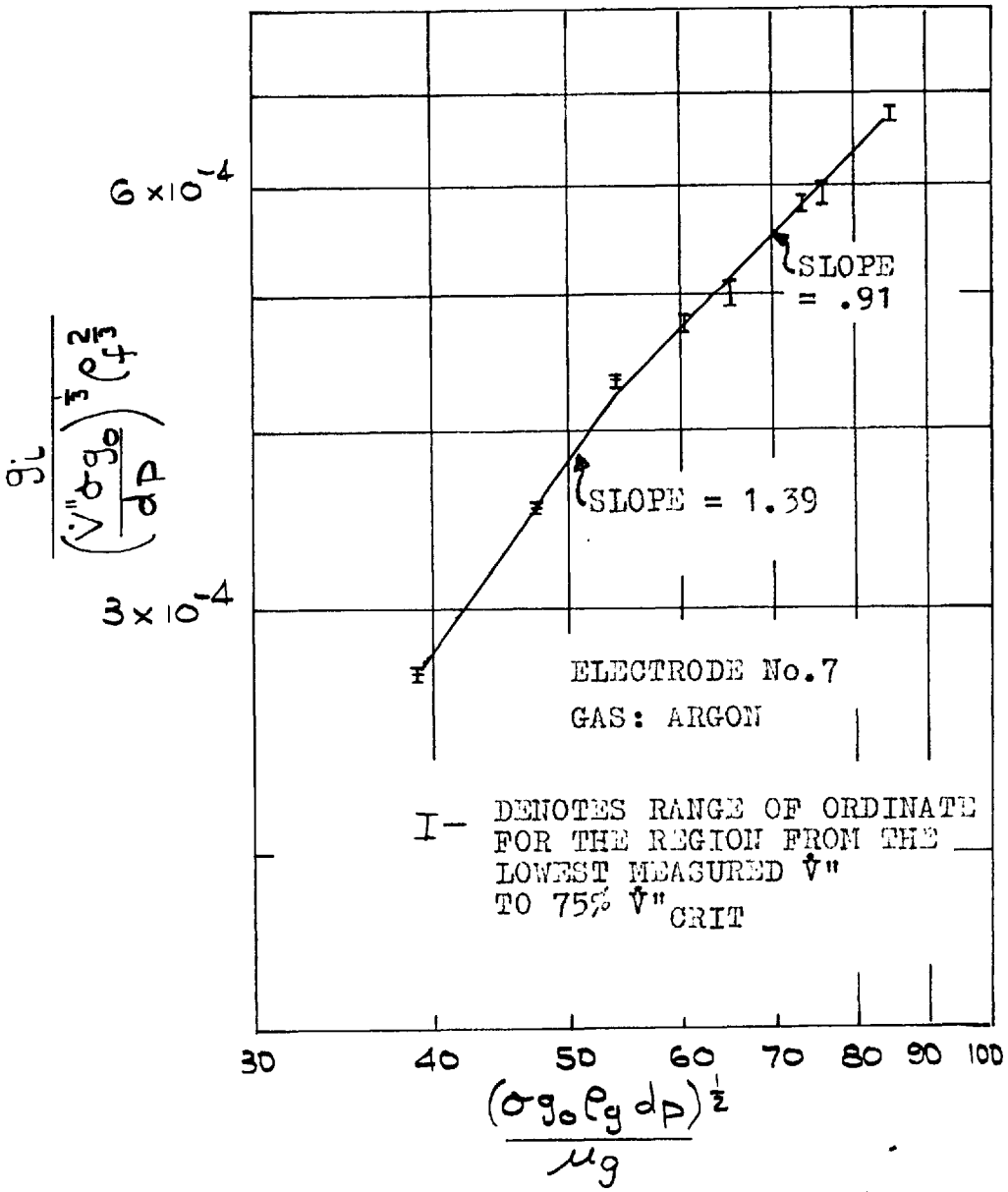

FIG. 7.6 DIMENSIONLESS CONDUCTANCE VERSUS $\frac{(\sigma g_o \rho_g dp)^{1/2}}{\mu_g}$ FOR ARGON AT VARIOUS PRESSURES

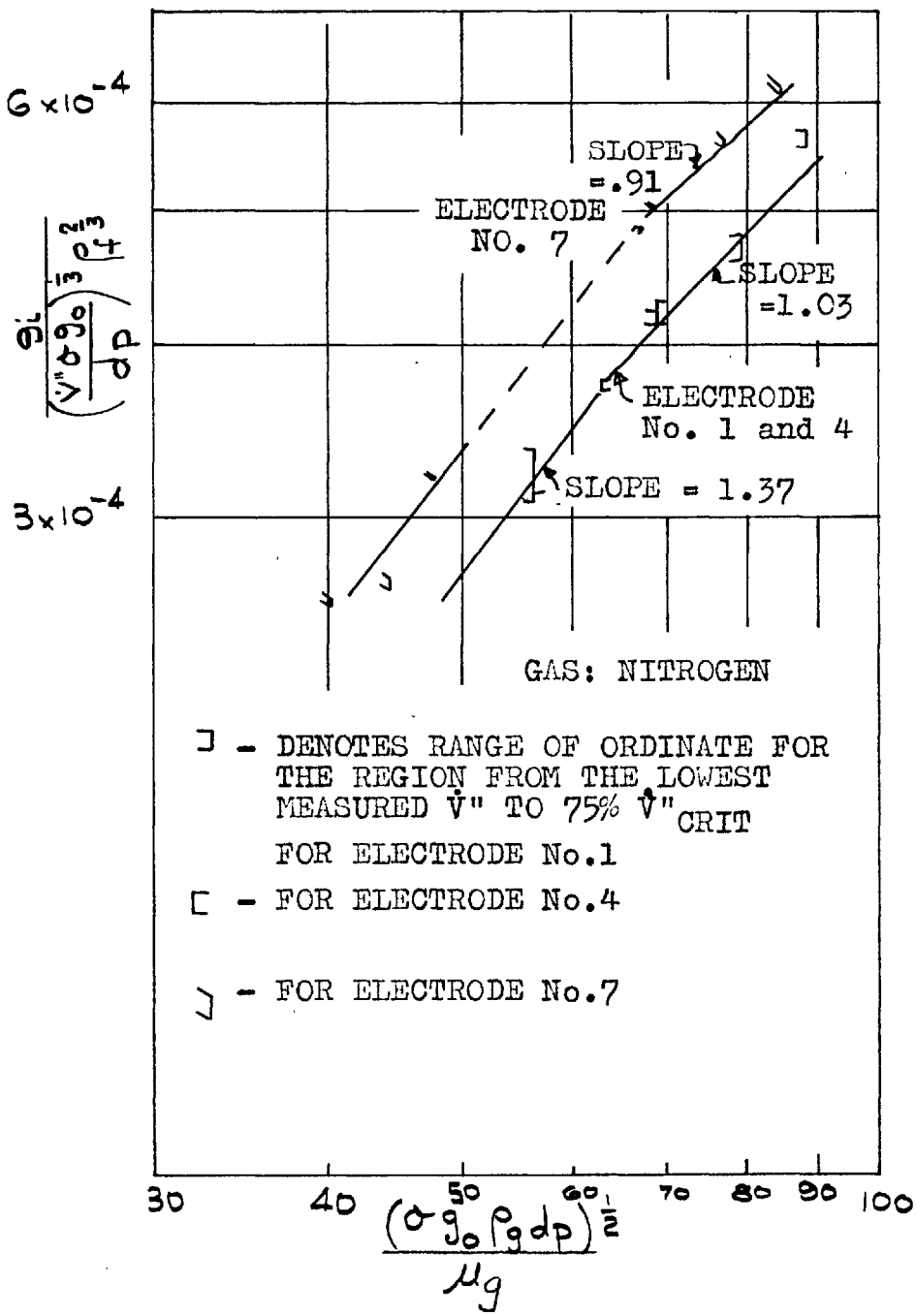

FIG. 7.7 DIMENSIONLESS CONDUCTANCE VERSUS $\frac{(\sigma g_o \rho_g dp)^{1/2}}{\mu_g}$ FOR NITROGEN AT VARIOUS PRESSURES

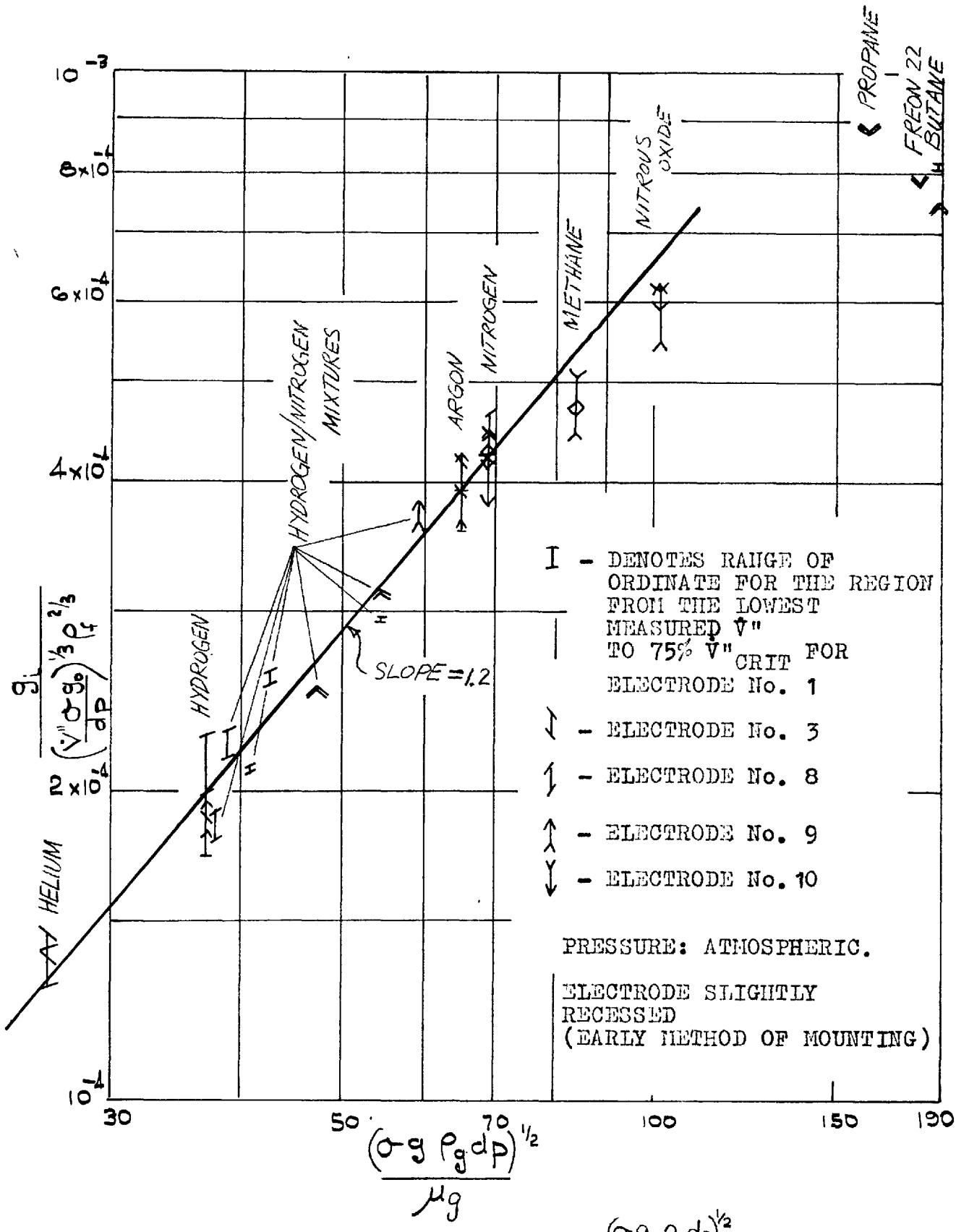

FIG. 7.8 DIMENSIONLESS CONDUCTANCE VERSUS $\frac{(\sigma g_0 \rho_g d_p)^{1/2}}{\mu_g}$ FOR VARIOUS GASES

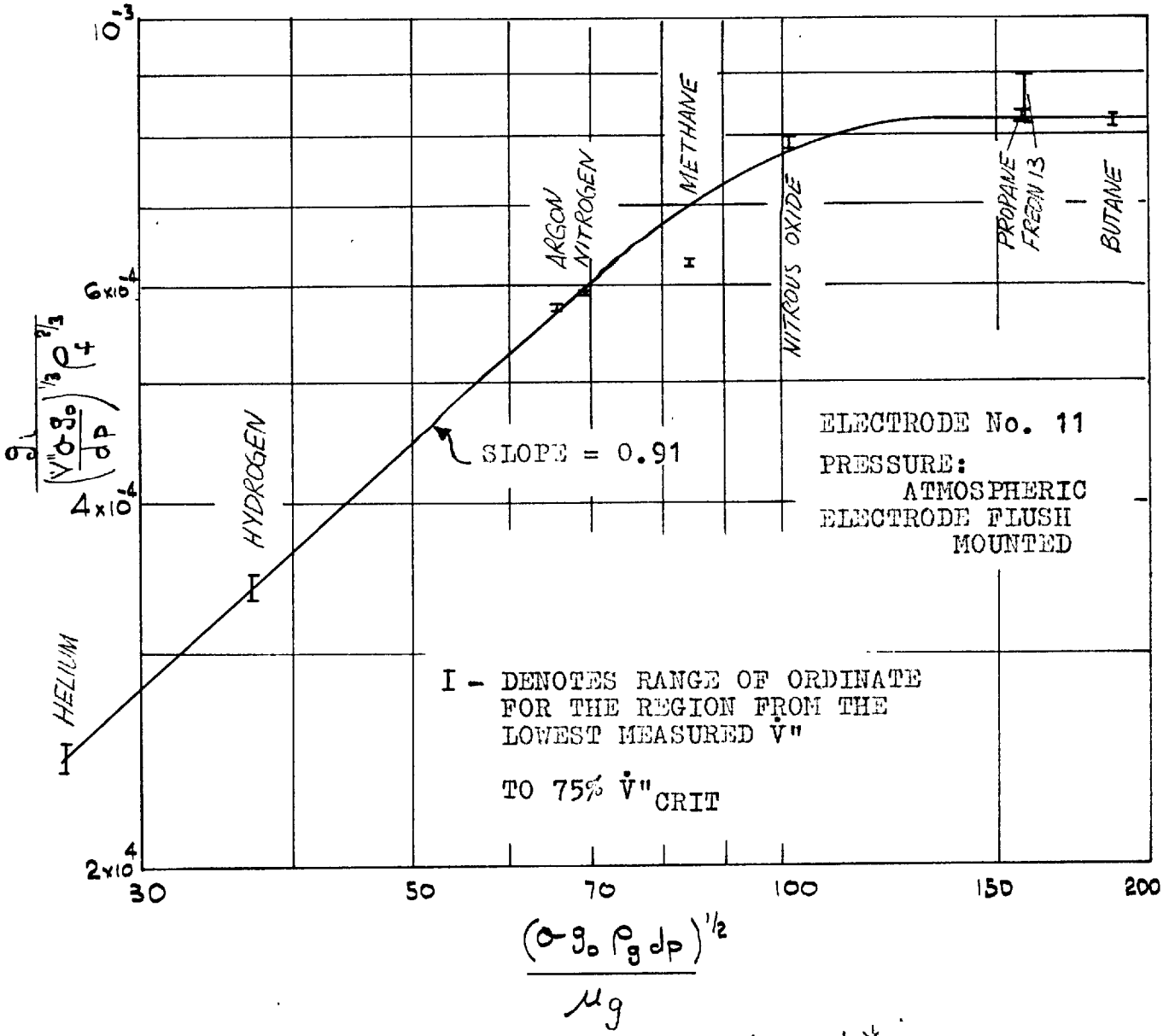

FIG. 7.9 DIMENSIONLESS CONDUCTANCE VERSUS $\frac{(\sigma g_0 \rho_g d_p)^{1/2}}{\mu_g}$ FOR VARIOUS GASES

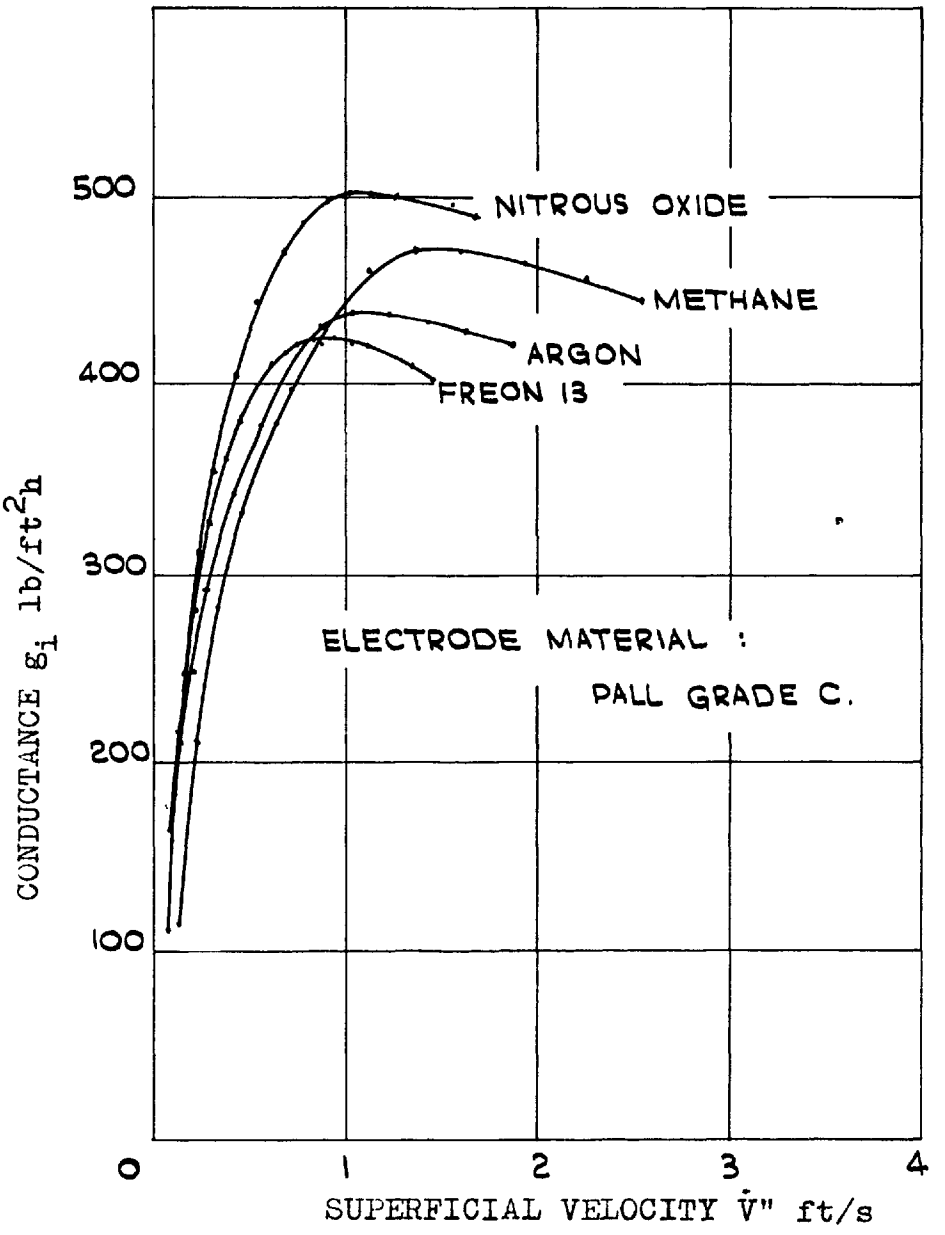

Fig. 7.10 CONDUCTANCE VERSUS SUPERFICIAL VELOCITY FOR VARIOUS GASES USING GRADE C POROUS MATERIAL

'PALL' GRADE C MATERIAL
ATMOSPHERIC PRESSURE.

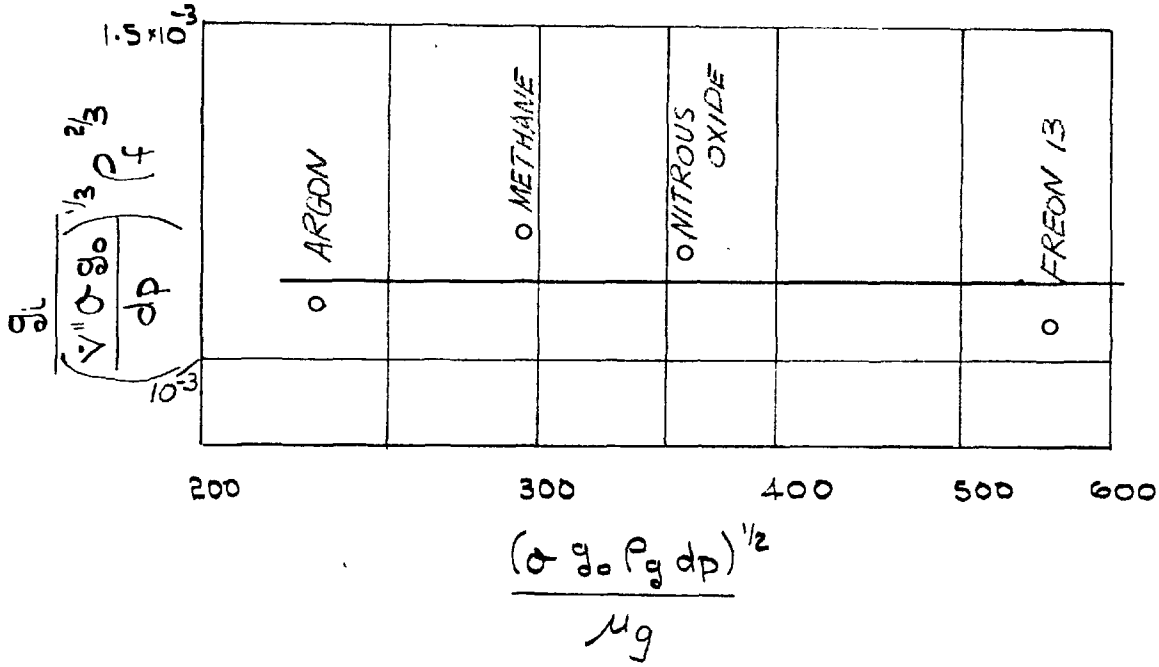

$$\frac{g_i}{\left(\frac{\dot{V}''\sigma g_o}{dp}\right)^{1/3} \rho_f^{2/3}}$$

$$\frac{(\sigma g_o \rho_g dp)^{1/2}}{\mu_g}$$

$\frac{g_i}{\left(\frac{\dot{V}''\sigma g_o}{dp}\right)^{1/3} \rho_f^{2/3}}$ WAS EVALUATED AT THE POINT OF MAXIMUM $\frac{g_i}{\dot{V}''^{1/3}}$

FIG. 7.11 DIMENSIONLESS CONDUCTANCE VERSUS $\frac{(\sigma g \rho_g dp)^{1/2}}{\mu_g}$ FOR VARICUS GASES USING 'PALL' GRADE C MATERIAL.

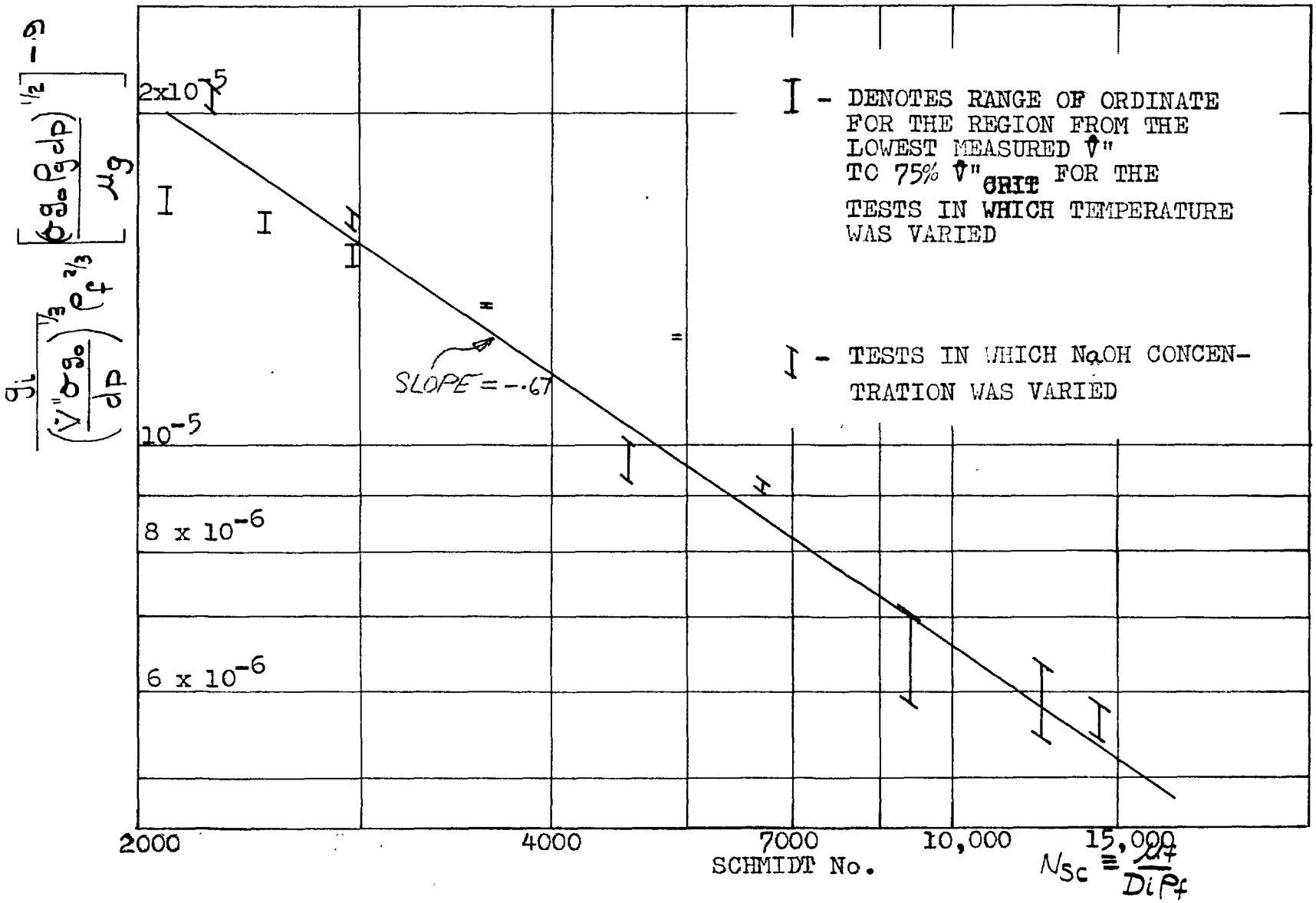

FIG. 7.12 DIMENSIONLESS CONDUCTANCE VERSUS SCHMIDT NUMBER

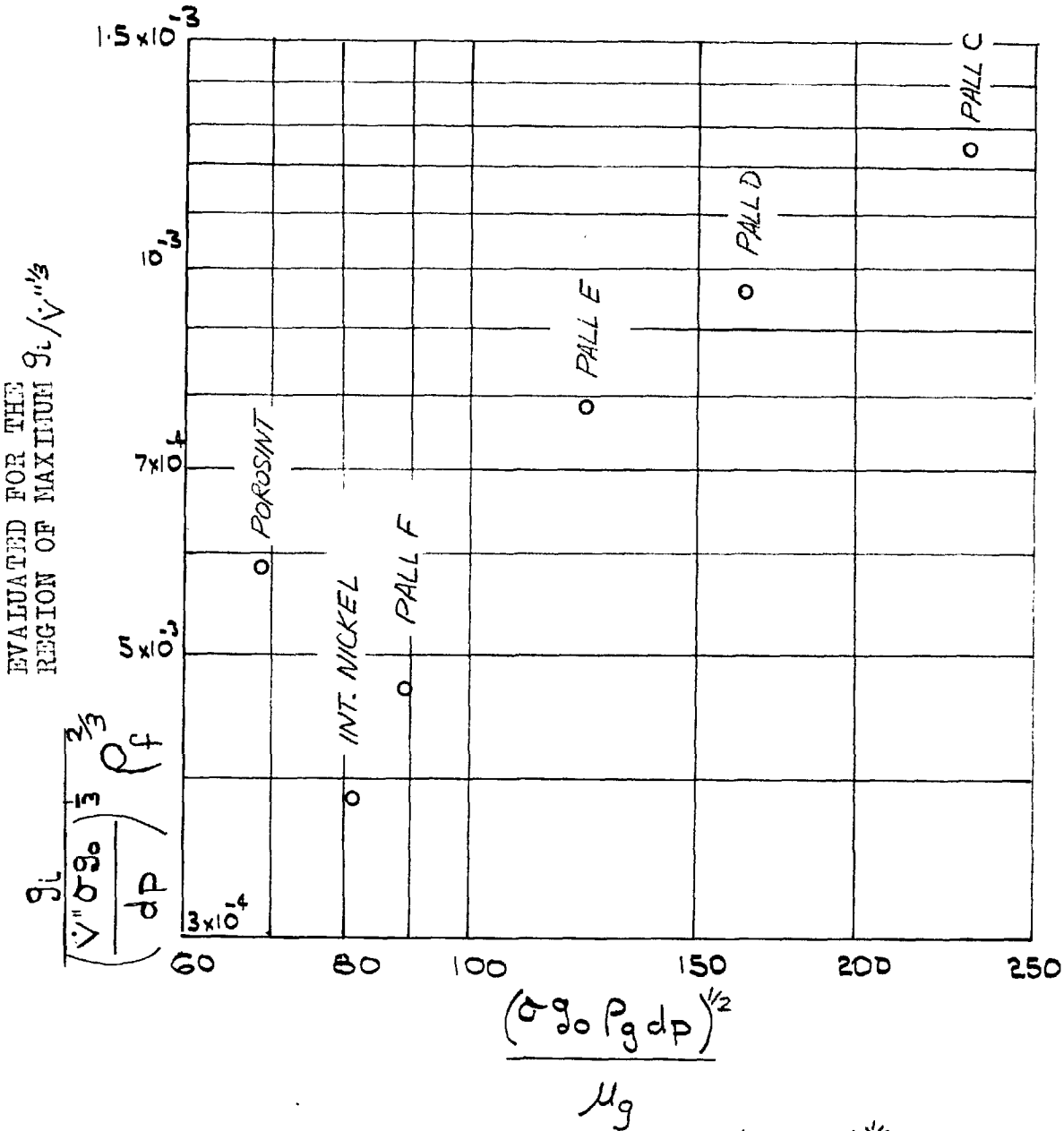

FIG. 7.13 DIMENSIONLESS CONDUCTANCE VERSUS $\frac{(\sigma g_0 \rho_g d_p)^{1/2}}{\mu_g}$ FOR VARIOUS POROUS MATERIALS

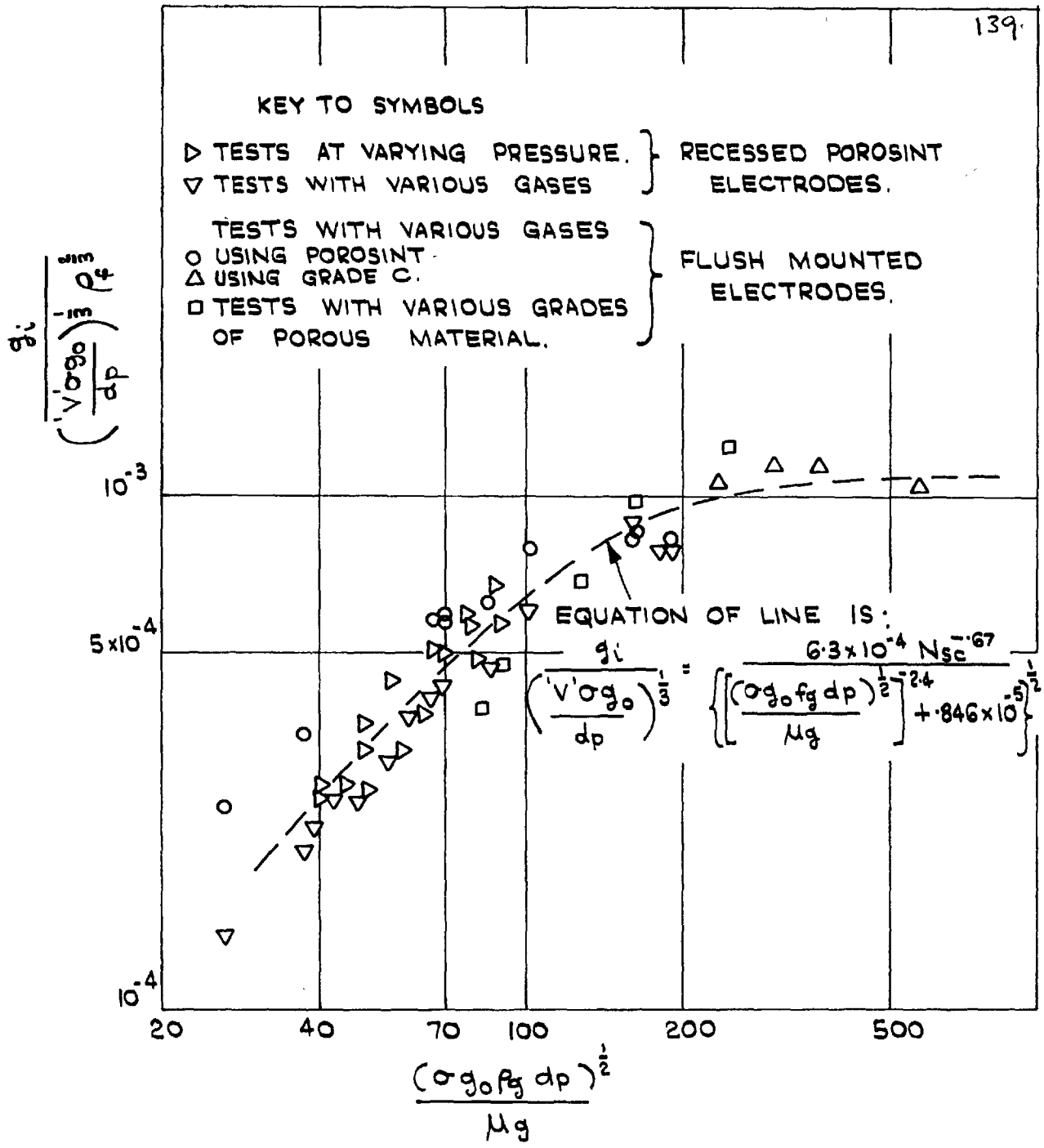

Fig. 7.14 DIMENSIONLESS CONDUCTANCE VERSUS PORE GROUP FOR ALL TESTS IN WHICH THE PORE GROUP WAS VARIED

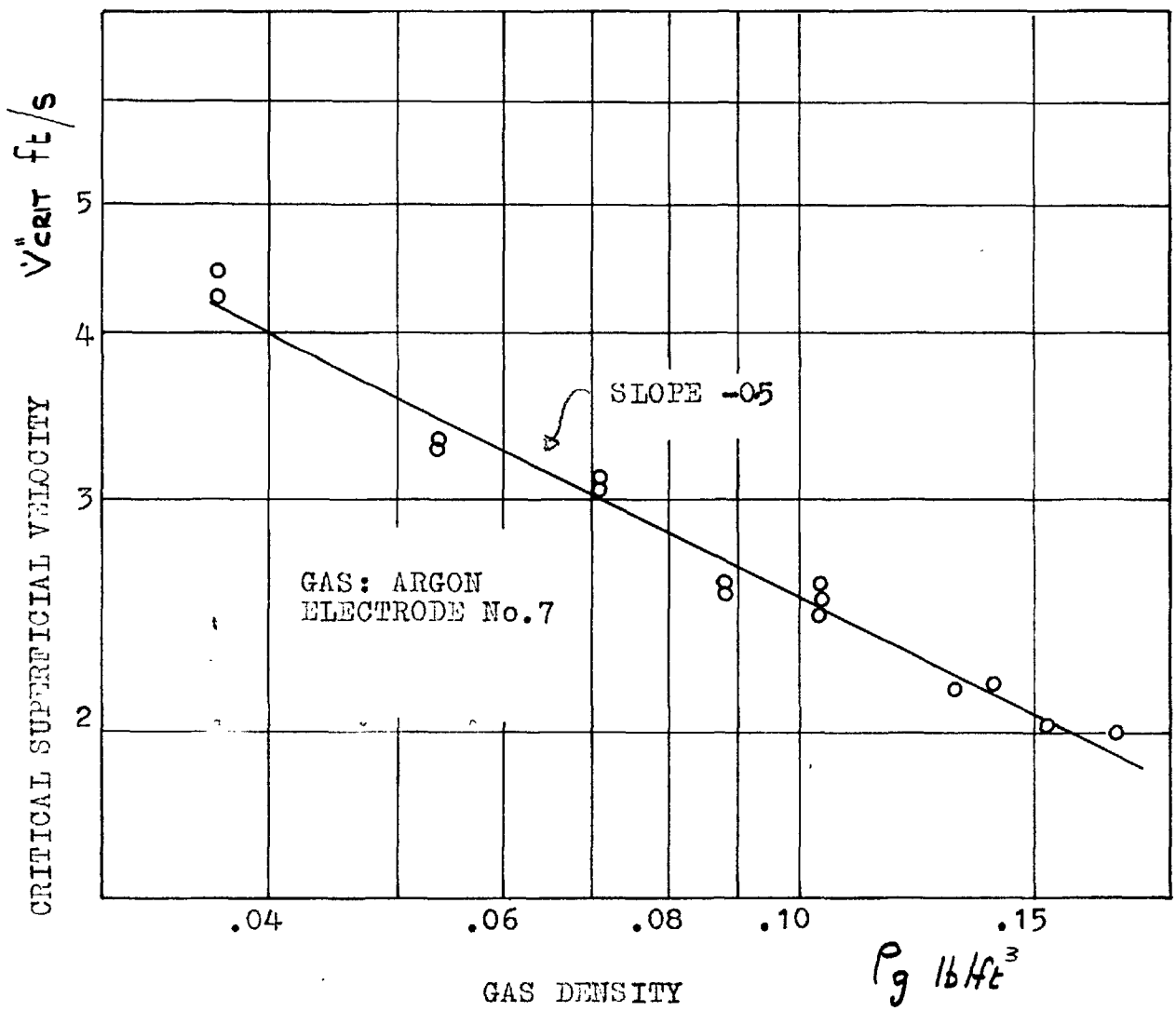

FIG. 7.15 EFFECT OF GAS DENSITY ON THE CRITICAL SUPERFICIAL VELOCITY

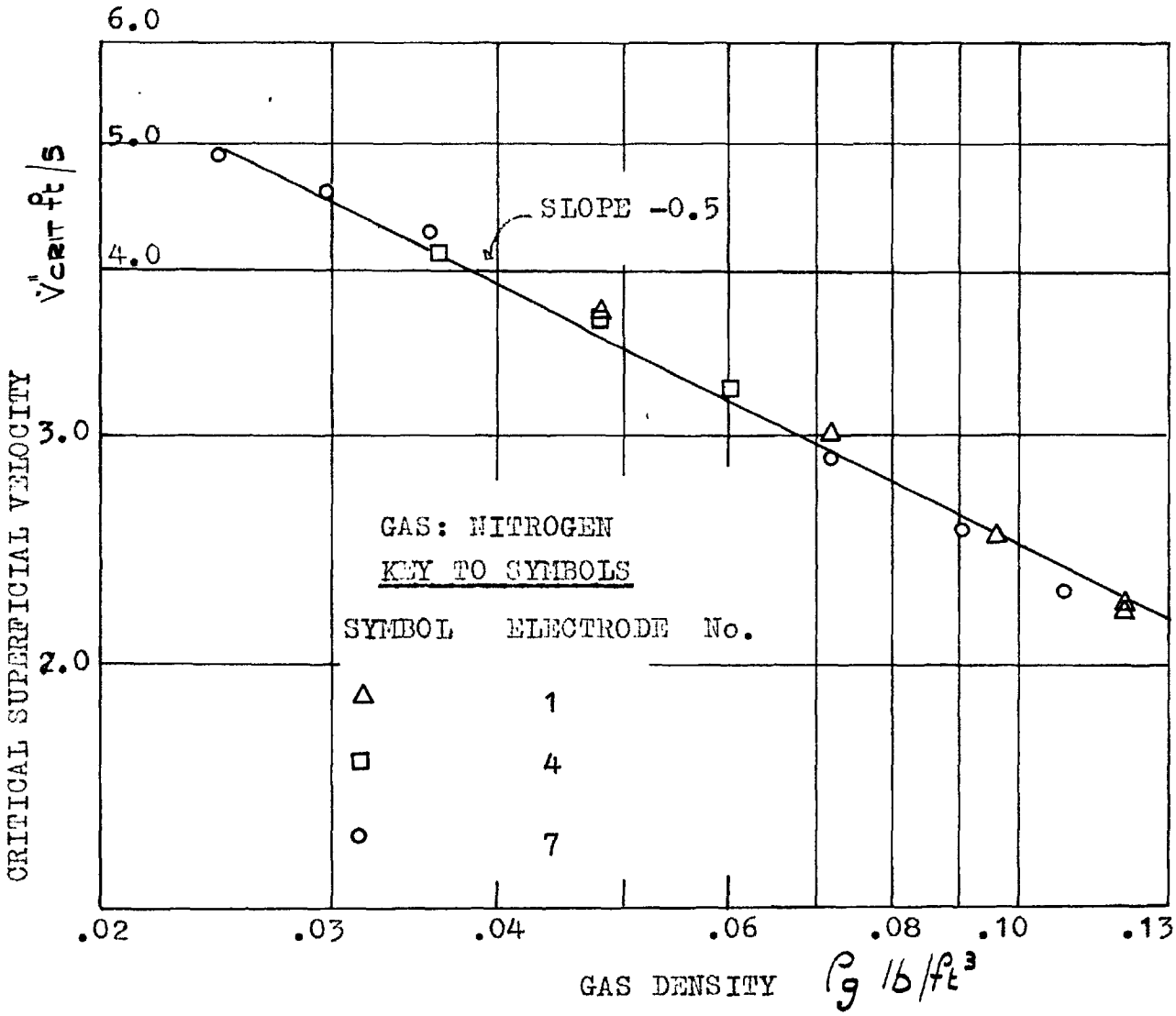

FIG. 7.16 EFFECT OF GAS DENSITY ON THE CRITICAL SUPERFICIAL VELOCITY

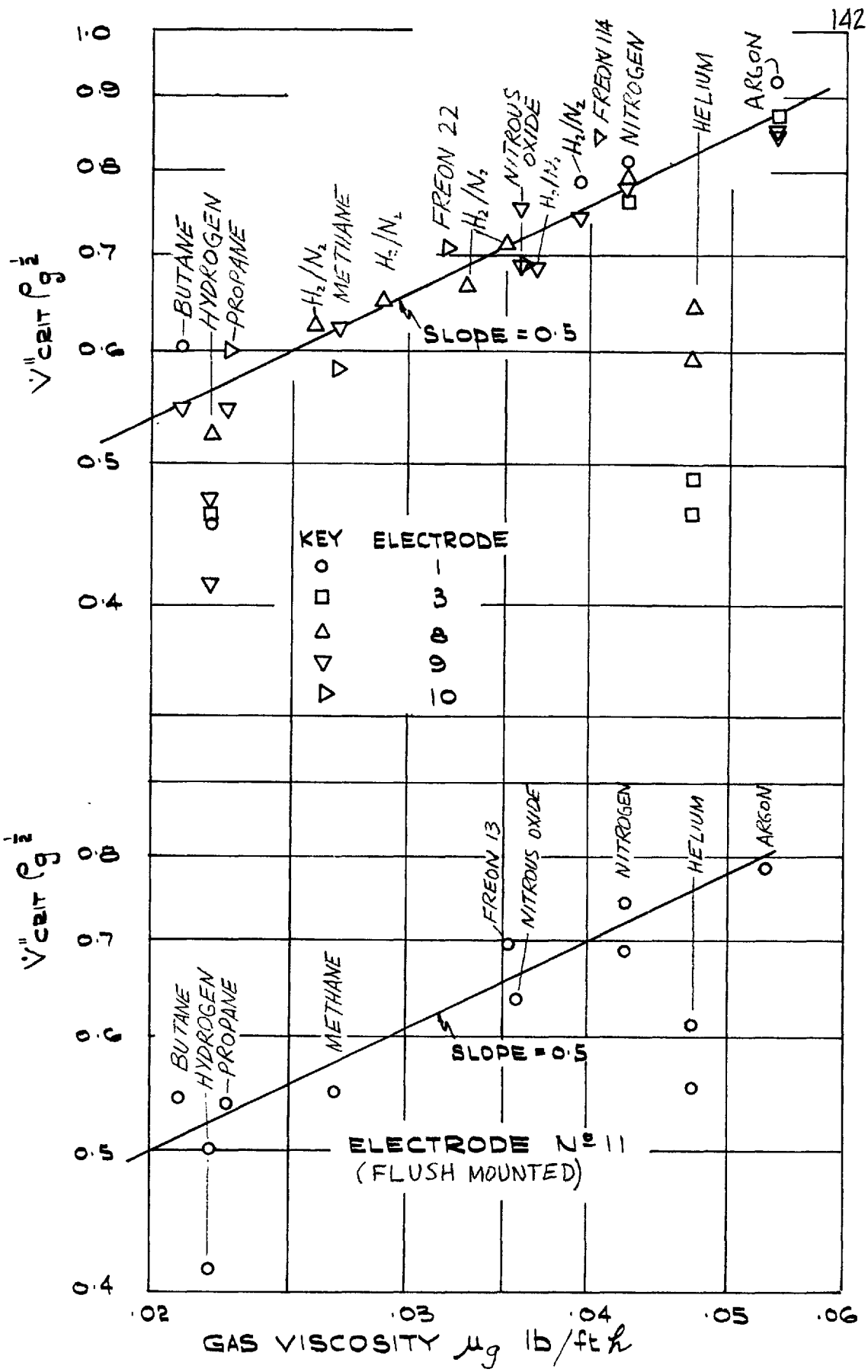

FIG. 7.17 EFFECT OF GAS VISCOSITY ON THE CRITICAL SUPERFICIAL VELOCITY

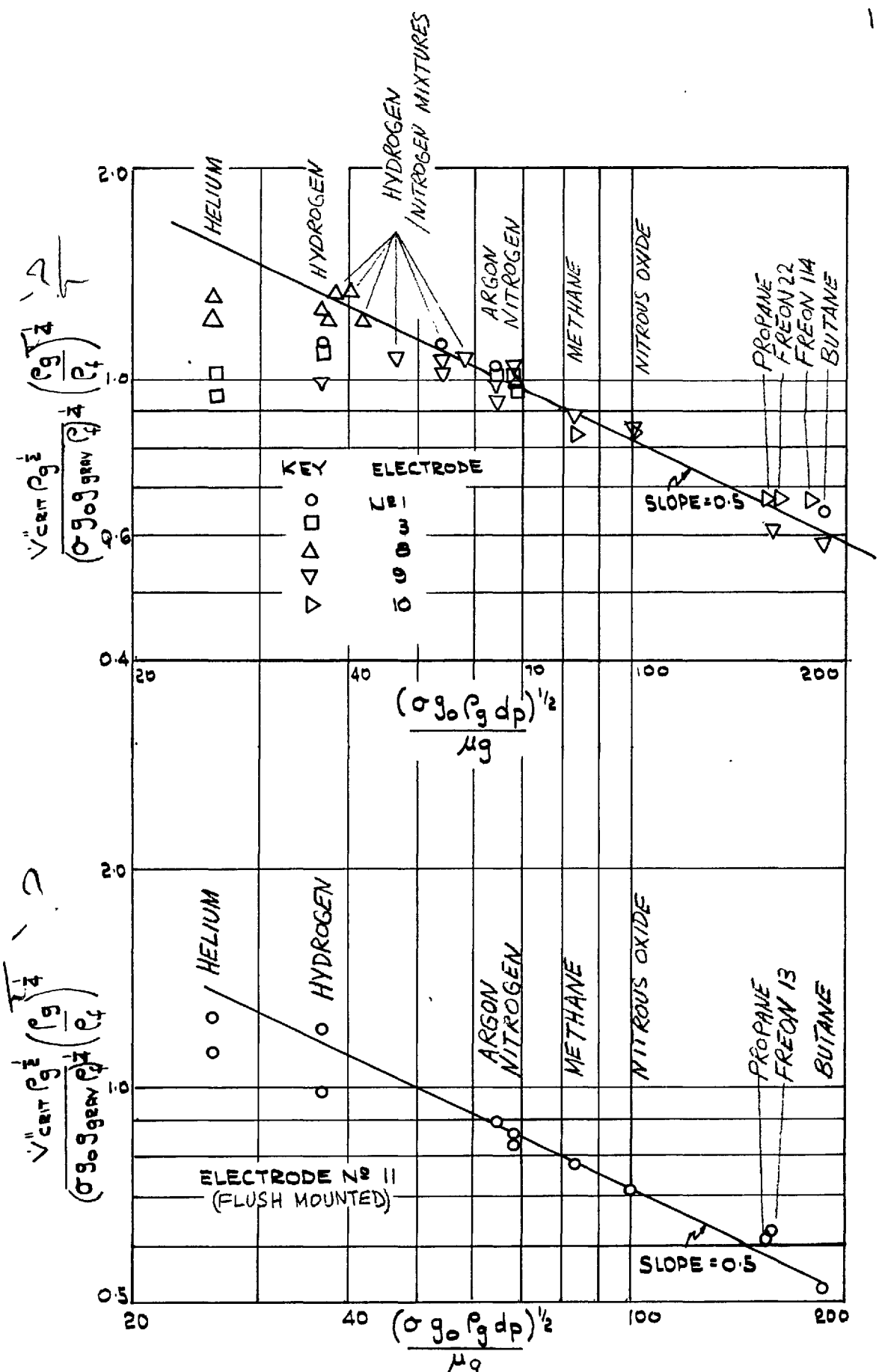

Fig.7.18 DIM'LESS $\dot{V}''_{crit}$ VERSUS $(\sigma g_o \rho_g d_p)^{1/2}/\mu_g$ FOR VARIOUS GASES

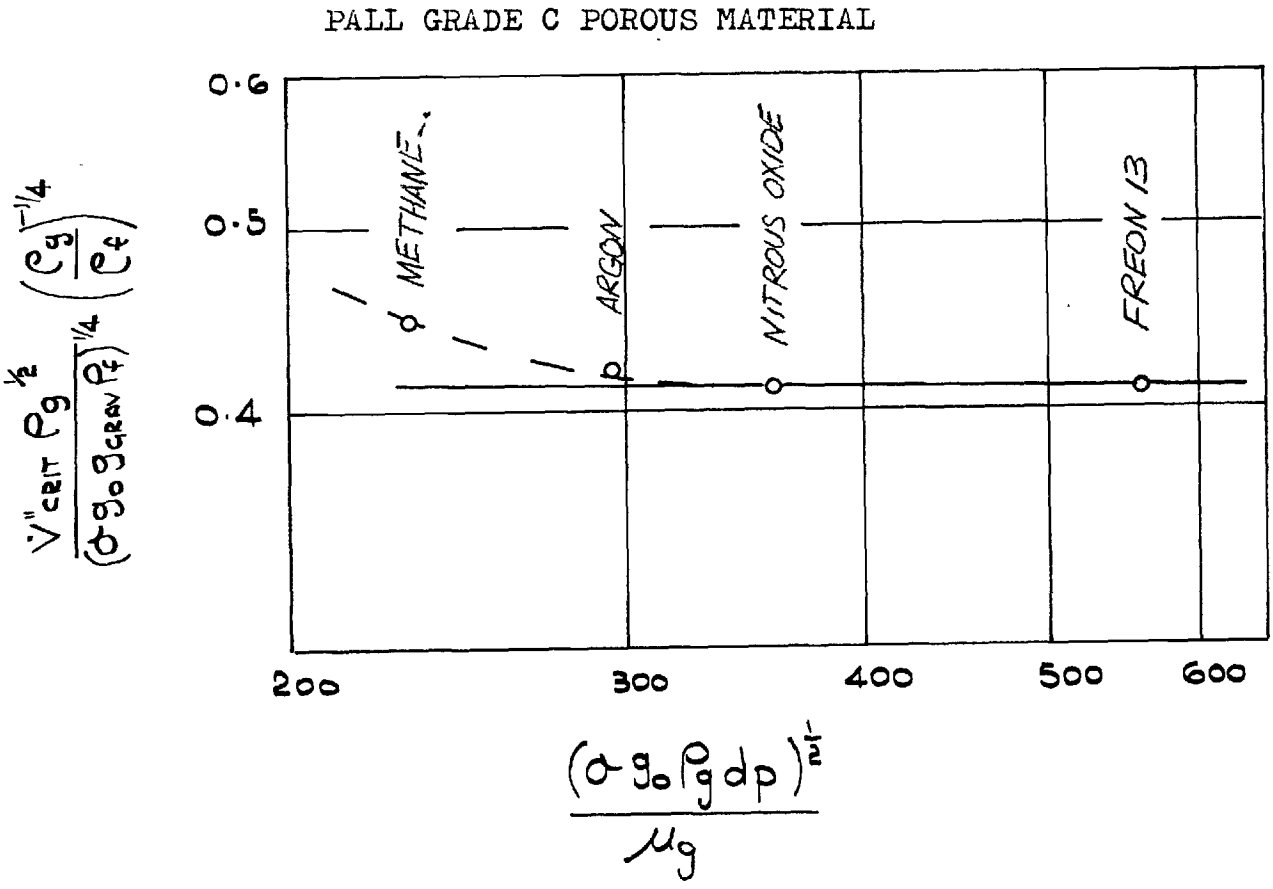

Fig. 7.19 DIMENSIONLESS CRITICAL SUPERFICIAL VELOCITY VERSUS $\frac{(\sigma g_o \rho_g d_p)^{1/2}}{\mu_g}$ FOR VARIOUS GASES WITH GRADE C MATERIAL

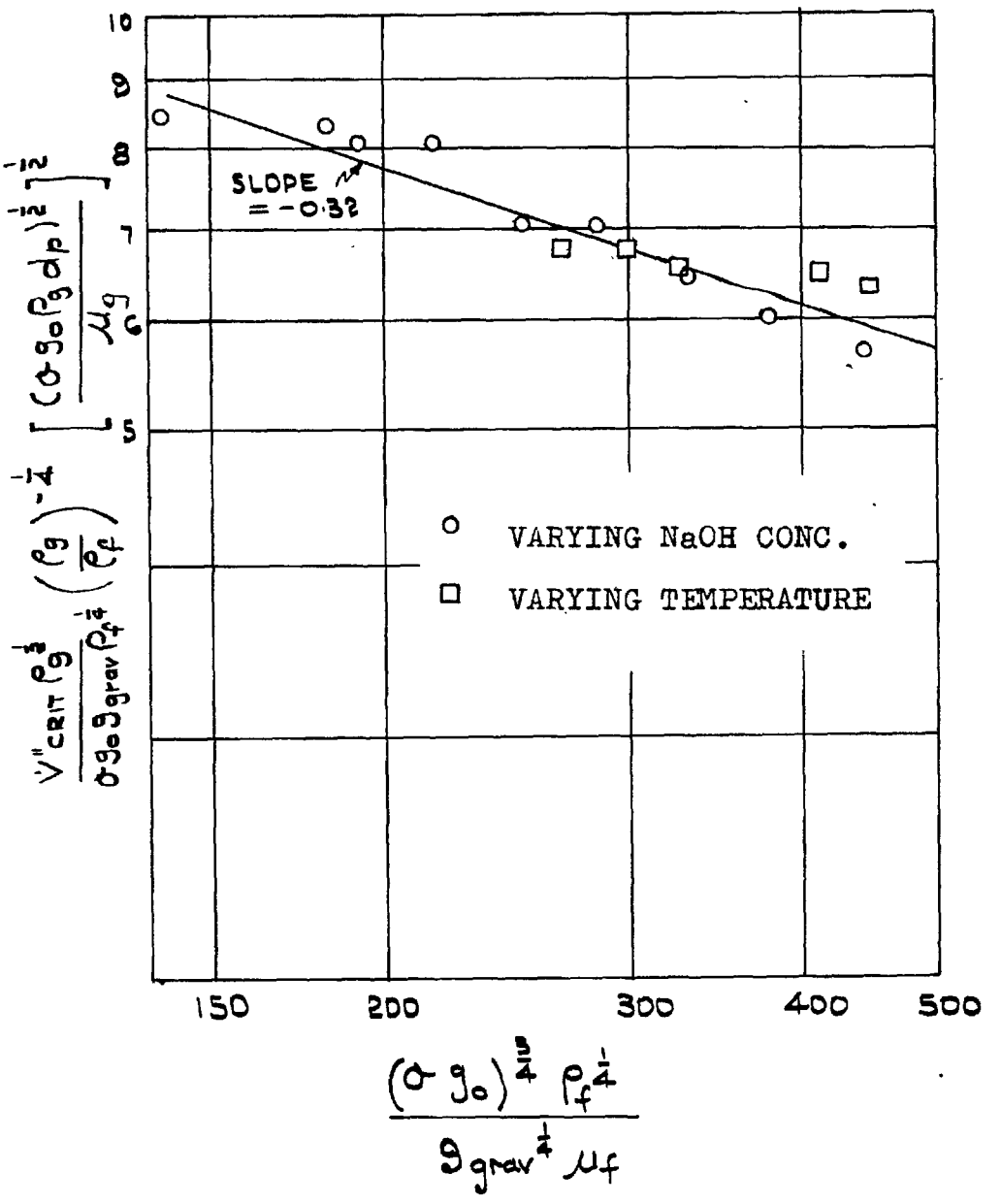

Fig. 7.20 EFFECT OF LIQUID PROPERTIES ON THE DIMENSIONLESS CRITICAL SUPERFICIAL VELOCITY

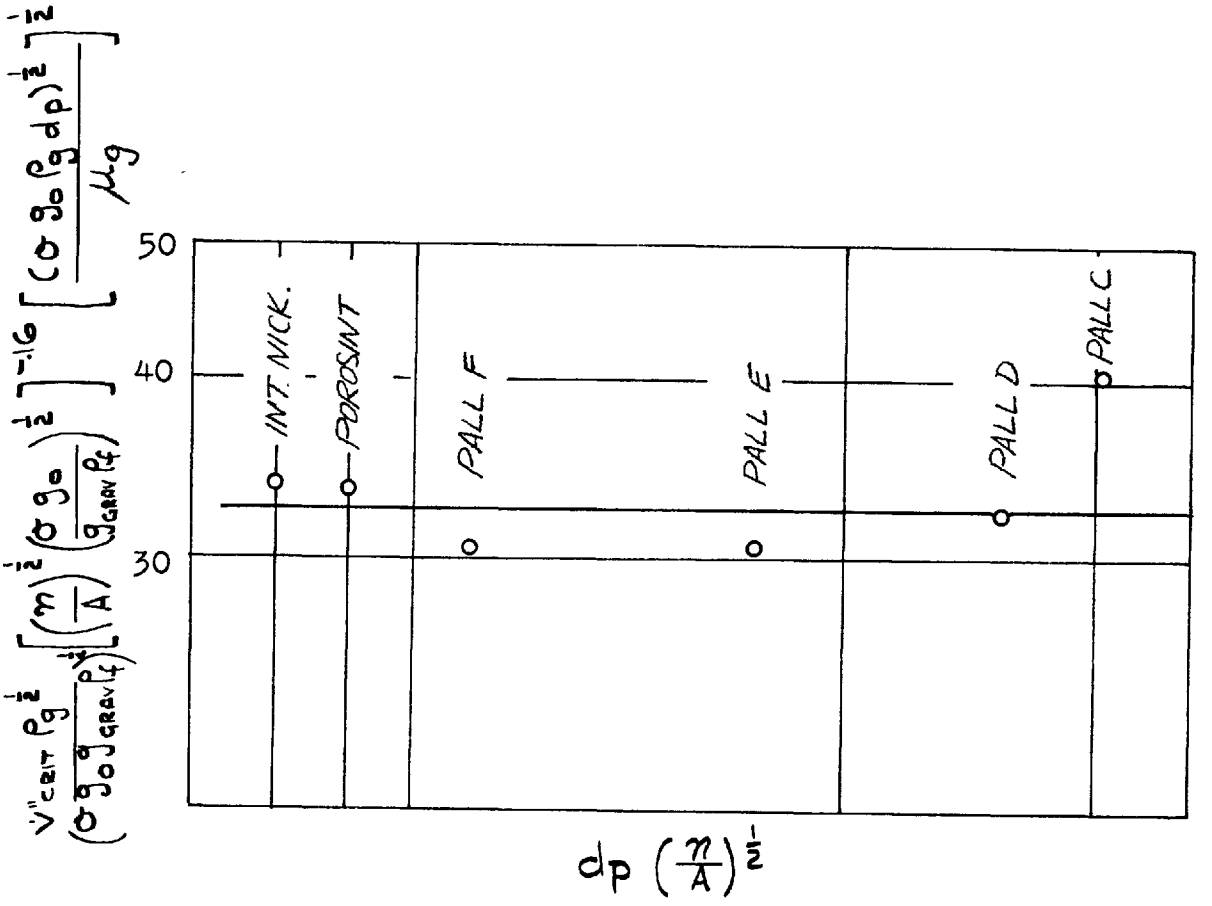

Fig. 7.21 CORRELATION OF EFFECTS OF GRADE OF POROUS MATERIAL ON THE DIMENSIONLESS CRITICAL SUPERFICIAL VELOCITY

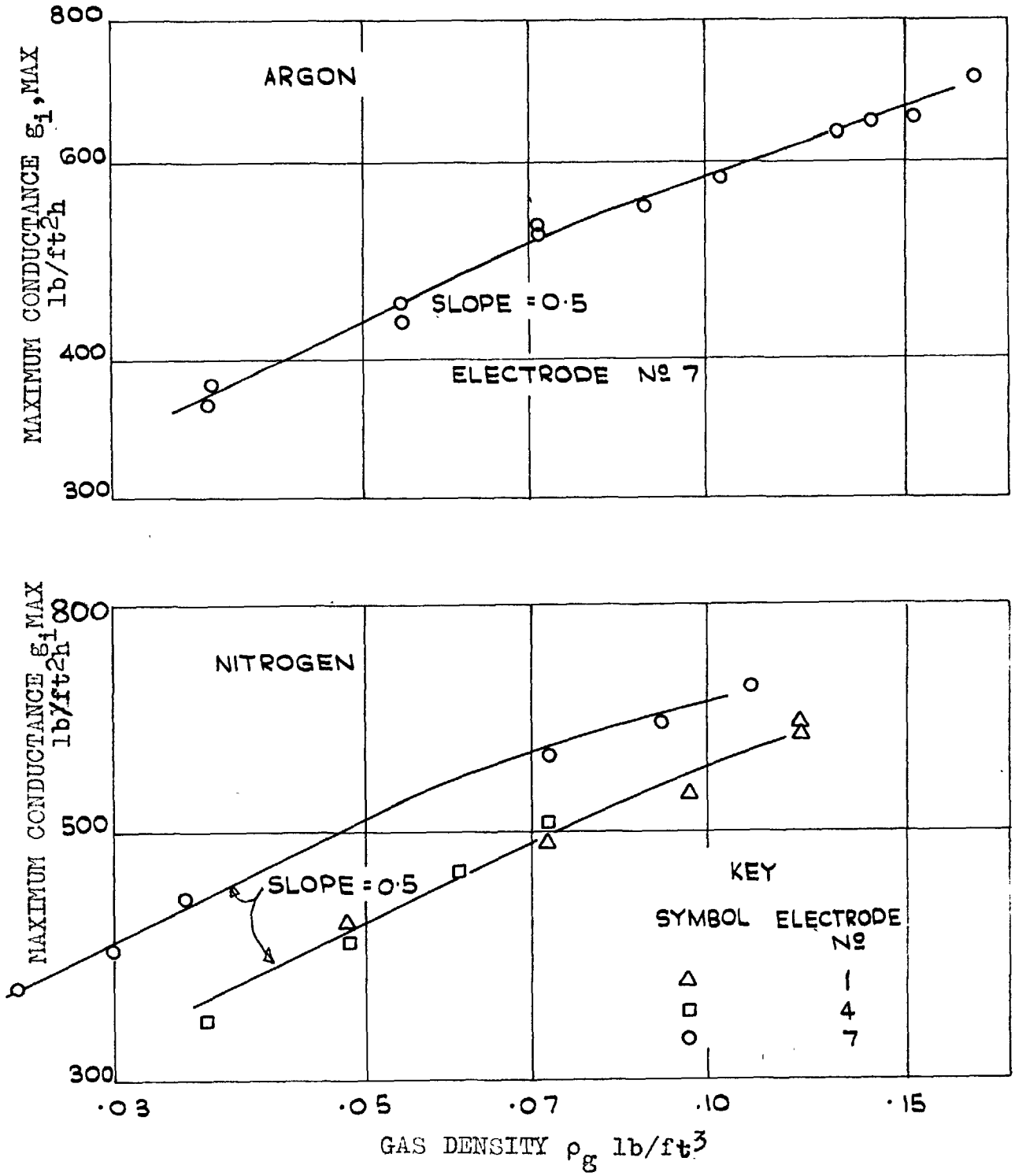

FIG. 7.22 VARIATION OF MAXIMUM CONDUCTANCE WITH GAS DENSITY FOR ARGON AND NITROGEN AT VARIOUS PRESSURES.

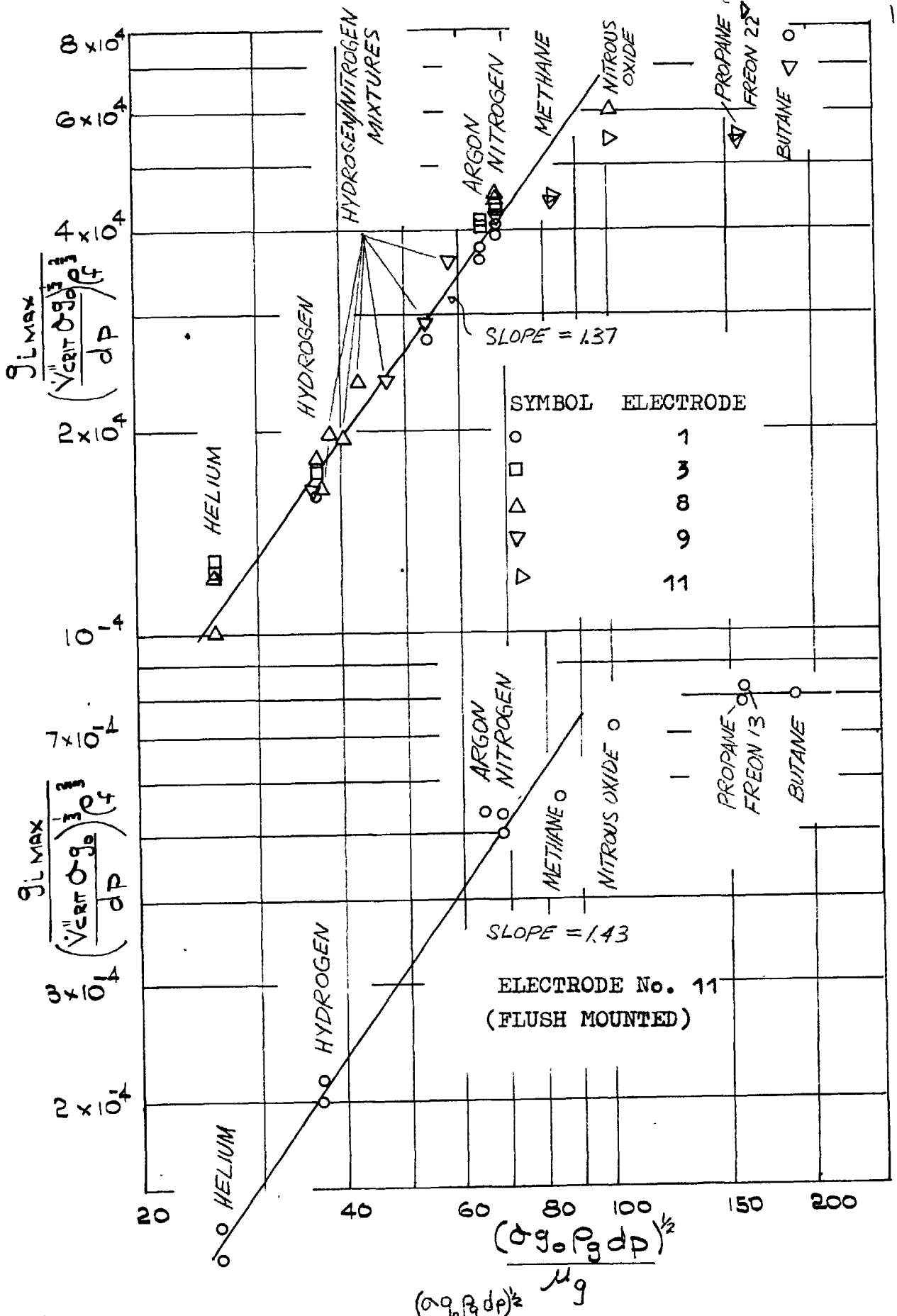

Fig.7.23 DIM'LESS $g_{i,MAX}$ VERSUS $\frac{(\sigma g_0 \rho_g dp)^{1/2}}{\mu_g}$ FOR VARIOUS GASES

PALL GRADE C POROUS CATHODE

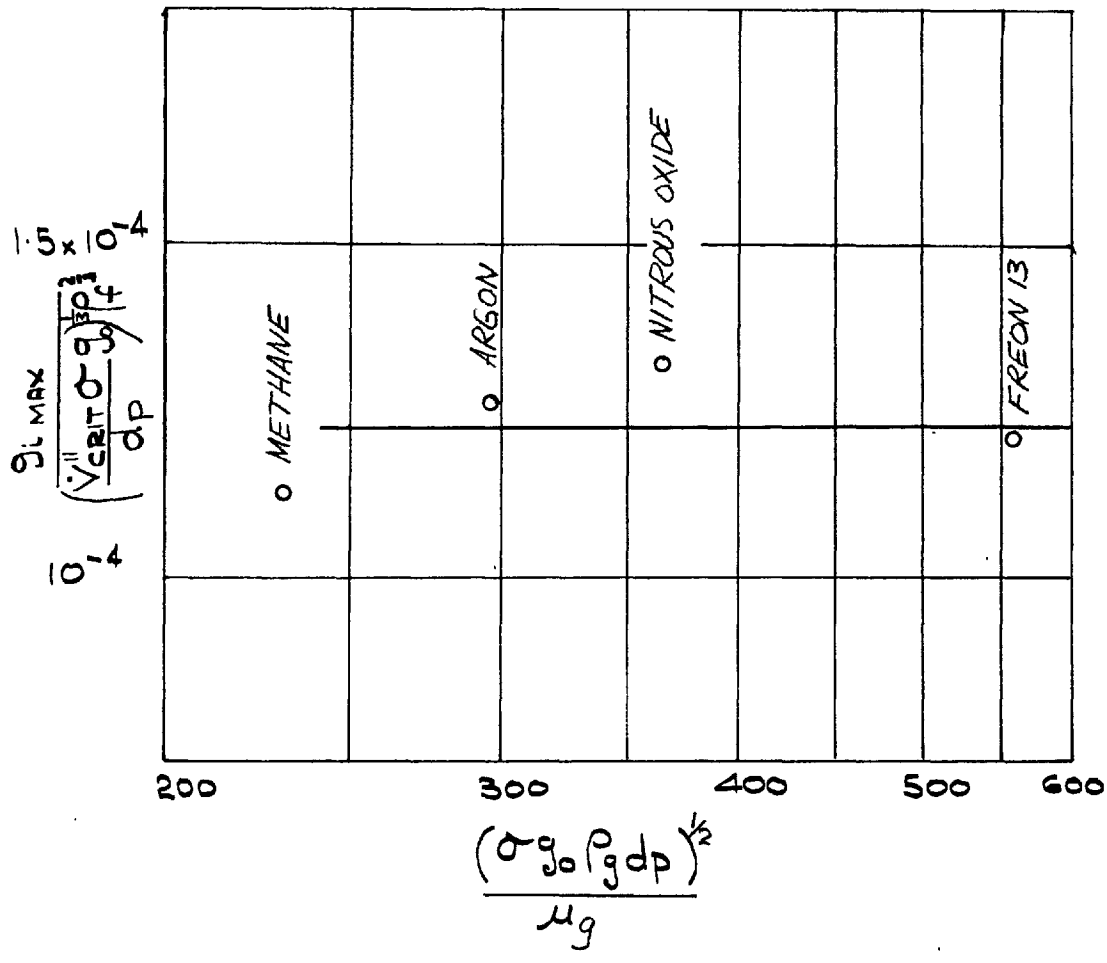

Fig. 7.24 DIMENSIONLESS MAXIMUM CONDUCTANCE VERSUS $\frac{(\sigma g_0 \rho_g d_p)^{1/2}}{\mu_g}$ FOR VARIOUS GASES WITH GRADE C

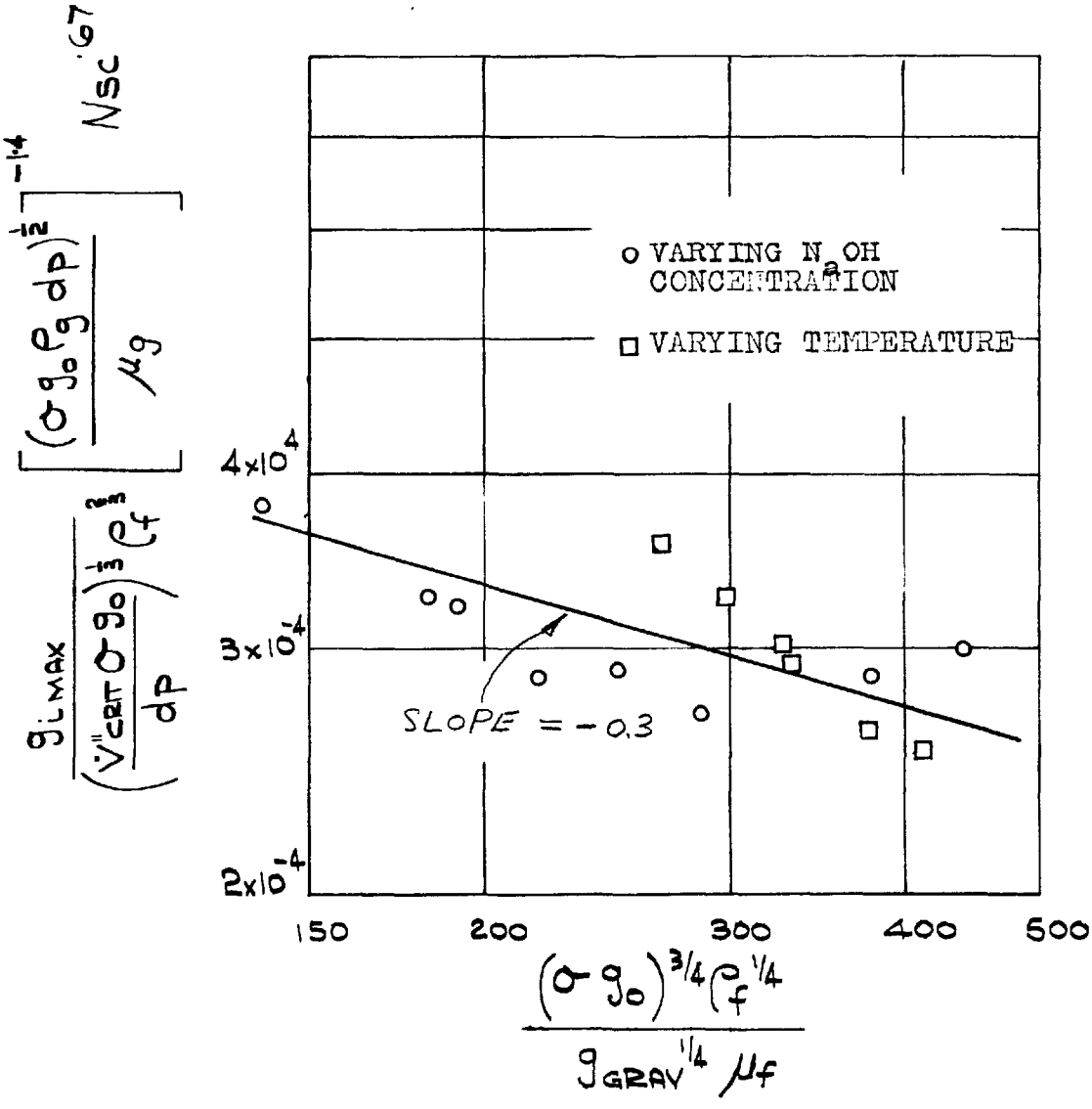

FIG. 7.25 DIMENSIONLESS CORRELATION OF LIQUID PROPERTY EFFECTS ON THE MAXIMUM CONDUCTANCE.

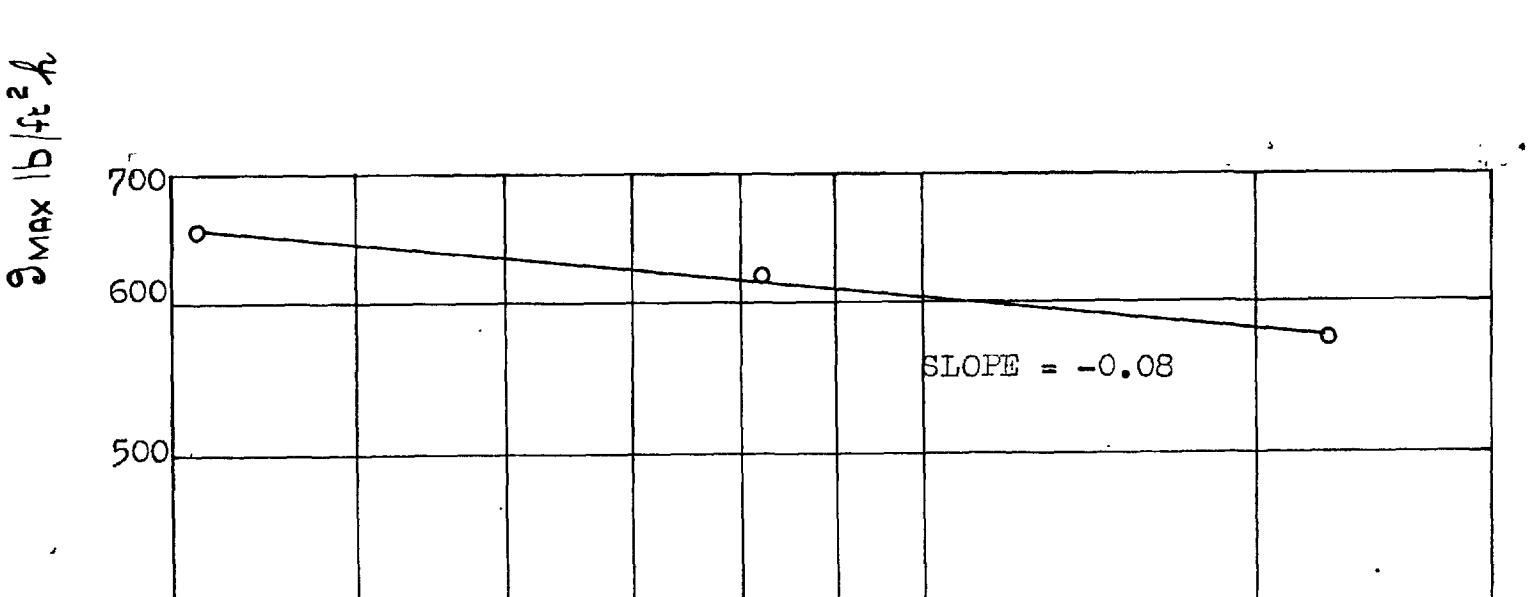

FIG. 7.26 EFFECT OF ELECTRODE THICKNESS ON THE MAXIMUM CONDUCTANCE.

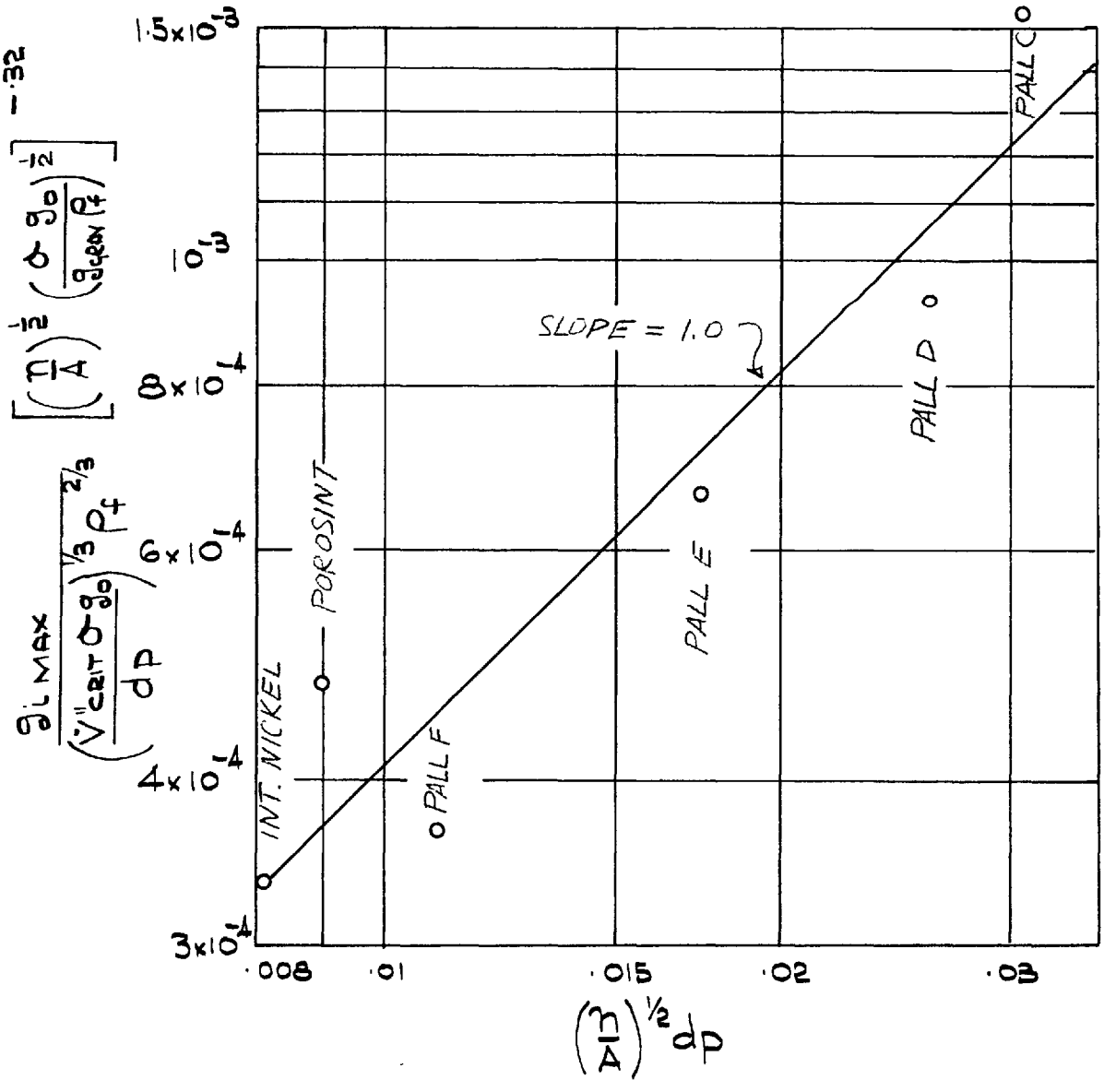

FIG. 7.27 CORRELATION OF THE EFFECTS OF THE GRADE OF THE POROUS MATERIAL ON THE MAXIMUM CONDUCTANCE.

Chapter 8 Discussion of results.

8.1 Comparisons with other barbotage results.

Included under this heading are comparisons with results of investigations using electrolytic gas evolution. The various investigations reported in the literature were reviewed in the Introduction; in this section, the results of these investigations are described and compared with the theory and experimental results of the present work.

8.1.1 The sub-critical region.

(i) The results of Gose et al. [28].

Gose et al. correlated their entire data using the following equation:

$$\frac{h}{k_f}\left(\frac{\mu_f^2}{\rho_f^2 g_{grav}}\right)^{\frac{1}{3}} N_{Pr}^{-\frac{1}{3}} = f\left[\dot{V}''\left(\frac{\rho_f C_{p_f}}{g_{grav} k_f}\right)^{\frac{1}{3}}\right] \qquad 8.1$$

where h is the heat transfer coefficient

N_{Pr} is the liquid Prandtl Number

the remaining symbols have their usual meaning and are defined in the nomenclature.

Note that the surface tension and the pore diameter are absent from the above correlation.

The function f was plotted against the dimensionless gas injection rate on logarithmic coordinates by Gose et al; a separate figure was presented for the two porous plates

and for each drilled plate for both horizontal and vertical orientations. The general form of f exhibits three regions:

(a) At low gas injection rates the slope of the f versus dimensionless superficial velocity curve is very small; this is presumably a region in which natural convection dominates.

(b) In the second region the slope increases as the bubbling becomes more profuse. A straight line can be drawn through the rather scattered data points in this region. The slope of the straight line for the horizontal porous plates is 0.4, but for all other plates including the vertical porous plates, the slope is greater than 0.4 (0.65 for one of the drilled plates).

(c) The third region is the critical region in which the function f reaches a maximum. This maximum is not achieved in the case of the drilled plates.

Comparisons in this section are restricted to the second region, (b).

Figure 8.1 shows the Gose data for horizontal porous plates. In the sub-critical region (region (b)), the results can be correlated by the following relation:

$$\frac{h}{k_f}\left(\frac{\mu_f^2}{\rho_f^2 g_{grav}}\right)^{\frac{1}{3}}\left(\frac{\mu_f C_{p_f}}{k_f}\right)^{\frac{1}{3}} = \text{const}\left[\dot{V}''\left(\frac{\rho_f C_{p_f}}{g_{grav} k_f}\right)^{\frac{1}{3}}\right]^{0.4} \qquad 8.2$$

The dependence of h on $\dot{V}''$, i.e. $h \propto \dot{V}''^{0.4}$ agrees well with the result, $g_i \propto \dot{V}''^{0.38}$ obtained in the present work and reasonably well with the theoretical prediction of $h \propto \dot{V}''^{.33}$. The higher values of the exponent $\dot{V}''$ for drilled plates agrees qualitatively with the similar effect obtained with the coarser porous electrodes in the present investigation.

Rearranging equation 8.2 to give groups which are comparable to those in the present work, it becomes:

$$\frac{h}{C_{p_f}\left(\frac{\dot{V}''\sigma g_o}{d_p}\right)^{\frac{1}{3}}\rho_f^{\frac{2}{3}}} = \text{const}\left(\frac{\mu_f C_{p_f}}{k_f}\right)^{-5/9}\left[\dot{V}''\left(\frac{\rho_f C_{p_f}}{g_{grav} k_f}\right)^{\frac{1}{3}}\right]^{.07}\left[\frac{d_p^3 \mu_f^2 g_{grav}^2 \rho_f}{(\sigma g_o)^3}\right]^{1/9} \qquad 8.3$$

With the correlation in this form, the exponent of the Prandtl Number is -.55 which is lower than the -0.67 exponent of the Schmidt Number obtained in the present work. However this result was obtained in a lower range of the Prandtl/Schmidt Number than the present work, namely 3.4 to 574 compared with 1,320 to 17,270.

Gose et al. did not consider the surface tension, or

the pore diameter, in their correlations of the data; had they done so, the group on the extreme right of equation 8.3 might not have appeared.

The two tests using helium performed by Gose et al. produced the same results as similar tests with air. This accords with the present findings, since in both of Gose's tests the value of the pore group $\frac{(\sigma g_o \rho_g d_p)^{\frac{1}{2}}}{\mu_g}$ was in excess of 100, which is the criterion found for the dimensionless conductance (heat transfer coefficient) to be independent of the gas properties.

(ii) The results of Akturk [2].

Akturk did not attempt to correlate his data presented in ref. 2. His data were, however, plotted in dimensionless coordinates; these are

$$\frac{h}{k_f}\left[\frac{\sigma g_o}{g_{grav}(\rho_f-\rho_g)}\right]^{\frac{1}{2}} \quad \text{and} \quad \frac{3600\dot{V}''\rho_g^{\frac{1}{2}}}{\left[g_o g_{grav}\sigma(\rho_f-\rho_g)\right]^{\frac{1}{4}}} .$$

Plotted on logarithmic coordinates, the data of a single test exhibits three regions as shown by Figure 8.2 which is reproduced from reference 2 .:

(a) At low superficial velocities ($<0.1\ \dot{V}''_{CRIT}$) the slope of the curve decreases as $\dot{V}''$ increases.

(b) In the second region, the data points lie roughly on a straight line with a slope of between 0.15 and 0.31

depending on which test is considered.

(c) The third region is the critical region, in which the heat transfer coefficient reaches a maximum value and subsequently decreases.

Comparisons in this section are restricted to the second region, (b).

The slope of the line of proportionality between heat transfer coefficient and the superficial velocity in the sub-critical region, (b) is, in general, less than the values of the present work and of the theoretically predicted value.

Of the three parameters investigated by Akturk, the independence of the heat transfer coefficient of the porous plate diameter and the ratio of pool diameter to porous plate diameter, accords with the present findings. The effect of the third parameter, liquid temperature, can be represented approximately by the following equation:

$$\frac{h}{k_f}\left[\frac{\sigma g_o}{g_{grav}(\rho_f-\rho_g)}\right]^{\frac{1}{2}} = \text{const}\left[\frac{3600\ \dot{V}''\rho_g^{\frac{1}{2}}}{\left[g_o g_{grav}\sigma(\rho_f-\rho_g)\right]^{\frac{1}{4}}}\right]^{.22} N_{Pr}^{-.2} \qquad 8.4$$

This relation applies to the region (b) only ($0.1 < \frac{\dot{V}''}{\dot{V}''_{CRIT}} < 0.75$).

Rearranging equation 8.4 to give dimensionless groups which are comparable to those in the present work, it

becomes:

$$\frac{h}{C_{p_f}\left(\frac{\dot{V}\sigma g_o}{d_p}\right)^{\frac{1}{3}}\rho_f^{\frac{2}{3}}} = \text{const}\ N_{Pr}^{-1.2}\left[\frac{\dot{V}''\rho_g^{\frac{1}{2}}}{\left[g_o g_{grav}\sigma(\rho_f-\rho_g)\right]^{\frac{1}{4}}}\right]^{-.11}$$

$$\left[\frac{(\sigma g_o)^{\frac{3}{4}}\rho_f^{\frac{1}{4}}}{g_{grav}^{\frac{1}{4}}\mu_f}\right]^{-1}\left[d_p\left(\frac{g_{grav}\rho_f}{\sigma g_o}\right)^{\frac{1}{2}}\right]^{\frac{1}{3}}\left(\frac{\rho_g}{\rho_f}\right)^{1/6}\left(\frac{\rho_f-\rho_g}{\rho_f}\right)^{5/12} \qquad 8.5$$

The last three groups in equation 8.5 were effectively constant in Akturk's tests; there is no justification, therefore, in retaining them (this does not imply that the groups are unimportant, but merely that their effects cannot be known from the experimental evidence available).

If it is assumed that the temperature influences the dimensionless heat transfer coefficient through the Prandtl Number only, the group $\frac{(\sigma g_o)^{\frac{3}{4}}\rho_f^{\frac{1}{4}}}{g_{grav}^{\frac{1}{4}}\mu_f}$ can be replaced by N_{Pr} using the relation

$$\frac{(\sigma g_o)^{\frac{3}{4}}\rho_f^{\frac{1}{4}}}{g_{grav}^{\frac{1}{4}}\mu_f} \propto N_{Pr}^{-5/7}$$ which applies for water at varying temperatures.

Equation 8.5 now becomes:

$$\frac{h}{C_{p_f}\left(\frac{\dot{V}''\sigma g_o}{d_p}\right)^{\frac{1}{3}}\rho_f^{\frac{2}{3}}} = \text{const}\ N_{Pr}^{-.485}\left[\frac{\dot{V}''\rho_g^{\frac{1}{2}}}{\left[g_o g_{grav}\sigma(\rho_f-\rho_g)\right]^{\frac{1}{4}}}\right]^{-.11} \qquad 8.6$$

The exponent of the Prandtl Number in the above equation is rather less than the -.55 exponent of Gose's work and the -.67 exponent of the Schmidt Number in the present work. However, this result suggests that the Prandtl/Schmidt Number dependence of the dimensionless heat/mass transfer coefficient might be a function of the order of magnitude of the Prandtl/Schmidt Number. The table below which presents the results obtained so far, illustrates this point.

Source of result	Range of N_{Pr}/N_{Sc}	Exponent of N_{Pr}/N_{Sc}
Akturk	3.3 to 6.2	-.485
Gose et al.	3.4 to 574	-.55
Present work	1,320 to 17,270	-.67

A qualitatively similar result to this was observed by Spalding in reference 62 , for the case of ideal nucleate boiling in which the negative slope of the limiting curve of dimensionless heat transfer coefficient versus Prandtl Number, increased with Prandtl Number.

(iii) The results of Mixon et al. [47].

The heat transfer measurements of Mixon et al., although for extremely low rates of electrolytic gas evolution (maximum superficial velocity of 1.7×10^{-4} ft/s), show some interesting results. A correlation of the data was not presented by Mixon et al.

In Figure 6 of the above reference, reproduced here as Figure 8.3, the heat flux is plotted against gas evolution rate on logarithmic co-ordinates with the temperature difference between wall and bulk as a parameter. The bulk temperature was maintained at an almost constant value. For each temperature difference, $(T_S - T_B)$, the data points lie on a straight line, the slope of which is 0.27 at the lowest temperature difference ($20^{\circ}F$) and 0.30 at the highest ($120^{\circ}F$).

Theoretical considerations of the work done by bubbles and the dissipation of turbulent kinetic energy, for a system in which the bubbles are generated by electrolysis, yields the following result which is comparable with equation 3.6 of Chapter 3:

$$\frac{h}{c_{p_f}\left[\dot{V}''(\overline{P_b - P_f})\, g_o\right]^{\frac{1}{3}}\, \rho_f^{\frac{2}{3}}} = f\,(N_{Pr}) \qquad 8.7$$

where $\overline{P_b - P_f}$ is the time mean value of the pressure difference between the bubbles and the surrounding liquid and can be shown to be almost a constant, i.e. independent of liquid properties and of the rate of gas evolution.

Thus the dependence of heat flux, and therefore heat transfer coefficient, on the superficial velocity shown by the Mixon et al. data is in good agreement with equation 8.7.

For the range of temperatures covered by Mixon et al., the specific heat, C_{p_f} and the liquid density, ρ_f are approximately constant. The function of the Prandtl Number in equation 8.7 is obtained by plotting $h/\dot{V}''^{\frac{1}{3}}$ against Prandtl Number; the result is:

$$\frac{h}{\dot{V}''^{\frac{1}{3}}} \propto N_{Pr}{}^{a}$$

where $a = -.25$ for $\dot{V}'' = .28 \times 10^{-4}$ ft/s

$a = -.3$ for $\dot{V}'' = 1.7 \times 10^{-4}$ ft/s.

The values of the Prandtl Number exponent are considerably less than the values obtained from Akturk's and Gose's data for the same Prandtl Number range. This may be a consequence of the very low superficial velocities of the Mixon data, indeed from the two extreme values of the exponent evaluated above, there appears to be a tendency for the exponent to increase with the superficial velocity.

(iv) The results of Bhand et al. [8].

Bhand et al. measured heat transfer coefficients at varying rates of electrolytic gas evolution with liquid temperature as a parameter. A correlation of the data was not attempted by Bhand and the results presented do not permit any useful comparisons to be made in the sub-critical region.

8.1.2 The critical superficial velocity.

The expression correlating the critical superficial velocity in the present investigation is given by equation 7.13:

$$\frac{\dot{V}''_{CRIT}\rho_g^{\frac{1}{2}}}{(\sigma g_o g_{grav}\rho_f)^{\frac{1}{4}}} = 38\left(\frac{\rho_g}{\rho_f}\right)^{\frac{1}{4}}\left[\frac{(\sigma g_o \rho_g d_p)^{\frac{1}{2}}}{\mu_g}\right]^{-\frac{1}{2}}\left[\frac{(\sigma g_o)^{\frac{3}{4}}\rho_f^{\frac{1}{4}}}{g_{grav}^{\frac{1}{4}}\mu_f}\right]^{-.32}$$

$$\left[\left(\frac{n}{A}\right)^{\frac{1}{2}}\left(\frac{\sigma g_o}{g_{grav}\rho_f}\right)^{\frac{1}{2}}\right]^{.16}$$

This equation was derived from results obtained in the pore-controlled region. As discussed in the last chapter, this equation is assumed to apply in the pore-independent region if the pore group, $\frac{(\sigma g_o \rho_g d_p)^{\frac{1}{2}}}{\mu_g}$ is omitted.

When comparing this result with those obtained by other workers, it is desirable to know whether their results were obtained in the pore-controlled or pore-independent region. In most cases it has been possible to deduce that the results were obtained in the pore-independent region.

The comparisons in this section are divided according to the independent parameters which were investigated. Three sub-divisions are made, namely:

(i) Comparisons of the effects of geometry.

(ii) Comparisons of the effects of gas properties.

(iii) Comparisons of the effects of liquid properties.

(i) Comparisons of the effects of geometry.

In the experimental work of Gose et al. [28], several different porous and drilled heater plates were employed. A maximum heat transfer coefficient was achieved with the two sintered plates but not with any of the drilled plates. This suggests that the spacing between the holes of the drilled plates was too great for a break-down in the liquid continuity at the heater surface to occur.

For tests with the same liquid, the values of the critical superficial velocity for the two sintered plates were almost identical, despite a tenfold difference in the pore diameter. It is deduced that the critical superficial velocity for these tests, is independent of the pore group $\frac{(\sigma g_o \rho_g d_p)^{\frac{1}{2}}}{\mu_g}$, the values of which are estimated to be 100 and 350. In the present work, the critical superficial velocity was found to be independent of the pore group for values greater than 350.

Kutateladze and Moskvicheva [41] investigated the effects of pool depth and hole diameter (using perforated plates) on the critical superficial velocity for a liquid/liquid system (water/mercury). In non-dimensionalising the data, it was thought unwise to use the quantity $\left(\frac{\sigma g_o}{g_{grav} \rho_f}\right)^{\frac{1}{2}}$ to represent the order of magnitude of a depart-

ing bubble, since its value is considerably less than the diameter of the holes in the perforated plates. The pool depth is, therefore, expressed as a ratio of the hole diameter; this provides a single dimensionless group for both series of tests. Table 8.1 shows the results obtained by Kutateladze and Moskvicheva for the water/mercury system.

Table 8.1 Effect of hole diameter and pool depth on $\dot{V}''_{CRIT}$

Pool depth, h	Hole diameter d	Ratio h/d	$\dot{V}''_{CRIT}$
155 mm	10 mm	15.5	.048 m/s
245	10	24.5	.053
355	10	35.5	.056
425	10	42.5	.056
155	10	15.5	.048
155	5	31	no crisis
155	3	52	.057

Table 8.1 shows that a limiting value of h/d occurs, above which the critical superficial velocity is constant. This limiting value of h/d is approximately 30 and should be compared with a similar limiting value of $h\left(\frac{\rho_f g_{grav}}{\sigma g_o}\right)^{\frac{1}{2}}$ of 15 (Fig.7.1) obtained in the present work.

The porous plate diameter and the ratio of the pool diameter to that of the porous plate, were both shown by

Akturk [2] to have no effect on the critical superficial velocity. Except for the condition of the pool diameter approaching the porous plate diameter, the results of the present work agree with those of Akturk.

(ii) Comparisons of the effects of gas properties.

The tests carried out by Gose et al. with helium were not taken to very high superficial velocities and a maximum heat transfer coefficient was not achieved. The only other investigator to vary gas properties was Wallis [75] who, by purely hydrodynamic means, measured the critical superficial velocity for air at various pressures between 14.7 lb/in^2 and 55 lb/in^2. He also carried out a test with a different gas, Freon 12.

No pore or hole size was quoted by Wallis, however since the porous material is described as a 'fine brass mesh' it is presumed that the value of $\frac{(\sigma g_o \rho_g d_p)^{\frac{1}{2}}}{\mu_g}$ was sufficiently large to have no effect. The effect of changing the injected gas can, therefore, be correlated by the gas density alone. Figure 8.4 shows the Wallis data plotted as critical superficial velocity versus gas density on logarithmic co-ordinates. The erratic behaviour of the Freon 12 tests resulted in a spread of values of $\dot{V}''_{CRIT}$.

Considering the data for air alone, the best straight

line through the points on Figure 8.4 has a slope of 0.45. If, however, a mean value of the Freon data is also considered, the slope of the best line reduces to 0.35. These values compare, qualitatively at least, with 0.25 for the region independent of the pore flow, in the present work.

(iii) Comparisons of the effects of liquid properties.

Liquid properties were varied by all the other investigators. A close examination of the collated results led to the conclusion that the best correlation of the critical superficial velocity was obtained by plotting the data as a Kutateladze No. K_1 defined as:

$$K_1 \equiv \frac{\dot{V}''_{CRIT}\rho_g^{\frac{1}{2}}}{\left[\sigma g_o g_{grav}(\rho_f-\rho_g)\right]^{\frac{1}{4}}}$$

against the dimensionless liquid property group $\frac{(\sigma g_o)^{\frac{3}{4}}\rho_f^{\frac{1}{4}}}{g_{grav}^{\frac{1}{4}}\mu_f}$. Figure 8.5 shows the data plotted in this manner, indicating a result of the form:

$$K_1 = 0.066\left[\frac{(\sigma g_o)^{\frac{3}{4}}\rho_f^{\frac{1}{4}}}{g_{grav}^{\frac{1}{4}}\mu_f}\right]^{0.15}$$

Special note should be made of the close agreement of the Kutateladze and Moskvicheva data, for the two liquid/liquid systems, with the other barbotage data. Although the values of K_1 for Akturk's data are low, the variation

of K_1 with the liquid property group is qualitatively the same as that of the other workers.

The results obtained from the data of Gose et al. for the critical superficial velocity are shown in the table below, the values used are those extracted from the Gose data by Sims et al. [59], (Gose did not attempt to correlate the critical superficial velocity).

Table 8.2 Results of Gose et al.

Liquid	Critical superficial velocity V	K_1	$\frac{(\sigma g_o)^{\frac{3}{4}} \rho_f^{\frac{1}{4}}}{g_{grav}^{\frac{1}{4}} \mu_f}$
Water	2.0 ft/s	.13	758
Ethylene Glycol	3.45	.23	194
Shell Tellus Oil 15	1.85 to 2.1	.14 to .16	36.4
Shell Tellus Oil 69	0.24	.02	6.0

All the above results are for horizontal sintered plates with air injection.

The effects of the liquid property group on K_1 shown in table 8.2 are not consistent. Because of this, it was considered unprofitable to extend the scale of Figure 8.5 by a factor of three to include these points.

Having thus described the effect of liquid properties on the critical superficial velocity found by the other investigators, a comparison is now made with the results

of the present work. The data from the tests in which liquid properties were varied are shown plotted in Figure 8.5; the broken line drawn through the points has a slope of 0.33. An immediate observation is that the values of K_1 are within the same fairly narrow range as those of the other investigations. However, as the liquid property group is increased, the variation of K_1 is seen, in the present work, to be a slight decrease, as opposed to a slight increase, in the other investigations. An explanation of this difference has not been found and it is apparent that further experimentation is needed over a wider range of the liquid property group.

The values of the superficial velocities corresponding to the maximum heat transfer coefficients observed by Bhand et al. [8] (electrolytic gas evolution), are of the order of 10^{-3} ft/s. The explanations given by Bhand for the occurrence of the maxima (in some cases two maxima were observed) are not clear and these results have, therefore, been excluded from the comparisons.

8.2 Comparison with results from boiling heat transfer.

8.2.1 The sub-critical region.

Heat or mass transfer during barbotage is a similar process to that of nucleate boiling insofar as there is, in both cases, a transfer of heat or mass across a boundary

at which bubbles are generated. It seems reasonable, therefore, to compare the dependences of the heat or mass transfer coefficient on the rate of bubbling and system parameters in each case. However, a closer examination of the heat transfer mechanisms involved reveals some basic differences which should be considered when comparing the two processes.

The two basic differences between barbotage and saturated pool boiling are:

1. In barbotage, the heat or mass is transferred through the liquid between the porous wall and the bulk liquid, whereas in saturated pool boiling, the heat is transferred through the liquid from the heater wall to the vapour bubbles.

2. In barbotage, all the injected gas forms bubbles at the porous wall, whereas in saturated pool boiling, some of the vaporisation into the bubbles occurs after the bubbles have left the wall.

The heat transfer processes are affected by these differences in the following ways:

(a) The heat or mass flux in barbotage must traverse the whole of the thermal or diffusion boundary layer. In boiling, however, some of the heat can reach the bubble interface without travelling very far through the liquid; indeed recent experimental evidence [48, 52, 55, 44] has

suggested that a large proportion of the total heat flux in boiling (depending on the magnitude of the heat flux) reaches the bubble by conduction through a thin film of liquid at the base of the still-attached bubble. This 'short-cut' for part of the heat flux accounts for the heat trasnfer coefficients experienced in boiling being higher than those reported by Akturk and Gose et al. for heat transfer during barbotage.

(b) In barbotage, all the injected gas contributes towards the agitation of the region close to the wall where the temperature or concentration gradients are the greatest. Because some of the vaporisation in boiling occurs after the bubble has detached from the wall, only a part of the total vapour formed provides agitation in the region close to the wall. This effect is probably not as great as the one described in (a).

An important factor in both (a) and (b) is the amount of vaporisation in boiling occurring close to the wall. It is believed [26, 50, 54, 46, 80], and in one instance experimentally proved, that the percentage of vapour formed whilst the bubble is still attached to the wall increases with the total heat flux, reaching a value of almost 100% at the critical heat flux [50]. (It has here been presumed that the undefined term 'latent heat transport' used by several authors, refers to the amount of sensible heat converted to latent heat while the bubble is attached to

the wall.) This means that (a) the percentage of the total heat flux provided with a short-cut to the bubble interface and (b) the percentage of the total vapour formed, contributing to the agitation of the region close to the wall, both increase with the total heat flux in boiling. This explains why the heat transfer coefficient in boiling increases more rapidly with the total vapour generation rate (i.e. total heat flux) than in barbotage. An examination of the boiling data reported in the literature, shows the heat transfer coefficient to depend upon the heat flux to a power of between 0.4 and 0.85. This should be compared with the one third exponent of the superficial velocity which applies in barbotage.

Other than these very qualitative comparisons of the effects of the bubble generation rate on the heat transfer coefficient, comparisons of the effects of other quantities, such as the Prandtl Number, are impractical for two reasons:

(i) Correlations of the nucleate boiling heat transfer coefficient appearing in the literature, vary considerably in their predictions of the effects of the parameters correlated (see for example the reviews of Zuber [79, 80] and of Westwater [76]).

(ii) The method of correlating the heat or mass transfer coefficient used in the present work, and in

particular the form of the dimensionless heat or mass transfer coefficient, has no equivalent in the nucleate boiling correlations reported so far in the literature. To manipulate the existing correlations into a form suitable for comparisons would be extremely artificial and would yield no useful information.

Clearly the correlating methods usually employed are unsatisfactory, primarily because it is difficult to account for the effect of the fine structure of the heat transfer surface. The method proposed by Spalding [62], referred to in Chapter 3, considers an overall energy balance for the boiling layer; a means of correlating the effects of the nucleating characteristics of the surface is included in the proposals. A nucleate boiling correlation based on this method would provide an equation ideal for comparisons with the results of the present and other barbotage work. However, the development of such a correlation is still in its early stages and as such it cannot be utilised for the present comparisons.

8.2.2 The critical heat flux.

It is generally accepted that the critical heat flux or burn-out point in boiling occurs at a critical rate of vapour generation at or near to the heat transfer surface. Comparisons of the results of the present work with boil-

ing results are made possible by assuming that, at the critical point, all the heat flux is converted into vapour very close to the surface of the heater. The following relation can therefore be written:

$$\dot{V}''_{CRIT} = \frac{\dot{q}''_{CRIT}}{h_{fg}\rho_g} \qquad 8.8$$

where $\dot{q}''_{CRIT}$ = critical heat flux

h_{fg} = latent heat of vaporisation

ρ_g = vapour density.

The critical heat flux in boiling is well predicted by the equation first derived by Kutateladze [39, 40], shown below:

$$\frac{\dot{q}''_{CRIT}}{\rho_g^{\frac{1}{2}} h_{fg}\left[\sigma g_o g_{grav}(\rho_f-\rho_g)\right]^{\frac{1}{4}}} = K_1, \text{ a constant} \qquad 8.9$$

Replacing $\dot{q}''_{CRIT}$ by $\dot{V}''_{CRIT}$ from the assumed relation 8.8, the Kutateladze equation becomes:

$$\frac{\dot{V}''_{CRIT}\rho_g^{\frac{1}{2}}}{\left[\sigma g_o g_{grav}(\rho_f-\rho_g)\right]^{\frac{1}{4}}} = K_1 \qquad 8.10$$

Kutateladze evaluated K_1 for several liquids over a wide range of pressures and found its value to lie within the range 0.16 ± 0.03.

The equation found to correlate the critical superficial velocity in the present investigation is:

$$\frac{\dot{V}''_{CRIT}\rho_g^{\frac{1}{2}}}{\left[\sigma g_o g_{grav}\rho_f\right]^{\frac{1}{4}}} = 38\left(\frac{\rho_g}{\rho_f}\right)^{\frac{1}{4}}\left[\frac{(\sigma g_o)^{\frac{3}{4}}\rho_f^{\frac{1}{4}}}{\mu_f g_{grav}^{\frac{1}{4}}}\right]^{-.32}\left[\left(\frac{n}{A}\right)^{\frac{1}{2}}\left(\frac{\sigma g_o}{g_{grav}\rho_f}\right)^{\frac{1}{2}}\right]^{.16}$$

$$\left[\frac{(\sigma g_o \rho_g d_p)^{\frac{1}{2}}}{\mu_g}\right]^{-\frac{1}{2}} \qquad 8.11$$

A fresh examination of the boiling data is now made to find out if the constant, K_1 appearing in equation 8.10 is in fact a constant or if it is a function of the groups appearing on the right hand side of equation 8.11.

Borishanski [9] plotted the data of refs. 35, 38, 13 and 66 as K_1 versus N, where N is given by:

$$N \equiv \frac{(\sigma g_o)^{3/2}\rho_f}{g_{grav}^{\frac{1}{2}}\mu_f^2(\rho_f-\rho_g)^{\frac{1}{2}}} \quad .$$

His findings, reproduced here as Figure 8.6, show that the value of K_1 decreases as the liquid property group increases. Two alternative correlations were proposed by Borishansi, these are:

$$K_1 = 0.8N^{-.125} \qquad 8.12$$

and

$$K_1 = 0.13 + 4N^{-.4} \qquad 8.13$$

Although the latter form provides a better overall fit to the data, the former fits the data equally well in the range $10^4 < N < 10^6$, which is the range of N covered in the present investigation, and is in a more convenient form for making comparisons. The relation between K_1 and N,

evaluated for the present work, is seen from equation 8.11 to be:

$$K_1 = 0.37\ N^{-.16}$$

which agrees well with equation 8.12. of Borishanski. When making the above comparison, the substitution of $\rho_f - \rho_g$ for ρ_f in equation 8.11 was justified because ρ_g was always much less than ρ_f in the tests in the present work. In order to be strictly correct, however, equation 8.11 should contain an undetermined function of $\rho_f/(\rho_f - \rho_g)$.

An evaluation of the density ratio, ρ_g/ρ_f for the results used by Borishanski, exhibits a range represented by two orders of magnitude. It is concluded from this that, in the case of boiling, the quantity K_1 is independent of the density ratio. The term $(\rho_g/\rho_f)^{\frac{1}{4}}$ on the right hand side of equation 8.11 therefore represents a difference between the results of the present work and the corresponding result for boiling. It will be recalled, however, that the amount of data obtained in the region in which the critical superficial velocity was independent of the pore group (which presumably is the region in which to make comparisons with boiling) was limited to the results of four tests using different gases with grade C porous material (Figure 7.10). This is extremely scant evidence on which to base a result, and it may be that further tests in the 'pore-independent' region (for example at various

pressures) would yield a different result.

The bubble site density at the critical heat flux is seldom known and it is therefore difficult to assess whether or not an effect of $(\frac{n}{A})$ similar to that shown in equation 8.11 exists in boiling. However, it is generally found [53, 31, 6] that the surface finish (i.e. roughness) of the heat transfer surface does not influence the critical heat flux to any great extent. If it is accepted that the bubble site density is governed by the surface finish of the heater material, then it follows that the critical heat flux is almost independent of $(\frac{n}{A})$. In fair agreement with this, the results of the present work show only a slight dependence of the critical superficial velocity on $(\frac{n}{A})$ i.e. $\dot{V}''_{CRIT} \propto (\frac{n}{A})^{.08}$.

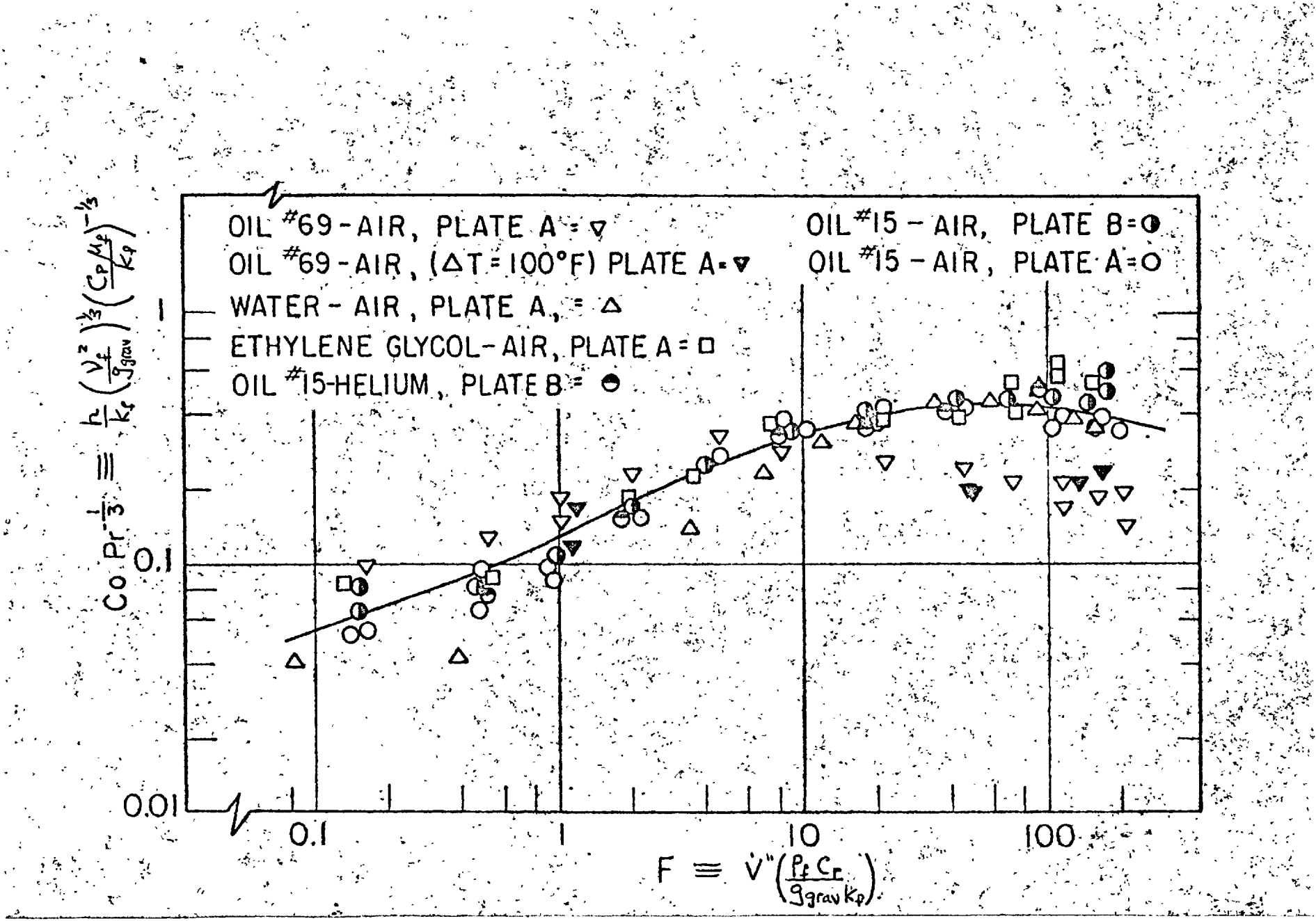

Fig.8.1 DIMENSIONLESS PLOT OF HEAT TRANSFER COEFFT. VERSUS SUPERFICIAL VELOCITY FROM REF [28] (GOSE et al.)

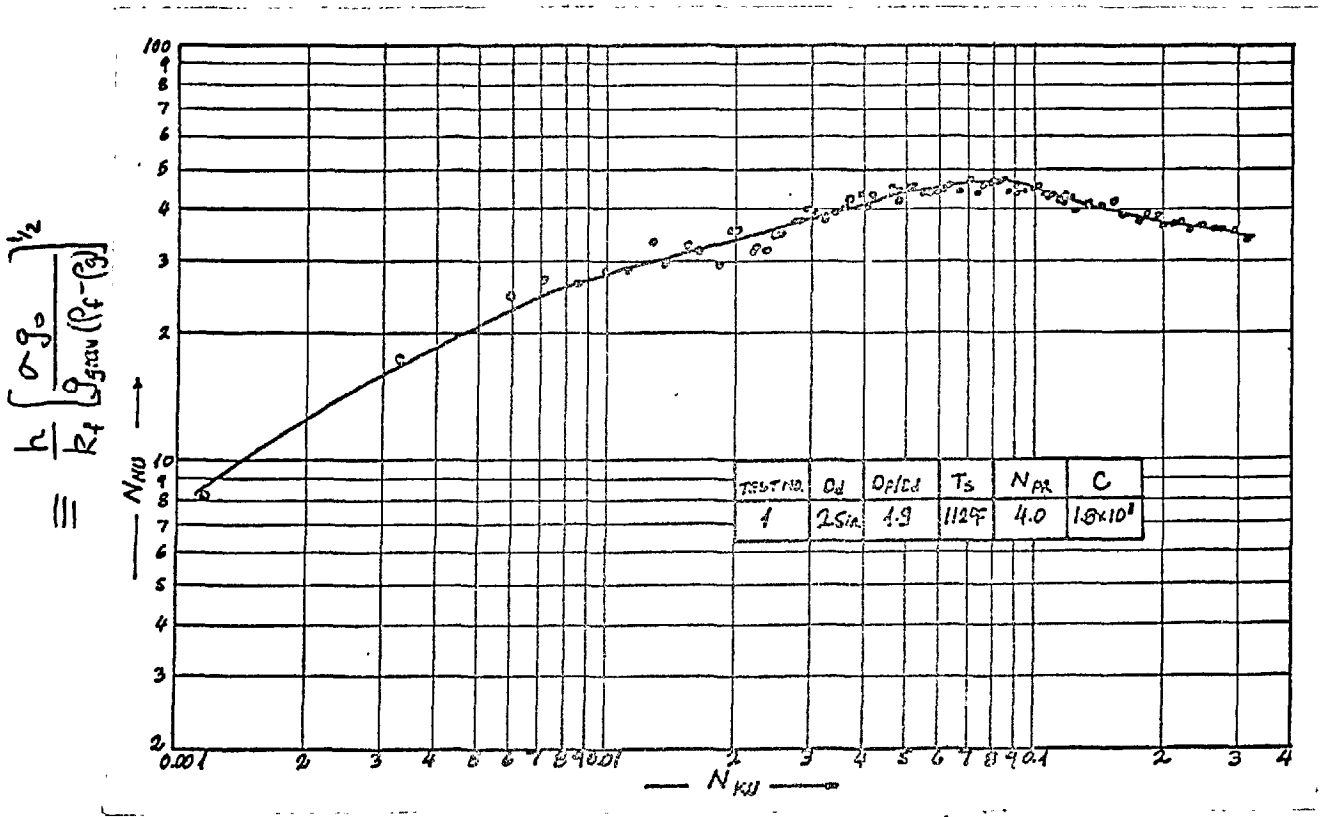

Fig. 8.2 DIMENSIONLESS PLOT OF HEAT TRANSFER COEFFT. VERSUS SUPERFICIAL VELOCITY -FROM REF [2] (AKTURK)

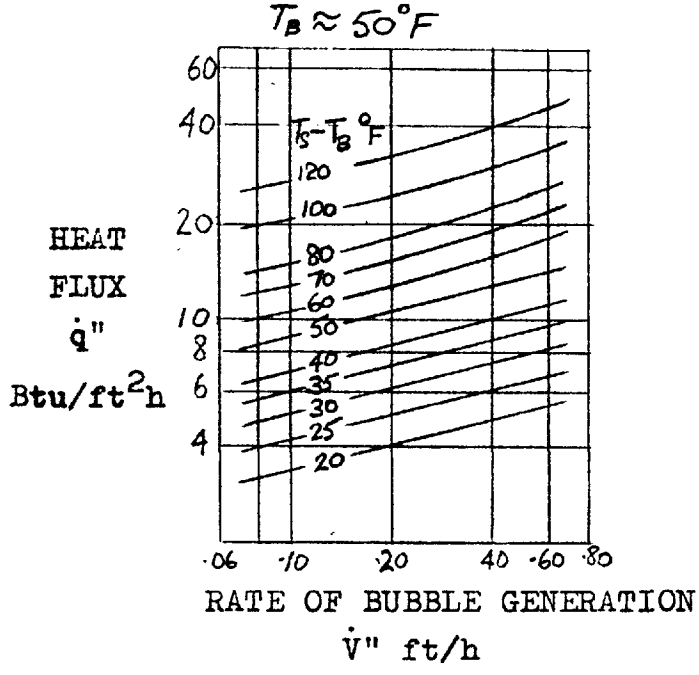

Fig. 8.3 EFFECT OF BUBBLE GENERATION ON HEAT TRANSFER TO NaOH SOLUTION-DATA OF MIXON et al [47]

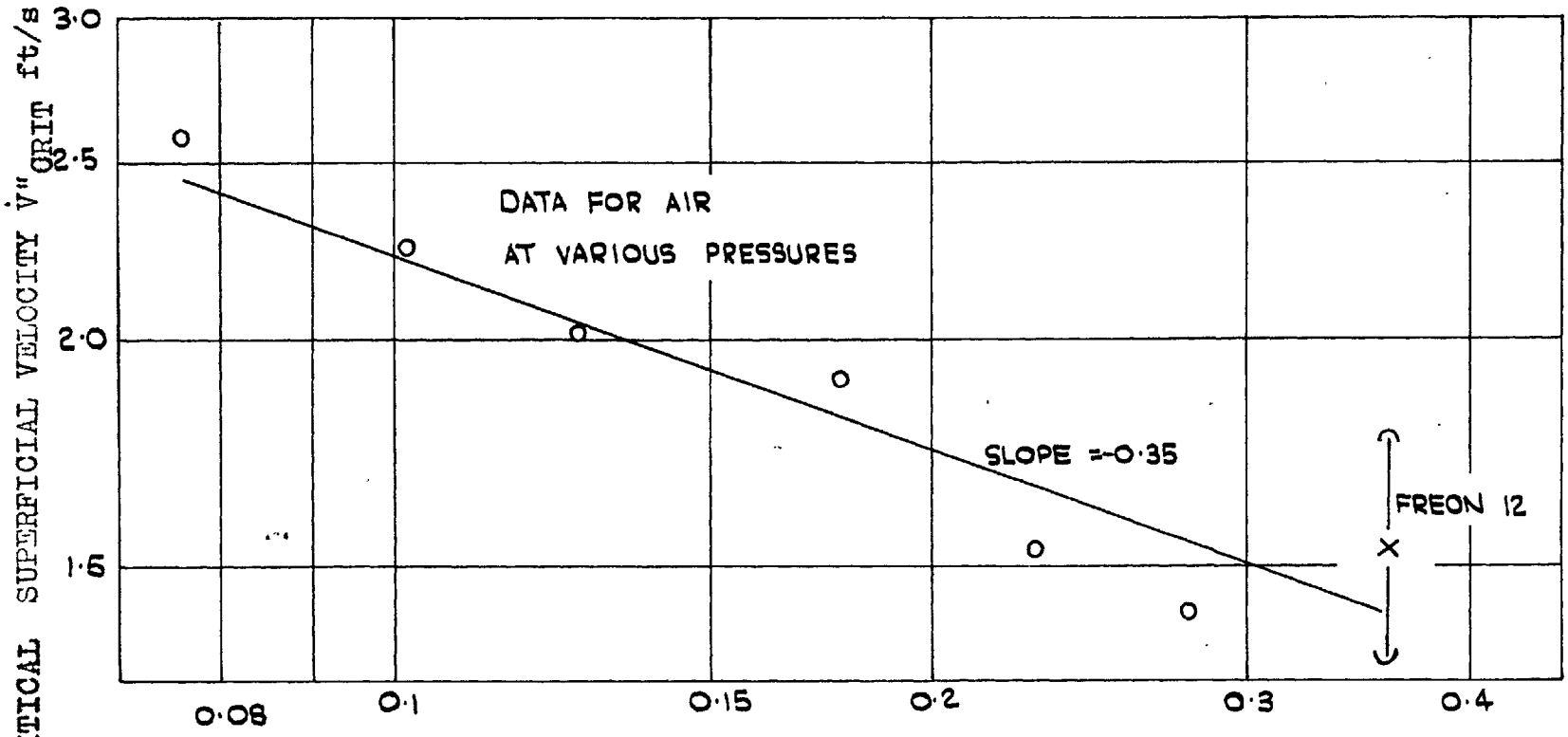

FIG. 8.4 VARIATION OF CRITICAL SUPERFICIAL VELOCITY WITH GAS DENSITY FOR THE DATA OF WALLIS [75]

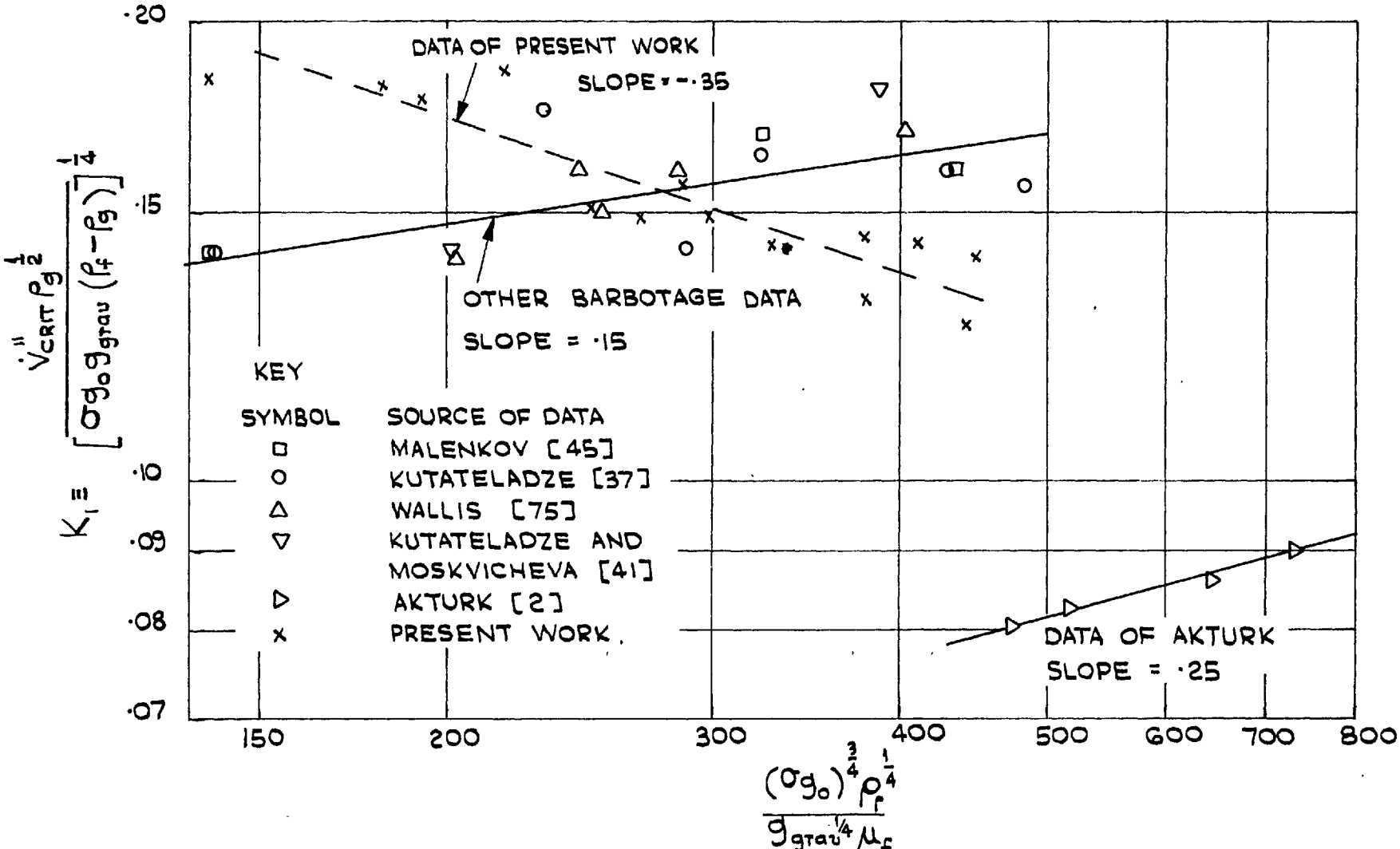

FIG. 8.5 VARIATION OF THE KUTATELADZE CONSTANT, K_1, WITH THE LIQUID PROPERTY GROUP - COMPARISON WITH OTHER BARBOTAGE RESULTS.

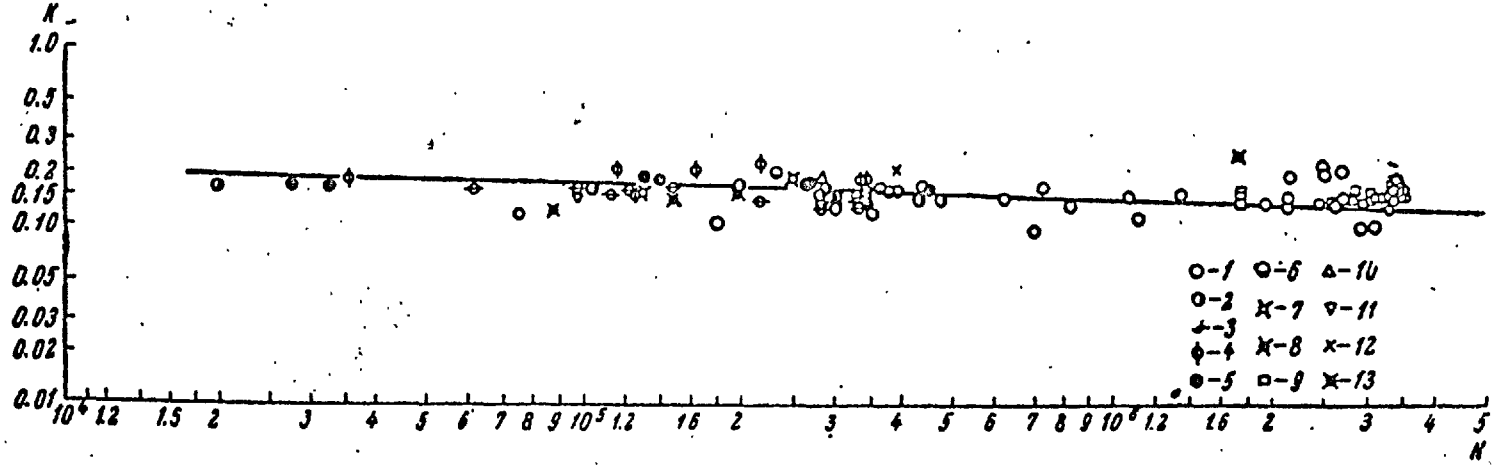

Fig. 1. Comparison of experimental data in the coordinates K and N. Line of formula $K = 0.8\,N^{-1/6}$.
1) Water 3; 2) benzene; 3) alcohol; 4) pentane; 5) pentane; 6) heptane; 7) propane; 8) propane 5; 9) water 4; 10) benzene; 11) alcohol; 12) heptane; 13) water 2.
1,10,11,12,13) Nichrome plate; 9) graphite plate (smooth); 2,3,4,5,6,7,8) chrome-plated copper plate; 2,5,6,8) experiments on a contaminated surface. The coefficient 1.15 introduced in [5] was used for comparison of data on clean and contaminated surfaces.

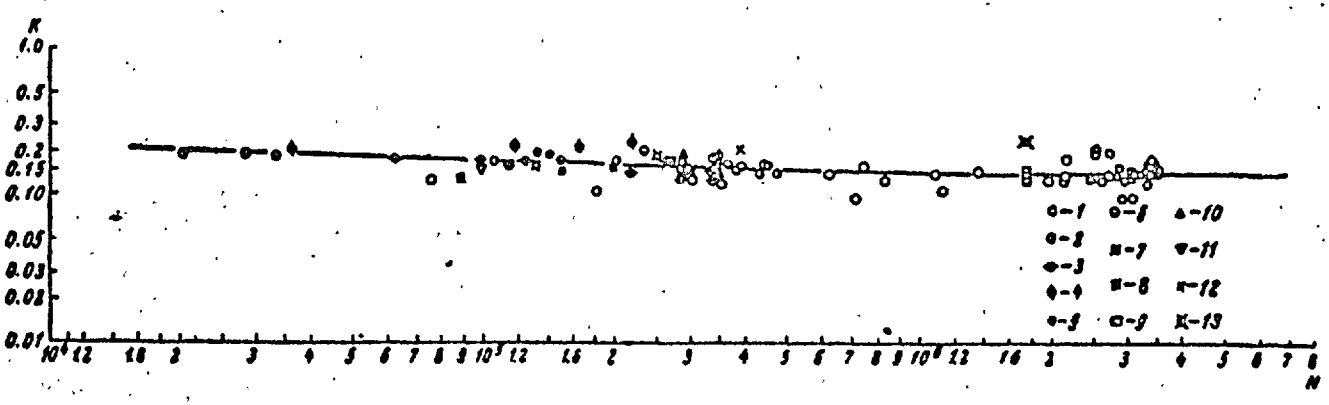

Fig. 2. Comparison of experiments with the line $K = 0.13 + 4N^{-0.4}$. All designations are the same as in Fig. 1.

Fig. 8.6 EFFECT OF LIQUID PROPERTIES ON K_1 -FROM REF [9] (BORISHANSKI.)

Chapter 9 Conclusions.

The following conclusions are drawn from the results of this investigation, and the comparisons made.

1. The electrolytic mass-transfer technique has proved a useful and convenient tool in the investigation of the convective and hydrodynamic phenomena associated with barbotage. It has enabled a large quantity of data to be amassed, covering many of the significant independent variables, a task which would have been forbidding in a similar heat-transfer investigation.

2. The relation between the sub-critical conductance and the superficial gas velocity was accurately predicted by the theoretical considerations (see section 7.3.1) which were used as a basis for the correlation of the sub-critical conductance.

3. In section 7.3.2, two regions were shown to exist for the sub-critical conductance. In one region, the conductance was influenced by the parameters governing the viscous flow of gas through the porous material i.e. gas properties and pore diameter. The dimensionless pore group, $\frac{(\sigma g_o \rho_g d_p)^{\frac{1}{2}}}{\mu_g}$ was found to characterise these effects. In the second region, the conductance was found to be independent of the dimensionless pore group. The criterion for the pore-controlled condition using the 'Porosint' porous material, was found to be a value of the pore group

of less than 100. Taking account of the results of tests with porous materials other than 'Porosint', however, the transition value of the pore group was shown in section 7.3.4 to be probably two or three times higher than 100.

4. Section 7.3.3 showed the dimensionless conductance to be proportional to the minus two thirds power of the Schmidt Number. Comparisons with other barbotage results suggest that the exponent of the Prandtl/Schmidt Number decreases with the order of magnitude of the Prandtl/Schmidt Number (see the table on page 159).

5. Nucleate boiling heat transfer results are not sufficiently well correlated at present, to permit any meaningful comparisons with the results of the pre~~vious~~sent work.

6. The maximum observed in the mass transfer coefficient, when plotted against the superficial gas velocity, is a result of a hydrodynamic crisis occurring in the two-phase boundary layer. It is similar to the crisis which occurs in boiling at the burn-out heat flux; this conclusion is supported by the close agreement of the Kutateladze constant evaluated for the critical data of the present work, with the values which have been found to apply in boiling burn-out.

7. A pore-controlled and a pore-independent region exist for the critical superficial velocity, though the transition from one region to the other was found to occur

(section 7.4.2) at a value of the pore group higher than in the case of the sub-critical conductance i.e. 300 compared with 100. The small amount of data obtained in the pore-independent region suggests that the critical superficial velocity is independent of the gas viscosity but proportional to the gas density to the minus one quarter power. This result agrees qualitatively with boiling results, though there is quantitative disagreement in the exponent of the gas density, the value of which is minus one half for the critical superficial vapour velocity in boiling. However, because of the limited amount of experimental evidence obtained in the pore-independent region, definite conclusions on this point are not justified; further experimentation is clearly needed.

8. The slight decrease in the dimensionless critical superficial velocity with the liquid property group, $\frac{(\sigma g_o)^{\frac{3}{4}} \rho_f^{\frac{1}{4}}}{g_{grav}^{\frac{1}{4}} \mu_f}$ (section 7.4.3), accords with the findings of Borishanski for the critical heat flux in boiling. A slight increase in the dimensionless critical superficial velocity with the liquid property group is indicated by the collected data of other barbotage investigations, though this slight trend could be attributed to the considerable scatter of the points which is in evidence. Further experimental results are needed, particularly at low values of the liquid property group, i.e. at high viscosities.

9. Bubble site density has only a small effect on the critical superficial velocity (section 7.4.5), a result comparable with the independence of the critical heat flux in boiling of the nucleating characteristics of the heat transfer surface.

10. Because of the many assumptions made, the equations presented for the maximum conductance (equations 7.22 - 7.24) are probably not as reliable as the correlations of the critical superficial velocity and the sub-critical conductance. However, it is considered that the equations obtained represent the best correlation which can be extracted from the experimental data available.

11. The conductance and the critical superficial velocity are influenced by the gross geometry of the system only below limiting values of certain dimensionless parameters (section 7.2); these parameters are those representing the dimensions of the liquid pool and the cathode.

12. The main value of this work lies in the contribution it makes towards understanding the mechanisms involved in boiling and burn-out, as indicated in the foregoing paragraphs. It is, however, also useful in its own right as a study of mass-transfer at a bubble-stirred interface, and in particular may be of interest to workers in the field of electrochemistry.

Notation.

		Equation or Section of first use.
A_p	Projected area of porous electrode, ft^2.	Eqn.6.5
C_d	Orifice discharge coefficient.	Eqn.6.4
C_p	Specific heat at constant pressure, Btu $lb^{-1}{}^{o}F^{-1}$.	Eqn.2.7
D_i	Diffusion coefficient of substance i, ft^2h^{-1}.	Eqn.2.6
d_{elec}	Diameter of porous electrode, ft.	Section 3.4
d_{or}	Diameter of orifice, ft.	Eqn.6.4
d_p	Pore diameter, ft.	Eqn.3.7
d_{pool}	Diameter of the liquid pool, ft.	Section 3.4
F	Faraday's Constant = 96,500 coulombs/grm equiv.	Eqn.2.2
ΔF_i	Standard free energy of activation, joules/grm mole.	Eqn.2.4
g_{grav}	Acceleration due to gravity, $ft.h^{-2}$.	Eqn.3.10
g_i	Mass transfer conductance, $lbft^{-2}h^{-1}$.	Eqn.2.1
g_o	Constant appearing in Newton's Second Law of Motion = $4.18x10^8$ lbft $lb_f{}^{-1}h^{-2}$.	Eqn.3.2
h	Depth of liquid pool, ft.	Section 3.4
h	Pressure differential across orifice, in. H_2O.	Eqn.6.3

h	Heat transfer coefficient, Btu $ft^{-2}h^{-1}{}^{o}F^{-1}$.	Eqn.8.1
h_{fg}	Latent heat of vaporisation, Btu lb^{-1}.	Eqn.8.8
I	Current density, amps ft^{-2}.	Eqn.2.2
K_1	Constant in Kutateladze's equation.	Eqn.8.9
k	Thermal conductivity, Btu $ft^{-1}h^{-1}\,{}^{o}F^{-1}$.	Eqn.2.7
k	Turbulent kinetic energy level, ft $lb_f lb^{-1}$.	Eqn.3.2
l	Length characteristic of the turbulence, ft.	Eqn.3.2
l	Characteristic length, ft.	Section 3.2.3
M_i	Molecular weight of substance i, gm/gm mole.	Eqn.2.2
m_i	Mass fraction of substance i.	Eqn.2.1
$\dot{m}''_i$	Mass flux of substance i, lb ft^{-2} h^{-1}.	Eqn.2.1
n	Number of electrons exchanger per reacting ion, grm equivalents/grm mole.	Eqn.2.2
n/A	Bubble site density, ft^{-2}.	Eqn.3.11
P	Pressure, $lb_f ft^{-2}$.	Eqn.3.1
ΔP_n	Bubble nucleation pressure difference $lb_f ft^{-2}$.	Eqn.A.2.8
ΔP_{TOT}	Total pressure drop across porous electrode, $lb_f ft^{-2}$.	Section A.2.5
$\dot{q}''$	Heat flux, Btu $ft^{-2}h^{-1}$.	Section 2.2
R	Gas constant, coulombs/grm mole ^{o}K.	Eqn.2.4

T	Temperature, ^{o}K.	Eqn.2.4
	^{o}R.	Section 2.2
t	Cathode thickness, ft.	Eqn.3.11
$\dot{V}$	Volume flow rate of gas, ft^3h^{-1}.	Eqn.6.3
$\dot{V}''$	Volume flow rate per unit projected area, ft h^{-1}.	Eqn.3.1
ΔV_{CATH}	Potential drop across the cathode ~ electrolyte interface, volts.	Eqn.2.4
v	Velocity vector at a point in the liquid, ft h^{-1}.	Eqn.2.6
$\dot{W}$	Work done by bubbles per unit time, ft $lb_f h^{-1}$.	Eqn.3.1
y	Distance normal to the electrode surface, ft.	Fig.3.1
δ	Specific gravity of dry gas relative to dry air.	Eqn.6.3
Γ	Mass exchange coefficient, lb $ft^{-1}h^{-1}$.	Section 3.11
θ	Bubble contact angle, degrees.	Eqn.3.7
μ	Viscosity, lb $ft^{-1}h^{-1}$.	Section 3.1.1
ρ	Density, lb ft^{-3}.	Eqn.2.7
σ	Surface tension coefficient, $lb_f ft^{-1}$	Eqn.3.7

Dimensionless groups

N_{Pr}	$\equiv \frac{\mu C_p}{k}$	Prandtl Number	Section 2.2
$N_{Re,OR}$	$\equiv \frac{4\dot{V}\rho_g}{\pi d_{OR}\mu_g}$	Orifice Reynolds Number	Eqn.6.4
N_{Sc}	$\equiv \frac{\mu}{D_i\rho}$	Schmidt Number	Section 2.2

Suffices.

b	bubble
CRIT	critical
e	effective
f	liquid
G	bulk liquid state
g	gas or vapour
i	ion species i
MAX	Maximum
o	upstream orifice conditions
s	liquid side of solid liquid interface
t	total turbulent.

Literature Cited.

1. Adams, J.M.

An analysis of the critical heat flux in nucleate boiling.

Preprint 131, AIChE Conference, Buffalow, N.Y. 1963.

2. Akturk, N.U.

Heat-transfer from a heated porous surface to a pool of liquid with gas injection at the interface.

Paper D.5 Symposium on two phase flow, Exeter, June 1965.

3. Batchelor, G.K.

The theory of homogeneous turbulence.

Cambridge University Press, 1953.

4. Bazan, J.C. and Arvia, A.J.

The diffusion of ferro- and ferricyanide ions in aqueous solutions of sodium hydroxide.

Electrochemica Acta, 10, 1025, 1965.

5. Beasant, W.R. and Jones, H.W.

The critical heat flux in pool boiling under combined effect of high acceleration and pressure.

AEEW - R275, 1963.

6. Berensen, P.J.

Transition boiling heat transfer from a horizontal surface.

M.I.T. Technical Report No.17, Mass., 1960.

7. Bird, R.B., Stewart, W.E. and Lightfoot, E.N.
Transport phenomena.
Wiley, 1962.

8. Bhand, S.E., Patgaonkar, G.V. and Gogate, D.V.
Convective heat transfer in weak electrolytes under the action of electrolytic currents.
Int. J. Heat and Mass Transfer, 8, No.1, 111, 1965.

9. Borishanski, V.M.
An equation generalising experimental data on the cessation of bubble boiling in a large volume of liquid.
Zhur. Tekh. Fiz., 26, 452, 1956. Translated in Soviet Physics-Technical Physics, 1, 438.

10. British Standards Institute
Flow Measurement.
B.S. 1042, 1943.

11. Chang, Y.P.
Some possible critical conditions in nucleate boiling.
Trans. ASME J. Heat Transfer, May, 39, 1963.

12. Chang, Y.P. and Snyder, N.W.
Heat transfer in saturated boiling.
Heat Transfer Conference, Storrs, 1960. Chem. Eng. Prog. Symposium, Series 56, No.30, 25, 1960.

13. Cichelli, M.T. and Bonilla, C.F.
Heat transfer to liquids boiling under pressure.
Trans. A.I.Che.E., 41, 755, 1945.

14. Clark, J.A. and Merte, H.

Nucleate, transition and film boiling heat transfer at zero gravity.

2nd Symposium Physics and Biol. Phenom., under Zero Gravity Conditions, L.A., 1963.

15. Cole, R.

A photographic study of pool boiling in the region of the critical heat flux.

A.I.Ch.E. Journal, 6, No.4, 533, 1960.

16. Costello, C.P. and Adams, J.M.

The interrelation of geometry, orientation and acceleration in the peak heat flux problem.

A.I.Ch.E. Journal, 9, No.5, 663, 1963.

17. Costello, C.P. and Tuthill, W.E.

Effects of acceleration on nucleate pool boiling.

Chem. Eng. Prog. Symposium Series 57, No.32,189, 1961.

18. Deissler, R.G.

Columbia University Heat Transfer Symposium, New York, 1954.

Original reference not obtained. Included in refs. 38 and 44.

19. Eisenberg, M., Tobias, C.W. and Wilke, C.R.

Ionic mass transfer and concentration polarisation at rotating electrodes.

J. Electrochem. Soc., 101, No.6, 307, 1954.

20. Eisenberg, M., Tobias, C.W. and Wilke, C.R.
Selected physical properties of ternary electrolytes employed in ionic mass transfer studies.
J. Electrochem. Soc., 103, No.7, 413, 1956.

21. Emmons, H.W.
Shear flow turbulence.
Proceedings 2nd Nat. Congress Appl. Mech., ASME, New York, 1954.

22. Eyring, H., Glasstone, S. and Laidler, K.J.
Application of the theory of absolute reaction rates to overvoltage.
J. Chem. Phys., 7, 1053, 1939.

23. Eyring, H., Marker, L. and Ting-Chang Kwoh
The theory of absolute reaction rates applied to the study of polarographic waves.
J. Phys. and Colloid Chem., 53, 1943, 1949.

24. Frea, W.J. et al.
Some experimental and analytical investigations on the critical heat flux in pool boiling.
A.I.Ch.E. Preprint 10. 8th National Heat Transfer Conference, L.A., 1965.

25. Fritz, W.
Berechnung des maximalvolumens von dampfblasen.
Physik. Zeits, 36, 379, 1935.

26. Gaertner, R.F.
Photographic study of nucleate pool boiling on a

horizontal surface.

Translated ASME, J. Heat Transfer, 87, 17, 1965.

27. Gerischer, H.

Bestimmung der Auslauschgeschwindigkeit beim Gleichgewichtspotential durch Polarisationsmessungen mit Gleich- und Wechselstrom.

Z. Electrochem 55, 98, 1951.

28. Gose, E.E., Acrivos, A. and Petersen, E.E.

Heat transfer to liquids with gas evolution at the interface.

Paper presented at the Mexico City meeting of the A.I.Ch.E., June, 1960.

29. Graham, R.W., Hendricks, R.C. and Ehlers, R.C.

Analytical and experimental study of pool boiling heating of liquid hydrogen over a range of accelerations

NASA TND - 1883, 1965.

30. Grassman, P., Ibl, N. and Trüb, J.

Electrochemische Messung von Stoffubergangszahlen.

Chem. Ing. Tech., 8, 529, 1961.

31. Griffith, P.

The correlation of nucleate boiling burnout data.

ASME Paper No. 57-HT-21. Heat Transfer Conference, University Park, Pa., 1957.

32. Gurinov, Y.S. and Gorbacher, S.V.

Effect of the electrolyte flow within wide velocity ranges on the electrical oxidation and reduction of the system. $K_3\left[Fe(CN)_6\right]/\ K_4\left[Fe(CN)_6\right]$.

Zhur. Fiz. Khim., 38, No.9, 2245, 1964.

33. Ivey, H.J.

Acceleration and the critical heat flux in pool boiling heat transfer.

Proc. Inst. Mech. Engineers, 177, No.1, 1, 1963.

34. Ivey, H.J.

Theoretical aspects of critical heat flux in saturation pool boiling.

AEEW - R104, 1961.

35. Kazakova, E.A.

Problems of heat exchange during changes of state.

Symposium, Water Power Institute, USSR, 1953.

36. Kimball, G.E.

The absolute rates of heterogeneous reaction.

J. Chem. Phys., 8, 199, 1940.

37. Kutateladze, S.S.

Heat and mass transfer and friction in turbulent boundary layers.

Novosibersk, 1964.

38. Kutateladze, S.S.

Heat transfer during boiling and condensation.

J. Tech. Phys., 20, 11, 1950.

39. Kutateladze, S.S.

Heat transfer in condensation and boiling. 1952.

Translated as U.S.A.E.C. Report AEC-tr-3770.

40. Kutateladze, S.S.

A hydrodynamic theory of changes in the boiling process under free convection conditions.

Irzv. Akad. Nauk. S.S.S.R. Otd. Tekh.Nauk, No.4, 529, 1951. Translated as U.S.A.E.C. Report, AEC-tr-1441.

41. Kutateladze, S.S., and Moskvicheva, V.N.

Hydrodynamics of a two-component layer as related to the theory of crises in the process of boiling.

Zh. Tek. Fiz., 29, No.9, 1135, 1959.

42. Levich, V.G.

Physico-chemical hydrodynamics.

Prentice-Hall, 1962.

43. Lin, C.S. et al.

Diffusion controlled electrode reactions.

Ind. Eng. Chem., 43, No.9, 2136, 1951.

44. Madsen, N.

Temperature fluctuations at a heated surface supporting pool boiling of water.

I. Mech. Engineers Symposium, Manchester, 1965.

45. Malenkov, R.G.

Critical phenomena in the bubbling and boiling processes.

Zh. Prik. Mek. Tek. Fiz., 6, 166, 1963. Translated as R.T.S. 2835.

46. Marcus, B.D.

Experiments on the mechanism of saturated nucleate pool boiling heat transfer.

Ph.D. thesis, Cornell University, 1963.

47. Mixon, F.O., Wan Yong Chon and Beatty, K.O.

The effect of electrolytic gas evolution on heat transfer.

Chem. Eng. Prog., 55, No.10, 49-53, 1959.

48. Moore, F.D. and Mesler, R.B.

The measurement of rapid surface temperature fluctuations during nucleate boiling of water.

A.I.Ch.E. J., 7, No.4, 620, 1961.

49. Prandtl, L.

Uber ein neues formelsystem fur die ausgebildete turbulenz.

Nachr. d. Akad. d. Wissensch. in Goltingen Math. und Phy. Klasse, 1945.

50. Rallis, C.J. and Jawurek, H.H.

Latent heat transport in saturated nucleate boiling.

International J. Heat and Mass Transfer, 7, No.10, 1051, 1964.

51. Reiss, L.P. and Hanratty, T.J.

Measurements of instantaneous rates of mass transfer to a small sink on a wall.

A.I.Ch.E.J., 8, No.2, 245, 1962.

52. Rogers, T.F. and Mesler, R.B.

An experimental study of surface cooling by bubbles during nucleate boiling of water.

A.I.Ch.E.J., 10, No.5, 656, 1964.

53. Seader, J.D., Miller, W.S. and Kalvinskas, L.A.

Boiling heat transfer for cryogenics.

NASA CR-243, 1965.

54. Séméria, R.

Les échanges thermiques en ébullition nucléée.

Extrait des Actes de la Semaine d'Information sur la transmission de la chaleur. Poitier, 1963.

55. Sharp, R.R.

The nature of liquid film evaporation during nucleate boiling.

NASA TND-1997, 1964.

56. Sherley, J.E.

Nucleate boiling heat transfer data for liquid hydrogen at standard and zero gravity.

Advances in Cryogenic Engineering, 8, 1963.

57. Shrier, L.L. and Smith, J.W.

Cathode polarisation potential during electro-deposition of copper. Pt 1, Non-reproducibility in acid copper sulphate solutions.

J. Electrochem. Soc. 98, No.5, 193, 1951.

58. Siegel, R., and Howell, J.R.

Critical heat flux for saturated pool boiling from

horizontal and vertical wires in reduced gravity.
NASA TND-3123, 1965.

59. Sims, G.E., Akturk, U.A. and Evans-Lutterodt, K.O.
Simulation of pool boiling heat transfer by gas injection at the interface.
Int. J. Heat and Mass Transfer, 6, 531, 1963.

60. Spalding, D.B.
Convective mass transfer.
Arnold, 1963.

61. Spalding, D.B.
Private communication to author. December 1965.

62. Spalding, D.B.
Some notes on the problem of correlating nucleate-boiling data.
Unpublished note, Imperial College, 1965.

63. Spalding, D.B. and Duffield, P.L.
Diffusion-controlled electrolysis with gas injection through the porous electrode.
Presented at the 3rd Int. Congress of Polarography, Southampton, 1964.

64. Stackelberg, M., Pilgrim, M. and Toome, V.
Bestimmung von Diffusionskoeffizienten einiger Ionen in wabriger Losung in Gegenwart von Fremdelektrolyten.
Z. Elektrochem. 57, 342, 1953.

65. Sterman, L.S.
On the theory of the heat transfer from a boiling

fluid.

Zhur. Tekh. Fizl., 23, (2), 341, 1953. Translated as C.T.S. No.62 (DSIR).

66. Styrikovich, M.A. and Poliakov, G.M.

The critical thermal load in the boiling of liquids in large volumes.

Izv. Akad. Nauk., SSSR, 5, 562, 1951. Translated as RAE No.873.

67. Trüb, J.

Eine elektrochemishe Methode zur Messung des Stoffubergangs.

Ph.D. Thesis, Zurich, 1960.

68. Usiskin, C.M. and Siegel, R.

An experimental study of boiling in reduced and zero gravity fields.

Trans. ASME J. Heat Transfer, 83, 243, 1961.

69. Van Shaw, P., Reiss, L.P., and Hanratty, T.J.

Rates of turbulent transfer to a pipe wall in the mass transfer entry region.

A.I.Ch.E.J., 9, No.3, 362, 1963.

70. Venczel, J.

Uber den Stofftransport en gasentwickelnden Electroden.

Ph.D. Thesis, Zurich, 1961.

71. Vogtlander, P.H. and Bakker, C.A.P.

An experimental study of mass transfer from a liquid

flow to wires and gauzes.

Chem. Eng. Sci., 18, 583, 1963.

72. Wallis, G.B.

A gas-liquid analogue of nucleate boiling.

Nuclear Power, 5, 99, 1960.

73. Wallis, G.B.

General correlations for the rise velocity of cylindrical bubbles in vertical tubes.

General Electric Report No.62GL130, 1962.

74. Wallis, G.B.

Some hydrodynamic aspects of two-phase flow and boiling.

Int. Dev. in Heat Transfer, Part II, ASME Paper 38, 319, 1962.

75. Wallis, G.B.

Two-phase flow aspects of pool boiling from a horizontal surface.

AEEW-R103, 1961.

76. Westwater, J.W.

Nucleate pool boiling.

Petro/Chem Engineer, August & September, 186 & 219, 1961.

77. Yamagata, K. et al.

Effect of air injection into water on heat transfer.

Kikaigakukai Rombunshu (Collected papers Soc. Mech. Engineers (Japan), 19, No.84, 4, 1953.

78. Zuber, N.

Hydrodynamic aspects of boiling heat transfer.

Thesis, University of California, 1959. U.S.A.E.C.

Report No. AECU-4439.

79. Zuber, N.

On the stability of boiling heat transfer.

Trans. ASME J. Heat Transfer, 80, 711, 1958.

80. Zuber, N.

Recent trends in boiling heat transfer research.

Pt. 1; Nucleate pool boiling.

Applied Mech. Rev., 17, 663, 1964.

81. Zuber, N. and Fried, E.

Two-phase flow and boiling heat transfer to cryogenic liquids.

Reprint ARS Journal, September, 1332, 1962.

82. Zuber, N. and Tribus, M.

Further remarks on the stability of boiling heat transfer.

AECU-3631, January 1958.

Appendix I. Calibration of Instruments.

A.I.1 The pen recorder.

The function of the pen recorder was to produce continuous traces of the ionic current through the cell, at each gas injection rate. Although basically an instrument for measuring potential difference, the recorder was arranged to record current by measuring the potential drop across a low resistance through which the ionic current was passed, as shown by the schematic diagram in Figure 4.3. The recorder and resistance were calibrated (as a unit) directly in milliamps by passing known currents (accurate to $\pm \frac{1}{2}\%$) through the resistance and noting the corresponding readings on the chart.

So as to take full advantage of the width of the recorder chart, the value of the resistance was adjusted, when necessary, to give a near full-scale deflection of the pen for the maximum ionic current of each test carried out. A calibration of the chart/resistance unit was performed each time the value of the resistance was changed. For these fairly frequent calibrations, only one calibration point was obtained at about 75% full-scale deflection on the recorder. At less frequent intervals, the linearity of the recorder was checked by calibrating the instrument at 5% intervals. The manufacturers of the recorder claim that it responds to a change in the input of .03%

of the full-scale reading. The accuracy with which a given current could be recorded was therefore governed by the accuracy of the calibrating procedure. This is estimated to be within $\pm \frac{1}{2}\%$.

A.1.2 The measuring orifice.

The function of the orifice was to measure the flow of gas to the porous electrode. Both the construction and the mounting of the orifice conformed with British Standard Specifications laid down in BS 1042 [10].

The calculations of flow rates were based on equation (5) (page 12) of the above reference. This equation may be written as:

$$\dot{V} = 90.5\ C_d \left(\frac{hP_o}{T_o \delta}\right)^{\frac{1}{2}} \qquad \text{A.I.1}$$

where $\dot{V}$ is the volumetric flow rate of gas ft^3/h at 14.7 lb/in^2 and 60^oF,

h is the pressure differential across the orifice, in.water,

P_o is the pressure upstream of the orifice in.Hg

T_o is the upstream temperature ^oR

δ is the specific gravity of dry gas relative to dry air

C_d is the discharge coefficient of the orifice.

The other factors appearing in equation (5) of BS 1042

are either included in the constant 90.5 or are negligible.

The discharge coefficient, C_d is a unique function of the Reynolds Number at the orifice.

$$\text{i.e. } C_d = f(N_{Re,OR}) \qquad \text{A.I.2}$$

The orifice Reynolds Number, $N_{Re,OR}$ is given by

$$N_{Re,OR} = \frac{4\dot{V}\rho_g}{\pi d_{OR}\mu_g} \qquad \text{A.I.3}$$

where ρ_g and μ_g are the gas density and viscosity at the upstream orifice conditions

d_{OR} is the orifice diameter (= $\frac{1}{8}$ in.).

To calibrate the orifice, values of the discharge coefficient, C_d and of the Reynolds Number were computed from equations A.I.1 and A.I.3 for the full range of Reynolds Numbers encountered in the investigation. Figure A.I.1 shows the variation obtained between C_d and $N_{Re,OR}$ for several calibrations carried out over a period of two years.

The gas flow rates in the calibration were measured with a soap bubble flow meter. This device consisted of a vertical glass tube six feet long and $3\frac{1}{2}$ inches in diameter, graduated from 0 to 10 litres. The gas flow to be measured was introduced in the bottom of the tube, where there was a shallow pool of soap solution. By careful positioning of the gas outlet into the soap

solution, plane, horizontal bubbles filling the full cross-section of the tube were produced which rose up the tube with the flow of gas. By measuring the time taken for a single bubble to sweep a given volume, indicated by the graduations on the tube, an accurate measurement of the gas flow rate at the temperature and pressure (atmospheric) of the bubble was obtained. Several different gases were used in the calibration, ranging in density from 0.00518 lb/ft^3 of hydrogen to 0.441 lb/ft^3 of freon 114, enabling the required range of Reynolds Number to be obtained.

The accuracy of the flow rate measurements using this method, judged by the reproducibility of three measurements taken for each flow rate, was probably better than 1%. Other inaccuracies occur in the measurement of the pressure differential, and of the upstream orifice pressure, resulting in a scatter of calibration points in Figure A.I.1 of around $\pm$ 2%.

A.I.3 The absorptiometer.

An absorptiometer was used to measure the concentration of the potassium ferricyanide in the electrolyte solution. This instrument relies on the light absorbing properties of a substance in solution. Light of a predetermined wavelength is projected through a sample of the solution contained in an optical cell. After passing through the solution, the light falls on a photoelectric

cell which measures the intensity of the light. By comparing the intensity of light transmitted by the solution with the intensity transmitted by the solvent alone, the amount of light absorbed by the solute is obtained. The instrument is designed to read the absorbance of the solute directly, indicated by a pointer on a scale.

Most solutes absorb light mainly in a particular waveband. Therefore, by selecting a wavelength at which the substance of interest (potassium ferricyanide in this case) has the greatest absorbance, the influence of other substances contained in the solution is minimised and often eliminated. In the present case, the instrument was set to operate at a wavelength of 410 $m\mu$. At this wavelength, the absorbance of potassium ferricyanide is a maximum whereas the absorbance of potassium ferrocyanide and sodium hydroxide are negligible.

To calibrate the instrument for the measurement of concentration of the potassium ferricyanide, the absorbances of several accurately made-up solutions were measured and a calibration chart of concentration against absorbance was prepared. This chart is shown as Figure A.I.2.

The accuracy of this method of measuring the concentration is estimated to be $\pm$ 1%, this being the accuracy with which the scale on the absorptiometer could be read.

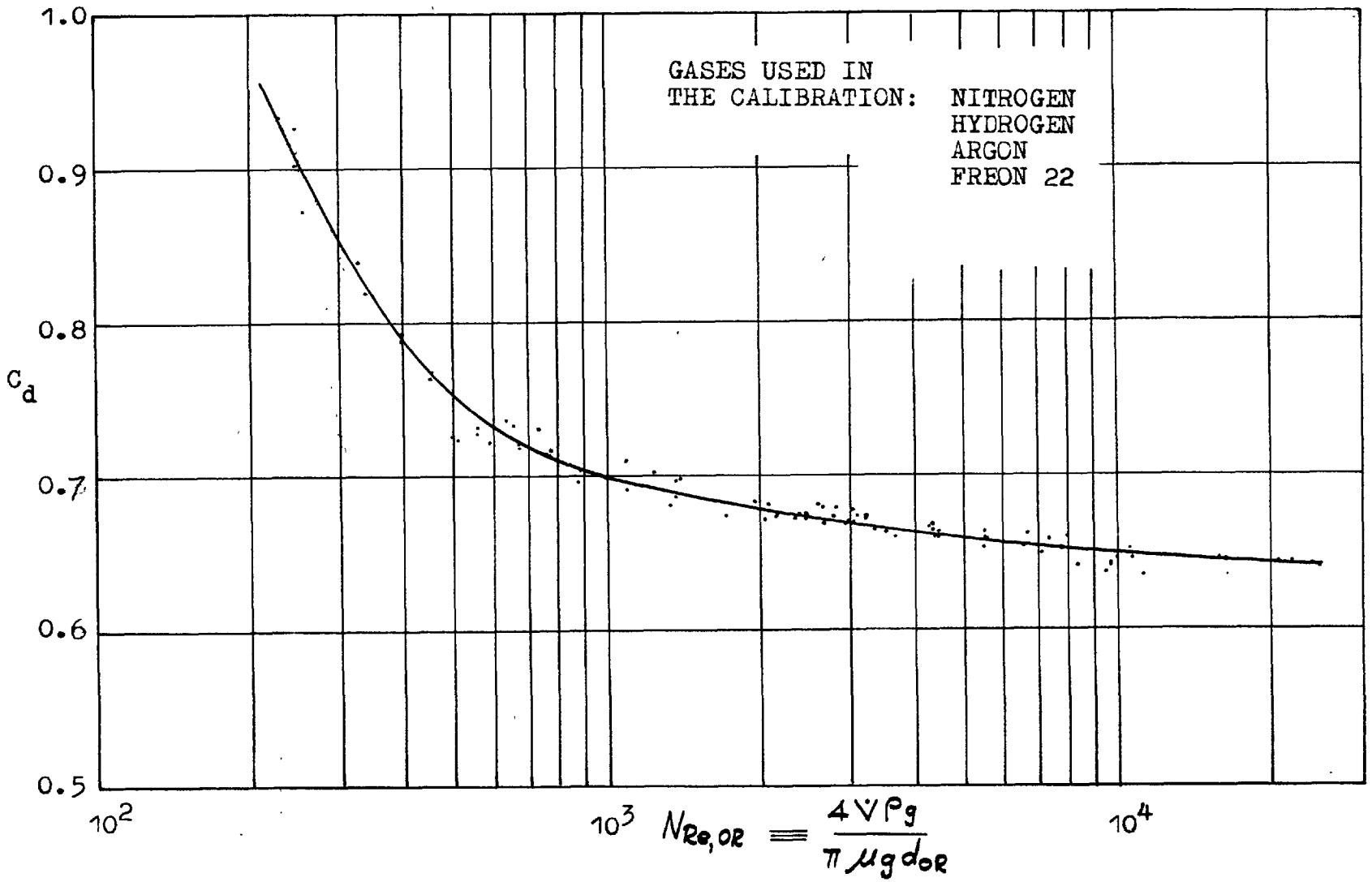

Fig. A.1.1 CALIBRATION CHART FOR $\frac{1}{8}$-IN. DIA. ORIFICE

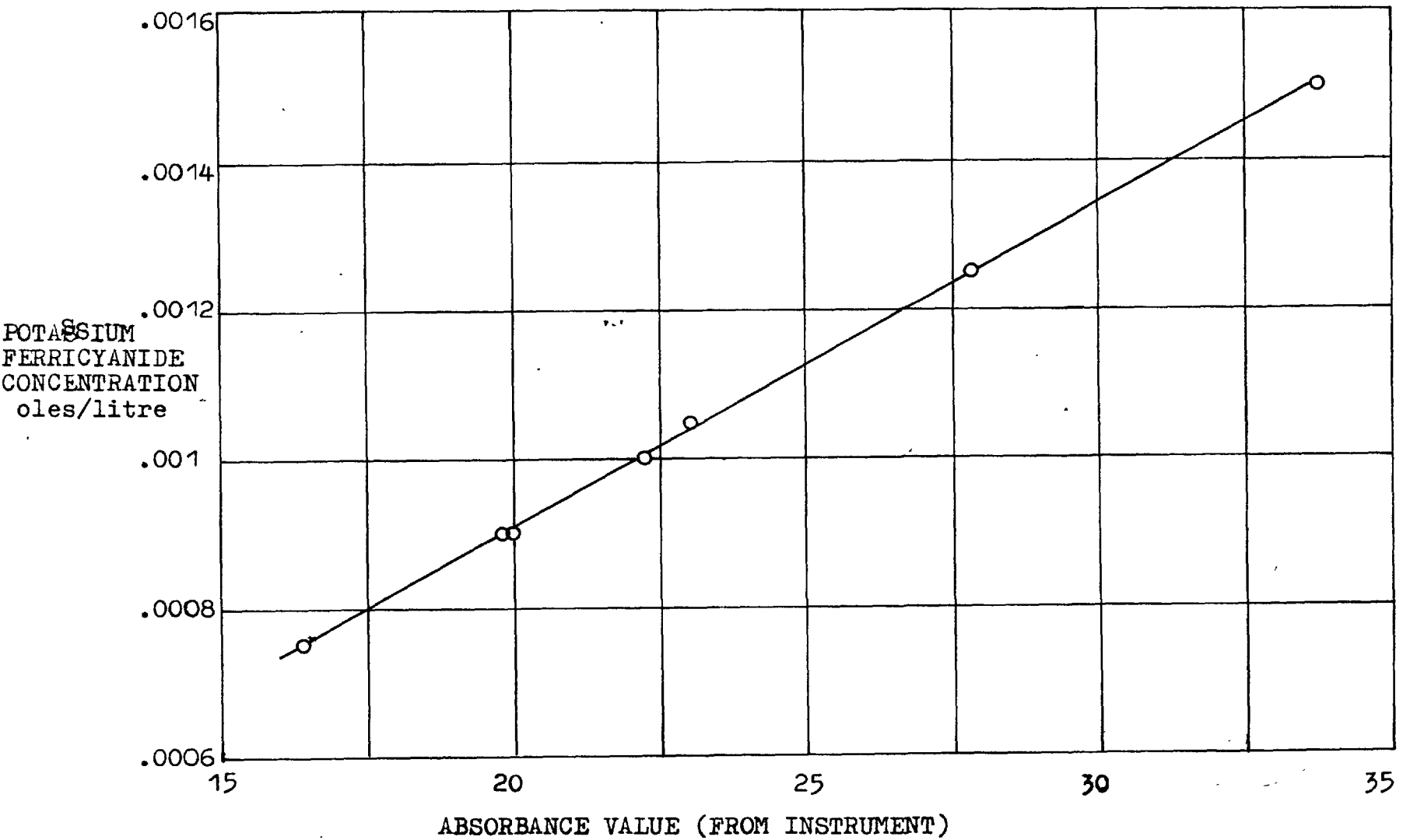

Fig. A.1.2 CALIBRATION OF THE ABSORPTIOMETER

Appendix II. Measurements of gas, liquid and geometrical properties.

A.II.1 Measurement of gas density.

The measurements of gas properties were necessary because the exact compositions of some of the gas mixtures used were unknown. A gas density vessel, comprising a spherical glass container fitted with two glass cocks was used for the density measurements. The following procedure was adopted.

The glass vessel was flushed and filled with each gas in turn, and then accurately weighed on a chemical balance. Before closing both cocks of the vessel, care was taken to ensure that the temperature and pressure inside the vessel were equal to those of the surrounding air. From the weight of the vessel filled with air and with water, the weight and the volume of the vessel were calculated. It was then a simple matter to calculate the density of each gas by subtracting the weight of vessel from weight of vessel plus gas and dividing by the volume.

The estimated accuracy of this method is from 2% for hydrogen to better than 1% for the heavier gases.

Table 5.1.2 shows the measured densities of the various gases used.

A.II.2 Measurement of gas viscosity.

Figure A.II.1 shows the apparatus used to measure

the viscosities of the various gases. With both valves A and B open, the gas was introduced under pressure at the point shown. When the water level in the burette reached a predetermined point, both valves were closed. Valve B was then opened and the time was measured for 20 ccs of gas to flow through the capillary tube under the pressure of the displaced water. The viscosity of the gas was proportional to the time taken. Several measurements were made with each gas until a reproducible value was obtained. The temperature of the gas was also measured.

Air was used to calibrate the apparatus since its viscosity is known accurately at all temperatures. The viscosity of the gases were calculated from the equation:

$$\mu_{GAS} = \mu_{AIR} \frac{t_{GAS}}{t_{AIR}}$$

where t is the time taken for the 20 ccs of gas to flow through the capillary tube.

The Reynolds Number of the flow through the capillary tube was calculated to ensure that the flow was laminar in all cases.

It was found that the viscosities measured for repeated tests varied by less than 1%. This value is taken to be the accuracy of the viscosities.

Some of the tests in the investigation using mixtures of hydrogen and nitrogen were performed at a time when the

facility for measuring gas viscosity was not available. In these cases, the viscosities were calculated from the following formula obtained from ref. 7 .

$$\mu_{MIX} = \sum_{i=1}^{n} \frac{x_i \mu_i}{\sum_{j=1}^{n} x_j \varphi_{ij}}$$

where $$\varphi_{ij} = \frac{1}{\sqrt{8}} \left(1+\frac{M_i}{M_j}\right)^{-\frac{1}{2}} \left[1+\left(\frac{\mu_i}{\mu_j}\right)^{\frac{1}{2}} \left(\frac{M_j}{M_i}\right)^{\frac{1}{4}}\right]^2$$

x_i is the mole fraction of i

μ_i is the viscosity of i

M_i is the molecular weight of i.

This formula was checked against some measured values of viscosity for hydrogen/nitrogen mixtures. The calculated values were between 3% and 6% higher than the corresponding measured values; this discrepancy might be explained by inaccuracies in the quoted composition of the gas mixtures.

The values of the viscosities of all the gases used are shown in Table 5.1.2.

A.II.3 Measurement of liquid properties.

The following properties of the electrolytic solution were measured:

(i) density

(ii) viscosity

and (iii) surface tension coefficient.

These measurements have been grouped together in one section since standard techniques, which require no description, were used in the three cases. The Table A.II.1 below shows the apparatus or method used for measuring each property, the calibrating liquid and the estimated accuracy.

Table A.II.1

Property measured	Apparatus or method used	Calibrating liquid	Estimated accuracy
Density	Hubbard specific gravity bottle	Water	Better than ± .05%
Viscosity	Standard U-tube viscometers	Glycerol	± .2%
Surface tension	Capillary rise	Water	± .5%

Measurements were made at various temperatures within the range 60-115°F for a constant NaOH concentration of 8% by weight and at various NaOH concentrations within the range 2 to 23% (0.5M to 7M) for a constant temperature of 77°F. The measuring equipment was located in a viscometer bath, ensuring temperature control to within ± 0.1°F of the required temperature. The NaOH concentration of each test solution was measured with an accuracy of ± 0.25% by titration against a standard hydrochloric acid solution.

Figures 5.3 and 5.1 show the variations of the liquid properties with temperature and with NaOH concentration.

The actual measured values of the liquid properties are given in Tables A.II.2 and A.II.3 at the end of this Appendix.

A.II.4 Measurement of diffusion coefficient.

There are considerable discrepancies in the values of the diffusion coefficient of potassium ferricyanide in sodium hydroxide solution which are quoted in the literature (see Figure A.II.4). There is also an absence of data giving the variation of the diffusion coefficient with temperature and with sodium hydroxide concentration. This absence of reliable data made it necessary to measure these variations before interpreting the results of the present work.

The method employed was similar to that of Stackelberg et al. [64] and makes use of the known solution to the ion mass transfer equation for the case of zero convection and zero migration with known boundary conditions.

A.II.4.1 Theory of the method.

Mass Conservation Equation.

The mass conservation equation of an ion species i, in the absence of electrical migration (previously equation 2.6) is:

$$\frac{\partial m_i}{\partial t} + V.\nabla m_i = D_i \nabla^2 m_i \qquad \text{A.II.1}$$

where m_i is the mass fraction of i

V is the velocity vector at the point considered

D_i is the diffusion coefficient of i.

For the case of (i) zero convection and (ii) diffusion in the y direction only, equation A.II.1 reduces to:

$$\frac{\partial m_i}{\partial t} = D_i \frac{\partial^2 m_i}{\partial y^2} \qquad \text{A.II.2}$$

which is Fick's 2nd law of diffusion.

This equation can be solved exactly for given boundary conditions.

Boundary conditions.

Consider the case of an electrode, initially at the same potential as the surrounding electrolyte in which there are no concentration gradients or convection currents. At time t=0, a potential is applied between the considered electrode and another larger electrode also immersed in the electrolyte. The resulting electrode reaction, involving the ion species, i is assumed to be so fast that the surface concentration of i, $m_{i,s}$ falls immediately to a value much lower than the bulk concentration, $m_{i,G}$. These boundary conditions may be written as:

$t = 0, \quad y > 0, \quad m_i = m_{i,G}$

$t \geq 0, \quad y = \infty, \quad m_i = m_{i,G}$

$t > 0$, $y = 0$, $m_i = m_{i,s} = 0$ compared with $m_{i,G}$.

Solution of the diffusion equation.

The solution to equation A.II.2 using the above boundary conditions is:

$$m_i = m_{i,G} \operatorname{erf}\left(\frac{y}{2\sqrt{D_i t}}\right)$$

Therefore the gradient at the wall is:

$$\left(\frac{\partial m_i}{\partial y}\right)_s = m_{i,G} (\pi t D_i)^{-\frac{1}{2}} \qquad \text{A.II.3}$$

The wall gradient, $\left(\frac{\partial m_i}{\partial y}\right)_s$ is related to the current density, I by:

$$I = \frac{nF}{M_i} \dot{m}_i'' = \frac{nF}{M_i} D_i \rho_f \left(\frac{\partial m_i}{\partial y}\right)_s \qquad \text{A.II.4}$$

where $\dot{m}_i''$ is the mass flux of i per unit time

n is the number of electrons exchanged per ion during the reaction

F is the Faraday constant

ρ_f is the electrolyte density

M_i is the molecular weight of the reacting ions.

From relations A.II.3 and A.II.4, an expression for the diffusion coefficient in terms of measurable quantities is obtained, i.e.

$$D_i = \left(\frac{IM_i}{nF\rho_f m_{i,G}}\right)^2 \pi t \qquad \text{A.II.5}$$

For the diffusion of potassium ferricyanide ions, $M_i = 211.95$ and $n = 1$ grm equivs./mole and equation A.II.5 becomes:

$$D_i = 0.958 \times 10^{-3} \left(\frac{I}{\rho_f M_{i,G}}\right)^2 t \quad ft^2/h \qquad \text{A.II.6}$$

where the units of I are amps/ft^2

of ρ_f are lb/ft^3

and of t are hours and $m_{i,G}$ is a dimensionless mass ratio.

Practical requirements.

The condition of zero convection is realised only if natural convection due to concentration gradients is avoided. For the reduction of potassium ferricyanide to potassium ferrocyanide, natural convection is avoided by using a horizontal, upward-facing plane cathode, since the ferrocyanide liberated at the cathode increases the solution density near the surface.

The 'one-dimensional' assumption is valid for the first few minutes of the reaction, when the diffusion layer thickness is small compared with the size of the electrode. (e.g. at t=300 secs, $\delta_D \approx .01$ ins.)

A.II.4.2 Apparatus.

The cell and electrical equipment used in the gas injection tests were employed in the diffusion coefficient measurements. The porous cathode was replaced by a finely polished solid nickel disc which was sealed into the base of the cell. A plastic tube, connected to a supply of high pressure nitrogen, projected down into the electrolyte solution to provide a means of stirring the liquid.

The concentrations of both the potassium ferricyanide and the potassium ferrocyanide used in the tests was 0.001M.

A.II.4.3 Procedure.

Both electrodes were cleaned in 50% hydrochloric acid and reduced together for one hour as described in Chapter 5. The electrolyte solution was introduced into the cell and brought to the required temperature by the heater and thermostat. Stirring of the liquid (by means of the nitrogen bubbles) was continued for a total period of about 20 minutes after the required temperature was reached, to ensure the complete elimination of concentration gradients in the solution. This was followed by a further period of about 20 minutes during which the solution was allowed to come to complete rest.

Having thus achieved the necessary initial conditions, a switch connecting the electrodes in the cell to the

potential source and current measuring circuit was closed; the pen recorder was simultaneously switched on.

The current was recorded for a period of five minutes, during which time the temperature of the solution was noted. A sample of the solution was taken for analysis to determine the potassium ferricyanide and the sodium hydroxide concentrations.

Tests were performed at several values of the applied potential difference to determine the range in which the current was diffusion-controlled, i.e. independent of the potential difference.

Measurements of the diffusion coefficient were made at various temperatures within the range 60-115°F for a constant NaOH concentration of 7.5% by weight and at various NaOH concentrations within the range 2 to 23% (0.5M to 7M) for a constant temperature of 77°F.

A.II.4.4 Results.

Figures A.II.2 and A.II.3 show the experimentally determined values of the diffusion coefficient plotted against temperature and against NaOH concentration. Included on Figure A.II.4, for purposes of comparison, are the values obtained by other workers.

The reproducibility of the values obtained using this method is illustrated by the small amount of scatter

($\pm 1\frac{1}{2}\%$) shown in Figure A.II.2. Comparisons with values obtained by other workers [20, 4, 69, 30], shown in Figure A.II.3, indicate differences between the various values of up to 10%. It is concluded that although the variations of diffusion coefficient with temperature and with NaOH concentration, measured by the present method are accurate, the absolute values may be in error by as much as $\pm$ 10%.

The actual measured values of diffusion coefficient are included in Tables A.II.2 and A.II.3 at the end of this Appendix.

A.II.5 Measurement of the pore diameter.

For each porous electrode material, a maximum and a minimum pore diameter were estimated from pressure drop measurements taken during barbotage. Figure A.II.4 shows a typical variation of the pressure drop across a porous electrode with superficial velocity during barbotage. The method used for estimating the pore diameters from the pressure drop curve was as follows:-

It was assumed that the total pressure drop ΔP_{TOT} across the porous electrode was the sum of a frictional pressure drop through the porous material, and the nucleation pressure drop ΔP_n of the smallest active pore. The frictional pressure drop is given by the Darcy equation and is proportional to the gas flow rate through the pores;

the nucleation pressure drop is given by:

$$\Delta P_n = \frac{4\sigma}{d_p} \sin\theta \qquad \text{A.II.8}$$

where d_p is the effective diameter of the smallest active pore

θ is the contact angle of the gas/liquid interface on the mouth of the pore.

On the basis of these assumptions, the form of the pressure drop curve in Figure A.II.4 can be explained. The first bubble occurs when the total pressure drop is equal to the nucleation pressure drop of the largest pore ($\dot{V}'' \approx 0$). As ΔP_{TOT} is further increased, so a greater number of progressively smaller pores become active until eventually the smallest potentially active pore is activated. At this point, the nucleation pressure drop reaches a maximum constant value and the total pressure drop becomes proportional to the superficial velocity of the gas. This linear region is clearly evident in Figure A.II.4.

The two limiting values of the nucleation pressure drop were estimated from the pressure drop curve, as indicated in Figure A.II.4. The maximum and minimum values of the pore diameter, were computed from equation A.II.8 for a contact angle of 90^o.

Table A.II.4 shows the two values of the pore diameter for each of the porous materials tested. In the analysis

of the experimental data in Chapter 7, the arithmetric mean of the two values was employed.

Table A.II.4 Values of the pore diameters.

Material	$d_{p,min.}$ microns	$d_{p,max.}$ microns
Porosint	15.3	18.1
Pall C	19.3	221
Pall D	82.4	106
Pall E	47.7	58.4
Pall F	26.1	29.2
Intern. Nickel	21.8	23.8

A.II.6 Measurement of bubble site density.

The second quantity used to characterise the grade of porous material was the maximum bubble site density, $(\frac{n}{A})$. A photographic method was used to estimate this quantity for each of the six porous materials used; a description of the procedure follows.

Photographs were taken of the surface of the porous material, through which nitrogen was injected into a very shallow pool of liquid. The liquid used was a mixture of water and alcohol which was chosen because of its non-foaming properties. The best results were obtained by keeping the depth of the liquid pool as shallow as possible but maintaining a sufficient depth to prevent the liquid

from being blown off the porous surface by the injected gas. Enlarging the photographs to 10 times the actual size of the surface allowed the number of active sites to be counted fairly easily. A typical enlarged photograph is shown in Figure A.II.5.

Photographs were taken at five superficial velocities in the range 0.1 $\dot{V}''_{CRIT}$ to 1.0 $\dot{V}''_{CRIT}$ for each of the porous materials. Measurements were taken at various superficial velocities to ensure that the active site density in the region of profuse nucleation was obtained.

Table A.II.5 shows the measured values of the maximum bubble site density for the various materials.

Table A.II.5 Values of bubble site density.

Material	Max. n/A ft^{-2}
Porosint	27,000
Pall C	2,000
Pall D	6,900
Pall E	10,000
Pall F	14,400
International Nickel	11,500

Table A.II.2 Measured values of liquid properties of 2M sodium hydroxide solution at various temperatures.

Temperature ^{o}F	Density lb/ft^3	Viscosity lb/fth	Surface tension lb_f/ft	Diffusion coefft. of ft^2/h
64.9	67.618	4.070	5.310×10^{-3}	
77.3	67.328	3.427	5.242	
87.4	67.290	3.025	5.208	
97.4	67.166	2.696	5.125	
106.7	67.015	2.435	5.084	
114.7	66.887	2.243	5.043	
68				1.783×10^{-5}
68.5				1.710
68.6				1.776
71				1.804
72.2				1.878
77				1.975
82.5				2.135
82.8				2.090
83.6				2.140
91.2				2.33
91.5				2.36
91.8				2.32
92.8				2.405
100.2				2.58
100.2				2.66
100.8				2.59

Table A.II.3 Measured values of liquid properties of sodium hydroxide solution at various concentrations and 25°C

Concentration Moles/litre	w/w	Density lb/ft^3	Viscosity lb/fth	Surface tension lb_f/ft	Diffusion coefft. ft^2/h
0.4953	.01942	63.601	2.464	4.947×10^{-3}	2.62×10^{-5}
0.621	.0242				2.58
1.350	.05123		2.960	5.126	
2.015	.0750	67.328	3.427	5.242	1.975
2.766	.09985		4.349	5.356	1.63
3.498	.1233		4.876	5.494	
3.910	.1360				1.23
4.815	.1631	73.648	6.926	5.722	.955
7.040	.2255	77.902	12.511	6.133	.577

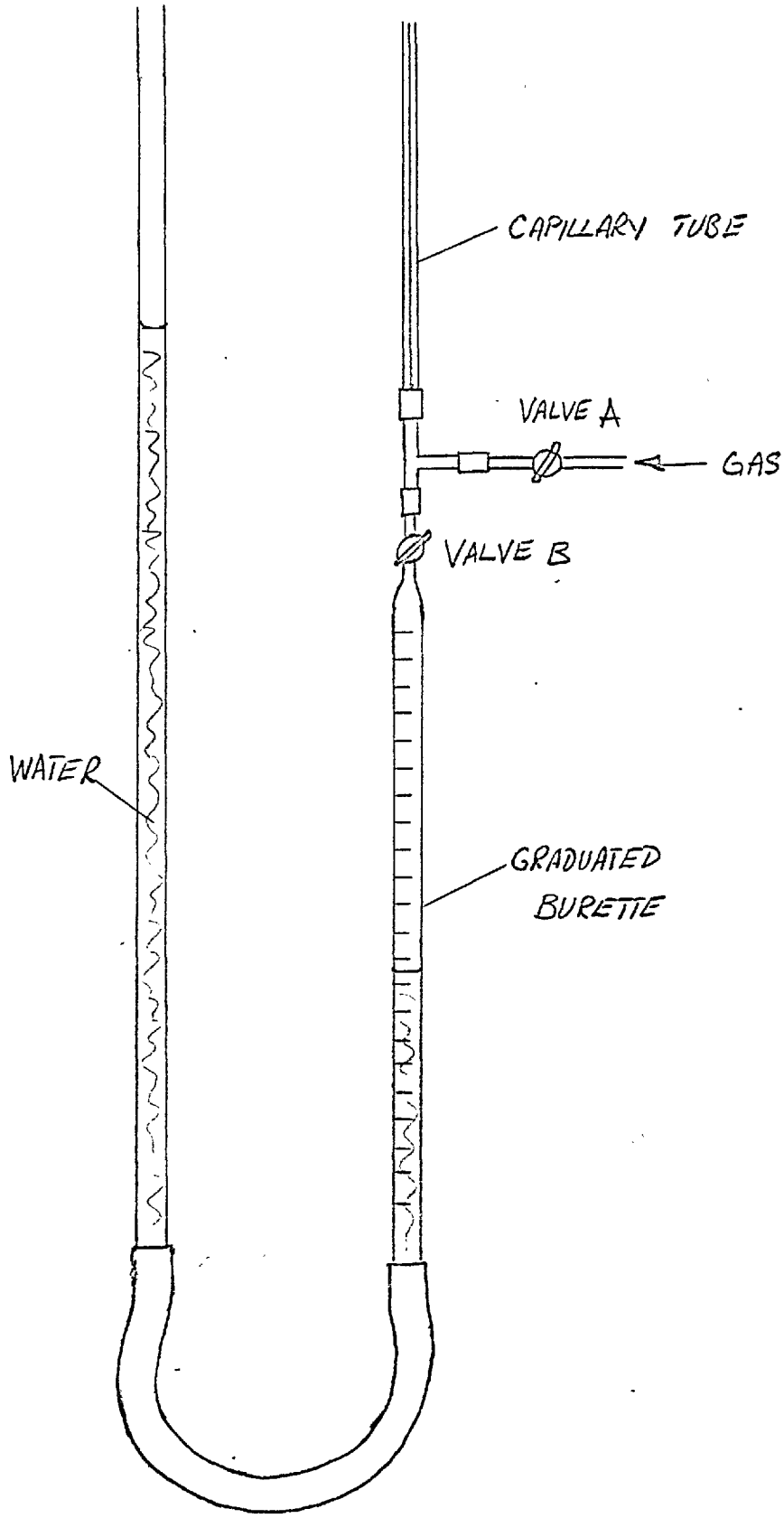

Fig.A.2.1. APPARATUS USED IN GAS VISCOSITY MEASUREMENTS

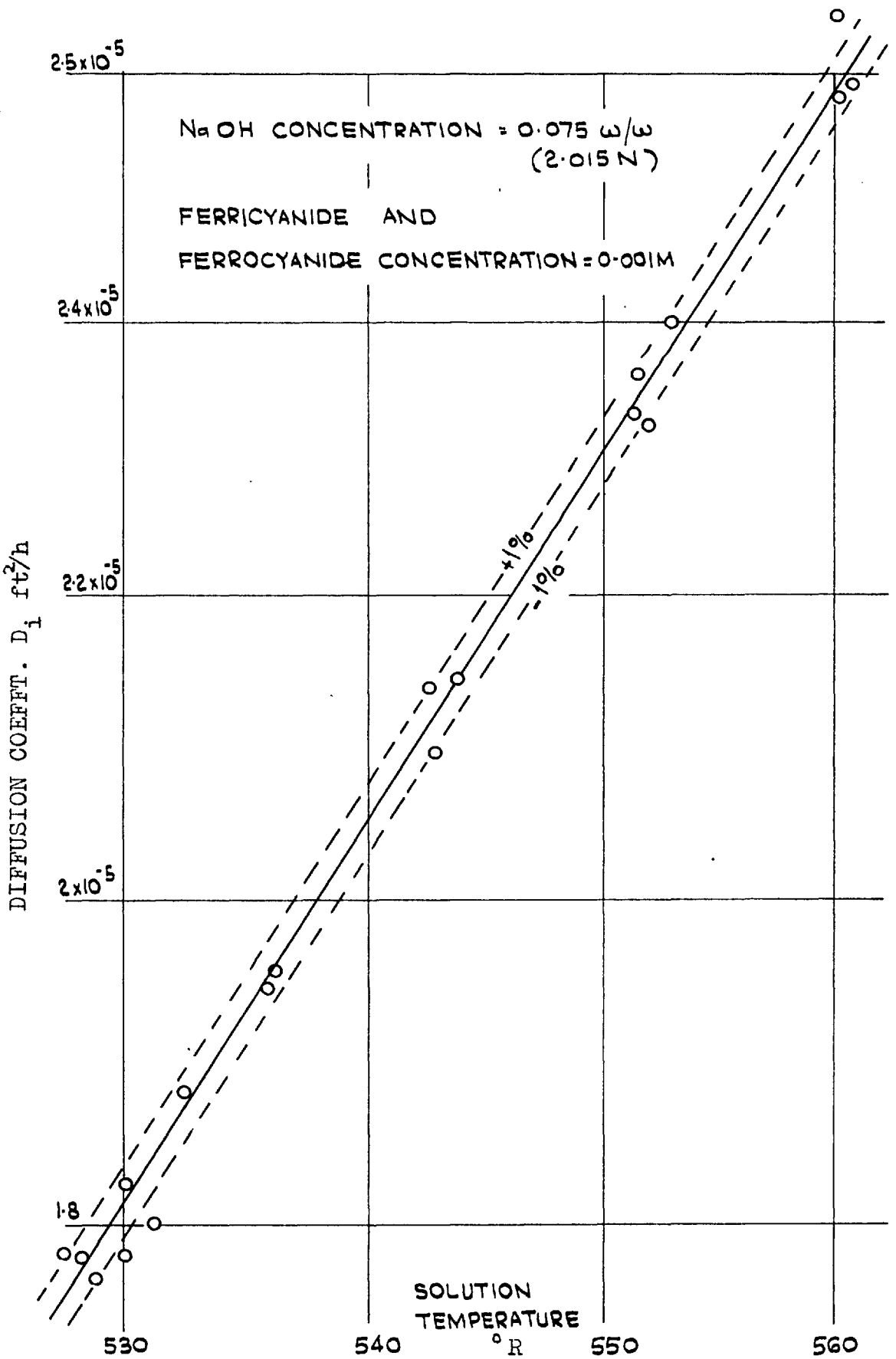

Fig. A.2.2 MEASURED VALUES OF DIFFUSION COEFFT VERSUS TEMP.

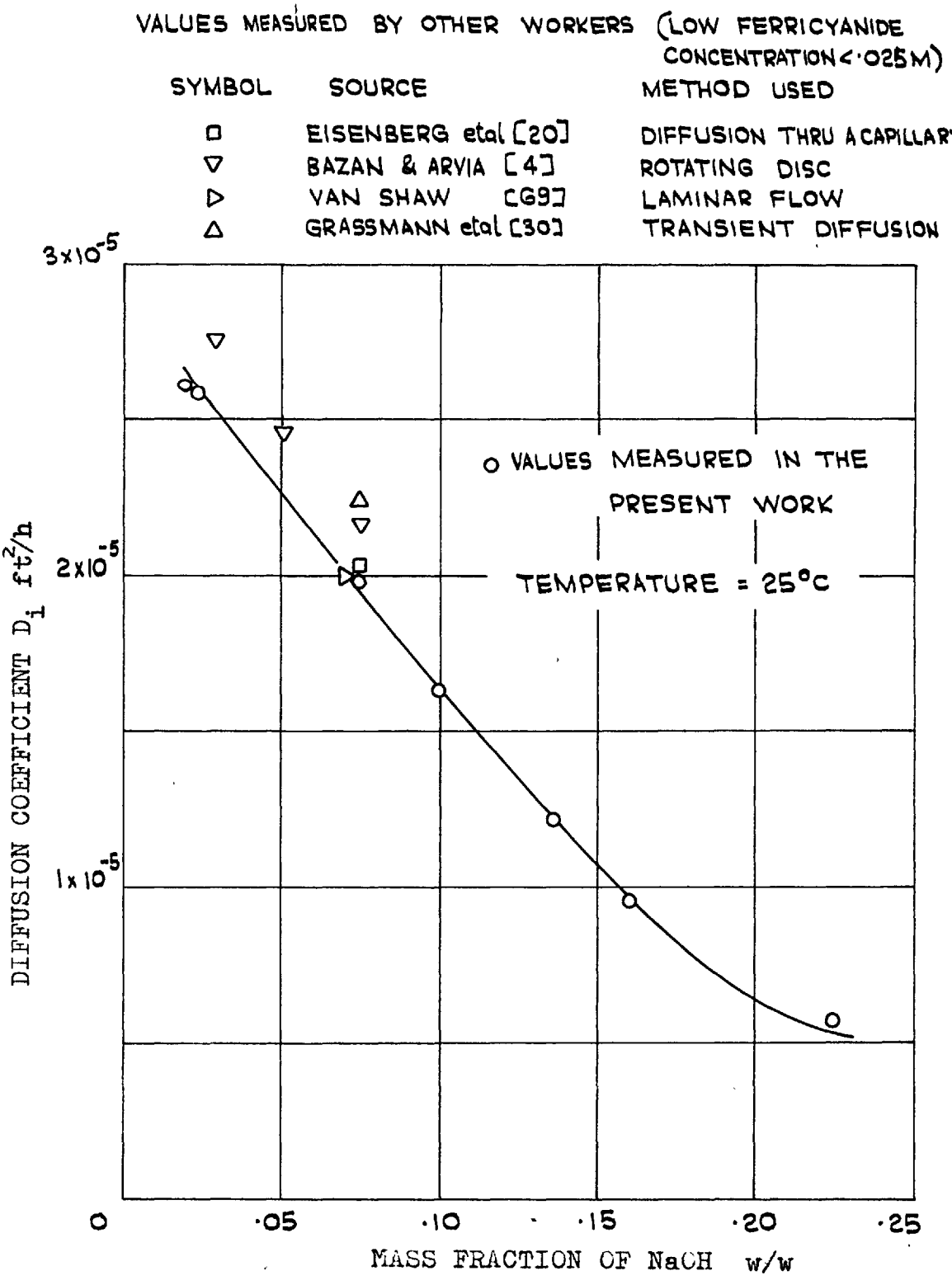

Fig. A.2.3 MEASURED VALUES OF DIFFUSION COEFFT AT VARIOUS NaOH CONCENTRATIONS AND COMPARISONS WITH VALUES OBTAINED BY OTHER WORKERS

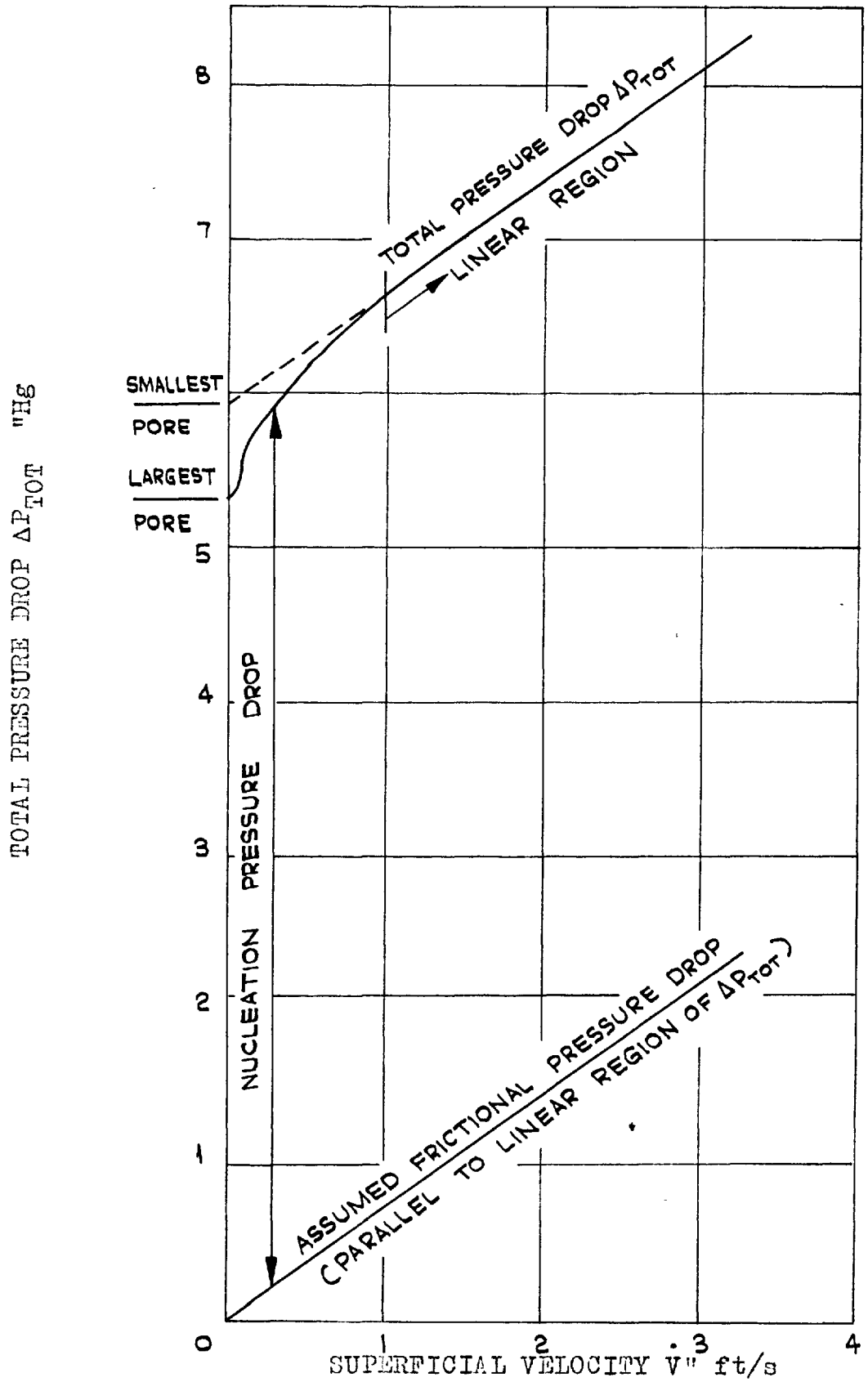

FIG. A.24 PRESSURE DROP ACROSS THE POROUS PLATE.

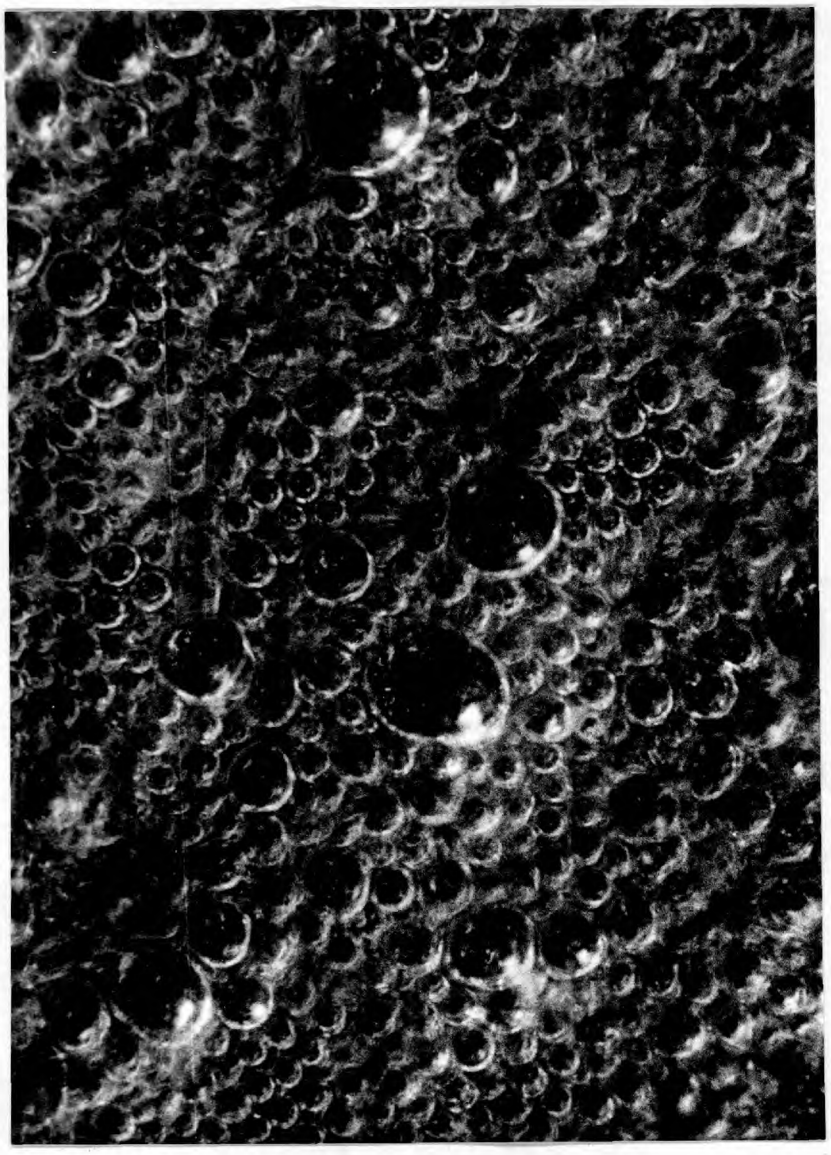

LINEAR ENLARGEMENT: x1o

MATERIAL: PALL GRADE D

SUPERFICIAL VELOCITY: 0.26 ft/s

Fig. A.2.5 PHOTOGRAPH OF BUBBLING SURFACE

Appendix III. Tables of experimental data.

In the following tables, the experimental data are presented as conductances, in the units of lb/ft^2h and superficial velocities, in the units ft/s. A separate table is employed for each test series; in the test series in which gas properties were varied, a separate table is employed for each electrode used. The figures to which the tables correspond are indicated.

TABLE A.3.1 VARYING THE POOL DEPTH

CORRESPONDING FIGURE : 6.2

POOL DEPTH	8"		4"		2"		0·25"		0·75"		6"		3"		1·5"	
TEST Nº	3019		3020		3021		3022		3023		3024		3025		3026	
	V"	g	V"	g	V"	g	V"	g	V"	g	V"	g	V"	g	V"	g
	·876	563·5	·630	546	·566	486	·796	567	·494	551	·491	548	·567	575	·494	540
	1·034	606·8	·882	599	·842	615	1·008	570	·692	600	·740	601	·840	620	·747	588
	1·230	630·8	1·039	627	1·008	651	1·181	572	·887	616	·922	626	1·041	648	·929	620
	1·368	608·4	1·236	633	1·243	663	1·303	573	1·007	635	1·107	646	1·210	661	1·149	642
	1·616	638	1·379	650	1·387	671	1·439	493	1·180	646	1·232	659	1·354	667	1·274	649
	1·825	638	1·585	660	1·539	674	1·588	419	1·330	656	1·398	668	1·486	671	1·430	656
	2·084	627·6	1·736	664	1·679	671			1·463	658	1·503	673	1·629	674	1·588	658
	2·285	607·6	1·875	661	1·800	662			1·609	657	1·643	673	1·759	679	1·81	660
	2·464	593·2	1·991	652	1·899	662			1·742	651	1·710	672	1·880	674	1·89	658
	4·885	492	2·112	644	1·983	660			1·885	646	1·831	670	1·994	667	2·02	655
	·332	569	2·248	631	2·174	649			1·999	635	1·946	667	2·162	657	2·12	650
	1·034	610	2·388	615	2·254	634			2·124	619	2·091	656	2·238	650	2·23	634
	1·230	627	2·534	598	2·487	609					2·211	642	2·337	634	2·335	619
	1·422	645			·404	555					2·321	630			2·455	608
	1·570	652			·705	604										
	1·704	658			1·044	654										
	1·826	658			1·241	665										
	1·961	651			1·436	688										
	2·065	648			1·585	691										
	2·187	640			1·719	692·5										
	2·317	630			1·882	687										
	2·421	617			1·997	676										
	2·535	607			2·122	669										
	2·726	590			2·272	650										
					2·397	635										

TABLE A.3.2 VARYING THE POOL DIAMETER

POOL DIA.	0.69"		3.44"		0.9"		1.1"	
TEST Nº	3042		3041		3043		3044	
	$\dot{V}$"	g_i	$\dot{V}$"	g_i	$\dot{V}$"	g_i	$\dot{V}$"	g_i
	.471	483.1	.472	418	.472	459	.477	413.5
	.839	564.1	.858	534	.853	573	.854	526.5
	1.023	604.2	1.134	594	1.128	625.8	1.169	592.2
	1.187	625.6	1.375	676	1.364	653.6	1.384	621.2
	1.384	663.9	1.610	636	1.612	674	1.820	643.5
	1.602	691.6	1.796	646	1.788	680.6	1.790	652.1
	1.777	711.2	2.006	654	1.995	687.9	1.998	657
	1.995	723.7	2.207	656	2.179	692.5	2.182	657
	2.199	733.4	2.388	652	2.386	695.3	2.388	653
	2.376	742.3	2.559	649	2.592	695.3	2.594	647.3
	2.543	766.3	2.734	645	2.786	692.5	2.793	639.6
	2.724	775.3	2.905	640	2.957	688.8	3.001	629
	2.899	781.5	3.072	632	3.152	686		
	3.078	788.7	3.254	627	3.334	680.6		
	3.238	787.6			3.523	675		
	3.392	785.1						
	3.549	782.4						
	3.719	772.6						
	3.903	765.5						
	4.070	764.6						
	4.277	758.4						

CORRESPONDING FIGURE: 6.3

TABLE A.3.3 TESTS WITH 1"DIA CATHODE

TEST Nº	3017		3018	
	$\dot{V}$"	g_i	$\dot{V}$"	g_i
	.257	265.3	.408	391.1
	.386	326.4	.603	450.7
	.488	372	.809	492.1
	.623	424.6	1.036	523.4
	.722	455.6	1.265	545.2
	.817	476.4	1.449	561.2
	.911	502.7	1.599	567.7
	1.029	525.9	1.744	573.6
	1.148	549.1	1.878	573.6
	1.255	559.2	2.001	573.6
	1.359	568.5	2.098	569.9
	1.460	577.0	2.218	567.7
	1.553	583.9	2.324	565.6
	1.634	587	2.427	559.8
	1.715	587.8	2.553	559.8
	1.797	587.8	2.695	549.6
	1.886	589.4		
	2.019	587.8		
	2.116	586.3		
	2.221	581.6		
	2.308	580.1		

TABLE A.3.4 VARYING THE GAS ELECTRODE: Nº 1

GAS	NITROGEN		HYDROGEN		ARGON		50/50 N/H		50/50 N/H		ARGON		BUTANE	
TEST Nº	63		66		69		70		71		72		73	
	V"	g_i	V"	g_i	V"	g_i	V"	g_i	V"	g_i	V"	g_i	V"	g_i
	1.470	405	·477	308.7	·606	287.4	·595	265.2	1.151	265.1	·738	2.735	·550	577.4
	1.776	448	·768	299.1	·969	318.1	1.081	274.3	1.626	285.4	1.458	3.618	1.017	733.3
	2.069	475	1.138	287.9	1.255	349.9	1.488	290.3	2.030	317.1	1.807	4.07.8	1.277	772.5
	2.321	498	1.503	277.1	1.503	384.5	1.814	313.7	2.416	334.7	2.107	4305	1.513	790
	2.550	514	1.928	242.3	1.735	413	2.169	338.8	2.709	349.2	2.322	4409	1.704	791.7
	2.730	517	2.259	237.6	1.944	432.5	2.468	353.4	2.991	354.6	2.535	451.9	1.873	791.7
	2.959	518	2632	235.3	2.125	444.2	2.711	365.8	3.322	362.3	2.738	452.6	2.029	775.2
	3.110	519	3.014	241.1	2.292	456.5	2.993	374	3.603	367.7	2.922	453.2	2.214	750.8
	3.312	517	3.372	244.6	2.447	459.8	3.252	377.2	3.899	370.9	3.121	448.9		
	3.506	514	3.742	246.5	2.608	464.9	3.519	379	4.192	368.6	3.268	444.6		
	4.344	501.5	4.435	250.6	2.766	468.2	3.796	384.1	4.520	366.4	3.415	441.5		
			5.186	254.8	2.897	469.3	4.055	388.6	4.808	364.1	3.600	432.3		
			5.952	255.7	3.066	468.2	4.300	381.8	5.060	362.3				
			6.627	255.1	3.269	463	4.510	379.5	5.261	360.9				
			7.270	252.2	3.371	459.3	4.795	377.2						
			7.843	251.9	3.506	454.8	5.028	374.9						
			8.514	249.3	3.725	448.1								
			9.185	245.5										
			10.06	241.4										

CORRESPONDING FIGURE: 6.8

ELECTRODE: Nº 3

NITROGEN		HELIUM		HYDROGEN	
103		105		108	
V"	g_i	V"	g_i	V"	g_i
878	347.5	1.687	171.5	2.262	263.1
1.384	419.9	2.335	170	3.254	265.8
1.702	458.6	2.941	174.9	4.033	269.4
2.029	460.5	3.552	179.6	4.766	270.4
2.278	511.3	3.978	181.1	5.351	276
2.452	521.5	4.385	182.8	5.861	277
2.651	526.6	4.804	181.7	6.449	277
2.847	530.4	5.099	180	6.920	276
3.025	529.0	5.385	178.7	7.490	274.7
3.178	520.2	5.733	178.5	8.087	272.7
3.381	515.1	6.131	176.8	8.640	269.8

GAS	HELIUM		ARGON	
TEST Nº	104		107	
	V"	g_i	V"	g_i
	2.366	168.4	1.187	366.7
	3.142	175.6	1.660	430.6
	3.621	179.0	2.012	461.9
	4.114	180.5	2.236	478.7
	4.609	181.1	2.404	490.6
	5.064	182.6	2.540	492.8
	5.470	179.4	2.636	497.6
	5.915	178.4	2.857	493.8
			3.045	491.7
			3.231	485.2

CORRESPONDING FIGURE: 6.9

GAS: ARGON

TABLE A.3.4 VARYING SYSTEM PRESSURE ELECTRODE: Nº 7

PRESSURE	0 g.		20" Hg g.		−10" Hg g		10" Hg g		−5" Hg g		−15" Hg g	
TEST Nº	149		152		154		156		158		162	
	V̇"	gᵢ	V̇"	gᵢ	V̇"	gᵢ	V̇"	gᵢ	V̇"	gᵢ	V̇"	gᵢ
	1.310	469.3	1.087	596.7	1.369	414.9	1.060	508.8	1.409	458.5	2.149	401
	1.712	537.7	1.267	637.2	1.765	458.7	1.354	572.6	1.789	508.6	2.525	426.4
	2.011	560.4	1.448	673.7	2.125	481.1	1.535	608.6	2.131	533.4	2.853	443.9
	2.233	569.6	1.606	692.4	2.446	503.5	1.672	621.6	2.376	544.7	3.188	448.9
	2.448	578.7	1.744	694.4	2.735	509.6	1.868	638.8	2.59	546.6	3.501	443.9
	2.614	578.7	1.874	706.2	3.50	515.0	2.023	650.3	2.802	543.5	3.796	443.9
	2.812	568.7	2.034	710.2	3.246	514.5	2.173	650.3	3.003	539.7	4.069	433.9
	2.988	560.4	2.168	710.2	3.46	507.9	2.323	648.6	3.182	532.7	4.367	431.4
			2.311	695.4	3.700	503.0	2.436	643.7	3.369	523.8		
			2.465	685.5	3.820	495.9	2.602	629				
							2.769	615.9				

PRESSURE	14" Hg g.		−20" Hg g.		0 g.		−15" Hg g		−10" Hg g		−20" Hg g.	
TEST Nº	151		153		155		157		161		163	
	V̇"	gᵢ	V̇"	gᵢ	V̇"	gᵢ	V̇"	gᵢ	V̇"	gᵢ	V̇"	gᵢ
	1.091	572	2.596	325.1	1.633	562.4	2.082	391.1	1.811	463.6	2.169	299.5
	1.357	616.3	3.163	348.6	1.881	583	2.457	411.3	2.135	493.2	2.824	333.2
	1.555	642.1	3.676	366.7	2.107	602.2	2.788	426.9	2.471	510.6	3.320	349.1
	1.725	652.2	4.100	369.4	2.309	603.6	3.093	430	2.746	521.4	3.725	357
	1.873	659.6	4.572	372.2	2.503	606.5	3.396	430	2.969	524.7	4.19	363
	2.019	659.6	4.936	367.8	2.676	607.2	3.73	429.4	3.199	524.1	4.62	361
	2.157	655	5.269	364	2.858	599.4	3.984	421.7	3.399	514	4.93	357
	2.314	655	5.638	357.9	2.978	588.7	4.324	411.8	3.631	507.3	5.44	351
	2.507	643.9			3.152	578.8						

CORRESPONDING FIGURE: 6.4

GAS: NITROGEN

ELECTRODE: Nº 1

PRESSURE	0 g.		−10" Hg g		0 g.	
TEST Nº	64		78		81	
	V̇"	gᵢ	V̇"	gᵢ	V̇"	gᵢ
	.741	334.8	1.538	301.0	.825	354
	1.105	374.4	2.086	370.3	1.300	406
	1.448	408.3	2.680	403.9	1.832	462.5
	1.695	430.1	3.245	412.4	2.28	496
	1.935	457.1	3.547	414	2.56	503
	2.138	471.4	3.839	414.8	2.79	505.5
	2.374	484.6	4.123	412.4	2.96	509
	2.570	489.8	4.363	410.1	3.095	505.5
	2.744	491.5	4.597	405.4	3.225	509
	2.961	495.5			3.41	503
	3.268	493.8			3.535	493
	3.449	490.9				
	3.676	480				

PRESSURE	10" Hg g.		−18" Hg g		20" Hg g	
TEST Nº	77		80		82	
	V̇"	gᵢ	V̇"	gᵢ	V̇"	gᵢ
	.8635	372.3	.745	258.3	.644	423
	1.130	419.7	1.408	257.2	.955	489
	1.357	449.6	2.225	274.1	1.323	545
	1.535	475.7	2.783	283.1	1.659	592
	1.729	500.9	3.214	287.3	1.870	608
	1.929	517	3.633	282.0	2.035	619.5
	2.164	532.3	4.097	276.7	2.21	622
	2.410	540			2.44	618
	2.690	540			2.63	609
	2.899	536.2			2.745	604
	3.163	524.7				

CORRESPONDING FIGURE: 6.5

GAS: NITROGEN

TABLE A.3.4 ELECTRODE: Nº4

PRESSURE	0 g		-5" Hg g		-15" Hg g	
TEST Nº	115		131		133	
	V̇"	gi	V̇'	gi	V̇"	gi
	·376	321.3	2.332	437.5	2.798	328
	·848	362.4	2.618	450.7	3.388	336.8
	1.290	398.6	2.986	454.9	3.907	338
	1.671	435.4	3.237	456.7	4.355	338
	2.086	478.9	3.465	454.9	4.710	332.5
	2.536	504.1	3.651	450.7	5.172	328.6
	2.861	508.4	3.818	447.7		
	3.036	504.1				
	3.288	501.0				
	3.615	492.4				

PRESSURE	-5" Hg g.		-10" Hg g	
TEST Nº	130		132	
	V̇"	gi	V̇'	gi
	2.155	423.6	2.382	373.4
	2.647	451.9	2.847	393.5
	2.923	455.5	3.301	397.1
	3.248	457.9	3.634	398.9
	3.473	456.7	3.898	395.9
	3.766	449.5	4.147	391.2
			4.470	384.1

CORRESPONDING FIGURE: 6.6

GAS: NITROGEN

ELECTRODE: Nº7

	-18" Hg g		-16" Hg g		7.5" Hg g	
	143		145		147	
	V̇'	gi	V̇'	gi	V̇'	gi
	2.005	292	2.536	379.3	1.507	552.2
	2.549	320.1	3.137	409.0	1.735	591.4
	3.092	344.5	3.664	423.1	1.977	615.6
	3.690	360.4	4.060	435.3	2.211	627.0
	4.033	384.3	4.511	432.8	2.436	629.8
	4.432	390.4	4.967	429.9	2.625	628.4
	4.795	390.9	5.382	421.6	2.804	622.7
	5.230	383.4			2.980	614.2
	5.620	379.6				
	6.115	372.6				

	-20" Hg g		0 g		15" Hg g	
	144		146		148	
	V̇"	gi	V̇"	gi	V̇"	gi
	3.097	331.9	1.855	536.7	1.194	556.7
	3.963	351.0	2.201	566.8	1.500	615.7
	4.608	361.0	2.472	578.1	1.759	647.0
	5.118	362.9	2.718	583.2	1.966	664.8
	5.585	358.1	2.944	581.8	2.163	673.1
	6.050	355.7	3.178	573.9	2.344	673.1
	6.538	354.3	3.398	565.3	2.507	656.4
					2.691	655.6

CORRESPONDING FIGURE: 6.7

TABLE A.3.4 VARYING THE GAS ELECTRODE: Nº 8

GAS TEST Nº	NITROGEN 164		NITROGEN 168		HYDROGEN 171		15/85 N/H 173		HELIUM 177	
	$\dot{V}''$	g_i	$\dot{V}''$	g_i	$\dot{V}''$	g_i	$\dot{V}''$	g_i	$\dot{V}''$	g_i
	1.603	450.7	2.708	302.9	3.181	288	3.387	278.2	2.792	155
	1.994	509.5	1.369	426.1	4.575	300.3	4.039	288.6	4.043	160.3
	2.232	523.0	1.819	490.2	5.630	304	4.633	293.8	4.931	162.2
	2.453	535.4	1.921	518.5	6.364	306.5	5.145	298.2	5.670	162.5
	2.666	543	2.240	543.6	7.029	307.7	5.650	296.4	6.319	162.2
	2.863	545.4	2.526	553.7	7.775	305.3	6.060	296.4	7.043	162.0
	3.072	547.2	2.779	565.6	8.432	304	6.563	292.7	7.814	159.6
	3.260	539.5	3.006	565.6	9.276	298.7	6.940	289.7		
	3.511	535.4	3.217	559.3			7.405	287.5		
	3.729	526.0	3.424	551.8						

GAS TEST Nº	HELIUM 166		20/80 N/H 169		4/96 N/H 172		8/92 N/H 175	
	$\dot{V}''$	g_i	$\dot{V}''$	g_i	$\dot{V}''$	g_i	$\dot{V}''$	g_i
	2.337	165.9	3.491	344.2	3.901	262.3	3.468	278
	3.007	173.2	4.178	354.2	4.963	269.5	4.272	306.8
	3.621	178.3	4.736	357.5	5.830	273.5	5.004	313.5
	4.115	181.3	5.260	355.9	6.577	275.3	5.649	317.9
	4.600	187.2	5.750	357.5	7.218	275.3	6.271	319.4
	5.018	188.2	6.183	353.4	7.841	271.7	6.961	319.4
	5.570	189.3	6.617	351.3	8.507	266.3	7.393	316.3
	6.271	189.3	7.212	345.1	9.084	261.9	7.917	313.5
	6.811	187.8					8.496	309.9
	7.417	187.2						
	8.047	186.1						
	8.671	183.1						

CORRESPONDING FIGURE: 6.10

ELECTRODE: Nº 9

NITROGEN 178		ARGON 179		50/50 N/H 184		HYDROGEN 186		N_2O 190	
$\dot{V}''$	g_i	$\dot{V}''$	g_i	$\dot{V}''$	g_i	$\dot{V}''$	g_i	$\dot{V}''$	g_i
.7217	279.1	.572	270	2.662	376.9	3.444	252.4	3.758	315.8
1.030	321.3	1.047	337	3.056	387.2	4.664	263.6	.5606	392.7
1.313	370.3	1.422	402.6	3.385	390	5.578	266.	.8192	472.8
1.556	418.0	1.903	453.9	3.715	390	6.347	267	1.075	538
1.766	453.9	2.038	478.5	4.026	388.9	7.198	265.3	1.351	598
2.018	478.8	2.302	488.1	4.332	384.9	8.047	265.3	1.62	640.6
2.307	521.6	2.530	492.2	4.679	377.5	8.832	259.6	1.831	667.6
2.580	524.4	2.736	492.9	5.352	365.6	9.607	251.7	2.028	681.5
2.828	527.1	2.948	486	2.775	378.7	3.371	258.2	2.303	689.6
3.051	525.1	3.209	473	3.131	384.9	4.584	264.3	2.388	688.8
3.302	514.7	3.550	454.6	3.484	387.8	5.618	265.3	2.548	680.6
3.585	503.7			3.797	390	6.518	263.3	2.714	674.1
				4.101	383.2	7.394	259.2	2.905	658.6
				4.397	381.5	8.217	255.5		
				4.723	376.4				

ARGON 180		NITROGEN 181		70/30 N/H 182		30/70 N/H 185		BUTANE 187		METHANE 191	
$\dot{V}''$	g_i	$\dot{V}''$	g_i	$\dot{V}''$	g_i	$\dot{V}''$	g_i	$\dot{V}''$	g_i	$\dot{V}''$	g_i
1.021	310.2	1.102	397.7	.9865	317.1	2.084	233.6	.5119	520.6	.8885	367.6
1.422	398.6	1.545	447.1	1.432	370.4	2.865	315.5	.7591	596	1.353	440.4
1.727	445.2	1.927	487.7	1.977	422.5	3.406	325.2	.9568	643.5	1.798	502.4
2.00	472.5	2.271	508.1	2.358	445.6	3.977	334.6	1.198	683	2.297	548.6
2.266	490	2.577	515	2.660	456.6	4.281	336.5	1.396	691.1	2.672	560.3
2.507	497.5	2.858	515	2.955	460.1	4.717	332.6	1.59	691.1	3.106	561.1
2.726	497.5	3.115	509.2	3.234	459.5	5.170	330.7	1.764	686.6	3.413	558
2.941	494.6	3.382	501.7	3.483	454.3	5.662	323.3	1.938	679.4	3.794	548.6
3.177	482.4	3.647	484.8	3.743	446.8			2.134	665.1	4.152	532.9
3.428	466.7										

CORRESPONDING FIGURE: 6.11

TABLE A.3.4 VARYING THE GAS ELECTRODE: Nº 10

GAS	FREON 22		NITROGEN		N_2O	
TEST Nº	194		198		201	
	$\dot{V}''$	g_i	$\dot{V}''$	g_i	$\dot{V}''$	g_i
	·6909	681.6	·8875	310.9	·8881	512.5
	·854	737.5	1·305	379.6	1·251	554.5
	1·041	789.6	1·685	433	1·517	683.3
	1·177	821.4	1·998	467.7	1·74	597.3
	1·299	833.9	2·284	484.2	1·941	606.2
	1·422	841.6	2·538	491.9	2·135	604.7
	1·565	839.7	2·762	492.4	2·303	598.1
	1·686	835.8	2·976	496.8	2·488	591.4
	1·814	817.5	3·185	484.7	2·684	583.3
	1·948	794.4	3·396	487.5	2·851	571.5
			3·577	482		
			3·760	475.9		

GAS	FREON 114		METHANE	
TEST Nº	195		199	
	$\dot{V}''$	g_i	$\dot{V}''$	g_i
	·2973	439.2	·8902	430.3
	·5032	547.8	1·282	450.2
	·667	598.2	1·721	492.
	·7919	625.6	2·148	517
	·906	653	2·519	530.7
	1·007	673.8	2·179	528.8
	1·035	701.2	2·664	543.8
	1·141	711.0	3·046	541.9
	1·222	713.2	3·462	537.5
	1·315	712.2	3·766	535
	1·402	704.5		

CORRESPONDING FIGURE: 6.12

TABLE A.3.4 VARYING THE NATURE OF THE GAS, ELECTRODE Nº: 11

GAS	NITROGEN		N_2O		METHANE		FREON 13		PROPANE		HYDROGEN		ARGON		HELIUM		HELIUM		HYDROGEN		BUTANE	
TEST Nº	209		210		212		215		219		222		224		226		228		229		235	
	$\dot{V}$"	g_i	$\dot{V}$"	g_i	$\dot{V}$"	g_i	$\dot{V}$"	g_i	$\dot{V}$"	g_i	$\dot{V}$"	g_i	$\dot{V}$"	g_i	$\dot{V}$"	g_i	$\dot{V}$"	g_i	$\dot{V}$"	g_i	$\dot{V}$"	g_i
	·1707	254.9	·1533	322.4	·272	340	·0594	230.8	·1142	253.5	·524	295.3	·1232	257.6	·4346	288.9	·184	248.4	·2573	312.1	·191	363
	·2573	278.4	·2225	382.4	·364	382	·1292	323.7	·2141	356.5	1·061	277.4	·2450	287	·7627	288.5	·2757	269.3	·3765	314.6	·270	431
	·4663	335.4	·3331	451.7	·585	465	·201	422.2	·3267	446	1·634	263.8	·3822	326.9	1·084	306.3	·3944	275.2	·5261	312.4	·350	486
	·6947	412.6	·4424	515.5	·797	521	·280	492.6	·4566	523	2·283	280.1	·5272	367.7	1·505	274.6	·5195	263.2	·6937	305.1	·494	563
	·9183	472.3	·6033	589.5	1·064	582	·396	579.8	·6463	614	3·015	300.2	·7141	421.5	2·323	270.8	·7471	238.5	·9109	296.4	·602	606
	1·181	528.6	·7781	645.7	1·45	633	·491	627.7	·8175	675	3·815	315.4	·8782	473.7	2·599	277.4	1·177	184.2	1·304	286.9	·755	660
	1·362	550.8	·9330	677.5	1·823	663	·595	674.1	·9993	725	4·365	320.3	1·095	519.3	3·066	285.6	1·533	163.3	1·686	278.8	·900	704
	1·611	589	1·138	716.9	2·107	676	·712	710.7	1·193	755	5·075	326.9	1·346	559.3	3·582	291.5	2·121	160.9	2·347	295.6	1·069	731
	1·820	606.5	1·326	745.1	2·383	684	·800	733.2	1·363	774	5·71	331.2	1·527	583.7	4·096	295	2·574	168.5	3·131	314.6	1·189	748
	2·039	627.3	1·501	761	2·652	685	·894	753	1·531	789	6·51	333.9	1·707	601.7	4·642	298.4	3·095	176	3·973	323.4	1·333	765
	2·233	634	1·646	769.4	2·955	682	·973	767.	1·677	786	7·14	331.2	1·847	613.1	5·218	301.2	3·601	183.2	4·612	327.1	1·467	774
	2·410	638	1·796	776.9	3·125	676	1·061	775.5	1·809	792	7·80	326.9	2·024	624.5	5·734	299.8	4·111	188.7	5·258	330.3	1·596	781
	2·63	638	1·94	776.9	3·365	668	1·150	783.9	1·967	794	8·77	317.6	2·206	631.8	6·210	298.4	4·637	192.5	5·911	331.4	1·721	781
	2·871	629.9	2·083	766.6			1·250	788.1	2·134	785			2·393	634.3	6·776	296.3	5·199	193.9	6·723	327.8	1·871	782
	3·117	621.2	2·236	759.1			1·346	789.5	2·30	765			2·572	632.7	7·396	294.6	5·757	195.2	7·406	328.9	2.00	771
							1·437	785.3					2·750	627.8	8·092	290.1	6·223	195.2	8·105	322.3	2.09	764
							1·530	776.9					2·874	620.4			6·793	193.9	9·047	315		

CORRESPONDING FIGURE: 6.13

TABLE A.3.5 VARYING THE NaOH CONCENTRATION CORRESPONDING FIGURE: 6.15

NaOH conc. w/w	·01948		·1616		·0498		·0998		·1198		·1935		·1383		·1551	
TEST Nº	5010		5011		5014		5015		5016		5017		5018		5022	
	V̇	g_i	V̇	g_i	V̇	g_i	V̇	g_i	V̇	g_i	V̇	g_i	V̇	g_i	V̇	g_i
	·0673	277.2	·07369	90	·06785	221.6	·06785	153.7	·06822	154.9	·06844	90.63	·07444	131.6	·06844	121
	·1107	349	·1192	104	·1115	283	·1154	189.7	·1062	180.5	·1106	112	·1101	152.8	·1084	138.8
	·1586	414	·1712	106.1	·1586	330.1	·1587	208	·1607	206.7	·1599	128.9	·1605	166	·1592	149.5
	·2065	467.6	·2352	129	·2159	364.6	·2161	219.6	·214	221.9	·2157	139.6	·2148	174.4	·2144	156.3
	·3121	561.1	·2921	137.2	·2687	391.5	·2691	229.4	·2693	236.4	·2686	147.2	·2658	177.2	·2604	160.2
	·3608	595.4	·3574	146.2	·3216	422.2	·321	242.2	·322	251.6	·3218	154.9	·3183	181.	·3187	164.2
	·4328	637.6	·4450	158	·4086	461.5	·4066	259.3	·4081	271.4	·4112	168.6	·4077	185.2	·4001	168.6
	·5043	672.9	·5258	168.7	·4816	491.3	·4822	277.6	·4834	286.5	·4862	175.9	·4835	189.9	·4833	178.5
	·5718	700.3	·625	182.2	·5715	522.9	·5751	300.1	·5772	302.8	·5835	185.1	·5830	199.8	·5866	184.4
	·6669	732.2	·750	196	·685	566.1	·6826	327	·6842	323.9	·6872	192.3	·6819	210.2	·6895	196.7
	·7568	758.5	·8601	207	·7876	597.8	·7856	353.8	·7876	340.7	·7951	202.7	·7948	223.3	·7939	205.8
	·8508	784.7	·9966	222.2	·9108	628.5	·9125	383.7	·9185	367.5	·9243	213.4	·9164	241.2	·9148	220.1
	·9553	806.4	1.166	239.5	1.063	657.2	1.060	407.5	1.067	390.2	1.071	223.7	1.066	262.8	1.067	238.4
	1.070	828.0	1.345	154	1.224	681.2	1.224	432.5	1.228	408.2	1.235	236.7	1.234	282.1	1.24	252.2
	1.185	847.4	1.502	166.5	1.365	700.4	1.366	452.6	1.371	421.6	1.386	246.3	1.384	297.6	1.385	264.9
	1.312	863.4	1.678	278.5	1.523	715.8	1.53	470.3	1.53	433.8	1.554	254.3	1.548	316.9	1.556	284
	1.447	886.2	1.849	289.5	1.677	729.2	1.68	485	1.686	445.5	1.699	262.3	1.689	329.6	1.699	295.9
	1.582	993	2.016	306	1.826	737.9	1.83	494.7	1.839	451.9	1.856	268.4	1.84	347.9	1.848	309.3
	1.712	897.6	2.175	311	1.968	743.6	1.974	506.3	1.984	450.5	2.004	273.3	1.989	360.1	1.998	325.2
	1.843	904.5	2.316	315	2.090	744.6	2.095	518.	2.110	461.2	2.130	279.9	2.112	369.1	2.124	337.1
	1.958	901.	2.458	317	2.217	740.7	2.223	515.5	2.234	463.5	2.256	283.4	2.238	376.6	2.246	347.
	2.065	904.5	2606	321	2.348	735	2.353	517.9	2.364	464.7	2.389	287.2	2.369	381.8	2.375	353
	2.183	899.9	2.754	323.5	2.48	733	2.493	517.9	2.505	464.1	2.533	292.2	2.511	387.9	2.522	360.5
	2.316	894.2	2.915	325	2.62	728.2	2.629	518.5	2.643	461.8	2.676	294.1	2.652	392.6	2.661	365.3
	2.470	888.5	3.088	326	2.774	724.4	2.783	516.7	2.799	460	2.834	295.2	2.808	397.3	2.819	370
	2.661	872.5	3.295	326	2.953	707.1	2.968	511.3	2.988	454.8	3.030	296.4	2.975	402.0	3.007	374.4
	2.852	864.5	3.498	324	3.131	701.4	3.148	509.4	3.167	451.3	3.214	296.4	3.173	401.5	3.181	372.8
	3.052	823.7	3.704	322	3.312	690.8	3.324	503.3	3.352	444.9	3.398	296.4	3.35	400.6	3.36	371.6
	3.277	812.1									3.544	295.6			3.515	369.6
											3.750	295.6			3.675	366.9

TABLE A.3.6 VARYING THE TEMPERATURE

TEMPERATURE	76·2°F		88		96·2		104.6		60·6		69	
TEST Nº	5001		5005		5006		5007		5008		5009	
	V̇"	g_i	V̇"	g_i	V̇"	g_i	V̇"	g_i	V̇"	g_i	V̇"	g_i
	·06687	209.1	·0653	243·3	·06951	276·5	·07014	312	·0669	184.6	·06689	206·7
	·1481	265·2	·1131	297	·1086	319.6	·1162	360	·1137	218.5	·1099	242
	·3209	296·9	·1524	317.7	·1588	346·8	·1596	374.4	·1577	238.8	·155	271.3
	·4511	370.2	·21	337.7	·2159	359.9	·2199	385.9	·2119	259.1	·2071	292
	·6000	421·8	·2621	353	·2666	378.7	·2695	401·3	·2566	275·2	·2604	316·1
	·7369	468	·3251	372·2	·3277	400.2	·3344	424.3	·3163	299.8	·3156	338·5
	·9314	516·8	·4152	406·7	·4211	426·5	·4246	454.1	·4017	334.5	·4029	377.3
	1·158	557.6	·4902	432	·5024	454.6	·5074	480·9	·4749	364.1	·474	409.1
	1·352	601.9	·6037	468.1	·6138	494.9	·6174	515.5	·5817	406·5	·5773	441
	1·524	611	·6967	501.9	·7093	521.1	·7165	547·2	·6767	433·6	·6725	469.4
	1·742	634·5	·8015	528·7	·8135	553	·8253	573·1	·7779	464·1	·7732	502·2
	1·937	651·7	·9215	558·7	·9399	584.9	·9511	604·8	·8985	495·4	·8946	532.3
	2·137	661·7	1·075	590·9	1·096	616.7	1·108	631·6	1·046	524.2	1·047	562·5
	2·306	660.8	1·248	613·9	1·265	636·4	1·273	652·8	1·203	550·4	1·204	583·1
	2·469	660·8	1·391	630·8	1·406	647·7	1·428	671	1·345	571·6	1·341	601·2
	2·628	657.1	1·545	643·1	1·567	674·8	1·586	683·5	1·499	588·6	1·499	617·6
	2·789	650·8	1·696	662·3	1·72	685·1	1·745	693·1	1·649	604·6	1·648	634
	2·769	643·6	1·948	668·4	1·878	693·6	1·904	701·7	1·799	618·2	1·797	644·3
			1·984	676·8	2·03	698·3	2·043	709·4	1·932	623·3	1·931	650·3
			2·114	683·8	2·142	703·9	2·174	715·2	2·053	630·9	2·054	656·4
			2·245	684·5	2·273	705·8	2·308	713·2	2·179	635·1	2·182	658·1
			2·377	684·5	2·411	703	2·448	711·3	2·313	640·2	2·313	659·7
			2·511	684·5	2·542	703·9	2·579	712·3	2·438	640·2	2·439	658·9
			2·655	681·4	2·695	694·5	2·735	704·6	2·582	638·5	2·58	661·5
			2·813	679·1	2·855	691·7	2·895	700·8	2·734	635·1	2·735	661·5
			2·984	666·9	3·028	638	3·076	687·3	2·904	628·4	2·906	651·2
			3·170	657·7	3·215	674·8	3·260	672	3·077	622·4	3·082	640·8
			3358	645·4	3·404	656·1	3·451	663·3	3·256	614	326	627·1

CORRESPONDING FIGURE : 6.16

TABLE A.3.7. EFFECT OF SURFACTANT

NO SURFACTANT		0.15% TEEPOL	
5026		5028	
V̇"	g_i	V̇"	g_i
·078	197·6	·3657	471·1
·1494	247	1·093	718.4
·2138	271·7	1·621	768·5
·3232	308·7	1·936	779·7
·4555	339·2	2·139	779·9
·6218	382·8	2·353	760·7
·8731	447·8	2·570	746·2
1.092	494		
1·357	535·1		
1·635	568		
1·904	587·8		
2·153	596·9		
2·424	599·3		
2·694	594·4		
2·931	584·5		
3·152	571·3		

CORRESPONDING FIGURE: 6.14

TABLE A.3.8 VARYING THE CATHODE THICKNESS

THICKNESS	.051"		.204"		.102"	
TEST Nº	4019		4023		4024	
	V'	g_i	V'	g_i	V'	g_i
	.0108	202.9	.0684	189.6	.06814	183.7
	.1112	240.4	.1354	276.4	.1196	230.8
	.1567	266.6	.2024	314.5	.1782	268.4
	.2153	286.3	.294	357.5	.2332	322.1
	.3074	323.5	.4327	358.8	.4074	358.9
	.4355	358	.6128	390.6	.6043	396.6
	.6186	408.1	.8484	434	.8408	441.7
	.827	465.8	1.078	469.5	1.055	475.7
	1.083	530.2	1.311	496.9	1.282	513.3
	1.303	561.7	1.654	532.4	1.564	560.4
	1.61	605.1	1.874	553.6	1.792	588.7
	1.82	626.1	2.095	566.9	2.041	607.5
	2.028	641.8	2.321	576.7	2.261	616.9
	2.423	653.	2.505	574.9	2.456	625.4
	2.261	652.3	2.734	575.3	2.679	621.7
	2.621	654.5	2.977	567.8	2.913	614.1
	2.86	651.5	3.213	566	3.150	603.8
	3.076	637.3				

CORRESPONDING FIGURE: 6.17

TABLE A.3.9 VARYING THE POROUS MATERIAL GRADE

MATERIAL	PALL D		PALL E		PALL C		INT. NICK		POROSINT		PALL F	
TEST Nº	4010		4012		4014		4016		4018		4008	
	V'	g_i	V'	g_i	V'	g_i	V'	g_i	V'	g_i	V'	g_i
	.0637	109.2	.06432	106.7	.0691	94.35	.0667	115.5	.0679	204.7	.0657	157
	.0932	146.7	.09611	143.6	.1057	133.4	.1136	157.3	.09505	240.3	.1299	209.4
	.1228	174.3	.130	177.3	.1386	164	.1733	168.3	.1263	271.4	.2626	244.3
	.151	194	.1644	210.5	.1722	184.1	.2181	173.6	.1589	290.3	.3010	275.8
	.1835	231	.1953	233.9	.2109	217.3	.2795	180.5	.2328	319.1	.4610	311.5
	.2125	252.5	.2288	259.7	.2487	234.3	.3768	194.5	.2888	338.8	.5620	325
	.2362	263.5	.2661	287.7	.3285	276.5	.4648	214.6	.3555	361.6	.6855	340.6
	.2701	284.9	.3037	306.9	.3862	318.8	.5499	232.5	.4285	388.1	.8146	350
	.3157	311.7	.3851	332.2	.4551	351.4	.6386	251.9	.5084	417.7	.959	3586
	.4198	341.1	.4316	343.9	.5055	361.8	.7284	265.6	.5973	445	1.096	364.8
	.488	357.6	.5035	362.6	.5657	383.9	.8166	276.6	.687	469.2	1.263	370.1
	.5847	387.9	.5773	374.3	.6335	404.1	.8937	284.5	.7867	497.3	1.368	372.9
	.6863	393.3	.6205	376.6	.7104	423	1.030	295.9	.8834	516.2	1.534	375.4
	.7746	401.3	.7175	386.5	.808	447	1.133	301.3	.9855	538.2	1.685	377
	.8913	408.4	.8369	396.3	.902	459.4	1.240	306.2	1.196	568.5	1.816	376.6
	1.090	413.8	.9538	401	1.001	467.9	1.364	312.7	1.311	582.2	1.981	375.8
	1.201	414.7	1.089	408	1.106	478.9	1.468	316.1	1.423	591.3	2.112	375
	1.321	413.8	1.233	409.4	1.217	481.5	1.58	318.4	1.554	601.1	2.251	373.4
	1.434	413.3	1.369	413.1	1.328	480.2	1.705	321	1.687	612.5	2.411	369.7
	1.556	412	1.518	413.1	1.443	479.6	1.807	322.5	1.826	621.6	2.578	366.4
	1.686	411.1	1.64	412.2	1.542	477.6	1.939	324.6	1.958	625.4	2.757	363.1
	1.846	408.4	1.79	410.8	1.678	472.4	2.060	325.2	2.090	625.4	2.897	357.8
	1.99	408	1.971	407.1	1.838	467.2	2.196	326.7	2.229	629.9	3.094	352
	2.138	406.6	2.133	402.9	1.992	464	2.301	326.7	2.35	630.7	3.341	343
	2.294	403.1	2.314	399.6	2.145	960	2.421	326.3	2.488	628.4		
	2.477	399	2.483	392.6	2.335	454.8	2.552	8237	2.64	625.4		
	2.642	395	2.643	388.3	2.516	448.3	2.708	322.9	2.776	621.6		
	2.774	390.1	2.801	382.3	2.689	443.1	2.893	319.1	2.907	612.5		
	2.906	3879	2.967	379	2.857	435.3			3.078	609.5		

CORRESPONDING FIGURE: 6.1

TABLE A.3.10 EFFECT OF ELECTRODE MOUNTING

TEST Nº	RECESSED 3045		FLUSH 3046	
	$\dot{V}$"	g_i	$\dot{V}$"	g_i
	·379	223	·0677	247.9
	·551	250	·1046	266.1
	·722	276	·1531	298.6
	·893	314	·2148	331.1
	·979	328	·3071	366.3
	1.145	366	·4334	418.1
	1.305	396	·615	474.3
	1.438	421	·8206	522.6
	1.562	440	1.072	572.7
	1.703	461	1.296	594.6
	1.845	480	1.599	616.6
	1.978	495	1.806	625.4
	2.109	506	2.010	631.5
	2.237	518	2.244	634.2
	2.36	524	2.404	634.2
	2.488	528	2.608	632.4
	2.616	530	2.841	626.3
	2.77	5305		
	2.921	530		
	3.085	526		
	3.275	523		

CORRESPONDING FIGURE: 6.19

TABLE A.3.11 VARIOUS GASES WITH PALL GRADE C

METHANE 240		ARGON 241		FREON 13 242		N_2O 243	
$\dot{V}$"	g_i	$\dot{V}$"	g_i	$\dot{V}$"	g_i	$\dot{V}$"	g_i
·1339	113.6	·0827	166	·0637	110	·1135	197
·2165	212	·133	215.5	·0935	159.4	·168	296
·339	282	·207	247	·140	209.5	·221	311
·453	330	·288	292	·209	281	·302	353
·645	379.5	·412	340	·292	327	·4395	405
·894	423	·577	379	·371	361	·545	447
1.128	462.5	·825	396	·452	379	·675	471
1.39	471	·898	432	·528	409	·79	487
1.64	470	1.05	437	·604	411.5	·9	499
1.955	464	1.25	437	·677	417	1.02	500
2.27	457	1.45	434	·748	420.5	1.13	501
2.54	444	1.64	429	·832	423	1.26	499
		1.838	421	·925	422	1.14	499
				1.030	421.5	1.57	496
				1.13	421	1.70	488
				1.24	415		
				1.35	409		
				1.47	403		

CORRESPONDING FIGURE: 7.10